

IOWA STATE UNIVERSITY

Digital Repository

Retrospective Theses and Dissertations

Iowa State University Capstones, Theses and
Dissertations

1970

Incompressible skewed turbulent boundary layer on an end wall of a curved two-dimensional diffuser

Marvin Dale Smith
Iowa State University

Follow this and additional works at: <https://lib.dr.iastate.edu/rtd>



Part of the [Mechanical Engineering Commons](#)

Recommended Citation

Smith, Marvin Dale, "Incompressible skewed turbulent boundary layer on an end wall of a curved two-dimensional diffuser" (1970).
Retrospective Theses and Dissertations. 4199.
<https://lib.dr.iastate.edu/rtd/4199>

This Dissertation is brought to you for free and open access by the Iowa State University Capstones, Theses and Dissertations at Iowa State University Digital Repository. It has been accepted for inclusion in Retrospective Theses and Dissertations by an authorized administrator of Iowa State University Digital Repository. For more information, please contact digirep@iastate.edu.



70-18,908

SMITH, Marvin Dale, 1935-
INCOMPRESSIBLE SKEWED TURBULENT BOUNDARY LAYER
ON AN END WALL OF A CURVED TWO-DIMENSIONAL
DIFFUSER.

Iowa State University, Ph.D., 1970
Engineering, mechanical

University Microfilms, A XEROX Company , Ann Arbor, Michigan

**INCOMPRESSIBLE SKEWED TURBULENT BOUNDARY LAYER ON AN END WALL
OF A CURVED TWO-DIMENSIONAL DIFFUSER**

by

Marvin Dale Smith

**A Dissertation Submitted to the
Graduate Faculty in Partial Fulfillment of
The Requirements for the Degree of
DOCTOR OF PHILOSOPHY**

**Major Subjects: Mechanical Engineering
Aerospace Engineering**

Approved:

Signature was redacted for privacy.

In Charge of Major Work

Signature was redacted for privacy.

Heads of Major Departments

Signature was redacted for privacy.

Dean of Graduate College

**Iowa State University
Of Science and Technology
Ames, Iowa**

1970

TABLE OF CONTENTS

	Page
	iv
SYMBOLS AND NOTATION	1
INTRODUCTION	9
REVIEW OF LITERATURE	28
The Two-Dimensional Turbulent Boundary Layer	9
The Skewed Turbulent Boundary Layer	50
THEORETICAL DEVELOPMENT	50
Similarity Parameters	50
Order of Magnitude Analysis	68
EXPERIMENTAL APPARATUS	74
EXPERIMENTAL PROCEDURES	85
Instrumentation Calibration	85
Preliminary Procedures	96
Data Acquisition	100
EXPERIMENTAL DATA REDUCTION	109
Calculation of Basic Flow Variables	109
Parameter Calculations	125
Data Uncertainty	128
ANALYSIS AND DISCUSSION OF DATA	140
Diffuser Data	140
Compiled Three-Dimensional Boundary Layer Data	160
Remarks on a Double-Skewed Turbulent Boundary Layer	184
Remarks on Velocity Profile Models	188
CONCLUSIONS	206
LITERATURE CITED	211

TABLE OF CONTENTS (Continued)

	Page
ACKNOWLEDGMENTS	218
APPENDIX A. SELECTED VELOCITY MODELS FOR THREE-DIMENSIONAL TURBULENT BOUNDARY LAYERS	219
APPENDIX B. TURBULENT FLOW EQUATIONS	225
APPENDIX C. HOT-WIRE INSTRUMENTATION	236
APPENDIX D. DIFFUSER EXPERIMENTAL DATA	264
APPENDIX E. DIFFUSER SIDE WALL COORDINATE SYSTEM	275
APPENDIX F. SELECTED EXPERIMENTAL DATA	277

SYMBOLS AND NOTATION¹

a	least squares coefficient (page 118)
A_u , A_v , A_w	parameters in hot-wire relations (page 250)
b	least squares coefficient (page 118)
B_u , B_v , B_w	parameters in hot-wire relations (page 251)
C_1 , C_2 , C_3	coefficients in second order least squares equation (page 92)
C_u , C_v , C_w	parameters in hot-wire relations (page 251)
e_u , e_v , e_w	fluctuating voltage associated with wires 1, 2 and 3, volts (page 237)
E	instantaneous voltage, volts (246)
\bar{E}	mean voltage, volts (page 246)
E_b	bridge voltage, volts (page 92)
E_α , E_β , E_γ	instantaneous voltage associated with wires 1, 2 and 3 at angles α , β and γ respectively, volts (page 237)
Δh	Pitot-static differential pressure, in. of H_2O
h	wall static pressure, in. of H_2O
h_1 , h_2 , h_3	coordinate scale factors (page 227)
H_1 or H-1	streamwise shape factor (page 127)
H_2 or H-2	crossflow shape factor (page 127)
k	velocity potential proportionality constant, ft/sec (page 55)
k	constant in hot-wire relations (pages 240, 241)
k_u , k_v , k_w	constant k which corresponds to wires 1, 2 and 3 respectively (page 237)

¹Symbols and notation not in this list are defined and used locally within the text.

K_1, K_2, K_3	coefficients in Kings equation (pages 91, 246)
L	characteristic body length in ξ -direction, ft (page 57)
l	characteristic body length in crossflow direction, ft (page 57)
MP	modified electrical power parameter, watts (page 112)
MPR	modified power ratio (page 113)
MP_θ, MP_{90}	modified power values corresponding to an arbitrary angle θ between the wire and the mean velocity direction, also shown in $\theta = 90^\circ$, watts
MP_α, MP_β	modified power values corresponding to the particular angular definitions, watts (page 239)
N	exponent in Kings equation (page 91)
P, \bar{P}, P'	instantaneous, mean and fluctuating fluid static pressure (page 51)
P^*	normalized static pressure (page 58)
q_s, q_n, q_t	fluctuating velocity values used in hot-wire equations, ft/sec (page 238)
$\overline{q_s q_t}, \overline{q_s q_n}, \overline{q_n q_t}$	Reynolds stress velocity terms from hot-wire calculations, $(\text{ft/sec})^2$, (pages 254, 255)
$\overline{q_t^2}$	total fluctuating velocity, $(\text{ft/sec})^2$ (page 183)
Q	velocity at the boundary layer edge, ft/sec (page 125)
Q_I	total instantaneous velocity at any point, ft/sec (page 239)
Q_S	total mean velocity at any point, ft/sec
$R_e h_1 \xi$	Reynolds number based on $h_1 \xi$ (page 69)
R_{sh}, R_{sc}, R_s	resistances, ohms (page 88)
$R_c, R_p, R_{p.h}, R_{cab}$	resistances, ohms (page 112)

R_t	resistance, ohms (page 92)
R_{oh}	overheat ratio (page 91)
$R_{p.w.}, R_{ctr}, R_{s.w.}$	radii of the pressure wall, centerline and suction wall, in. (page 107)
T_{sh}, T_s	sensor temperatures, $^{\circ}\text{F}$ (page 88)
ΔT	temperature difference, $^{\circ}\text{F}$ (page 88)
u, \bar{u}, u'	streamwise instantaneous, mean and fluctuating velocity
$\overline{u'v'}$	Reynolds stress velocity terms, $(\text{ft/sec})^2$
$\overline{u'w'}$	Reynolds stress velocity terms, $(\text{ft/sec})^2$
U	normalizing velocity, ft/sec (page 57)
U	equivalent velocity, ft/sec (page 240)
$(U/Q)_{C.L.}$ or UQCL	velocity ratio at the edge of the wall collateral layer (page 191)
u^*	normalized velocity (page 57)
u^+	boundary layer parameter (page 11)
u_τ	shearing velocity, ft/sec (page 11)
v, \bar{v}, v'	normal instantaneous, mean and fluctuating velocity components, ft/sec (page 51)
$\overline{v'w'}$	Reynolds stress velocity terms, $(\text{ft/sec})^2$
V	equivalent velocity, ft/sec (page 242)
V	normalizing velocity, ft/sec (page 57)
v^*	normalized velocity (page 57)
v_p	Head's entrainment velocity, ft/sec (page 27)
w, \bar{w}, w'	crossflow instantaneous, mean and fluctuating velocity components, ft/sec (page 51)

w	equivalent velocity, ft/sec (page 242)
w	normalizing velocity, ft/sec (page 57)
w^*	normalized velocity (page 57)
$\frac{w_c}{w}$ C.L.	ratio of the triangular crossflow velocity to the cross-flow velocity at the wall collateral layer edge (page 190)
$(\frac{w}{Q})_{C.L.}$	ratio of the crossflow velocity to the boundary layer edge velocity at the wall collateral layer edge (page 191)
$\frac{w/Q}{w_c'/Q}$	a particular crossflow velocity ratio (page 198)
x	cartesian coordinate in the streamwise direction, ft
y	cartesian coordinate in the direction normal to a surface, ft
y^+	boundary layer parameter (page 11)
z	cartesian coordinate which is orthogonal to x and y , ft
α	thermal resistivity, ${}^{\circ}\text{F}^{-1}$ (page 88)
$\alpha, \bar{\alpha}$	instantaneous and mean angle between the total mean velocity vector and sensor number respectively, deg (page 239)
α	angle between the boundary layer edge velocity vector and any local boundary layer velocity vector, deg
$\alpha_{C.L.}$ or ALPHA-CL	the value of α at the wall collateral layer edge, deg (page 125)
$\beta, \bar{\beta}$	instantaneous and mean angle between the total mean velocity vector and sensor number 2 respectively, deg (page 239)
γ	specific weight of manometer fluid, lb_m/ft^3
$\gamma, \bar{\gamma}$	instantaneous and mean angle between the total mean velocity vector and sensor number 3 respectively, deg (page 239)

δ or B.L. THK	boundary layer thickness, in. (page 125)
δ_1^* or DISP. THK 1	boundary layer displacement thickness, in. (page 126)
δ_2^* or DISP. THK 2	boundary layer displacement thickness, in. (page 126)
ϵ	the value of $\tan \alpha_{C.L.}$
ϵ_{uu} , ϵ_{vv} , ϵ_{ww}	parameters in the hot-wire relations (page 251)
ϵ_{uv} , ϵ_{uw} , ϵ_{vw}	parameters in the hot-wire relations (page 253)
ζ	curvilinear coordinate in the crossflow direction (page 225)
η	curvilinear coordinate perpendicular to the surface (page 225)
θ	centerline turning angle, deg
θ_{max}	maximum centerline turning angle or total turning angle of the duct, deg
θ_{11} or Mom. THK 11	streamwise momentum thickness, in. (page 126)
θ_{21} or Mom. THK 21	interaction momentum thickness, in. (page 127)
θ_{22} or Mom. THK 22	crossflow momentum thickness, in. (page 127)
θ_{12} or Mom. THK 12	interaction momentum thickness, in. (page 127)
κ_u , κ_v , κ_w	parameters in hot-wire relations, (page 251)
λ	bulk viscosity, $Lb_f \text{-sec}/ft^2$
μ	viscosity, $Lb_f \text{-sec}/ft^2$
ν	kinematic viscosity, ft^2/sec
ν_e	eddy viscosity, ft^2/sec
ξ	curvilinear coordinate in the streamwise direction (page 225)
ξ	an angle in the hot-wire relations, deg (page 239)

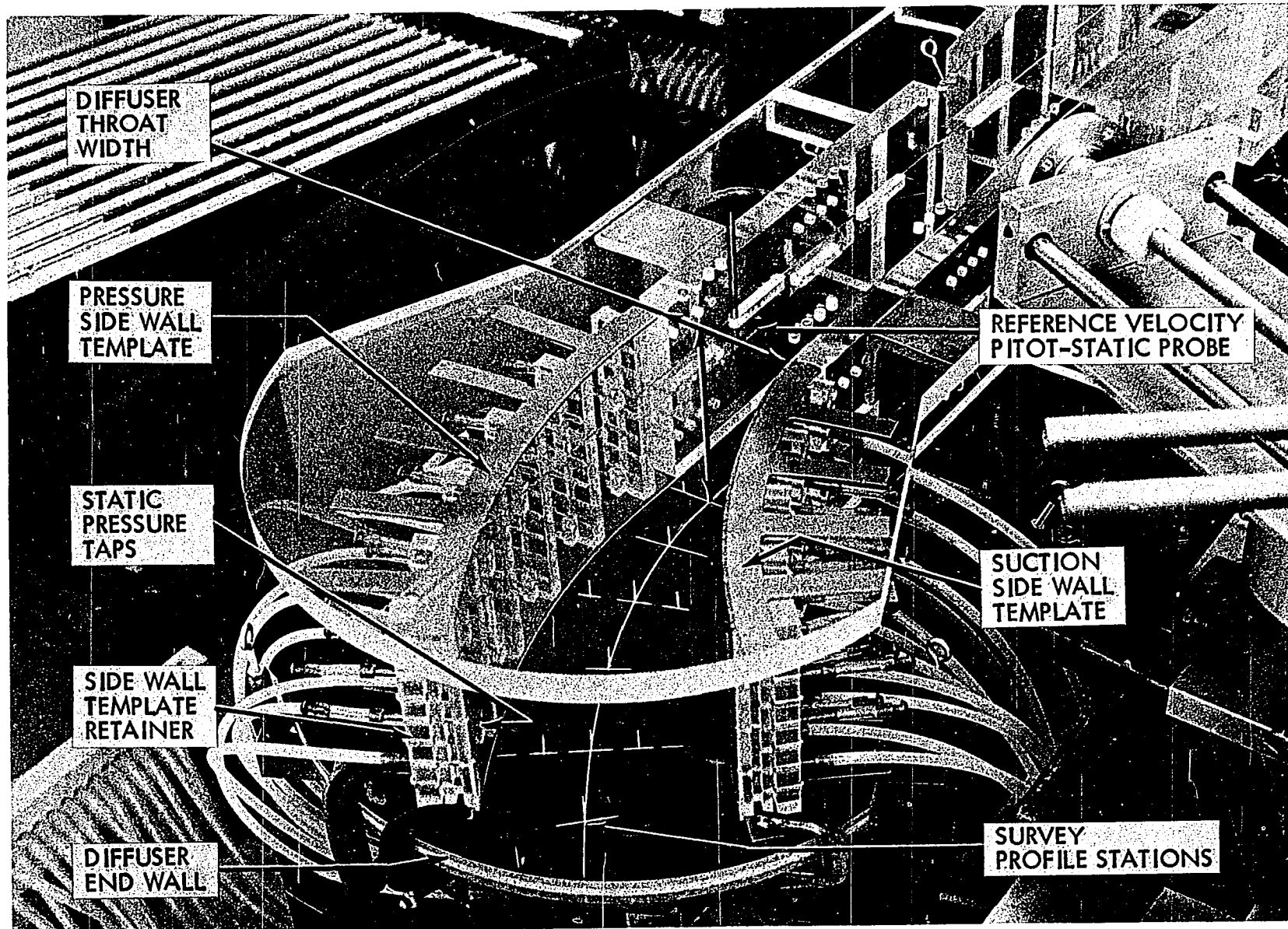
ρ	fluid density, slugs/ft ³
τ_{\max}	maximum shear stress in the boundary layer, lb _f /ft ²
τ_w	wall shear stress, lb _f /ft ²
ϕ	velocity potential, ft ² /sec (page 55)

INTRODUCTION

The three-dimensional turbulent boundary layer developing in an incompressible Newtonian fluid flow on the end wall of the diffuser shown in Figure 1 is the subject of concern in this dissertation. A number of experimental investigations have been concerned with the development of the boundary layer with a curved free stream streamline. The primary differences between this experimental investigation and others known to the author are that this work entails the development of a thin boundary layer in a curved diffusing passage and that the passage is considerably smaller than the others.

Boundary layers developing in a curved passage have a varying pressure gradient (both in magnitude and direction) and because of this an equilibrium boundary layer is not expected to exist, since two-dimensional equilibrium turbulent boundary layers require a specific relationship between the pressure gradient and the wall shear stress. Another difficulty in predicting the development of a boundary layer in a curved passage is that it is not a collateral boundary layer. A collateral boundary layer is one that has all of its velocity vectors in one direction. Since the boundary layer in a curved passage has its velocity vectors in various directions it is called a skewed turbulent boundary layer. Figure 2 shows a typical skewed turbulent boundary layer profile. Many times a portion of the skewed boundary layer near the surface is collateral and looking at the mean velocity profile from the top, Figure 2, the collateral portion would appear as a straight line. Throughout

Figure 1. Test section configuration and nomenclature



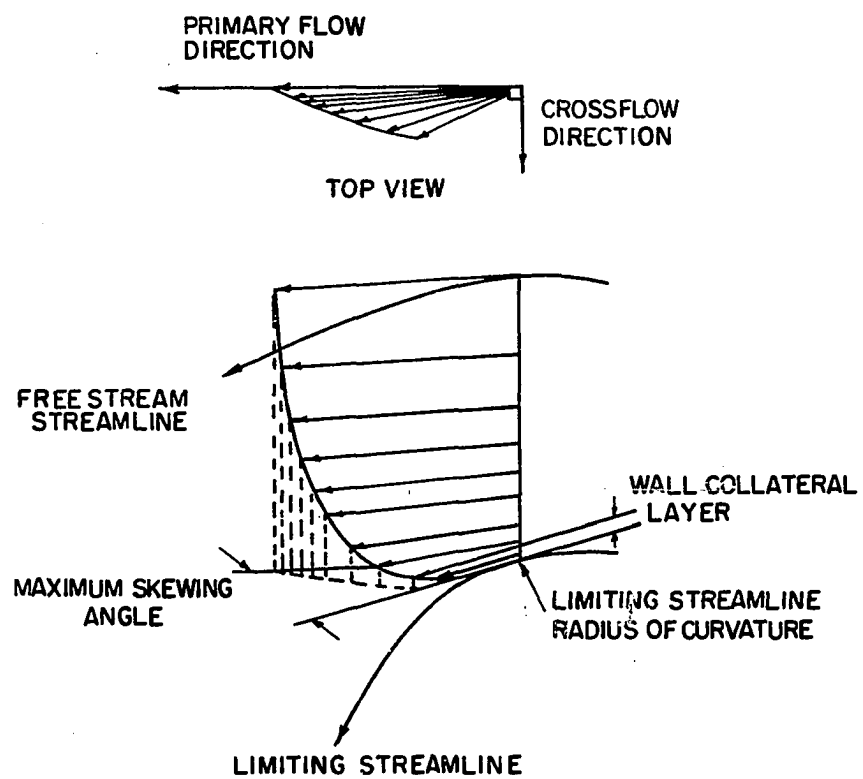


Figure 2. Skewed boundary layer velocity profile

the text this will be referred to as the wall collateral layer. The wall collateral layer, the wall shear stress, and the limiting streamline directions are the same. In this work the limiting streamline is defined as the streamline adjacent to the surface.

Pressure gradients induced by streamline curvature are the predominant skewing potential. If the free stream streamline has a finite radius of curvature, then a pressure gradient is developed along the radius of curvature or in other words perpendicular to the streamline. This pressure gradient is impressed on the entire boundary layer and since the momentum inside the boundary layer is less than at the free stream the streamlines within the boundary layer must turn more sharply to match the impressed pressure gradient. The limiting streamline has the maximum skewing angle if an inflection point is not present in the free stream streamline path. According to Horlock et al. (34) the crossflow pressure gradient also causes fluid to be fed directly into the end wall boundary layer.

Pressure gradients induced by streamline curvature are not the only driving forces for crossflow or secondary flow. Reynolds stresses are unique to turbulent flow and are thought to be the cause of secondary flow in straight rectangular cross-sectional ducts. Even though the turbulent boundary layer is in a developing stage a secondary flow exists. Pletcher (61) made a study of secondary flows during the development of turbulent boundary layers in a straight rectangular duct which indicated that secondary flows existed at all stages of boundary layer development but are different in pattern. It is not known what part Reynolds stresses

play in the development of skewed boundary layers in a curved duct, but since the secondary flow in straight ducts is only a small percent of the primary flow it will be assumed in this work that their contribution is insignificant compared to that of the pressure gradients due to streamline curvature.

Corner flows are another problem in the end wall flow pattern. Corner flows are complicated and the degree of complexity is probably reflected by the dearth of published material on this subject. Gersten (27) studied the corner effects in turbulent flow and his results indicate that for high Reynolds numbers and short plates the displacement effects are small. It was assumed for this study that a sufficient distance from the corners was maintained in order to neglect corner effects.

Wall effects other than the corner flow displacement effect involve the flow of fluid off the pressure side wall, through the corner region and mixing with the end wall flow or flow from the end wall to the suction side wall. If the velocity profiles in the small duct were completely anomalous compared to the other published data then a possible cause would be the wall effects. If wall effects were not detected then the results of this data along with data from larger passages could be used as a very rough approximation of what would be expected in a blade row or between stators in turbomachines. The approximation should not be any worse than potential flow solutions between blades. If wall effects were detected, then data would necessarily be obtained in small, more difficult to measure, passages if turbomachinery information was desired.

Experimental investigations concerning the skewed turbulent boundary

layer have been made in circular-arc curved non-diffusing ducts, in apparatus that causes the flow to stagnate and turn, and in flow fields around bodies which produce streamline curvature. An important type of flow field was not investigated, that of flow on an end wall of a two-dimensional curved diffuser. Curved diffusing passages are found in practice and in addition the flow has some similarity to that in a blade-to-blade passage in a compressor or pump. A curved diffusing passage has an adverse pressure gradient in the primary direction of flow and a favorable pressure gradient in the direction of crossflow. This combination of gradients would tend to increase the skewing angle on the end wall compared to non-diffusing curved passages. This experimental investigation was conducted to provide information which would add to understanding the behavior of the skewed turbulent boundary layer and to present the actual development characteristics of a skewed turbulent boundary layer in a particular diffusing passage. In addition, it was conducted in a small passage to determine whether anomalous velocity profiles resulted when compared to curved ducts of larger size. The experimental program consisted of measurements of the mean velocity profiles and directional measurements in a skewed turbulent boundary layer on the end wall centerline and on both sides of it through the duct as indicated by the survey profile stations shown in Figure 1. Wall static pressure data were also obtained. The diffuser data were compared with skewed turbulent boundary layer data from other published sources. In addition, a fractional analysis of the continuity equation and the Navier-Stokes equations for three-dimensional flow of an incompressible Newtonian fluid with constant

viscosity was conducted to determine similarity parameters and develop the pertinent boundary layer equations.

REVIEW OF LITERATURE

In order to better comprehend most aspects of the problems related to predicting turbulent boundary layer behavior, a review of some basic concepts seemed essential. First, a review of two-dimensional turbulent boundary layer mechanisms is attempted. Included also in this section is a compendium of various phenomena which effect the boundary layer velocity profile and a brief discussion of non-equilibrium turbulent boundary layers. Following the first phase of the review, a summary of skewed turbulent boundary layer research to date is presented. This phase of the review contains a discussion concerning the driving potentials causing skewing, some velocity models, and models and methods of solving skewed turbulent boundary layer problems.

The Two-Dimensional Turbulent Boundary Layer

Basic mechanisms

According to Schlichting (67), the most striking feature of turbulent motion is the fact that both pressure and velocity at a fixed point in space are not constant with respect to time, but fluctuate irregularly at a high frequency. These fluctuations have a definite influence on the shape of the mean velocity profile, the resistance to fluid deformation, and the transfer of momentum and energy. Turbulent flow can be thought of as an eddy or mixing flow superimposed on a main flow. Reynolds introduced a method of formulating this mathematically and it has been a tool which all turbulent flow theoreticians have used since.

Explicitly, it is expressed as

$$u = \bar{u} + u'$$

u = instantaneous velocity

\bar{u} = mean velocity

u' = fluctuating velocity

and

$$\bar{u} = \frac{1}{T} \int_{t_0}^{t_0 + T} u dt$$

t_0 = initial time of time interval T

T = length of time interval which is sufficiently long to make \bar{u} independent of time

which is the time average at a fixed point in space. Since \bar{u} is related to u and u' as shown above and is defined as an integral over time, then it follows that \bar{u}' is zero. A more general formulation of the instantaneous properties and some operating rules are expressed in APPENDIX B.

Turbulent boundary layers are normally divided into various regions parallel to the surface over which a fluid flows. The name given to each region attempts to connotate the mechanisms which predominate in each one. The structural profile has different designations and numbers of zones, e.g., Knudsen and Katz (46) identify three zones (laminar layer, buffer layer and turbulent layer) while Kline (42) resorts to four divisions with the designation of viscous sublayer, buffer zone, log zone and wake zone. This dissertation will use the latter terminology.

Figure 3 shows the various regions and their corresponding bounding values.

Figure 3. Turbulent boundary layer velocity profile

$$u^+ = u/u_\tau \quad u_\tau = (\tau_w/\rho)^{1/2} \quad y^+ = yu_\tau/v$$

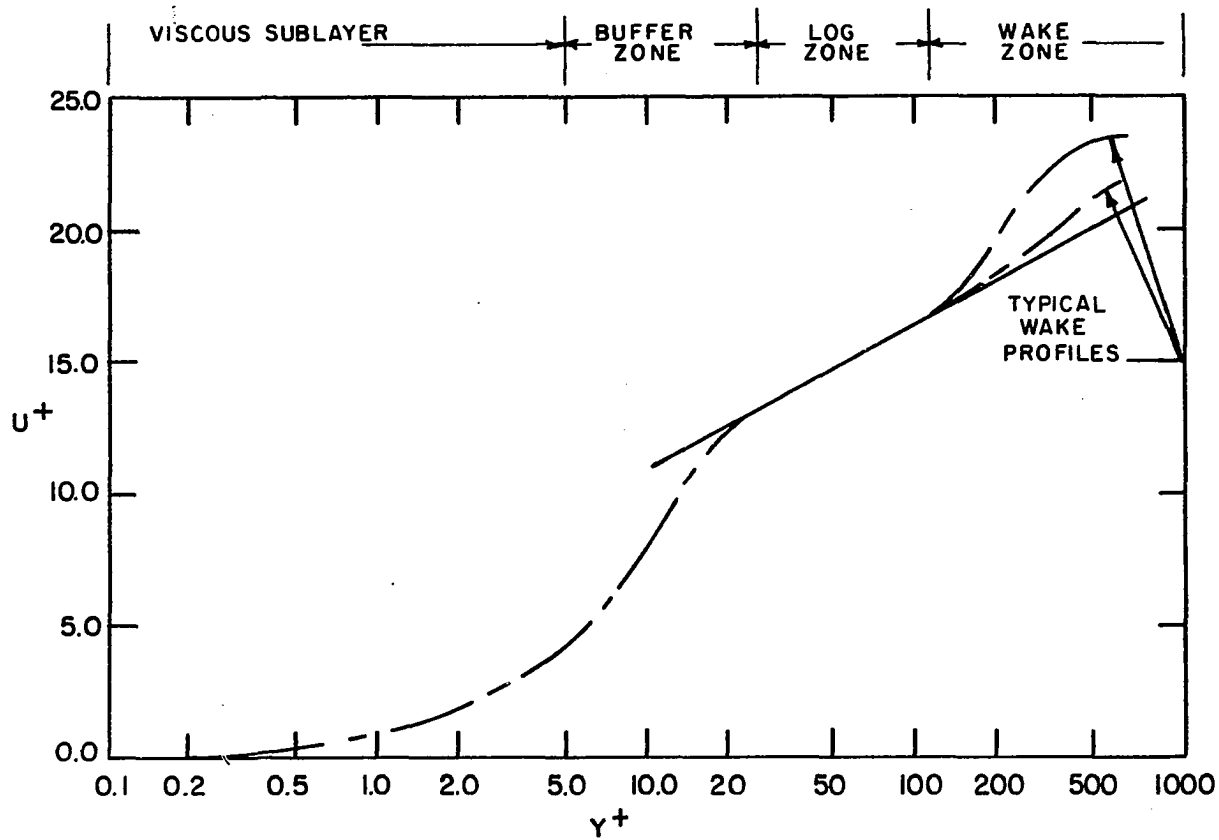


Figure 3. Turbulent boundary layer velocity profile

Viscous sublayer Adjacent to the surface is the thinnest layer of the complete structure. The viscous sublayer, or laminar sublayer as it is commonly known, is a region of controversy. Some authors deduce that the viscous sublayer plays an active role in the boundary layer structure while others contend it is strictly passive. Most of the work in this area indicates to the author, that the viscous sublayer could strongly influence the behavior of the skewed turbulent boundary layer structure. With this in mind, a discussion of some of the differing concepts pertaining to viscous sublayers will follow.

Goldstein (30) defines the viscous sublayer as a very thin region having a high rate of shear produced primarily by viscous stresses since the turbulent velocity component normal to the surface is too small to create a significant apparent Reynolds stress. The same general idea is conveyed by Schlichting (67). His interpretation of the viscous sublayer is that it behaves as one in laminar motion and has such small velocities that the viscous forces dominate over the inertia forces and eradicate any turbulent fluctuations. These concepts of the sublayer are typical textbook approaches and are not too enlightening relative to possible information pertinent to skewed layers.

Kline and his colleagues have conducted a series of investigations pertaining to sublayer mechanisms. Their conclusions are based on the results of visualization studies in water with both dye and minute (≈ 0.0005 in. dia.) hydrogen bubbles which were corroborated with hot-wire anemometer data. Kline (42) described the viscous sublayer as a strongly three-dimensional, time-dependent streaky structure with

identifiable streaks of fluid flowing slowly outward from the surface. The streaky structure results from the existence of fast and slow motion regions side by side. A relatively regular wave pattern of transverse wave lengths is formed by the streaks and the transverse wave lengths become shorter for adverse pressure gradients and longer for favorable pressure gradients. Characteristically the slow speed streaks are relatively quiescent and show only small fluctuations as they move downstream close to the wall and gradually away from the wall into the buffer zone. In a later paper, Kline et al. (45) report that the unsteady three-dimensional motions in the sublayer displays a velocity which is a large fraction of the local mean velocity even at the wall. They make the analogy of the waving and oscillating of the streaks in the sublayer to the motion of a flag. In adverse pressure gradients the streaks tend to become shorter and wave more violently whereas in favorable pressure gradients the opposite occurs. In a sufficiently favorable pressure gradient the entire boundary layer will relaminarize and the wall streaks disappear, which tends to confirm the contention that streaks are unique to turbulent flow.

Clark (12) has made extensive surveys well into the viscous sublayer, $y^+ < 12$, with a hot-wire anemometer. His results tend to support Kline's interpretation of the viscous sublayer mechanisms. In the viscous sublayer large velocity fluctuations in the streamwise direction of greater magnitude than any which are present in the outer layers was reported. This implication of an active role in the production of turbulence by the viscous sublayer is a paradox since amplification of

fluid disturbances occurs due to viscosity concurrently with dampening and dissipation effects of viscosity. Another factor involving Kline's interpretation of the sublayer mechanisms with which Clark concurred was that long streaky three-dimensional, time dependent structures, which are thin normal to the wall, existed. This was deduced from the three turbulence intensity component measurements which showed that the streamwise intensity was much greater than either the transverse or normal intensities.

Bradshaw (4) contends that local production and dissipation are not nominally equal in the viscous sublayer (although this is essentially true in other parts of the inner layer) but differ by the rate of direct dissipation of the inactive motion energy impressed on it from the outer boundary layers. He implies that the extra dissipation occurs only in the viscous sublayer and not distributed over the remaining inner layer. The inactive motion referred to is the large scale eddy structure which primarily arises in the outer layer and is impressed on the inner layer contrary to the active motion which is produced in the inner layer and is considered responsible for shear stress production. The following paragraph essentially refers to the same type of mechanism.

As pointed out by Bull (8), Kraichnan concluded through theoretical considerations that pressure fluctuations at a point are produced by quite local velocity fluctuations. Bull (8) has made an investigation of wall pressure fluctuations which disclosed that pressure fluctuations received contributions from two wave number families. A wave number family consists of disturbances having a given wave length band. High

wave number families correspond to small scale eddies and low wave number families to large scale eddies. The high and low wave number families originate in the inner and outer boundary layer respectively with the former contributing 75 percent of the pressure fluctuating driving mechanism. The strong contribution of the fine scale motion decreases rapidly as the spatial separation from the source increases at the wall, indicating a local effect from the high wave number family.

Tritton (78) advocates abandoning the feature of streaks in the sublayer moving away from the wall and erupting, performing an active role in turbulence production. In essence, his argument is based on correlation measurements indicating a positive contribution of the Reynolds stresses near the wall. He maintains that a stagnation type flow away from or towards a wall would require a negative contribution to the Reynolds stresses and this would involve a change of sign in the correlation coefficient for the axial and transverse velocity fluctuations at large separations in the transverse direction. He interprets his results as showing no such change. The rebuttal pertaining to Kline's visual studies is the presumption that the dye was injected through the wall causing the fluid to have an outward motion, ultimately erupting. These opposing views were presented in order to indicate the dubious characteristics of sublayer mechanisms.

The viscous sublayer is very dependent on the disturbance propagation direction and wave number. According to Sternberg (73) the energy containing disturbances are strongly aligned with the flow direction. His conclusions were based on a theoretical analysis which included the

effects of obliquity (the angle with which the wave propagation makes with the flow direction). As the obliquity is increased the transverse velocity fluctuating component decreases. The theory is a linear one but could be utilized to indicate some trends involving changes in flow direction by transverse pressure gradients. It should be noted that the viscous sublayer as Sternberg defines it includes the buffer zone and log zone by the definitions used in this work.

Buffer zone Next to the viscous sublayer is the region denoted the "buffer zone". This zone is on the order of five times thicker than the sublayer but is next to the thinnest layer. Kline (42) depicts the buffer zone as also being strongly three-dimensional and time dependent consisting of streaks having more pronounced transverse oscillations and incipient streak "breakup". Breakups are a form of strong instabilities which result from violent, short duration erupting low speed streaks occurring intermittently. Surrounding streaks often suddenly shift transversely due to breakups and the breakups appears to receive an impulsive normal outward motion. It seems that the majority of breakups occur in the region $10 < y^+ < 30$ according to Kline et al. (45). They also suggest a physical explanation of the streaks as a transverse vortex line stretching or compressing as a result of local secondary flow away from or toward the wall. A low speed streak would convect away from the wall, stretch, then oscillate, finally bursting violently. Transverse vorticity is primarily a function of $\partial u / \partial y$ (streamwise velocity gradient normal to the surface). Streak breakups would then influence this gradient, both in the normal and crossflow directions, assuming the

breakups could be associated with vortex stretching. In order to relate the mechanisms which are proposed in the next paragraph to the ones presented in this one we would have to accept the premise that local transverse pressure gradients are the forcing functions for the streaks and streak breakups.

Schubert and Corcos (68) concluded that the only forcing function of importance near a wall was the transverse pressure gradient. Such a gradient causes a transverse velocity fluctuation which induces a normal velocity component because of continuity. In turn, the normal velocity component interacts with the mean velocity profile which becomes the primary forcing function for the streamwise velocity fluctuations. Therefore, the displacement of the mean velocity profile by the normal velocity component, not the pressure gradient in the streamwise direction, is the principal source of the axial velocity fluctuations according to Schubert and Corcos.

Clark (12) maintains that the buffer layer is significantly influenced by inertial, viscous and pressure forces. Within this region the large turbulence level, according to Clark, is produced by the amplification of impressed fluid fluctuations of a particular range of wave numbers.

Bull (8) has indicated that most of the contributions to the wall pressure field have their source in the region $5 < y^+ < 30$ which is the buffer zone as defined in this work. The influence of these contributions are experienced only locally at the wall but are convected downstream so as to influence regions up to a distance of around 2.4δ in the same

layer in the buffer zone.

Log zone The log zone or as it is sometimes termed, the overlap region, is the third region from the wall and its thickness varies with both inner and outer layer influences. Kline (42) has indicated that the log zone disappears under flow conditions near separation. This was substantiated by Stratford, Townsend, and Schubauer and Klebanoff according to Kline. For the near separation condition it appears that the outer flow properties dominate. In general, the log zone shows no intermittency, that is, it is turbulent all the time, also no "streaky structure" occurs. Kline et al. (45) also points out that various scales of motion are evident in the log zone. This would also indicate an influence from both inner and outer layer properties. The inner layers eject the small breakup eddies into the log zone and larger scale turbulence is impressed on it from outer regions.

Wake zone Much of the turbulent boundary layer in terms of physical thickness consists of the region denoted the "wake zone". It is primarily a layer of large eddy structure (as compared to the buffer zone) with intermittent turbulence. The outer boundary is adjacent to the free stream, or quasi-inviscid fluid and is defined as the position where the velocity is $0.995 U$. U is the free stream velocity. Coles (16) views the wake region as one demonstrating a large scale mixing process which is influenced primarily by inertia forces and secondarily by viscosity. Townsend (76) maintains that the large eddies in the wake zone regulate the intensity of the turbulent motion and the rate of entrainment of the nonturbulent fluid. On the other hand Kline et al.

(45) hypothesized that some of the streaks ejected from the inner layers become entwined with the outer flow, producing more nearly equal apparent streamwise and transverse scales of motion. Kline (42) implies that the intermittency factor in the wake zone has a universal shape. It should be noted that his premise was predicated on near equilibrium* flows with constant pressure. Other than being based on constant pressure data, his conclusions could be fairly universally applied since the collected data had influences from rough and smooth walls, a considerable range of Reynolds number, eddy viscosity and boundary layer thickness values.

Bradshaw (6) describes the wake zone as having turbulent eddies of length scales of the order of the boundary layer thickness and is responsible for the "memory" of the outer layer (wake zone). This memory time corresponds roughly to the time required for an eddy to travel a streamwise distance of approximately ten times the boundary layer thickness. The eddy originates in the inner layer (buffer and log zone) and slowly propagates towards the outer edge of the boundary layer, during which time it grows, exchanges turbulent energy with smaller eddies, increases the boundary layer thickness by entraining fluid from the free stream and then eventually dies away.

This concludes the review of two-dimensional turbulent boundary layer mechanisms which have been suggested to prevail in the various layers. These mechanisms are conceptual and their value as a basis for

*Equilibrium boundary layers are not uniquely defined and therefore results in some difficulty in understanding the term. Some of the various definitions are presented, beginning on page 25.

formulating approaches to analytically explain boundary layer behavior would be enhanced by a knowledge of physical parameters which influence the flow field.

Flow influence parameters

In order to attempt to develop a model for predicting the behavior of a flow phenomena, the degree of influence by each flow variable on the phenomena is essential for a complete and valid representation. Since complete understanding of turbulent flow phenomena is far from realization, an attempt to compile some experimentally indicated concepts regarding the influential characteristics of various flow parameters will ensue. The primary parameters pertinent to this work are pressure gradients, turbulence, Reynolds stress, shear stress, Reynolds number and velocity components. Wall roughness effects will not be considered in this work, although wall roughness has been shown to be of considerable importance in boundary layer behavior. Other effects not considered are heat transfer, fluid injection into the boundary layer and boundary layer suction.

Pressure gradients Pressure gradients, both adverse and favorable, appear to be a salient feature in regards to influencing the flow field. Streamwise turbulence profiles within the boundary layer change with increasing pressure gradients according to Sandborn and Slogar (66). As the pressure gradient is increased, the high turbulence propagates farther out into the boundary layer before decaying.

Another adverse pressure gradient effect is its influence on skin

friction according to Clauser (14). For the equilibrium boundary layer experiments performed under his direction the skin friction decreased considerably for even the mildest adverse pressure gradient.

Clauser (13) has shown that wall flow correlations for the velocity profile appear to be independent of pressure gradients for equilibrium boundary layers. His physical argument attempting to corroborate wall flow pressure independency is that frictional forces are of such greater magnitude that they make pressure effects negligible. The independency argument based on the correlations seems dubious to the author because the correlation parameter is a function of the skin friction and as was related in the previous paragraph, skin friction is a strong function of pressure gradients. This seems to indicate at least an implicit relation between inner flow and pressure gradients. This does not suggest replacing the shear stress by the pressure gradient in the correlation parameter, because as indicated by Goldberg (29) shear stress cannot be characterized by pressure gradient alone.

An experimental investigation by Herring and Norbury (32) indicate that favorable pressure gradients in an equilibrium turbulent boundary layer yield a monotonically decreasing shear stress as distance from the wall is increased. The rate of decrease is greater for stronger favorable pressure gradients. Also, using Clauser's adverse pressure gradient data, a trend is established showing shear stress increasing from the wall value to a maximum and then decreasing to the free stream value as distance from the wall is increased. The "peaks" increase in magnitude with an increase in adverse pressure gradients. Bradshaw (5) also

experimentally verified this, showing for three different equilibrium boundary layers that the peak or "maximum" shear increases in absolute value and the wall shear decreases in absolute value for an increasing adverse pressure gradient.

According to Bradshaw (5) the large eddies in the outer region of a boundary layer increase in strength relative to the rest of the turbulence as the adverse pressure gradient and turbulence level increase. He bases this on an increased distinction of peaks in the turbulence spectra. Since he maintains that large eddies produce a large part of the shear stress in the outer region of a boundary layer, then it seems feasible to assume that local stress increases with increasing adverse pressure gradient and turbulence level. This is substantiated fairly well by the previous paragraph.

Turbulence Another factor influencing the flow field is external turbulence. This is the turbulence generated outside of the boundary layer and impresses its fluctuating motion onto the boundary layer. The following is a brief confrontation with some relevant effects.

Coles (16) points out the dependence of the wake zone on the external turbulence level. It appears that as turbulence increases the values of u^+ decrease for a given y^+ . See Figure 3 for definition of terms and a typical distribution.

Kline (42) states that data has been obtained which show that free stream turbulence exercises an appreciable change in the inner layer if the free stream turbulence exceeds that of the inner layer. Under this extreme case, the turbulence intensity increased considerably in the wake

zone and the mean velocity profile was flattened. Also wall shear and boundary layer thickness increased with the increased free stream turbulence intensity.

Free stream turbulence affects the boundary layer especially if spatial variations are induced by screens or protuberances. As shown by Bradshaw (3) turbulence produced by wind tunnel dampening screens induces a transverse variation of the surface shear stress and boundary layer thickness.

Reynolds stresses At this point, effects of Reynolds stress on the flow field will not be discussed in detail as their salient feature is more relevant to skewing effects and will be expressed in that section. One facet does warrant mention at this time, that of local relationship. Phillips (56) derived expressions which displayed the principle that Reynolds stresses are not a local property of the fluid motion. He indicates this factor has been verified experimentally but offered no reference to substantiate it. His equations do imply that the Reynolds stress "gradient" is a local property in that the normal distance from the wall is the only space variable in the relationship. However, an integral time scale parameter is involved. Goldberg (29) studied the upstream history effect and experimentally verified that Reynolds stresses were not a local parameter. His basis for this conclusion was the rate of decay of the shape factor to its equilibrium value after a constant pressure was imposed subsequent to an arbitrary adverse pressure gradient.

Reynolds number Reynolds number influence on the flow field in a turbulent flow involving equilibrium boundary layers with a zero

pressure gradient and adverse pressure gradients will not be fully covered. One effect reported by Clauser (14) was that skin friction coefficient decreased with increasing Reynolds number for the range of Reynolds number values covered by his tests. Also the local Reynolds number has an influence on the coefficients in the log law according to Compte-Bellot as was cited by Kline et al. (45). This is plausible in view of the indication that skin friction is a function of Reynolds number and the constants (log law coefficients) are normally based on wall shear stress data.

In recapitulating, it seems evident that pressure gradient effects are the most prominent. Increased adverse pressure gradients result in increased turbulence intensity, a decrease in wall shear stress, an increase in the maximum shear stress in the boundary layer as well as changing the location at which it occurs in the boundary layer and an increase in boundary layer thickness. All these effects are based on measurements of so called "equilibrium boundary layers" and do not necessarily apply to non-equilibrium boundary layers. In the next section some definitions of equilibrium boundary layers will be expressed.

Non-equilibrium boundary layers

Some features about non-equilibrium boundary layers should be expressed, since equilibrium boundary layer flows are normally found only in laboratory experiments and even then are difficult to produce. It seems most appropriate at this time to relate some definitions of equilibrium boundary layers since non-equilibrium boundary layers are

those not adhering to definitions of the former.

Definitions According to Clauser (14) there are two gross forces on the boundary layer, one being the skin friction (wall shear) and the other the pressure acting over some effective area δ' . He defines an equilibrium boundary layer as one having a constant ratio of these two forces, $(dp/dx) \cdot (\delta'/\tau_w)$, over the length of the boundary layer. Bradshaw (5) indicates that three definitions of equilibrium boundary layers exist for incompressible turbulent flows which are the following:

$$(1) U \propto x^a$$

$$(2) \delta_1^* \frac{dp}{dx} \frac{1}{\tau_w} \quad (\delta_1^* \text{ is the displacement thickness})$$

$$(3) \text{the ideal boundary layer (at infinite Reynolds number) with exactly similar wake profiles.}$$

Equilibrium turbulent boundary layers do not yield entirely similar profiles as in laminar boundary layers but are their closest counterpart. Townsend (76) refers to equilibrium turbulent boundary layers as "self-preserving". He indicates that to ensure self-preserving development it is not sufficient to have a certain variation of free stream velocity, but the boundary layer must be matched to the pressure gradient.

Noted observations In the log zone (overlap region) the effective viscosity has the same relationship for both equilibrium and non-equilibrium flows providing the shear stress in the layer is approximately equal to the wall shear stress, according to Mellor (50). It might have wider application, but Mellor points out that it has been

experimentally verified only for cases having shear stress in the layer and at the wall approximately equal. This is plausible in view of Clauser's (13) observation that experiments show that response distance for the wall layers is very short, sufficiently so that wall flow can always be considered in equilibrium.

Bradshaw (5) observed that it has been found empirically that v_p/U , $\left\{ v_p = \frac{d}{dx} U (\delta - \delta_1^*) \right\}$, is nearly proportional to $\tau_{max}/\rho U^2$ in the wake zone of both equilibrium and non-equilibrium boundary layers. In other words, the entrainment velocity v_p (mean rate of propagation of turbulent fluid into the free stream) is proportional to the maximum shear stress in the boundary layer which is a strong function of the pressure gradient. In addition, Bradshaw claimed that for non-equilibrium turbulent boundary layers the turbulence convection is not small for $y/\delta < 0.7$, so that turbulence energy production is not nearly equal to dissipation.

Studying the degree of departure of the non-equilibrium boundary layer from the equilibrium boundary layer and its tendency to return to the equilibrium form has been one approach used in attempting to find solutions to the non-equilibrium boundary layer characteristics. McDonald (49) has taken this approach which yielded the implication that equality between production and dissipation of kinetic energy of turbulence is an indication of equilibrium turbulent boundary layers.

The Skewed Turbulent Boundary Layer

Skewed boundary layer geometry has been well defined by Taylor (74). In essence, it is a boundary layer which has no single direction of flow throughout. An ordinary two-dimensional or collateral boundary layer has all of its mean velocity vectors in one direction but a skewed boundary layer can have velocity vectors departing from the free stream direction either to one side or the other or to both sides at the same time. Various influences are capable of causing this skewing action as will be discussed next.

Skewing driving potentials

Some of the mechanisms that cause deviations from collateral layers are pressure gradients transverse to the main flow, an uneven lateral distribution of free stream turbulence and transverse stress gradients.

Free stream turbulence As was shown by Bradshaw (3) proper selection of wind tunnel screens, primarily the screen adjacent to the contraction section, could essentially eliminate the free stream turbulence as a skewing potential or promote it since it is the controlling cause. It will be assumed for this work that proper precautions in designing the wind tunnel have been taken to eliminate this potential.

Stress gradients The stress gradients which will be considered in this work as possible skewing potentials are related to the velocity fluctuating components within the boundary layer, primarily in the corner regions containing the flow medium. Tracy (77) maintains that secondary flow in straight rectangular ducts are produced primarily from

Reynolds stresses. His interpretation of the experimental data indicate the predominant stresses are the Reynolds normal stresses in directions perpendicular to the main flow, both parallel and perpendicular to the channel floor. He contends that Reynolds shear stresses are a result of mean secondary flow. This author has reservations about Tracy's hypothesis indicating that the existence of apparent shear stress is caused by mean motion in the direction or directions of the velocity fluctuation components of which the Reynolds shear stress is comprised. Regardless of the active or passive role of the Reynolds' shearing stresses, the Reynolds' normal stresses appear to be of such magnitude and distribution to induce secondary flow. Also, the distribution of the secondary flow velocity indicates a decreasing magnitude of velocity as the distance from the wall is increased which would tend to confirm a skewing motion.

Gessner and Jones (28) determined experimental values for each term in the momentum equation along a secondary streamline with the exceptions of the pressure term which was used as a closing value because of the inability to measure pressures of such small magnitude (maximum gradient = 0.0007 in H₂O/inches). They concluded that secondary flow is the result of complex interactions between both Reynolds stresses (normal and shear) and the static pressure. Their work also produced some interesting facts pertaining to secondary flow in a straight channel which are the following: (a) Local wall shear stress becomes increasingly skewed as the corners are approached. (b) When comparing the behavior of wall shear skewing in a square and rectangular cross sectional duct, (longest dimension on rectangle is equal to the square wall dimension i.e. the

aspect ratio effect) results indicate a skewing angle distribution on the longest rectangular side was comparable to the square duct but the short side of the rectangle had considerably less skewing at comparable length percentages. (c) Transverse velocity measurements showed a greater non-dimensionalized velocity, w/U , for the rectangular (long side) section than the square section. (d) Data for either section revealed that w/U decreased for increasing Reynolds number.

Pressure gradients Pressure gradients promoting skewed boundary layers are associated with streamline curvature. This usually entails having an object placed within the flow field or dictated by confining walls. A departure from the curvature induced gradient was related by Clauser (14) in which a small opening in the tunnel top allowed a pressure gradient to be established that entrained boundary layer air from the bottom walls, requiring lateral flow. His experience, along with others in the field, have disclosed the ease with which transverse flow will occur, especially in retarded boundary layers.

When streamline curvature occurs, a pressure gradient develops along the radius of the curvature attempting to balance the centrifugal force of the fluid. If the radius of curvature is in the plane parallel to the floor, then the pressure gradient in the main stream is impressed on the floor boundary layer, resulting in an unbalance of force because of the inability of the low momentum fluid to reach equilibrium with the pressure gradient. As was stated in a previous section, the responses of the inner layers in a turbulent boundary layer are so rapid that they can be considered in equilibrium at all times. This holds true for the

skewing action too. The inner layers quickly turn towards the center of curvature to increase the low momentum fluids centrifugal force in order to balance the pressure gradient and this action propagates through the boundary layer out to the free stream. This perforce, results in a skewed boundary layer. An inflection point in the main streamline curvature also reflects the response of the inner layers, since immediately downstream of the inflection point the inner layers skew towards the new center of curvature while the outer layers are still skewed towards the previous center of curvature, consequently yielding a double signed skewing profile. This is sometimes referred to as the "s" shaped crossflow profile. In the next section some analytical models will be presented which attempt to predict velocity profile skewing.

Skewed velocity models

This portion of the review outlines the main types of three-dimensional turbulent boundary layer velocity models. Each velocity model is presented in chronological order with regard to a basic type and variations on the basic types are presented and discussed chronologically within their respective sections. Because some investigators have examined the merits of various velocity models, their names appear often during the discussion.

Velocity models may be considered to be included in one of four main types: polynomial model, wake model, triangular model or hybrid model. At least one example of the mathematical expressions for each model is contained in APPENDIX A.

Polynomial velocity models Prandtl, as cited by Francis (24), Joubert et al. (40) and Francis and Pierce (25) was credited with suggesting that velocity profiles for the streamwise and crossflow components for turbulent boundary layers be in the form of polynomials or power laws having their independent parameters as a function of boundary layer thickness, normal distance from the wall, and shape factors. The proportionality factor for the crossflow velocity was taken as the tangent of the angle between the wall shear vector and the free stream velocity vector. This method has been the basis used by various researchers to represent limited data with only modest success. As pointed out by Francis (24) none of the expressions proposed by Mager, Moore and Richardson, Cooke or Becker provided a good fit near the wall. Each of the proposed equations was at most a fit of two sets of data and differed primarily by the form of the exponent.

An extension of the Prandtl method by Eichelbrenner (20) and Eichelbrenner and Peube (21,22) retains Mager's form for the streamwise velocity expression, but the crossflow velocity resulted in a fifth degree polynomial based on experimental polar plots of Johnston (39) and their own. A salient feature was the parameter "C" which was introduced to allow a change in sign of the crossflow. This parameter was formulated such that a differential equation which was a function of free stream properties resulted. Knowing the free stream properties, integration could be performed resulting in a global value of "C" which then could be used in determining the crossflow velocity profile. Johnston

(38) has produced polar plots showing the comparison of the proposed expressions with four sets of data. The comparison was good in the peak region in all cases but deviated in the outer portion of the layer for some cases. As shown by Joubert et al. (40) the outer portion of the layer does not adhere to a linear distribution if the upstream flow is not two-dimensional. This restricts the expression for crossflow expressed by the fifth degree polynomial, since it was based on a linear distribution at the outer edge. Smith (70) claims that Eichelbrenner's fifth degree polynomial is invalid since it is based on the assumption that the second derivative of the crossflow velocity with respect to the streamwise velocity at the wall is zero. According to Smith, this assumption implies that the limiting streamline is normal to an isobar which is contrary to experimental data.

Wake velocity models Another general approach for determining the streamwise and crossflow velocity profiles in turbulent three-dimensional boundary layers was proposed by Coles (16) as an extension of his law of the wake in two-dimensional turbulent boundary layers. His modification of the two-dimensional form was primarily that of making it a vector representation. The total velocity vector is comprised of a vector in the surface shear stress direction with a magnitude dictated by the law of wall and a closing vector in the pressure gradient direction with a characteristic wake-like distribution. Both vectors are a function of a friction velocity vector having its direction the same as the surface shearing stress. Coles was reasonably successful in representing the data of Kuethe et al. (47) by his method. The only other

available data at that time was that of Gruschwitz (31) which was erroneous according to Coles. Subsequently, many investigators have attempted to verify Coles original vectorial representation for turbulent, three-dimensional boundary layers. A review of these should be enlightening.

Johnston (39) attempted to correlate Coles method with his data with little success. Coles (15) also analyzed Johnston's data with his method and was unsuccessful in correlating the wake function even on the flow centerline. He implied that a high turbulence level might be present in the flow field. This would invalidate his wake function since it is predicated on low turbulence flow fields.

Blackman and Joubert (2) devised an experiment to validate the vector representation of Coles law of the wake. Measurements were taken at the trailing edge of a delta wing model. The resulting yaw flow angles were less than 5 degrees and the pressure was too small to accurately determine the pressure gradient. From this data they determined the two wake functions oriented parallel and perpendicular to the wall shear stress direction. The perpendicular wake component was the component of the total vector in that direction. For the parallel wake component, intermediate steps were required. Resolving the total vector in the parallel direction was the first step. Fitting this to the law of the wall followed and the deviation of the measured parallel component from the law of the wall was considered the parallel wake component. Confirmation of Coles hypothesis that the wake vector is in the direction of the pressure gradient was inconclusive because of the data character-

istics as previously stated. Considerable scatter in the parallel wake component data caused some apprehension but it was suggested that the primary reasons were the inability to determine the friction velocity accurately and the ambiguous definition of the sublayer edge. Since the perpendicular wake component was representative of Coles characteristic wake shape and the least squares fit of the parallel wake component was also a reasonable facsimile, they maintained their analysis corroborated Coles hypothesis of the law of the wake in three dimensions. This conclusion could possibly be deduced from their data if the ratio of the parallel to perpendicular wake component was constant. Because of the small angle of yaw and the poor pressure data it appears that a better test is required to justify general statements on the validity of Coles hypothesis.

Hornung and Joubert (36) instituted an experimental investigation to determine the validity of both Johnston's (39) and Coles' (16) three-dimensional velocity models. The discussion pertaining to Johnston's model will be delayed until his model has been presented. In previous experiments the turbulence level was a possible cause of poor correlation of Coles method with experimental data. This feature was taken into consideration by Hornung and Joubert and they attempted to keep the turbulence level below 0.5 percent but were unsuccessful, although they reported a turbulence level of 0.56 percent at 88 feet per second. They assumed that Coles' model could be checked by plotting $2Q_s \cdot \sin \alpha / Q_{f.s.}$ $\sin \alpha_{f.s.}$ against y/δ . Q_s represents the total velocity at any point

and α is the angle between the wall shear stress direction and Q_s . The subscripts, f.s., designate free stream conditions. A plot of these parameters derived from their data indicate a very poor fit of Coles' wake function. They concluded that Coles hypothesis appears to break down in laterally divergent flows with rising pressure.

Francis (24) and Francis and Pierce (25) also compared Coles' three-dimensional theory with data from a straight rectangular channel downstream of a 60 degree curved channel. Data from the curved channel was not compared since the law of the wall did not hold for that flow and Coles method is dependent on the existence of the law of the wall. It was found that although Coles hypothesis did not agree with experimental data immediately downstream of the curve, the trend indicated a tendency to approach the law of the wake as downstream distance increased. As in Hornung and Joubert's (36) data, the characteristic inflection point of the wake function was nonexistent in the data distribution. Again it was concluded that Coles' hypothesis does not apply to the type of flow encountered in their tests.

Another reviewer of Coles' method concluded that the law of the wake in three-dimensional flows is valid, contrary to most previous works. Pierce (57) analyzed the flow data from Johnston, Blackman and Joubert, Hornung and Joubert, Kehl, and Pierce, and found that portions of the data were obtained in a transient or undeveloped situation which would invalidate any use of Coles' three-dimensional law of the wake since it applies only to fully developed flow. From the data, it was shown that the wake function resembled a quarter sine wave for either a developing

plane of symmetry flow or a well developed two-dimensional flow taken into an incipient three-dimensional separation region. For the developing plane of symmetry flow it was observed that as downstream distance from the position of initial diffusion increased, Coles' wake distribution was approached which tends to confirm his hypothesis for fully developed flows. This was also implied by the data of Francis (24).

A velocity model for three-dimensional turbulent flow of Coles' type was derived by Nelson (53). It is basically a modification of Coles' law of the wake in three dimensions in which the vector components are in the directions of Johnston's triangular plot components as described below. He proposed two universal functions partially based on Clauser (13) and Townsend (76) for equilibrium boundary layers in collateral turbulent flow. His "universal" functions ended up not being universal.

Triangular velocity model A third type of representation of three-dimensional turbulent velocity relationships was introduced by Johnston (39). His model was a result of observing the characteristic triangular shape of polar plots from three sets of data, Gruschwitz (31), Kuethe et al. (47) and his own. This triangle has its base in the free stream direction, one leg in the direction of the limiting streamline and the other leg composed of the locus of the tips of the boundary layer velocity vectors. He divides the crossflow velocity expression into two regions. The first region includes the distance from the wall surface to the vertex of the triangle which Johnston erroneously claimed to be the edge of the sublayer. This crossflow equation is a simple relation of the product of streamwise velocity and the tangent of the angle between

the free stream direction and the limiting streamline direction. The other region, which is between the vertex of the triangle and the outer edge of the boundary layer, has a similar crossflow relation except for a parameter "A" which is related to the mainstream turning angle. He demonstrates that $A = -2\alpha$ for the following conditions:

- (1) Q is constant along a streamline
- (2) $\partial\alpha/\partial y = 0$
- (3) $Q - u \approx 0$ (velocity defect)

α , is measured relative to the free stream flow direction at the beginning of the turn to the free stream flow direction at the position in question. Q is the free stream velocity, u is a boundary layer velocity in the free stream direction and y represents the normal distance from the wall. Horlock (33) expressed surprise that $A = -2\alpha$, since it just represents secondary vorticity if variations in the flow normal to the main streamlines are neglected. Squire and Winter (72) express the axial vorticity as $-2\alpha \partial u / \partial y$ in which $\partial u / \partial y$ is the gradient in the approaching stream and α is defined above. In view of subsequent experimental research, it appears that the relation between the parameter "A" and the turning angle is at most representative for small angles. Johnston (37) concedes that the linearized inviscid theory yielding $A = -2\alpha$ is invalid, except possibly for small free stream turning angles.

As in the case of Coles' model, Johnston's model has been analyzed and compared with more recent experimental data. It would be instructive to review some of these works.

Blackman and Joubert (2) claim that they were unable to correlate their data with Johnston's flow model. A presentation of their attempt was not made which is unfortunate since the difficulty confronting them is not obvious.

The data of Hornung and Joubert (36) indicated that a triangular model was representative even in the region of backflow but the value of y^+ at the vertex of the triangle ranged from 15 to 150 which invalidates Johnston's assumption that the vertex coincided with the edge of the sublayer. It was shown that poor agreement existed between $\tan^{-1} A$ and α representing both theory ($A = -2\alpha$) and experimental results, which tends to invalidate another portion of Johnston's theory. Possibly, based on the scatter in the correlating plot, another parameter in conjunction with α would be conducive in correlating $\tan^{-1} A$ and α . The authors assert that the scatter cannot be attributed to experimental error.

Francis (24) studied the boundary layer on the floor of two 60 degree curved channels which yielded some velocity polar plots with a marked difference from Johnston's polar plots. The value of y^+ at the peak of the plot ranged up to 330, supporting Hornung and Jouberts data indicating that the peak does not coincide with the laminar sublayer. Another deviation from Johnston's plots consisted of flat portions near the maximum crossflow. The portion of the polar plot representing conditions near the boundary layer edge were curved in some cases, although some of the plots concurred with Johnston's model.

It was shown by Joubert et al. (40) that non-two-dimensional upstream flow causes the outer portion of the polar plots to depart from Johnston's triangular model. A hill with a variable slope across the wind tunnel was placed upstream of their cylindrical model, which had induced skewing for all their previous experimental measurements, in order to alter the upstream profile. In view of the accepted fact that boundary layers are dependent on their history in the outer regions, it seems intuitive that a deviation from a model based on two-dimensional upstream flow should occur when upstream conditions are modified.

Eichelbrenner and Peube (21) criticized Johnston's model primarily because it disallowed a change in sign for the polar plot. They relate tests on flattened ellipsoids which yield data giving polar plots an "S" shape, i.e. one change in sign. As was reported earlier in this section, Eichelbrenner used several of Johnston's model concepts to derive his form.

Hybrid velocity models Another velocity model, probably best categorized as a hybrid, was proposed by Perry and Joubert (55). As is customary in two-dimensional boundary layer theory, they divided the skewed boundary layer into two regions, designated simply as inner and outer. For a two-dimensional upstream velocity profile, they found the data of Hornung and Joubert (36) to be better represented in the outer region by a velocity defect expression equal to the product of a vector π , which is similar to Coles parameter, and a velocity defect distribution parameter of the undisturbed upstream profile, also similar to Coles wake function. Both sides of the equation are divided by the

respective local shear velocity. It seems plausible that this approach could have been suggested by the Johnston triangular polar plot, since as pointed out by Taylor (74) a straight portion in a polar plot is indicative of a coordinate system moving with respect to a given velocity. Therefore a velocity defect parameter would be logical because it is essentially a velocity relative to a moving coordinate system. To attempt to demonstrate the validity of this model they plotted a velocity defect parameter from one station against velocity defect parameters at other stations and at corresponding distances from the wall. A straight line should be obtained if the theory were correct. This was realized except for portions of the profiles near the outer edge of the boundary layer. The inner region model for the velocity profile is basically a modification of the two-dimensional law of the wall with the magnitude of the velocity, u , replaced by the length of arc on the curve of the Johnston plot. They refer to this as the "developed" velocity distribution. In deriving this relationship they began with the assumption that since the two-dimensional law of the wall normally was derived from a differential equation relating shear stress, eddy viscosity and the rate of strain (velocity gradient) then a direct analogy could be made for three-dimensional flow. A formulation of a differential equation in the parameters mentioned above ensued, followed by an integration to get the law of the wall for three-dimensional flow. They showed mathematically that the significant quantity for the law of the wall in three-dimensional flow was the length of arc in the Johnston plot. The range of validity which they placed on their law of the wall was the value of "y" (normal distance

from the wall) which coincides with the outer limit of the curved portion in the polar plots. Comparison of their theory with data and Clauser lines on the Clauser plot was made which indicated for low mean-flow inertia forces their theory and Clauser lines coincided but as the mean-flow inertia forces became high a significant difference between their theory and Clauser lines resulted. Joubert et al. (40) reported that subsequent to publication of the paper under discussion, the three-dimensional law of the wall was compared with Johnston's (39) experimental data and poor correlation resulted. As mentioned in the next paragraph, this approach has been abandoned in favor of a regional similarity approach.

Joubert et al. (40) proposed essentially the same type of velocity defect equation as was discussed in the previous paragraph and it was compared with both the data of Hornung and Joubert (36) and Johnston (39) with good agreement. The inner region profile model has been modified from the three-dimensional law of the wall to the regional similarity approach. Regional similarity for two-dimensional flow with pressure gradients was introduced by Perry et al. (54) which is essentially dividing the wall flow into three regions, an inner region, Region I, influenced by τ_0 , ρ , v and y , an intermediate region, Region II, influenced by τ_0 , ρ and y and the outer region of the wall flow, Region III, influenced by σ , ρ and y . Their nomenclature is as follows: τ_0 is the local wall shear stress, σ is the local kinematic pressure gradient $(1/\rho)(dp/dx)$ where p is the static pressure, ρ is the fluid density, v is the kinematic viscosity and y is the normal distance from the wall.

By the use of dimensional analysis and blending requirements along with some physical requirements they arrived at a modified logarithmic law of the wall for Region II and an expression which they refer to as the "half-power law" for Region III. Again, the three-dimensional version of the regional similarity analysis, as for the three-dimensional law of the wall, was modified to use the developed velocity profiles, i.e. the curved portion of a Johnston plot. A comparison of both the data of Johnston (39) and Hornung and Joubert (36) with the half-power law using two-dimensional constants but the developed profiles showed encouraging agreement. The available data was not sufficiently accurate or adequate to support further theorizing and suggests that further experimental studies should be carried out in this field.

As can be inferred from the previous paragraphs pertaining to three-dimensional turbulent velocity profiles, considerable effort will be required to enable a prediction of profiles in general flow situations since presently, even particular flow situations cannot be predicted. It appears that two approaches can be taken, one being that of understanding the basic mechanisms of three-dimensional turbulent flow and generating the velocity models from those considerations or that of compiling abundant data and correlating it in a manner which inspires the formulation of a good empirical velocity expression. In either case, experimental data must be obtained for a variety of flow situations which encompass the majority of flow characteristics encountered.

Velocity models are only a part of solving the three-dimensional turbulent boundary layer problem. In order to describe the global

behavior of boundary layers the equations of motion, or momentum equations, energy equations and the equation of continuity must be solved in some form depending on the simplifying assumptions which are allowed. A brief discussion of boundary layer equations and methods for the solution of three-dimensional turbulent boundary layer flow will follow.

Skewed turbulent boundary layer analytical methods

The term analytical methods, as used in this section does not imply a strictly theoretical mathematical formulation of the problem dependent only on initial conditions and boundary conditions for the solution. Perusal of current material in the turbulent boundary layer field has disclosed that every method for solving the problem entails some type of empirical expression.

One of a number of derivations of the time-average boundary layer equations for three-dimensional flow with the customary simplifying assumptions has been presented by Sherman (69). The greatest majority of authors write the basic equations in terms of the "intrinsic coordinates" which are simply coordinates tangent and perpendicular to the free stream, inviscid flow, streamlines. This has the advantage of having only one mean velocity component at the boundary layer edge, the streamline component. Another common practice is to write the boundary layer equations in curvilinear coordinate systems, of which the intrinsic coordinates are a special form, so that the curvatures of the streamlines and their orthogonal trajectories are geodesic curvatures. Geodesic curvature as defined by Sherman (69) is the curvature of the projection

of a surface curve onto the tangent plane which coincides with the point on the surface that is in question. Geodesics are surface curves that have no geodesic curvature, which implies that if a view of the projection on the tangent plane is seen along a normal at the point in question, a straight line segment would appear. His example is that of the "great circle" routes over the earth's surface from a designated city to a multitude of others which shows that an infinite number of geodesic curvatures can pass through one point with its own tangent direction such that the projections on the tangent plane are straight line segments.

As was discussed in the review papers of Cooke (18), Horlock et al. (35) and Sherman (69), considerable literature in laminar flow over infinite yawed wings has been published because of the "independence" principle. This principle maintains that chordwise flow is independent of crosswise flow so the chordwise components of flow satisfy the ordinary two-dimensional boundary layer equations. This principle is not applicable for turbulent flow. Ashkenas and Riddell (1) helped to confirm this experimentally and, after Rott and Crabtree, showed it theoretically. Their method of proof was to express the boundary layer growth following two different paths over a yawed flat plate. One path was along the potential flow streamline and the other was along a path perpendicular to the leading edge of the yawed flat plate which implies the spanwise potential flow is along a layer of constant thickness. The latter essentially being the independence principle. Comparing the two thicknesses at a common point yields an identity for laminar flow but an inequality for turbulent flow. This inequality is primarily attributed

to the Reynolds stresses present in turbulent flow.

Cooke (18) has assumed that crosswise components of velocity and its derivatives are small. This leads to the standard momentum-integral equation for flow over an axisymmetric body, hence he calls it the "axially-symmetric" analogy. This restricts the flows only to the three-dimensional effect of diverging or converging streamlines. As reported by Horlock et al. (35) this approach is essentially paralleled by Eichelbrenner and Oudart which they name the "principle of prevalence" or in more commonplace terms, "small crossflow". Eichelbrenner and Peube (22) has related that this computational method has been tested against data from an inclined ellipsoid of revolution in a plane of symmetry and a marked discrepancy between theory and data occurred.

Pierce (58) has analyzed the momentum equations for the plane of symmetry of a collateral three-dimensional boundary layer. This implies no lateral velocity (no skewing) but spreading or diverging flow. This more simplified flow requires the simultaneous solution of a momentum integral equation, a wall shear coefficient law and a variation of shape parameter equation. His comparison of experimental data and theory was not impressive. He also compared the momentum growth with two-dimensional equations and found poor agreement.

Francis (24) and Francis and Pierce (25) have reviewed the boundary layer growth models for turbulent incompressible flow. It is suggested that these references be consulted for a synopsis of the models of Mager, Becker, Johnston, Cooke, and Nelson. Every model is essentially the same, in that all use the streamwise and crossflow momentum integral

equations for steady flow which involve seven unknowns. This requires five auxiliary equations to be formulated. The various velocity models were used in some form or other as one auxiliary equation. Another common auxiliary equation was some form of a two-dimensional shear law. Various shape parameters were also formulated for use as an auxiliary equation.

Carmichael (9) essentially added another method similar to those reported by Francis in the previous paragraph. His basic assumption was small crossflow, and the main difference from other methods was the use of an empirical correlation between a crossflow shape factor and the streamwise shape factor. Only fair agreement between theory and the data he based it on was realized.

Gumpsty and Head (19) used the momentum integral equations as all prior investigators, but they retained all the terms. This alleviates the restriction of small crossflows. In their method they equate the increase of mass flux in the boundary layer to the rate at which free stream fluid is entrained. They assume the entrainment rate is directly controlled by the velocity deficit in the outer portion of the boundary layer. From these considerations, a nondimensional form parameter is derived which is used in an entrainment function. In conjunction with this, an auxiliary equation, their entrainment equation, was derived with the entrainment function as one of the variables. The remaining auxiliary equations were similar to others investigated. The method of solution was a computerized iteration process which began with two-dimensional momentum integral equations, progressed to Cooke's "axially-

"symmetric" momentum integral equations and then to the three-dimensional momentum integral equations. No comparison was made with data.

Bradshaw et al. (7) have suggested that the boundary layer development for three-dimensional flow could be calculated using the turbulent energy equation, mean momentum equation and the mean continuity equation. The turbulent energy equation, through the use of empirical relations for the production, diffusion and dissipation vectors, could be put into differential equation form to calculate the rate of change of the shear stress vector along a mean streamline. The resulting system of equations could be solved numerically. They suggest a difficulty may arise in determining the direction of the production vector. To this authors knowledge, this method has not been pursued any further than the original outline.

Mellor (51) has developed a technique for calculating turbulent boundary layer development which is valid for flows along a plane of symmetry which has diverging or converging crossflows. It might be emphasized that this is not for the general skewed turbulent boundary layers. His approach is that of converting the turbulent boundary layer equations into ordinary differential equations. In conjunction with the transformed boundary layer equations he derived relationships for the effective viscosity. With these equations and boundary conditions at the inner and outer edge of the boundary layer, an iteration scheme is employed for numerical integration across the boundary layer. Spalding (71) classifies this procedure as the cross-stream integration method. To calculate the boundary layer growth, the streamwise variation in the

free stream velocity and the streamwise distribution of the crossflow velocity gradient with respect to the crossflow direction, viz., $U(x)$ and $W_z(x)$ must be input information. An important assumption utilized in this method is that the eddy viscosity is a scalar function so that $-\partial(\bar{w})/\partial z = v_e \partial^2 w/\partial z \partial y$. An advantage of this method is that the velocity profile across the boundary layer is not an input but is a result of the calculations. He compared this technique with some of Johnston's (39) data along a plane of symmetry which resulted in excellent agreement for the streamwise velocity profile but was only fair for the crossflow profile.

It seems trite to indicate that the methods and models available to the engineers involved in skewed boundary layer work are inadequate and inaccurate, although no other conclusion could conscientiously be derived from the available data. This situation will certainly not be remedied by this work or even several which might follow, but by the amalgamation of many theoretical and experimental studies complementing each other.

THEORETICAL DEVELOPMENT

Because of the complexity of the three-dimensional boundary layer it seemed desirable to approach the problem by fractional analysis, and to use the information gained to explore a more sophisticated approach. Fractional analysis, as defined by Kline (41), is any procedure for obtaining some information about the answer to a problem in the absence of methods or time for finding a complete solution. The approach used here is the fractional analysis of governing equations and conditions by non-dimensionalizing with terms comparable in both magnitude and dimension. This section is divided into two parts, one concerned with the development of similarity parameters and the other with determination of the significant terms in the governing equations.

Similarity Parameters

In APPENDIX B, the governing equations for the particular problem of incompressible, three-dimensional constant viscosity boundary layers have been developed in terms of instantaneous variables. As stated in the Literature Review, for turbulent flow the instantaneous variables can be expressed as the sum of a mean value and a fluctuating value of the variable. Also in APPENDIX B there are some remarks and rules pertaining to averaging fluctuating variables. These are used in this section. Since density and viscosity have been assumed constant, the remaining variables which are allowed to fluctuate are u , v , w and P . As in

APPENDIX B, these variables can be expressed as

$$\left. \begin{aligned} u &\equiv \bar{u} + u' \\ v &\equiv \bar{v} + v' \\ w &\equiv \bar{w} + w' \\ p &\equiv \bar{p} + p' \end{aligned} \right\} \quad (1)$$

Normally these equations are introduced into the boundary layer equations, that is, the Navier-Stokes equations after certain approximations peculiar to boundary layer flow have been used to reduce their complexity. Because of a possibility of neglecting some significant terms in the reduced equations by looking only at the instantaneous values, it appeared appropriate to introduce the expressions for the instantaneous values into the Navier-Stokes equations before reducing them. The motivation for this is the experimental result, Sandborn and Slogar (66), that $\frac{\partial v'^2}{\partial y}$ is a significant term in a two-dimensional boundary layer with an adverse pressure gradient, whereas $\frac{\partial \bar{v}}{\partial y}$ is not. Since instantaneous values are usually assumed approximately equal to the mean value, it would seem feasible to also think of the gradient of the instantaneous value as being approximately equal to the gradient of the mean value which might lead to a spurious set of reduced equations.

Before expanding the Navier-Stokes equations in terms of mean and fluctuating components it is advantageous to inspect the equations and determine if they are in the most appropriate form for averaging. In Equations B-16, B-17 and B-18 the first three terms, the acceleration terms, of each of the components of the Navier-Stokes equations include

the form

$$\frac{u_i}{h_i} \frac{\partial u_j}{\partial x_i} \quad i = 1, 3 \\ j = 1, 3 .$$

It may be concluded that this form is not first order and would thereby probably not result in a zero value for the fluctuating variations, but is a difficult expression to verify experimentally. As was suggested by Rouse (62), the combination of the continuity equation multiplied by an appropriate term and the first three acceleration terms in each equation would result in a more amenable form for averaging the fluctuating terms. For instance, if the continuity equation is multiplied by u , then added to the first three terms of Equation B-16, it can readily be seen after factoring $1/h_1 h_2 h_3$ from the combined terms that the sum of derivatives of products exists as:

$$\frac{1}{h_1 h_2 h_3} \left\{ u h_2 h_3 \frac{\partial u}{\partial \xi} + v h_1 h_3 \frac{\partial u}{\partial \eta} + w h_1 h_2 \frac{\partial u}{\partial \zeta} + u \frac{\partial(u h_2 h_3)}{\partial \xi} \right. \\ \left. + u \frac{\partial(v h_1 h_3)}{\partial \eta} + u \frac{\partial(w h_1 h_2)}{\partial \zeta} \right\} = \frac{1}{h_1 h_2 h_3} \left\{ \frac{\partial(u^2 h_2 h_3)}{\partial \xi} \right. \\ \left. + \frac{\partial(u v h_1 h_3)}{\partial \eta} + \frac{\partial(u w h_1 h_2)}{\partial \zeta} \right\} . \quad (2)$$

By analogy, the other accelerating terms are arranged in the same form.

After the Equations 1 are introduced into Equation B-16 with the modified form given by Equation 2, integration can be performed using the rules in APPENDIX B and noting that the space coordinates are independent of time so the integration can be performed inside the derivative. Upon expansion of all the acceleration terms, and through the use of the mean continuity equation, the first three mean acceleration

terms in each equation are reverted back to the form in Equation B-16.

This series of operations results in the following equation:

ξ -Equation

$$\begin{aligned}
 & \frac{\bar{u}}{h_1} \frac{\partial \bar{u}}{\partial \xi} + \frac{\bar{v}}{h_2} \frac{\partial \bar{u}}{\partial \eta} + \frac{\bar{w}}{h_3} \frac{\partial \bar{u}}{\partial \zeta} - \frac{\bar{v}^2}{h_1 h_2} \frac{\partial h_2}{\partial \xi} - \frac{\bar{w}^2}{h_1 h_3} \frac{\partial h_3}{\partial \xi} + \frac{\bar{u}\bar{v}}{h_1 h_2} \frac{\partial h_1}{\partial \eta} + \frac{\bar{u}\bar{w}}{h_1 h_3} \frac{\partial h_1}{\partial \zeta} \\
 & + \frac{1}{h_1 h_2 h_3} \frac{\partial (\bar{u}'^2 h_2 h_3)}{\partial \xi} + \frac{1}{h_1 h_2 h_3} \frac{\partial (\bar{u}' \bar{v}' h_1 h_3)}{\partial \eta} + \frac{1}{h_1 h_2 h_3} \frac{\partial (\bar{u}' \bar{w}' h_1 h_2)}{\partial \zeta} - \frac{\bar{v}'^2}{h_1 h_2} \frac{\partial h_2}{\partial \xi} \\
 & - \frac{\bar{w}'^2}{h_1 h_3} \frac{\partial h_3}{\partial \xi} + \frac{\bar{u}' \bar{v}'}{h_1 h_2} \frac{\partial h_1}{\partial \eta} + \frac{\bar{u}' \bar{w}'}{h_1 h_3} \frac{\partial h_1}{\partial \zeta} = - \frac{1}{\rho h_1} \frac{\partial \bar{P}}{\partial \xi} + \frac{\mu}{h_1 h_2 h_3 \rho} \frac{\partial}{\partial \xi} \left(\frac{h_2 h_3}{h_1} \frac{\partial \bar{u}}{\partial \xi} \right) \\
 & + \frac{\mu}{h_1 h_2 h_3 \rho} \frac{\partial}{\partial \eta} \left(\frac{h_1 h_3}{h_2} \frac{\partial \bar{u}}{\partial \eta} \right) + \frac{\mu}{h_1 h_2 h_3 \rho} \frac{\partial}{\partial \zeta} \left(\frac{h_1 h_2}{h_3} \frac{\partial \bar{u}}{\partial \zeta} \right). \tag{3}
 \end{aligned}$$

Similarly, the η and ζ direction equations are obtained.

η -Equation

$$\begin{aligned}
 & \frac{\bar{u}}{h_1} \frac{\partial \bar{v}}{\partial \xi} + \frac{\bar{v}}{h_2} \frac{\partial \bar{v}}{\partial \eta} + \frac{\bar{w}}{h_3} \frac{\partial \bar{v}}{\partial \zeta} - \frac{\bar{u}^2}{h_1 h_2} \frac{\partial h_1}{\partial \eta} - \frac{\bar{w}^2}{h_2 h_3} \frac{\partial h_3}{\partial \eta} + \frac{\bar{u}\bar{v}}{h_1 h_2} \frac{\partial h_2}{\partial \xi} + \frac{\bar{w}\bar{v}}{h_2 h_3} \frac{\partial h_2}{\partial \zeta} \\
 & + \frac{1}{h_1 h_2 h_3} \frac{\partial (\bar{u}' \bar{v}' h_2 h_3)}{\partial \xi} + \frac{1}{h_1 h_2 h_3} \frac{\partial (\bar{v}'^2 h_1 h_3)}{\partial \eta} + \frac{1}{h_1 h_2 h_3} \frac{\partial (\bar{v}' \bar{w}' h_1 h_2)}{\partial \zeta} - \frac{\bar{u}'^2}{h_1 h_2} \frac{\partial h_1}{\partial \eta} \\
 & - \frac{\bar{w}'^2}{h_2 h_3} \frac{\partial h_3}{\partial \eta} + \frac{\bar{u}' \bar{v}'}{h_1 h_2} \frac{\partial h_2}{\partial \xi} + \frac{\bar{w}' \bar{v}'}{h_2 h_3} \frac{\partial h_2}{\partial \zeta} = - \frac{1}{h_2 \rho} \frac{\partial \bar{P}}{\partial \eta} + \frac{\mu}{h_1 h_2 h_3 \rho} \frac{\partial}{\partial \xi} \left(\frac{h_2 h_3}{h_1} \frac{\partial \bar{v}}{\partial \xi} \right) \\
 & + \frac{\mu}{h_1 h_2 h_3 \rho} \frac{\partial}{\partial \eta} \left(\frac{h_1 h_3}{h_2} \frac{\partial \bar{v}}{\partial \eta} \right) + \frac{\mu}{h_1 h_2 h_3 \rho} \frac{\partial}{\partial \zeta} \left(\frac{h_1 h_2}{h_3} \frac{\partial \bar{v}}{\partial \zeta} \right). \tag{4}
 \end{aligned}$$

ζ -Equation

$$\begin{aligned}
 & \frac{\bar{u}}{h_1} \frac{\partial \bar{w}}{\partial \xi} + \frac{\bar{v}}{h_2} \frac{\partial \bar{w}}{\partial \eta} + \frac{\bar{w}}{h_3} \frac{\partial \bar{w}}{\partial \zeta} - \frac{\bar{u}^2}{h_1 h_3} \frac{\partial h_1}{\partial \zeta} - \frac{\bar{v}^2}{h_2 h_3} \frac{\partial h_2}{\partial \zeta} + \frac{\bar{u}\bar{w}}{h_1 h_3} \frac{\partial h_3}{\partial \xi} + \frac{\bar{v}\bar{w}}{h_2 h_3} \frac{\partial h_3}{\partial \eta} \\
 & + \frac{1}{h_1 h_2 h_3} \frac{\partial (\bar{u}' w' h_2 h_3)}{\partial \xi} + \frac{1}{h_1 h_2 h_3} \frac{\partial (\bar{v}' w' h_1 h_3)}{\partial \eta} + \frac{1}{h_1 h_2 h_3} \frac{\partial (\bar{w}'^2 h_1 h_2)}{\partial \zeta} - \frac{\bar{u}'^2}{h_1 h_3} \frac{\partial h_1}{\partial \zeta} \\
 & - \frac{\bar{v}'^2}{h_2 h_3} \frac{\partial h_2}{\partial \zeta} + \frac{\bar{u}' w'}{h_1 h_3} \frac{\partial h_3}{\partial \xi} + \frac{\bar{v}' w'}{h_2 h_3} \frac{\partial h_3}{\partial \eta} = - \frac{1}{h_3^o} \frac{\partial \bar{P}}{\partial \zeta} + \frac{\mu}{h_1 h_2 h_3^o} \frac{\partial}{\partial \zeta} \left(\frac{h_2 h_3}{h_1} \frac{\partial \bar{w}}{\partial \xi} \right) \\
 & + \frac{\mu}{h_1 h_2 h_3^o} \frac{\partial}{\partial \eta} \left(\frac{h_1 h_3}{h_2} \frac{\partial \bar{w}}{\partial \eta} \right) + \frac{\mu}{h_1 h_2 h_3^o} \frac{\partial}{\partial \zeta} \left(\frac{h_1 h_2}{h_3} \frac{\partial \bar{w}}{\partial \zeta} \right)
 \end{aligned} \tag{5}$$

Since the continuity equation is of first order in the dependent variables, then the continuity equation retains the instantaneous form with the mean values replacing the instantaneous values. The expanded form of the continuity equation is

$$\begin{aligned}
 & \frac{\bar{u}}{h_1 h_2 h_3} \frac{\partial (h_2 h_3)}{\partial \xi} + \frac{\bar{v}}{h_1 h_2 h_3} \frac{\partial (h_1 h_3)}{\partial \eta} + \frac{\bar{w}}{h_1 h_2 h_3} \frac{\partial (h_1 h_2)}{\partial \zeta} \\
 & + \frac{1}{h_1} \frac{\partial \bar{u}}{\partial \xi} + \frac{1}{h_2} \frac{\partial \bar{v}}{\partial \eta} + \frac{1}{h_3} \frac{\partial \bar{w}}{\partial \zeta} = 0 .
 \end{aligned} \tag{6}$$

Equations 3, 4, 5 and 6 are in a form which would allow fractional analysis if the normalizing terms were known. There are sixteen variables which require a normalizing factor. They are \bar{u} , \bar{v} , \bar{w} , ξ , η , ζ , h_1 , h_2 , h_3 , \bar{u}'^2 , \bar{v}'^2 , \bar{w}'^2 , $\bar{u}' v'$, $\bar{u}' w'$, $\bar{v}' w'$ and \bar{P} . In order to determine the normalizing factors, various approaches were taken which entailed theory, physical reasoning and experimental data.

The scale factors h_1 , h_2 and h_3 indicate the flow field configuration and are the starting point for this analysis. Cumpsty and Head (19) have used the definition of the velocity potential to obtain h_1 . They concluded that h_1 could be represented as $1/U$, where U is the resultant velocity outside the boundary layer. This analysis used the same approach but it was found for the present coordinate system that Cumpsty and Head's representation for h_1 was not dimensionally compatible with the continuity equation. In addition, if the flow field approached a rectangular configuration then the free stream velocity must approach a value of one to reflect the correct scale factor value. For curvilinear coordinates the velocity potentials given by Rouse (62) are:

$$u = \frac{1}{h_1} \frac{\partial \phi}{\partial \xi}, \quad v = \frac{1}{h_2} \frac{\partial \phi}{\partial \eta} \text{ and } w = \frac{1}{h_3} \frac{\partial \phi}{\partial \zeta} .$$

Since ξ was selected as the coordinate along the streamline at the outer edge of the boundary layer and the flow was assumed irrotational then lines of constant ξ and constant ϕ coincide. This being so would allow the expression $\phi = k\xi$ to be valid. Assuming k is constant and has dimensions of velocity, then the following approximate relation would result

$$u_{\eta=\delta} = U = \frac{1}{h_1} k \frac{\partial \xi}{\partial \xi} = \frac{k}{h_1}$$

or $h_1 = \frac{k}{U}$.

This is consistent with the other expressions for the velocity potential. Since ξ , η and ζ are independent then $\frac{\partial \phi}{\partial \eta}$ and $\frac{\partial \phi}{\partial \zeta}$ are zero which agrees with the definition of the coordinate system in that $v_{\eta=\delta}$ and $w_{\eta=\delta}$ are zero.

Unless a separation point is being approached it is a fair approximation to assume that flow over a flat surface within the boundary layer is approximately orthogonal to a normal to the wall or in other words h_2 is approximately one. It will be assumed that $h_2 = 1$.

Having values for h_1 and h_2 it is now possible to use the continuity equation to determine an approximation for h_3 . Since continuity must be valid at all points in the flow field, then by definition of the coordinate system Equation 6 would have the following form at the outer edge of the boundary layer:

$$\frac{U}{h_1 h_3} \frac{\partial h_3}{\partial \xi} + \frac{1}{h_1} \frac{\partial U}{\partial \xi} = 0 .$$

Rearranging this equation and using the expression for h_1 results in:

$$\frac{U^2}{kh_3} \frac{\partial h_3}{\partial \xi} = - \frac{U}{k} \frac{\partial U}{\partial \xi}$$

or

$$\frac{1}{kh_3} \frac{\partial h_3}{\partial \xi} = - \frac{1}{kU} \frac{\partial U}{\partial \xi} .$$

As a result of the above equation, $h_3 = \frac{k}{U}$ to satisfy continuity.

With these approximations for h_1 , h_2 and h_3 , a set of approximations for \bar{u} , \bar{v} , \bar{w} , ξ , n and ζ may be determined. From two-dimensional fractional analysis arguments which have proven to be useful, it is assumed the value for \bar{u} will be of the order of U and the value of ξ will be of the order of L , L being some characteristic length. All the remaining variables will be determined from a parallel approach. A summary of these follows. The notation $\bar{u} = \sigma(U)$ means that \bar{u} is of the order of magnitude of U .

$\bar{u} = \sigma(U)$ U is the free stream velocity

$\bar{v} = \sigma(V)$ V is some undefined velocity

$\bar{w} = \sigma(W)$ W is some undefined velocity

$\xi = \sigma(L)$ L is a characteristic body length

$\eta = \sigma(\delta)$ δ is the boundary layer thickness

$\zeta = \sigma(l)$ l is an undefined length

$$h_1 = \sigma\left(\frac{k}{U}\right)$$

$$h_2 = 1$$

$$h_3 = \sigma\left(\frac{k}{U}\right)$$

It is now possible to define a preliminary set of dimensionless quantities so more information can be gained pertaining to the undefined parameters above. These normalized quantities are:

$$u^* = \frac{\bar{u}}{U} \quad \xi^* = \frac{\xi}{L} \quad h_1^* = \frac{h_1}{(k/U)}$$

$$v^* = \frac{\bar{v}}{V} \quad \eta^* = \frac{\eta}{\delta} \quad h_2^* = 1$$

$$w^* = \frac{\bar{w}}{W} \quad \zeta^* = \frac{\zeta}{l} \quad h_3^* = \frac{h_3}{(k/U)}$$

Because the continuity equation must be valid independent of the influence of viscosity or the position in the flow field it was used to find the order of magnitude for V and W. Writing Equation 6 in terms of the normalized quantities yields:

$$\begin{aligned} & \frac{U^2}{kL} \frac{u^*}{h_1^* h_3^*} \frac{\partial h_3^*}{\partial \xi^*} + \frac{V}{\delta} \frac{v^*}{h_1^* h_3^*} \frac{\partial (h_1^* h_3^*)}{\partial \eta^*} + \frac{UW}{k\ell} \frac{w^*}{h_1^* h_3^*} \frac{\partial h_1^*}{\partial \zeta^*} \\ & + \frac{U^2}{kL} \frac{\partial u^*}{\partial \xi^*} + \frac{V}{\delta} \frac{\partial v^*}{\partial \eta^*} + \frac{UW}{k\ell} \frac{\partial w^*}{\partial \zeta^*} = 0 . \end{aligned}$$

Analogous to two-dimensional analysis, the term $\frac{\partial u^*}{\partial \xi^*}$ was considered to be of order one, therefore by dividing all terms by U^2/kL each term should be of order one. If the normalized factors were chosen correctly the coefficients of each term would be of order one. Assuming this is so then

$$\frac{V/\delta}{U^2/kL} = \sigma(1)$$

and

$$\frac{UW/k\ell}{U^2/kL} = \sigma(1) .$$

A new approximation for the two undefined velocities would be

$$V \approx \frac{U^2 \delta}{kL}$$

and

$$W \approx \frac{U \ell}{L}$$

where ℓ is still an undetermined length.

Assuming the viscous terms and also the turbulence terms to be negligible at the boundary layer edge, an approximation for pressure is determined. By virtue of these assumptions and the definition of the coordinate system, Equation 3 becomes

$$\frac{\bar{u}}{h_1} \frac{\partial \bar{u}}{\partial \xi} = - \frac{1}{\rho h_1} \frac{\partial \bar{P}}{\partial \xi} .$$

Putting this equation in terms of the previously normalized parameters and in addition with $P^* = \bar{P}/PR$ yields:

$$\frac{U^3}{kL} \frac{u^*}{h_1^*} \frac{\partial u^*}{\partial \xi^*} = - \frac{U PR}{\rho k L h_1^*} \frac{\partial P^*}{\partial \xi^*}$$

which implies that

$$\bar{P} = \sigma(\rho U^2) .$$

The only terms which have not been normalized are the fluctuating terms. As was discussed in the Literature Review, the Reynolds stresses are zero at the wall and depending on the pressure gradient they reach a peak near the wall and decay to zero at the boundary layer edge. Sandborn and Slogar (66) obtained two-dimensional boundary layer data in a pressure gradient field which showed that $\overline{\rho u' w'}/\tau_w$, $\overline{\rho v'^2}/\tau_w$ and $\overline{\rho w'^2}/\tau_w$ varied from approximately one near the wall to zero at the boundary layer edge, while $\overline{\rho u'^2}/\tau_w$ varied from approximately four to zero. τ_w is the shear stress at the wall. It is assumed that the turbulence terms in three-dimensional boundary layers are approximately the same order of magnitude as in two-dimensional boundary layers so that the normalizing factor for the turbulence terms is τ_w/ρ .

All the normalizing factors have now been determined and the normalized variables are summarized below.

$$\begin{array}{ll}
 u^* = \sigma\left(\frac{u}{U}\right) & \xi^* = \sigma\left(\frac{\xi}{L}\right) \\
 v^* = \sigma\left(\frac{\bar{v}}{U^2 \delta / L k}\right) & n^* = \sigma\left(\frac{n}{\delta}\right) \\
 w^* = \sigma\left(\frac{\bar{w}}{U \ell / L}\right) & \zeta^* = \sigma\left(\frac{\zeta}{\ell}\right) \\
 u'^* = \sigma\left(\frac{\overline{u'^2}}{\tau_w / \rho}\right) & h_1^* = \sigma\left(\frac{h_1}{k/U}\right) \\
 v'^* = \sigma\left(\frac{\overline{v'^2}}{\tau_w / \rho}\right) & h_3^* = 1 \\
 w'^* = \sigma\left(\frac{\overline{w'^2}}{\tau_w / \rho}\right) & h_3^* = \sigma\left(\frac{h_3}{k/U}\right)
 \end{array}$$

$$\overline{u'v'}^* = \sigma\left(\frac{\overline{u'v'}}{\tau_w/\rho}\right)$$

$$\overline{u'w'}^* = \sigma\left(\frac{\overline{u'w'}}{\tau_w/\rho}\right)$$

$$\overline{v'w'}^* = \sigma\left(\frac{\overline{v'w'}}{\tau_w/\rho}\right)$$

$$P^* = \sigma\left(\frac{P}{\rho U^2}\right)$$

Since U is not a function of η and the scale factors are only a function of U and a constant, then the derivatives of the scale factors with respect to U are zero. This is expressed as

$$\frac{\partial h_i}{\partial \eta} = 0, \quad i = 1, 3 \quad (7)$$

for later reference.

Upon rewriting Equations 3, 4 and 5 in terms of the normalized variables, and dividing each term in the equation by one of the coefficients, modified coefficients which are significant in two respects result. These modified coefficients take the form of similarity parameters and in addition they indicate the significance of each term in relation to all the other terms in the equation. Similarity parameters are discussed first. Tables 1, 2 and 3 summarize the normalized terms, their coefficients and the modified coefficients. For the particular case shown, the modified coefficients for the normalized ξ -equation were obtained by dividing by the coefficients of the mean acceleration terms, which are generally significant terms in the streamwise direction. In case of the normalized η -equation the modified coefficients were obtained by dividing by the pressure gradient term coefficient as it is the one normally retained in two-dimensional boundary layer theory. The ζ -equation modified coefficients were also obtained by dividing by the

Table 1. ξ -Equation normalized terms

Term no.	Normalized terms	Coefficient of terms	Modified coefficients
1	$\frac{u^*}{h_1^*} \frac{\partial u^*}{\partial \xi^*}$	$\frac{U^3}{kL}$	1
2	$v^* \frac{\partial u^*}{\partial \eta^*}$	$\frac{U^3}{kL}$	1
3	$\frac{w^*}{h_3^*} \frac{\partial u^*}{\partial \zeta^*}$	$\frac{U^3}{kL}$	1
4	Equals zero by definition of h_2 .	0	0
5	$\frac{w^{*2}}{h_1^* h_3^*} \frac{\partial h_3^*}{\partial \xi^*}$	$\frac{U^3}{kL} \frac{l^2}{L^2}$	$\left(\frac{l}{L}\right)^2$
6	Equals zero by virtue of Equation 7.	0	0
7	$\frac{u^* w^*}{h_1^* h_3^*} \frac{\partial h_1^*}{\partial \zeta^*}$	$\frac{U^3}{kL}$	1
8	$\frac{1}{h_1^* h_3^*} \frac{\partial (u'^* h_3^*)}{\partial \xi^*}$	$\frac{U}{kL} \frac{\tau_w}{\rho}$	$\frac{\tau_w}{\rho U^2}$
9	$\frac{\partial (\overline{u'} v'^*)}{\partial \eta^*}$	$\frac{\tau_w}{\rho \delta}$	$\frac{L(k/U)}{\delta} \frac{\tau_w}{\rho U^2}$
10	$\frac{1}{h_1^* h_3^*} \frac{(u'^* w'^* h_1^*)}{\partial \zeta^*}$	$\frac{U}{k l} \frac{\tau_w}{\rho}$	$\frac{L}{l} \frac{\tau_w}{\rho U^2}$
11	Equals zero by definition of h_2 .	0	0

Table 1 (Continued)

Term no.	Normalized terms	Coefficient of terms	Modified coefficients
12	$\frac{w^*}{h_1^* h_3^*} \frac{\partial h_3^*}{\partial \xi}$	$\frac{U}{kL} \frac{\tau_w}{\rho}$	$\frac{\tau_w}{\rho U^2}$
13	Equals zero by virtue of Equation 7.	0	0
14	$\frac{u^* w^*}{h_1^* h_3^*} \frac{\partial h_1^*}{\partial \zeta^*}$	$\frac{U}{k\ell} \frac{\tau_w}{\rho}$	$\frac{L}{\ell} \frac{\tau_w}{\rho U^2}$
15	$\frac{1}{h_1^*} \frac{p^*}{\partial \xi}$	$\frac{U^3}{kL}$	1
16	$\frac{1}{h_1^* h_3^*} \frac{\partial}{\partial \xi^*} \left(\frac{h_3^*}{h_1^*} \frac{\partial u^*}{\partial \xi^*} \right)$	$\frac{\mu}{\rho L} \frac{U^3}{k^2 L}$	$\frac{\mu}{\rho UL(k/U)}$
17	$\frac{1}{h_1^* h_3^*} \frac{\partial}{\partial \eta^*} \left(h_1^* h_3^* \frac{\partial u^*}{\partial \eta^*} \right)$	$\frac{\mu}{\rho} \frac{U}{\delta^2}$	$\frac{\mu}{\rho UL(k/U)} \left(\frac{L(k/U)}{\delta} \right)^2$
18	$\frac{1}{h_1^* h_3^*} \frac{\partial}{\partial \zeta^*} \left(\frac{h_1^*}{h_3^*} \frac{\partial u^*}{\partial \zeta^*} \right)$	$\frac{\mu}{\rho} \frac{U^3}{k^2 \ell^2}$	$\frac{\mu}{\rho UL(k/U)} \left(\frac{L}{\ell} \right)^2$

Table 2. η -Equation normalized terms

Term no.	Normalized terms	Coefficient of terms	Modified coefficients
1	$\frac{u^*}{h_1^*} \frac{\partial v^*}{\partial \xi^*}$	$\frac{U^4 \delta}{k^2 L^2}$	$\left(\frac{\delta}{(k/U)L} \right)^2$
2	$v^* \frac{\partial v^*}{\partial \eta^*}$	$\frac{U^4 \delta}{k^2 L^2}$	$\left(\frac{\delta}{(k/U)L} \right)^2$
3	$\frac{w^*}{h_3^*} \frac{\partial v^*}{\partial \xi^*}$	$\frac{U^4 \delta}{k^2 L^2} \frac{\ell}{L}$	$\left(\frac{\delta}{(k/U)L} \right)^2 \frac{\ell}{L}$
4	Equals zero by virtue of Equation 7.	0	0
5	Equals zero by virtue of Equation 7.	0	0
6	Equals zero by definition of h_2 .	0	0
7	Equals zero by definition of h_2 .	0	0
8	$\frac{1}{h_1^* h_3^*} \frac{\partial (\overline{u'v'})^* h_3^*}{\partial \xi^*}$	$\frac{U}{kL} \frac{\tau_w}{\rho}$	$\frac{\tau_w}{\rho U^2} \left(\frac{\delta}{(k/U)L} \right)$
9	$\frac{1}{h_1^* h_3^*} \frac{\partial v'^*}{\partial \eta^*}$	$\frac{\tau_w}{\rho \delta}$	$\frac{\tau_w}{\rho U^2}$
10	$\frac{1}{h_1^* h_3^*} \frac{\partial (\overline{v'w'})^* h_1^*}{\partial \xi^*}$	$\frac{U}{k\ell} \frac{\tau_w}{\rho}$	$\frac{\tau_w}{\rho U^2} \left(\frac{\delta}{(k/U)\ell} \right)$
11	Equals zero by virtue of Equation 7.	0	0

Table 2 (Continued)

Term no.	Normalized terms	Coefficient of terms	Modified coefficients
12	Equals zero by virtue of Equation 7.	0	0
13	Equals zero by definition of h_2 .	0	0
14	Equals zero by definition of h_2 .	0	0
15	$\frac{\partial P^*}{\partial \eta^*}$	$\frac{U^2}{\delta}$	1
16	$\frac{1}{h_1^* h_3^*} \frac{\partial}{\partial \xi^*} \left(\frac{h_3^*}{h_1^*} \frac{\partial v^*}{\partial \xi^*} \right)$	$\frac{\mu}{\rho} \left(\frac{U^4 \delta}{k^2 L^2} \right) \frac{1}{kL}$	$\frac{\mu}{\rho U(k/U)L} \left(\frac{\delta}{(k/U)L} \right)^2$
17	$\frac{\partial}{\partial \eta^*} \left(\frac{\partial v^*}{\partial \eta^*} \right)$	$\frac{\mu}{\rho k L} \frac{U^2}{\delta}$	$\frac{\mu}{\rho U(k/U)L}$
18	$\frac{1}{h_1^* h_3^*} \frac{\partial}{\partial \xi^*} \left(\frac{h_1^*}{h_3^*} \frac{\partial v^*}{\partial \xi^*} \right)$	$\frac{\mu}{\rho} \left(\frac{U^4 \delta}{k^2 L^2} \right) \frac{1}{kL}$	$\frac{\mu}{\rho U(k/U)L} \left(\frac{\delta}{(k/U)L} \right)^2$

Table 3. ζ -Equation normalized terms

Term no.	Normalized terms	Coefficient of terms	Modified coefficients
1	$\frac{u^*}{h_1^*} \frac{\partial w^*}{\partial \xi^*}$	$\frac{U^3}{kL} \frac{l}{L}$	$\frac{l^2}{L^2}$
2	$v^* \frac{\partial w^*}{\partial \eta^*}$	$\frac{U^3}{kL} \frac{l}{L}$	$\frac{l^2}{L^2}$
3	$\frac{w^*}{h_3^*} \frac{\partial w^*}{\partial \xi^*}$	$\frac{U^3}{kL} \frac{l}{L}$	$\frac{l^2}{L^2}$
4	$\frac{u^{*2}}{h_1^* h_3^*} \frac{\partial h_1^*}{\partial \xi^*}$	$\frac{U^3}{k\ell}$	1
5	Equal zero by definition of h_2^* .	0	0
6	$\frac{u^* w^*}{h_1^* h_3^*} \frac{\partial h_3^*}{\partial \xi^*}$	$\frac{U^3}{kL} \frac{l}{L}$	$\frac{l^2}{L^2}$
7	Equals zero by virtue of Equation 7.	0	0
8	$\frac{1}{h_1^* h_3^*} \frac{\partial (u' w')^*}{\partial \xi^*} h_3^*$	$\frac{U}{kL} \frac{\tau_w}{\rho}$	$\frac{\tau_w}{\rho U^2} \left(\frac{l}{L} \right)$
9	$\frac{(v' w')^*}{\partial \eta}$	$\frac{\tau_w}{\rho \delta}$	$\frac{\tau_w}{\rho U^2} \frac{(k/U)l}{\delta}$
10	$\frac{1}{h_1^* h_3^*} \frac{\partial (w'^* h_1^*)}{\partial \xi^*}$	$\frac{U}{k\ell} \frac{\tau_w}{\rho}$	$\frac{\tau_w}{\rho U^2}$
11	$\frac{u'^*}{h_1^* h_3^*} \frac{\partial h_1^*}{\partial \xi^*}$	$\frac{U}{k\ell} \frac{\tau_w}{\rho}$	$\frac{\tau_w}{\rho U^2}$

Table 3 (Continued)

Term no.	Normalized terms	Coefficient of terms	Modified coefficients
12	Equals zero by definition of h_2 .	0	0
13	$\frac{u'w'^*}{h_1^*h_3^*} \frac{\partial h_3^*}{\partial \xi^*}$	$\frac{U}{kL} \frac{\tau_w}{\rho}$	$\frac{\tau_w}{\rho U^2} \left(\frac{\ell}{L} \right)$
14	Equals zero by virtue of Equation 7.	0	0
15	$\frac{1}{h_3^*} \frac{\partial P^*}{\partial \zeta^*}$	$\frac{U^3}{k\ell}$	1
16	$\frac{1}{h_1^*h_3^*} \frac{\partial}{\partial \xi^*} \left(\frac{h_3^*}{h_1^*} \frac{\partial w^*}{\partial \xi^*} \right)$	$\frac{\mu}{\rho} \frac{U^3 \ell}{k^2 L^3}$	$\frac{\mu}{\rho U(k/U)L} \left(\frac{\ell}{L} \right)^2$
17	$\frac{\partial}{\partial \eta^*} \left(\frac{\partial w^*}{\partial \eta^*} \right)$	$\frac{\mu}{\rho} \frac{U \ell}{L \delta^2}$	$\frac{\mu}{\rho U(k/U)L} \left(\frac{(k/U) \ell}{\delta} \right)^2$
18	$\frac{1}{h_1^*h_3^*} \frac{\partial}{\partial \zeta^*} \left(\frac{h_1^*}{h_3^*} \frac{\partial w^*}{\partial \zeta^*} \right)$	$\frac{\mu}{\rho} \frac{U^3}{k^2 L \ell}$	$\frac{\mu}{\rho U(k/U)L}$

coefficient of the pressure gradient term. It was reasoned that cross-flow is primarily induced by the pressure gradient and all other terms should be compared to it.

Many of the similarity parameters that were obtained by the fractional analysis method are very similar to those found in two-dimensional boundary layers. It is seen that the Reynolds number is based on $h_1 \xi$ instead of x as in two-dimensional boundary layers. The similarity parameter $\tau_w / \rho U^2$ can be rewritten as $(U_\tau / U)^2$ or $(u^+)^2$ and is recognized as the square of the dependent variable in the law of the wall for two-dimensional boundary layers. As stated in the Literature Review, Bradshaw (6) found that $\tau_{\max} / \rho U^2$ was nearly proportional to v_p / U in both equilibrium and non-equilibrium boundary layers. The analysis could have used τ_{\max} instead of τ_w which would have yielded Bradshaw's parameter. Another similarity parameter which was obtained from the fractional analysis was $h_1 \xi \tau_w / \delta \rho U^2$. Inertia force in the ξ direction per unit volume is proportional to $\rho U^2 / h_1 \xi$ and the shearing force per unit volume is approximately τ_w / δ . If this parameter is of order one, then

$$\delta \approx \frac{\tau_w}{\rho U^2 / h_1 \xi} .$$

A check with experimental data would be the only way to verify this equation. A preliminary check of various two-dimensional data, Coles and Hirst (17), indicated the parameter $x \tau_w / \delta \rho U^2$ varied from approximately 1.0 to 0.1 and was a function of the pressure gradient. Only one of the similarity parameters appeared to indicate anything pertaining to a method for determining a velocity model and it was the one that probably

should be modified to be $\tau_{\max}/\rho U^2$ instead of $\tau_w/\rho U^2$.

Order of Magnitude Analysis

An approach often used in boundary layer analysis is used again, that of reducing the complexity of the governing equations by eliminating terms having lower orders of magnitude. This method is quite approximate and depends on the behavior of the terms as well as the original variables. Flow regions, such as those where viscosity is important and regions where it can be neglected, must also be considered in this type of analysis. Using Tables 1, 2 and 3 the Navier-Stokes equations are reduced to the governing equations for a three-dimensional boundary layer over a flat surface.

Terms in Table 1 are discussed first. Term number 5 is dependent on the relative magnitude of ℓ with respect to L if this term would remain in the final equation. It is noted that ℓ is still an undefined variable, except as a characteristic dimension in the crossflow direction. One method of determining an approximate value for the ratio would be to study the normalizing parameter for the crossflow velocity

$$W = \frac{U\ell}{L}$$

or

$$\frac{\ell}{L} = \frac{W}{U} .$$

Data from internal flow having skewed turbulent boundary layers indicated that the maximum value of the crossflow velocity ratio w/U was approximately 0.4. To be conservative it is assumed to be of order one. Terms number 8 and 12 have a coefficient which is twice the skin friction

coefficient. This coefficient is much less than order one. A short discussion has already been presented pertaining to term 9 and assuming the scale factors, k/U , are of order one then it is also assumed to be of order one. Since ℓ/L has been assumed to be of order one, then terms number 10 and 14 are orders of magnitude less than one. Because the present flow problem occurs at high values of the Reynolds number, then terms number 16 and 18 have coefficients of order of magnitude much less than one. As in two-dimensional flow, for three-dimensional flow the boundary layer thickness is considered much less than the characteristic length in the streamwise direction and the square of L/δ was assumed of the same order of magnitude as the Reynolds number. This makes the coefficient of term number 17 of order one. With the previous assumptions the remaining terms are numbers 1, 2, 3, 5, 6, 9, 15 and 17. The equations are written explicitly after Tables 2 and 3 are discussed.

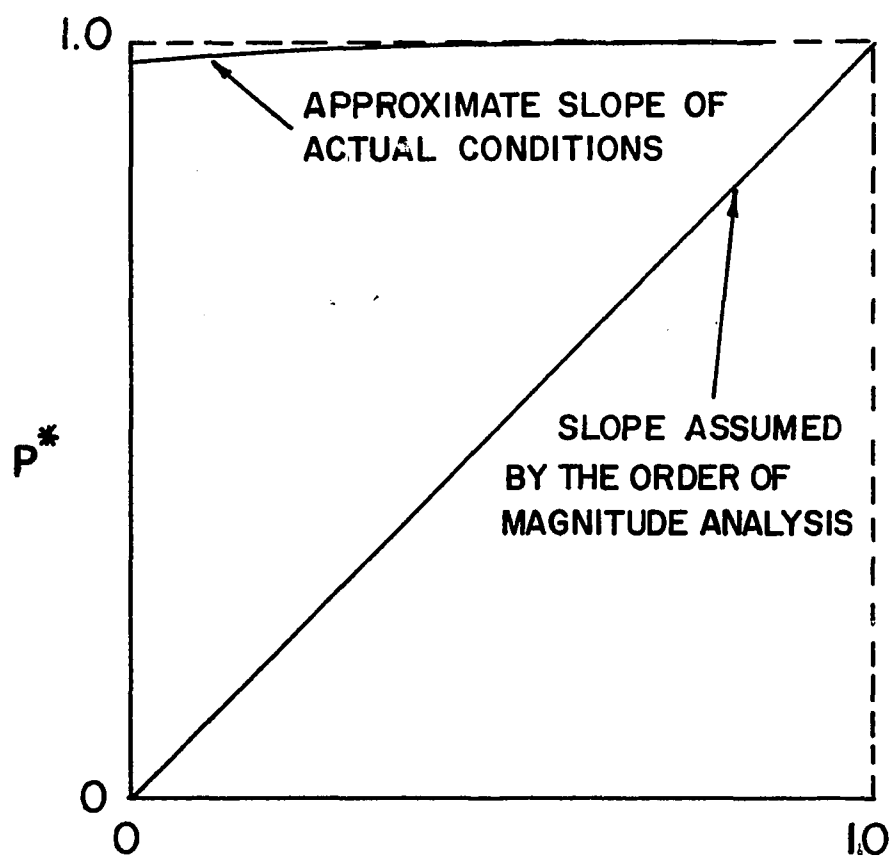
The equation of motion in the direction normal to the surface for two-dimensional flow has been determined experimentally to be

$$\frac{\partial v'^2}{\partial \eta} = - \frac{1}{\rho} \frac{\partial P}{\partial \eta} .$$

Using the same assumptions pertaining to the coefficients as were made for the ξ -direction equation it is seen that terms 1, 2, 3 and 17 have coefficients of order $1/R_{e_{h_1}\xi}$ ($R_{e_{h_1}\xi}$ = Reynolds number based on the scale factor times ξ). Terms 16 and 18 have coefficients of order $1/(R_{e_{h_1}\xi})^2$. Since it was assumed that $\frac{(k/U)L}{\delta} \frac{\tau_w}{\rho U^2}$ was of order one, then terms 8 and 10 have coefficients of order $1/R_{e_{h_1}\xi}$. The remaining two terms are the

counterparts of the two terms which comprise the equation of motion in the two-dimensional case. The difference in this case is that this particular fractional analysis shows that the coefficient of the turbulence term is of order of the magnitude of $1/(R_{e_{h_1}} \xi)^{1/4}$ and the pressure term of order one. An inspection of the method for determining the magnitude of the coefficient for the pressure gradient term indicates that it predicts an excessive magnitude. Figure 4 shows this graphically. Not only must the normalizing factor be of the correct magnitude but it must also be used carefully when determining slopes of terms. Kline (41) states that there should be a distinction between magnitudes depending on the direction of interest. Pressure is independent of direction at a point but the gradient of pressure depends on direction, therefore the magnitude of the normalized terms must be construed to indicate the correct gradient dependent on the desired direction. Terms 9 and 15 are retained as in the two-dimensional case.

In determining which terms should be retained in the ξ -direction equation using Table 3, a conservative approach was used and terms having a modified coefficient of $(\ell/L)^2$ were retained. This was a result of assuming ℓ was of order L and by doing so term 9 was retained based on the arguments used for the ξ -direction equation. Similarly, term 17 was retained. Of course the primary skewing potential, term 15, was retained. An interesting sidelight is that if ℓ is of the order of δ then by this particular analysis the only terms which would be retained are terms 4 and 15 which are the only terms of significance at the boundary layer edge, that is, the quasi-inviscid flow. In summary, terms 1, 2, 3, 4, 6,



$$\eta^* \\ P^* = \sigma \left(\frac{P}{\rho U^2} \right) \approx \sigma(1)$$

$$\eta^* = \sigma(\eta/\delta) \approx \sigma(1)$$

$$\text{but } \frac{\partial P^*}{\partial \eta^*} \neq \sigma(1)$$

Figure 4. Comparison of pressure gradient values

9, 15 and 17 were retained.

The resulting governing equations based on the fractional analysis method and two-dimensional experimental data for the case of steady, incompressible, constant viscosity fluid flowing over a flat surface at high Reynolds numbers are:

ξ -Boundary layer equation

$$\begin{aligned} \frac{\bar{u}}{h_1} \frac{\partial \bar{u}}{\partial \xi} + \frac{\bar{v} \partial \bar{u}}{\partial \eta} + \frac{\bar{w}}{h_3} \frac{\partial \bar{u}}{\partial \zeta} - \frac{\bar{w}^2}{h_1 h_3} \frac{\partial h_3}{\partial \xi} + \frac{\bar{u} \bar{w}}{h_1 h_3} \frac{\partial h_1}{\partial \zeta} + \frac{\partial \bar{u}' \bar{v}'}{\partial \eta} \\ = - \frac{1}{\rho h_1} \frac{\partial \bar{P}}{\partial \xi} + \frac{\mu}{\rho} \frac{\partial^2 \bar{u}}{\partial \eta^2} \end{aligned} \quad (8)$$

η -Boundary layer equation

$$\frac{\partial \bar{v}'^2}{\partial \eta} = - \frac{1}{\rho} \frac{\partial \bar{P}}{\partial \eta} \quad (9)$$

ζ -Boundary layer equation

$$\begin{aligned} \frac{\bar{u}}{h_1} \frac{\partial \bar{w}}{\partial \xi} + \frac{\bar{v} \partial \bar{w}}{\partial \eta} + \frac{\bar{w}}{h_3} \frac{\partial \bar{w}}{\partial \zeta} - \frac{\bar{u}^2}{h_1 h_3} \frac{\partial h_1}{\partial \xi} + \frac{\bar{u} \bar{w}}{h_1 h_3} \frac{\partial h_3}{\partial \xi} + \frac{\partial \bar{v}' \bar{w}'}{\partial \eta} \\ = - \frac{1}{\rho h_3} \frac{\partial \bar{P}}{\partial \xi} + \frac{\mu}{\rho} \frac{\partial^2 \bar{w}}{\partial \eta^2} \end{aligned} \quad (10)$$

Continuity with boundary layer approximations

$$\frac{\bar{u}}{h_1 h_3} \frac{\partial (h_3)}{\partial \xi} + \frac{\bar{w}}{h_1 h_3} \frac{\partial h_1}{\partial \xi} + \frac{1}{h_1} \frac{\partial \bar{u}}{\partial \xi} + \frac{\partial \bar{v}}{\partial \eta} + \frac{1}{h_3} \frac{\partial \bar{w}}{\partial \xi} = 0 \quad (11)$$

Equations 8 and 10 are nonlinear equations and are difficult to solve in general. If the geometry of the flow field is assumed to be known or calculated using potential flow theory as a first approximation then there are seven dependent variables. Because there are only four equations available, three more equations must be determined. Experimental data are required for at least some of the auxiliary equations. Turbulence data are required since empirical equations are the only hope at present for predicting the Reynolds stresses. In an attempt to circumvent the problem of directly predicting the Reynolds stresses, Equations 8 and 10 can be written in terms of the turbulent shearing stresses

$$\tau_{t_{\xi\eta}} = \mu \frac{\partial \bar{u}}{\partial \eta} - \rho \bar{u}' \bar{v}'$$

$$\tau_{t_{\eta\xi}} = \mu \frac{\partial \bar{w}}{\partial \eta} - \rho \bar{v}' \bar{w}' .$$

Empiricism is still required but two terms combine into one in each of Equations 8 and 10 and a first order partial differential equation results. At present, a general expression for the mean velocity profiles does not exist. Some have been proposed but only appear to approximate the few sets of data they are based on. It seems evident that experimental data taken under a variety of conditions is required so that a more basic understanding of the three-dimensional boundary layer can be obtained. This would eventually result in a more reliable method for predicting boundary layer behavior.

EXPERIMENTAL APPARATUS

The experimental apparatus consisted of a blower group, a varying duct group, and the test section group. The purpose of the blower group was that of supplying a continuous quantity of air at a prescribed pressure. Effectively, the varying duct group served as a flow modifier which confined the air so that a uniform flow entered the test section with low turbulence intensity. The test section group produced the three-dimensional flow which was investigated and contained the necessary support equipment to assist in the measurement of fluid flow properties. These three apparatus groups are depicted in Figure 5 along with the components of each group. Figure 5 also serves as a nomenclature list for the test apparatus. In Figure 6 the test section group is shown in detail. The various components of the test apparatus are discussed in the sequence which corresponded to the path that fluid would take as it passed through the system.

An enclosure around the blower had an opening which was approximately four feet by four feet and was covered with treated Fiberglas filter material to minimize instrument sensor contamination. The purpose of the blower enclosure was three-fold. One was for deadening some of the blower noise, another for an energy absorption device in case of blower blade failure and the final purpose was to have an air filtering system with an easily accessible filtering device. A P456150 Caterpillar axial-

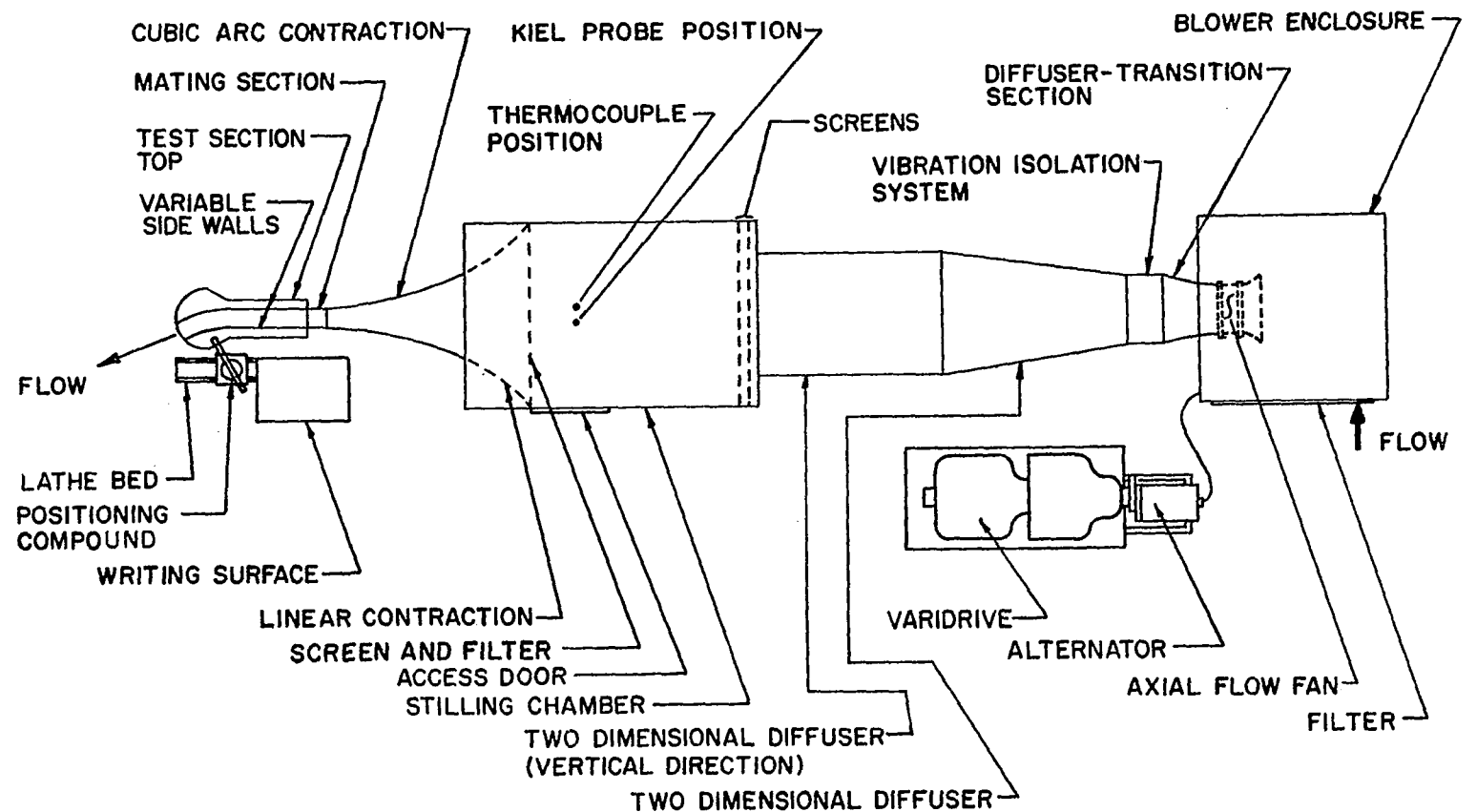
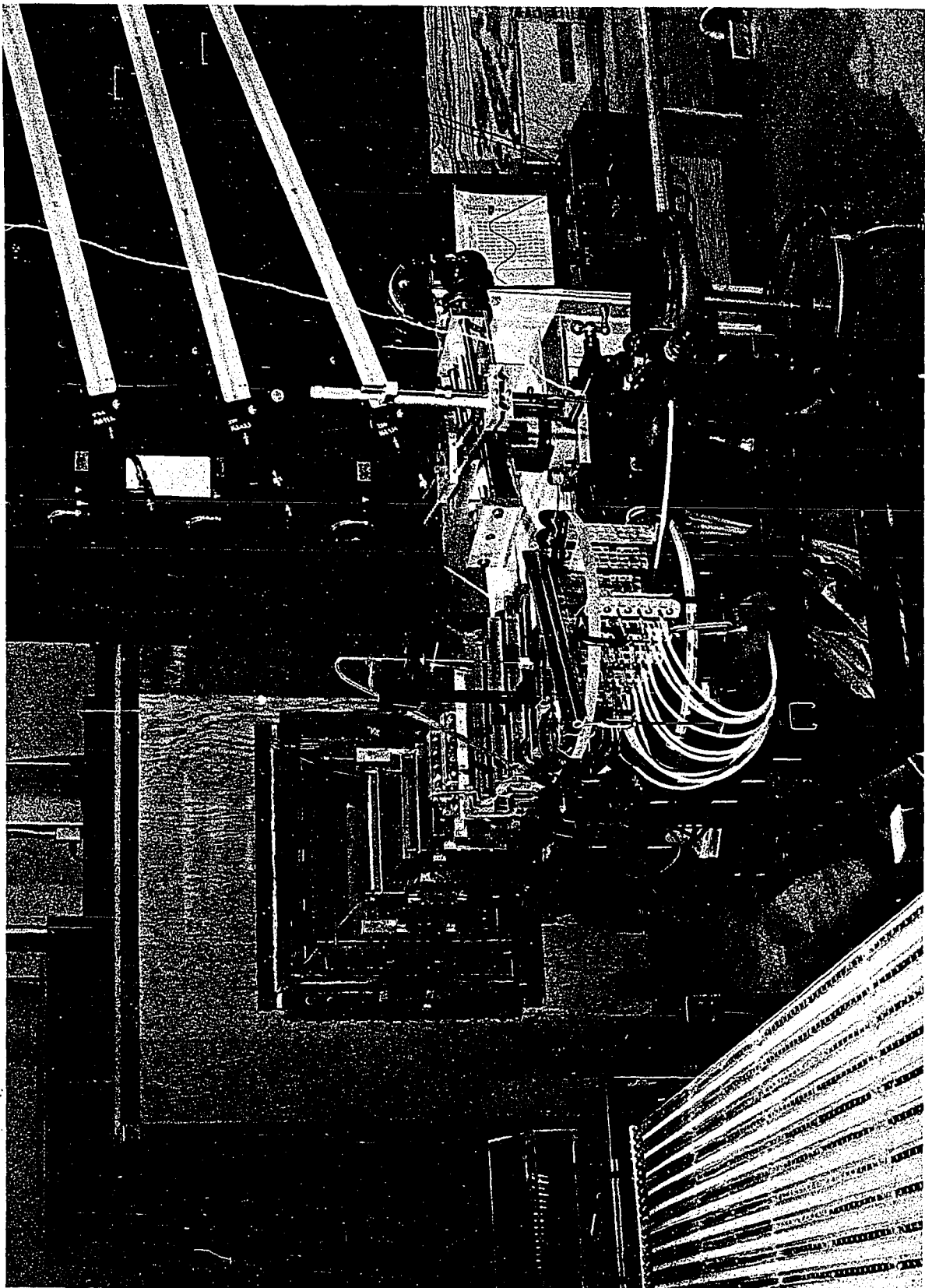


Figure 5. Diagram of test apparatus

Figure 6. Test section group



flow blower¹ capable of delivering approximately 5000 cubic feet of air at 7300 rpm with a pressure rise of approximately ten inches of water was used. The axial-flow blower housing was secured to the inside wall and floor of the enclosure by an angle iron frame. Air passed through the filtered opening into the blower housing cavity and entered the blower at a right angle with respect to the flow through the filter. The axial-flow fan generated noise which was primarily propagated along the blower axis, so the right angle turn was made in an attempt to attenuate the noise.

Immediately downstream from the blower was a combination diffuser-transition section which resulted in a square cross section. Blower vibrations were isolated from the remainder of the test system by means of a section constructed of double-thickness duck-cloth. Fluid then flowed through two two-dimensional diffusers in series. Each diffuser was constructed of three-quarter inch plywood having an area ratio of 1.72 and having an axial length to inlet width ratio of 2.74. According to Kline et al. (43) this configuration would be out of the appreciable stall regime. The diffusers were required because of the relatively short plenum chamber.

Within the three-quarter inch plywood plenum chamber, which measures approximately four feet by four feet by six feet, was a series of screens

¹The blower motor was supplied electricity from a Caterpillar P352840 alternator which produced 400 cycles, 440 volts at 6000 rpm. The alternator was mechanically coupled to a United States Electrical Motors Incorporated varidrive which had an rpm range of 2400 to 12,000. The axial-flow blower and alternator were gifts of the Caterpillar Tractor Company through the efforts of Mr. N. K. Lammers.

and a linear contraction section. An access door was situated in the plenum chamber such that the number or type of screens could easily be changed. Instrumentation within the stilling chamber consisted of a Kiel probe and a copper-constantan thermocouple. A maximum velocity of approximately three feet per second was expected at the maximum cross section.

Linear contraction existed inside the plenum chamber down to a square area having 22-inch sides. Connected to the plenum chamber was a Plexiglas contraction section with a cubic arc curvature based on a design criteria by Rouse and Hassan (63). The junction between the linear contraction section and the cubic arc was a line of tangency. The Plexiglas contraction section had a contraction ratio of 19.36. A computer program was developed to calculate the coordinates for the curvatures of each template and side wall. Data on IBM punched cards was obtained first, then the data was converted to a punched tape which was used to control a numerically controlled milling machine with 0.001 inch minimum step size. The author is grateful to Fisher-Governor Company, Marshalltown, Iowa, and to Mrs. Linda Berg for operating the machines which transferred the data from cards to tape.

Connected to the contraction section was a mating section with an inside area of 25 square inches (five inch sides) for smooth matching characteristics between the contraction section and the test section.

A variable test section was conceived and designed which allowed wall curvature, area ratio and aspect ratio variation. A preliminary model of the test section was built and tested to insure the feasibility of the design and in addition determine the required measurement technique

and type of instrumentation. Some of the design objectives were the following:

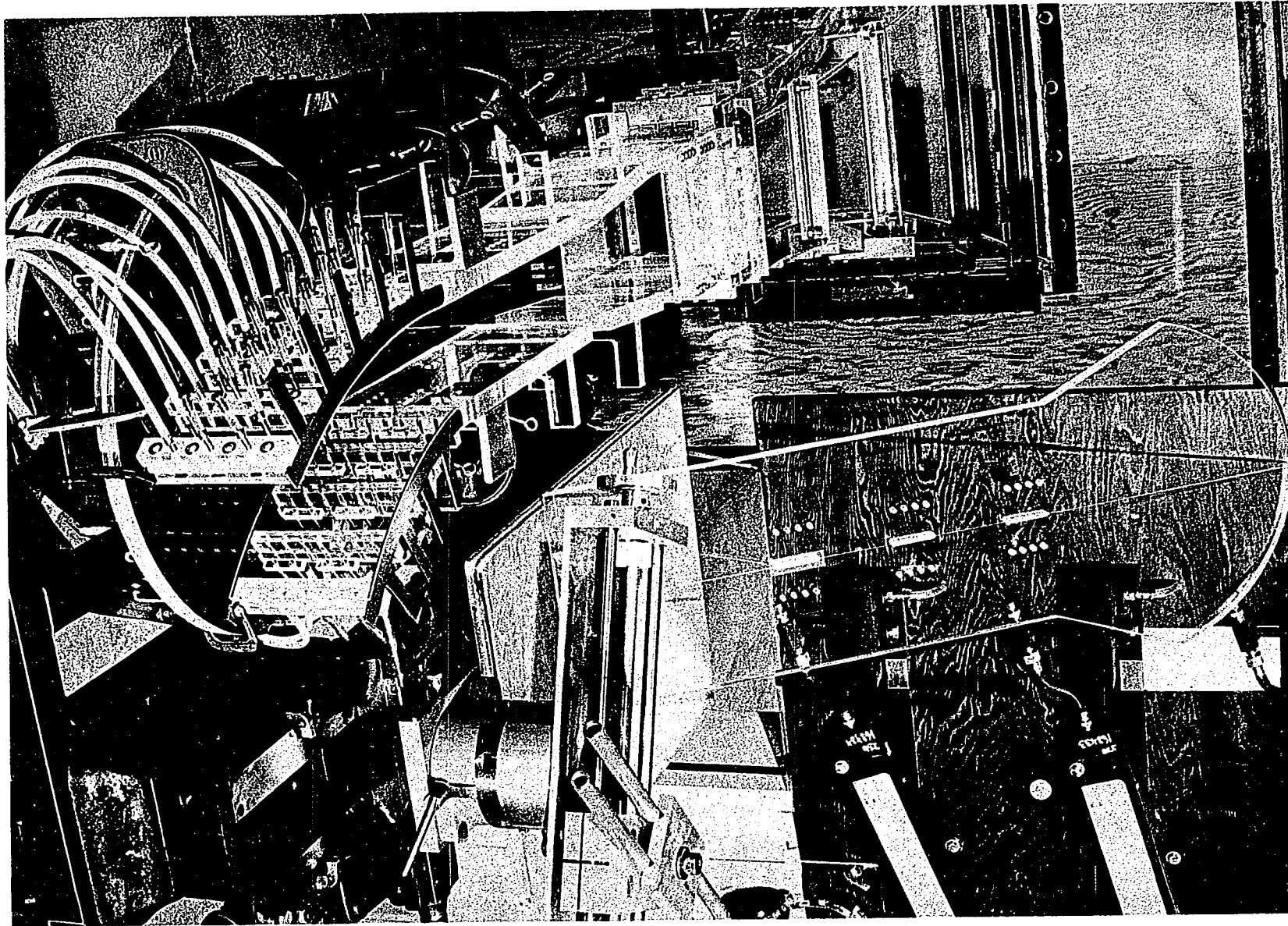
- (1) Utilize one basic set of parts and adjust them to produce multiple test section configurations with accuracy and relative ease
- (2) Have self-sealing movable parts, also easily replaceable moving parts
- (3) Be compatible with an instrumentation surveying technique which would allow infinite positioning resolution within the test section
- (4) Be economical to build.

The resulting test section is shown in Figure 7. As can be seen, the primary material was Plexiglas. Plexiglas was used because of its transparent characteristics and its elastic characteristics when in thin sheets.

The floor of the test section, which will at times be referred to as an end wall, was ten inches wide which allows a minimum practical aspect ratio (height to width ratio) of approximately 0.80. On the discharge end, the curvature was selected so that the nominal distance from the side wall ends to the floor edge would be approximately the same for the particular wall curvatures and aspect ratios used in this investigation. A reflective surface is advantageous when positioning a probe near it and this feature was incorporated into the floor by painting the back side of the Plexiglas.

The test section top had the same basic dimensions as the floor. It had additional features such as a series of discrete instrumentation insertion points along the centerline, and a centerline was scribed into

Figure 7. Experimental test section with top removed



the external surface for reference purposes as discussed in Experimental Procedure. By removal of a few bolts the top could be disassembled from the remainder of the test section.

Both side walls were basically the same except the pressure side wall was longer. They consisted mainly of a thin Plexiglas sheet with thick reinforcing plates at positions where flexibility was not desired. As in the top, the side walls also had discrete instrumentation insertion points. The distance from the end of the most downstream reinforcing plate to the end of the suction side wall was 9.00 inches and the corresponding length of the pressure side wall was 11.25 inches. Each side wall was 5.00 inches high. For an aspect ratio of 1.5, a turning angle of 40 degrees could be effected based on an estimate using the stall criteria of Fox and Kline (23). Both side walls were designed to accept an extension if it was necessary to lengthen them. A series of vertical side wall stiffeners were attached to the flexible section of the side walls and are shorter than the side walls by twice the template thickness which furnished a recess for them to be placed. A set of template retainers were used to draw the templates flush against the side walls to form the desired curvature.

Another part of the test section group was the stand on which the test section and positioning compound rested. This Unistrut structure had sufficient adjustments so the positioning compound and the test section floor could be placed in parallel planes. A dial indicator was mounted on a probe and the lathe carriage was positioned in order to measure the variation in the entire end wall area. Ten adjustment points

on the test section floor were used to effect a parallel plane. After this was completed, another set of adjustments was made to position the test section floor into the same plane as the mating section floor to effect a smooth transition.

The next section has a description of the required adjustments and utilization of the three test apparatus groups.

EXPERIMENTAL PROCEDURES

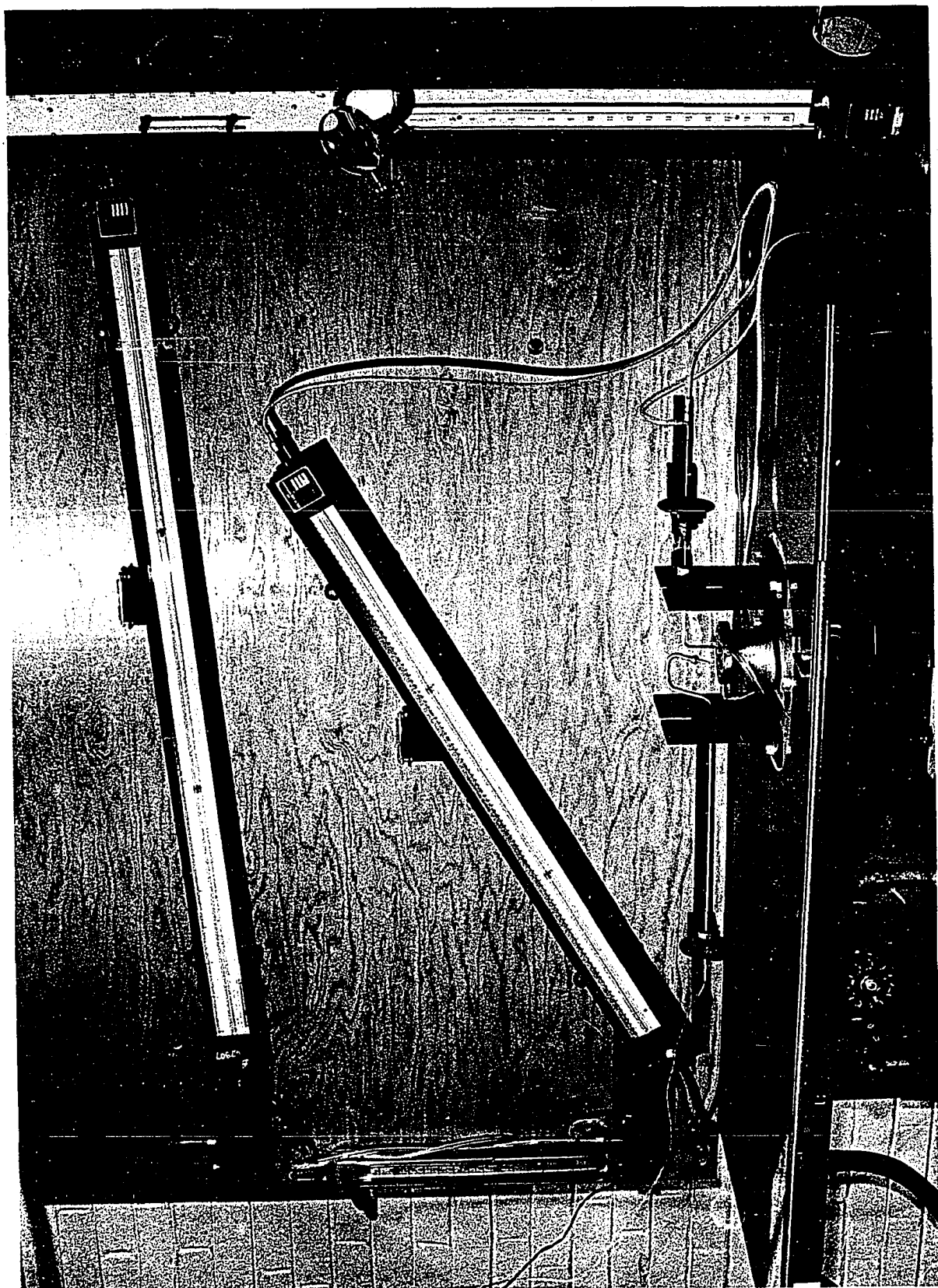
This section is divided into three basic parts: Instrumentation Calibration, Preliminary Procedures, and Data Acquisition. Encompassed by the Instrumentation Calibration subsection are the procedures, equations and assumptions required to calibrate the instruments used in this experimental investigation. In the Preliminary Procedures subsection a summary of the various adjustments which were required prior to acquiring data is presented. A few of these are the test section configuration adjustments, determination of instrumentation positions and equipment adjustments. Finally, the Data Acquisition subsection is comprised of information pertaining to the various instruments, their application and an outline of the data procurement procedure.

Instrumentation Calibration

The standard used for velocity calibration in this work is taken as the Pitot-static probe. A Meriam micromanometer is the standard used for pressure measuring devices and a mercury in-glass thermometer the standard for temperature measurements. The Iowa State University Engineering Research Institute Electronic Shop performed calibrations on the electronic components used in this experimental investigation.

Hot-wire anemometer sensor calibration entails both a velocity and an angle calibration procedure. A calibration tunnel, Figure 8, was designed and built under the direction of Dr. G. H. Junkhan which used regulated compressed air for the flow medium. The tunnel throat has a

Figure 8. Calibration tunnel



diameter of 1.00 inches and the nozzle has a contraction ratio of 144 to 1. A probe holder was designed to allow the hot-wire sensors to be rotated about a given point in the flow field so that they would always sense the same velocity vector. Figure 9 shows the apparatus used to adjust the probe so the probe rotated in the same flow field and to determine the reference angle for calibration.

Assuming that each hot-wire sensor had a linear resistance-temperature relationship so that the following equation was valid

$$\frac{R_{sh}}{R_{sc}} = 1.0 + \alpha (T_{sh} - T_s)$$

where

R_{sh} = resistance of the heated sensor, ohms

R_{sc} = resistance of the cold sensor, that is, the resistance of the sensor at the ambient flow temperature, ohms

α = thermal resistivity, $^{\circ}\text{F}^{-1}$

T_{sh} = temperature of the heated sensor, $^{\circ}\text{F}$

T_s = stream temperature, $^{\circ}\text{F}$

and in addition assuming that density and viscosity variations could be neglected, a relationship of the form

$$i_s^2 R_s = F(V, \Delta T)$$

or

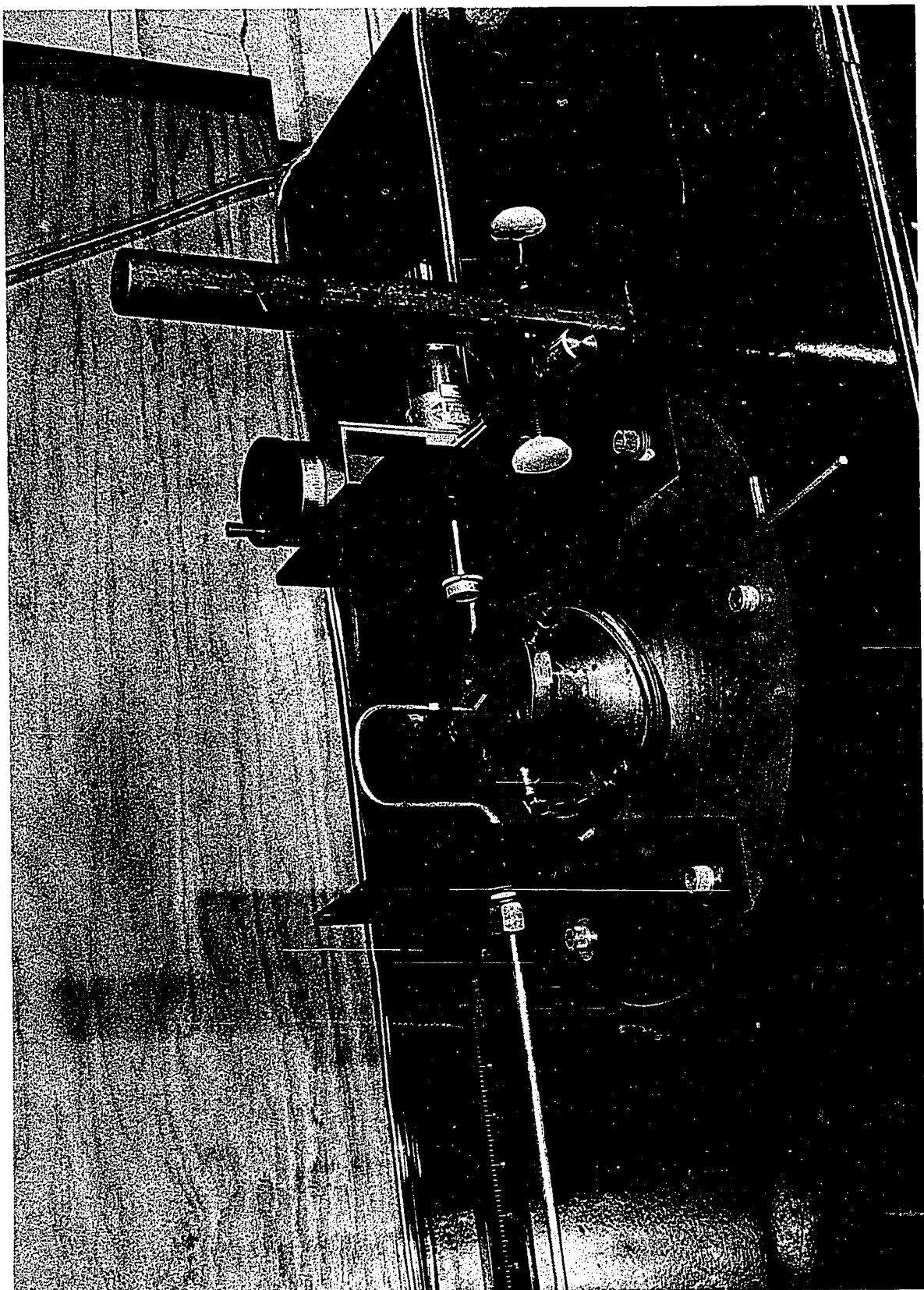
$$i_s^2 R_s = f(V) g(\Delta T)$$

where

i_s = sensor current, amperes

R_s = sensor resistance, ohms

Figure 9. Sensor positioning apparatus



V = fluid velocity

ΔT = temperature difference between the sensor and fluid

could be used. This relationship also implies that heat conduction effects to the sensor needle supports are negligible and to obtain the final form the radiation heat transfer is also neglected. In effect, the final working equation states that the electrical energy dissipated is equal to the energy associated with the convective heat transfer.

One form of the final equation is known as Kings equation which is

$$i_s^2 R_s = (K_2 + K_3 \sqrt{V}) \Delta T$$

where

K_2 = a constant dependent on free convection heat transfer properties

K_3 = a constant dependent on forced convection heat transfer properties.

If ΔT is replaced by $\frac{1}{\alpha} \left(\frac{R_{sh}}{R_{sc}} - 1 \right)$ and then allowing K_2 and K_3 to absorb $\frac{1}{\alpha}$ the equation becomes

$$i_s^2 R_s = (K_2 + K_3 \sqrt{V}) \left(\frac{R_{sh}}{R_{sc}} - 1 \right).$$

$\frac{R_{sh}}{R_{sc}}$ is known as the overheat ratio and will be redefined as R_{oh} .

Rearranging the above equation yields

$$\frac{i_s^2 R_s}{(R_{oh} - 1)} = K_2 + K_3 V^{\frac{1}{2}}.$$

Sandborn (65) shows that calibration data appears to be best fit by the relation

$$\frac{i_s^2 R_s}{(R_{oh} - 1)} = K_2 + K_3 V^N$$

the value of N is dependent on the velocity range and varied from 0.2 to 0.5 for the particular calibration curve Sandborn exhibited. For a constant temperature hot-wire anemometer it is more convenient to express i_s^2 in terms of bridge voltage and resistance of the elements involved in measuring the bridge voltage. If E_b represents bridge voltage and R_t the total resistance of the elements

$$i_s^2 = \frac{E_b^2}{R_t^2}$$

R_t = sensor resistance + probe resistance + probe holder resistance + probe cable resistance + bridge leg resistance.

Incorporating these expressions into the energy balance relation yields

$$\frac{\frac{E_b^2 R_s}{R_t^2 (R_{oh} - 1.0)}}{ } = K_2 + K_3 V^N .$$

This form of the equation requires a knowledge of the constant K_2 to determine the values for K_3 and "N" graphically. As can be seen from the equation, K_2 is the value of the power dissipation when there is no mean flow or it is primarily the free convection heat transfer. The value of K_2 also indicates the non-linearity of the curve on log-log paper if $\frac{E_b^2 R_s}{R_t^2 (R_{oh} - 1.0)}$ is plotted against V . A short computer program was developed to determine the best values for K_2 , K_3 , and N from the calibration values of velocity and the modified power. Another equation also used to fit the data is

$$\frac{\frac{E_b^2 R_s}{R_t^2 (R_{oh} - 1.0)}}{ } = C_1 + C_2 V + C_3 V^2$$

where C_1 , C_2 , and C_3 are coefficients calculated using a second order least squares set of equations. Both equations gave results which were within 0.4 percent of the data for the majority of calibration points and never departed from the calibration by more than one percent. Table 4 shows a typical calibration set and a comparison of the values predicted by the two equations. Because of the straight forward manner of determining the coefficients C_1 , C_2 , and C_3 compared to the iteration required to determine K_2 , K_3 and n , it was decided to use the last equation to represent the calibration data in the calculations. More will be said about this aspect in Data Reduction.

Table 4. Calibration data comparison

Calibration velocity	Calibration	Second order least squares fit	Least squares fit using Kings law
Values for MP_{90} = $\frac{E_b^2 R_s}{R_t^2 (R_{oh} - 1.0)}$			
48.6	0.0444	0.0445	0.0444
68.8	0.0490	0.0489	0.0491
84.8	0.0521	0.0521	0.0521
97.3	0.0544	0.0543	0.0542
109.0	0.0561	0.0562	0.0561
119.4	0.0577	0.0578	0.0575
128.9	0.0586	0.0591	0.0588
137.6	0.0600	0.0602	0.0600
146.9	0.0612	0.0612	0.0611
154.8	0.0619	0.0620	0.0620

A Pitot-static tube was placed in the same velocity field as the hot-wire sensor and through the use of the following equation, velocity was calculated:

$$V = \sqrt{2g_c \frac{\gamma}{\rho} \Delta h}$$

where

g_c = gravitational constant, $32.174 \text{ lb}_m \cdot \text{ft}/(\text{lb}_f \text{ sec}^2)$

γ = specific weight of manometer fluid, lb_m/ft^3

ρ = density of flow medium, lb_m/ft^3

Δh = differential height of the manometer fluid produced by the Pitot-static tube connection, inches of water.

No correction factors were applied to this relation as the flow was less than 0.2 Mach number which allowed the incompressibility assumption and there was insufficient information available to correct for any other effect. Probable errors are assumed insignificant, especially since velocity ratios are of primary concern.

Each sensor was oriented 90 degrees to the flow field and a value for $E_b^2 R_s / (R_t^2 [R_{oh} - 1.0])$ was required for every value of velocity in the predetermined calibration set. In addition, a value for $E_b^2 R_s / (R_t^2 [R_{oh} - 1.0])$ is required for each wire at angles of 15, 30, 45, 60 and 75 degrees corresponding to the highest and lowest velocity value for the 90 degree calibration set and selected intermediate velocity values.

All the inclined Meriam manometers were calibrated by supplying a common pressure to the inclined manometer to be calibrated and to a Meriam micromanometer which was considered the standard. After the inclined manometer was positioned to read the same pressure as the micromanometer

then the applied pressure was released and a check was made to determine if the inclined manometer re-zeroed. If it re-zeroed the calibration was complete. If not, the angle was changed, a new zero was set and the pressure was again applied to see if the two manometer readings matched. The above processes were repeated until the inclined manometer matched the micromanometer reading at both ends of the scale. A leveling bubble mounted on each inclined manometer was adjusted so it would indicate the calibration status.

A bank of manometers initially designed for vertical use was improvised to operate as an inclined bank of manometers. Because of irregularities in the mounting surface and the scale, each of the 24 tubes had to be individually calibrated. Calibration was effected by having a common pressure applied to both an inclined tube and an inclined Meriam manometer and noting the reading on both. This was accomplished for six readings over an eight-inch pressure range with four readings being less than atmospheric pressure. A computer program was developed to interpolate between the calibration points and yield the "true" value of pressure corresponding to a given tube reading.

After the initial calibrations were made, checks were performed on the instruments to insure correct readings. If any drift from the calibration value was detected the required calibration procedure was repeated.

Preliminary Procedures

After a given test-section configuration was selected and a set of templates made for positioning, the test section was adjusted. Other positioning requirements pertaining to test apparatus components were also conducted. The geometrical properties which were variables for this work are shown in Table 5 with the corresponding devices used to accomplish the adjustments.

As mentioned in Experimental Apparatus, the test section side walls were adjustable in the lateral direction with relatively few constraints. A part of the preparation procedure entails positioning them in a prescribed configuration. Two steel templates were milled for each flexible side wall so that two desired curvatures resulted and "fingers" protruded away from the flow area for clamping purposes. The suction wall template had a radius of 13.75 inches and the pressure wall template had a radius of 16.35 inches. These templates were then placed in a recess designed for them and secured. The side walls were still movable but constrained to move with a given curvature. With the test section top removed, see Figure 7, a template with parallel sides was placed between the two straight sections of the side walls which form the throat of the diffusing passage. This template governed the aspect ratio since the height was constant. Through a trial and error process the template was clamped between the straight side walls such that these straight sections were equidistant from the centerline of the contraction section over the entire length of the side wall straight section. This was checked with dial

Table 5. Geometrical properties and instrumentation

Diffuser geometrical properties	Throat aspect ratio (height/width)	Pressure wall radius	Centerline radius	Suction wall radius	Area ratio (measured parallel to the centerline radius)	Data profile position	Data reference position
Helios dial calipers 7" and 11"	X		X		X	X	
South bend rotary indexing table 4" dia.				X		X	
Micrometer head vertical positioner			X			X	
I.S.U. traversing mechanism				X		X	
Lathe carriage						X	
Lathe Crossfeed						X	
United sensor manual traverse units							X
Sidewall curvature templates		X		X			
Sidewall positioning template						X	
Parallel Walls template	X						

^aDiffuser centerline radius is the one tangent to the throat axial centerline.

calipers from the test section floor edge to the straight wall section. Both walls were then clamped securely to the test section floor. Another template which had the form of a prescribed area distribution for the pressure and suction side walls was placed between the two walls. APPENDIX E shows the side wall coordinate system. This template was positioned so that a reference line on the template coincided with the inside of the suction side wall straight section. The diffusing section was then clamped securely to the test section floor. After both templates were removed from between the side walls, the test section top was put in place and secured. An axial centerline scribed in the test section top served as a reference for positioning the sensor.

In order to position the lathe carriage and the lathe crossfeed to coincide with the center of curvature of the centerline radius a series of steps were taken. First the traversing mechanism was required to be adjusted to traverse on a line perpendicular to the passage centerline at the diffuser throat. This was accomplished by placing a machined parallel bar directly over the throat of the diffuser. (The throat is defined as the downstream end of the straight parallel section which can be identified by the termination of the three-quarter inch side wall stiffeners.) By attaching a dial indicator to the traversing mechanism such that it touched the parallel bar when traversed, the rotary indexing table was adjusted until no appreciable change resulted in the dial indicator reading. With that step accomplished, the lathe carriage was required to be placed such that the traversing mechanism axial centerline coincided with the diffuser throat (parallel bar edge). This aligned the

rotary indexing table center with the diffuser throat. Knowing a particular centerline radius for the diffusing passage which was consistent with the side wall coordinate system, the lathe crossfeed was grossly adjusted with a rule. After the gross adjustment was made a plumb-bob arrangement on the traversing mechanism was used to locate the distance from the rotary indexing table center to the throat centerline. This process required the following steps. First the plumb-bob point was placed on the intersection of the throat centerline and parallel bar at the throat. The rotary indexing table was rotated so the plumb-bob was located on a flat surface secured to one end of the lathe bed. (This flat surface was used as a writing surface during data procurement, see Figure 5.) A piece of carbon paper was placed under the plumb-bob point and it marked an initial position. From this point the rotary indexing table was turned 30 degrees and another mark was made. An 11-inch dial caliper was used to measure the chord length which resulted in sufficient data to calculate the radius. If the radius was not the required one, the lathe crossfeed was adjusted to correct it.

The probe with the sensor inserted was mounted in the vertical positioner and through the use of the extension rods the sensor was placed at one of the reference points on the flat surface. In addition to positioning the sensor at a known radius, it must also be in a plane parallel to the test section floor (diffuser end wall). After that adjustment was accomplished and a check made to verify the radius described by the sensor was not altered, a zero reference reading was determined. The sensor was positioned close to the wall by "eye-ball"ing"

the distance between the sensor and its image, then the distance between the wire and the wire image was measured with a Gaertner slide micrometer, Figure 10. Since the microscope had only a two-inch focal length, the reference location could only be found near the diffuser exit. A reading was noted from the vertical positioner micrometer head and used as a reference over the entire survey area. To attempt to correct for floor and positioner variations, a dial indicator was connected to the traversing compound and variations from the initial reference point were determined.

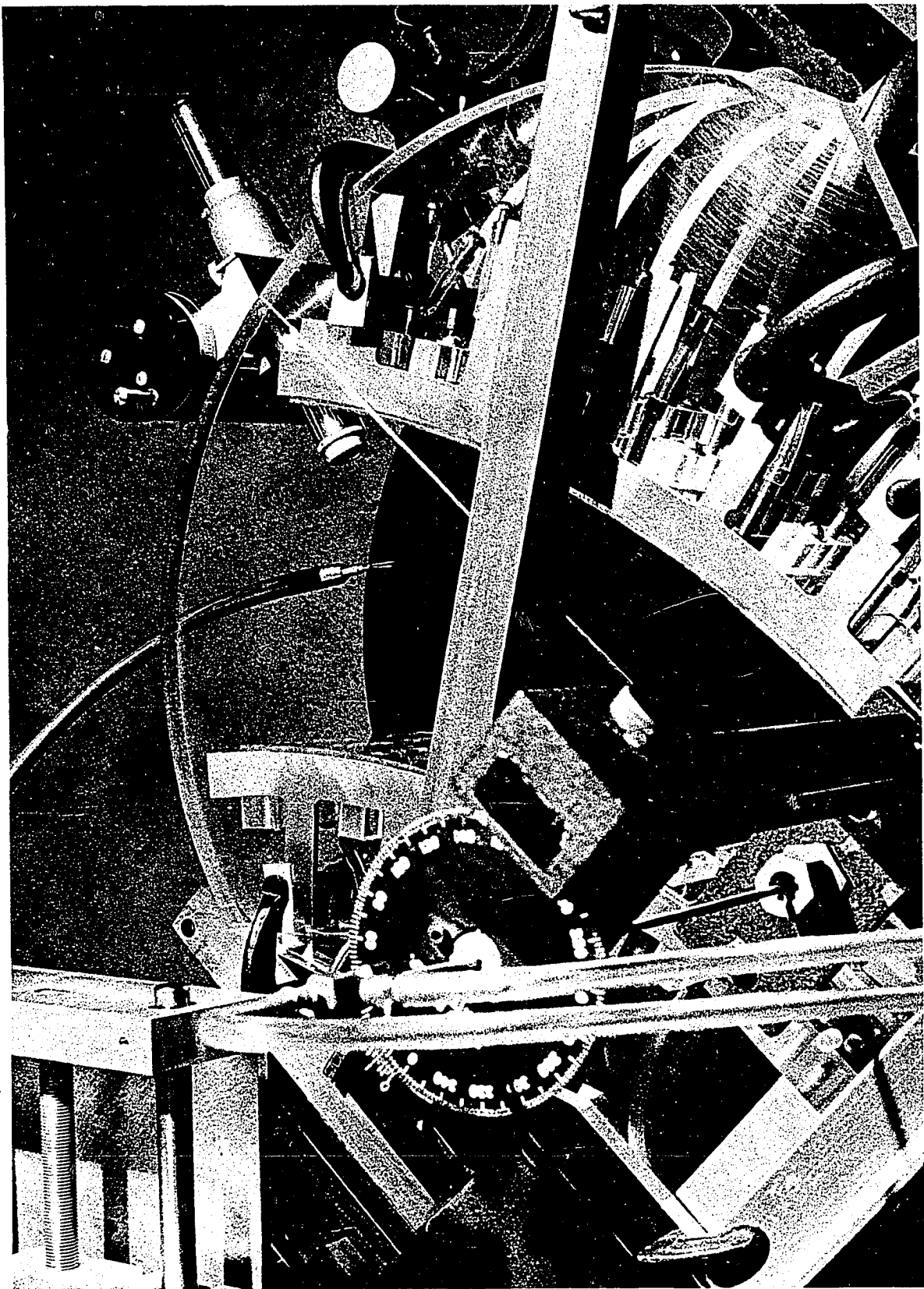
A Pitot-static tube was used to obtain the reference velocity. It was positioned with a United Sensor probe positioner and the "zero" position was attained by noting when the probe and probe sensor appeared to touch the end wall surface. The axial alignment was accomplished by rotating the probe until it became parallel with the scribed axial centerline on the test section top.

Other preparatory requirements included preventive maintenance on the varidrive and alternator. With the completion of initial positioning and equipment checks, data procurement procedures commenced.

Data Acquisition

Even after all mechanical checks and adjustments were made, more pre-data acquisition tasks were required. It was noticed that both instrumentation and fluid system "warm up" time required approximately two and a half hours to reach equilibrium. During this time alternator rpm adjustments were made and monitored with a General Radio Company

Figure 10. Initial probe positioning



strobotac, air bypass adjustments were made and a visual check of the test fixture and instrumentation operation was conducted.

Once the plenum chamber temperature and the instrumentation cabinet temperature ceased to change appreciably, the system was considered in steady state and final preparations for measurements were made. Table 6 shows all the fluid properties which were measured during each run and the corresponding instrumentation required to procure the data. In the following paragraphs the procedure for operating the instruments is briefly outlined and it is implied that the table had been consulted for the complete instrumentation nomenclature.

Final checks were made on the probe position reference values, instrumentation readout reference positions and the zero readings on the inclined manometers. A value for the combined resistance of each sensor, probe, probe support and cable were known from prior measurements so a value for the cold resistance of the sensor was calculated from the following equation:

$$\text{Cold sensor resistance} = \text{resistance bank reading} - (\text{resistance of probe + probe support + cable}).$$

The resulting value of cold resistance was multiplied by a predetermined overheat ratio and that product added to the combined resistance of the probe, probe support and cable. Having obtained the additive resistance for each wire, each value was dialed into the resistance bank of its respective hot-wire channel. Each bridge balance was adjusted to the voltage value corresponding to its calibration standby voltage.

Table 6. Fluid properties and instrumentation

Fluid Properties	Velocity					Pressure					Temperature												
		a)	mean value	b)	mean direction	c)	fluctuating	components	d)	reference	value	a)	reference	static	b)	plenum chamber	c)	wall static	d)	barometric	e)	ambient	
2 Thermo-Systems 1010A constant temperature not-wire anemometers			X	X	X											a)	plenum chamber	b)	local ambient	c)	barometer	d)	ambient
2 Disa type 55D 30 digital voltmeters				X	X																		
1 Thermo-Systems 1015B correlator					X																		
1 Brüel and Kjaer type 2417 random noise meter					X																		
1 Brüel and Kjaer type 2107 frequency analyzer					X																		
1 Tektronix type 502A dual beam oscilloscope					X																		
1 Leeds and Northrup No. 8686 potentiometer with Cu-C thermocouple																X							
2 Mercury in glass ther- mometers																	X	X					
1 Mercury barometer																		X					
3 Meriam inclined manometers 2-12" H ₂ O 1-20" H ₂ O									X		X		X										
1 Inclined manometer bank 24 tubes																		X					

Both hot-wire channels were adjusted to the run position. A dual beam oscilloscope displayed the behavior of the sensor signals and was primarily used for detecting any anomalies in the signals.

A series of repetitive steps were taken to obtain the hot-wire data. To begin with, the micrometer was read which indicated the sensor position in a plane perpendicular to the end wall, then the rotary indexing table scale was read to determine the sensors angular displacement with respect to the diffuser throat. To complete the sensor location readings, a dial caliper was used to determine the radial position. With the digital volt meters variable dampener set in the position for the least fluctuations but with the best response, a reading was taken from each meter which was the value of bridge voltage for each sensor. The two bridge voltage readings were taken two more times at the same sensor position.

If turbulence measurements were taken the correlator was adjusted so one random noise meter read the fluctuating voltage from one wire and the other random noise meter read it from the opposite wire. One random noise meter was a component of the frequency analyzer listed in Table 6. Next the correlator was adjusted so one random noise meter read the sum of the fluctuating signals from the two wires and the other random noise meter read the difference of the fluctuating signals of the two wires. This same procedure was repeated twice more for the same sensor location.

In order to obtain a boundary layer profile the probe was moved vertically from the wall and a series of data points were taken. For

the particular tests which were run, the wall radius of curvatures and profile positions are shown in Figure 11. The profile positions are from a top view. The particular aspect ratio of the diffuser was decided on because another investigation (24) used the same value, eliminating one variable when comparing data. APPENDIX E contains some pertinent information about the particular side wall configuration.

In addition to obtaining the coordinate values and the electrical values previously mentioned, other readings were taken periodically during a run. The following values were obtained at least three times for a given value of angular positioning of the probe. A Pitot-static probe which was connected to an inclined manometer yielded a fluid column height which was used to determine the reference velocity. A "T" was placed in the static tap line of the Pitot-static probe and connected to an inclined manometer to indicate the reference static pressure. A glass thermometer located on the inclined manometer board was used to determine the ambient temperature. Plenum temperature was obtained from the voltage output of a copper-constantan thermocouple which was read from a millivolt potentiometer. The potentiometer readings were referenced to the ambient temperature so that each time it changed the reference voltage in the potentiometer was changed. A Kiel-probe was inserted into the plenum chamber and connected to an inclined manometer which then indicated the total pressure. A barometer and the barometer ambient temperature readings were obtained to determine the atmospheric pressure. Twenty-three wall pressure taps were connected to the inclined manometer bank. The twenty-fourth manometer tube in the bank was vented to atmosphere to

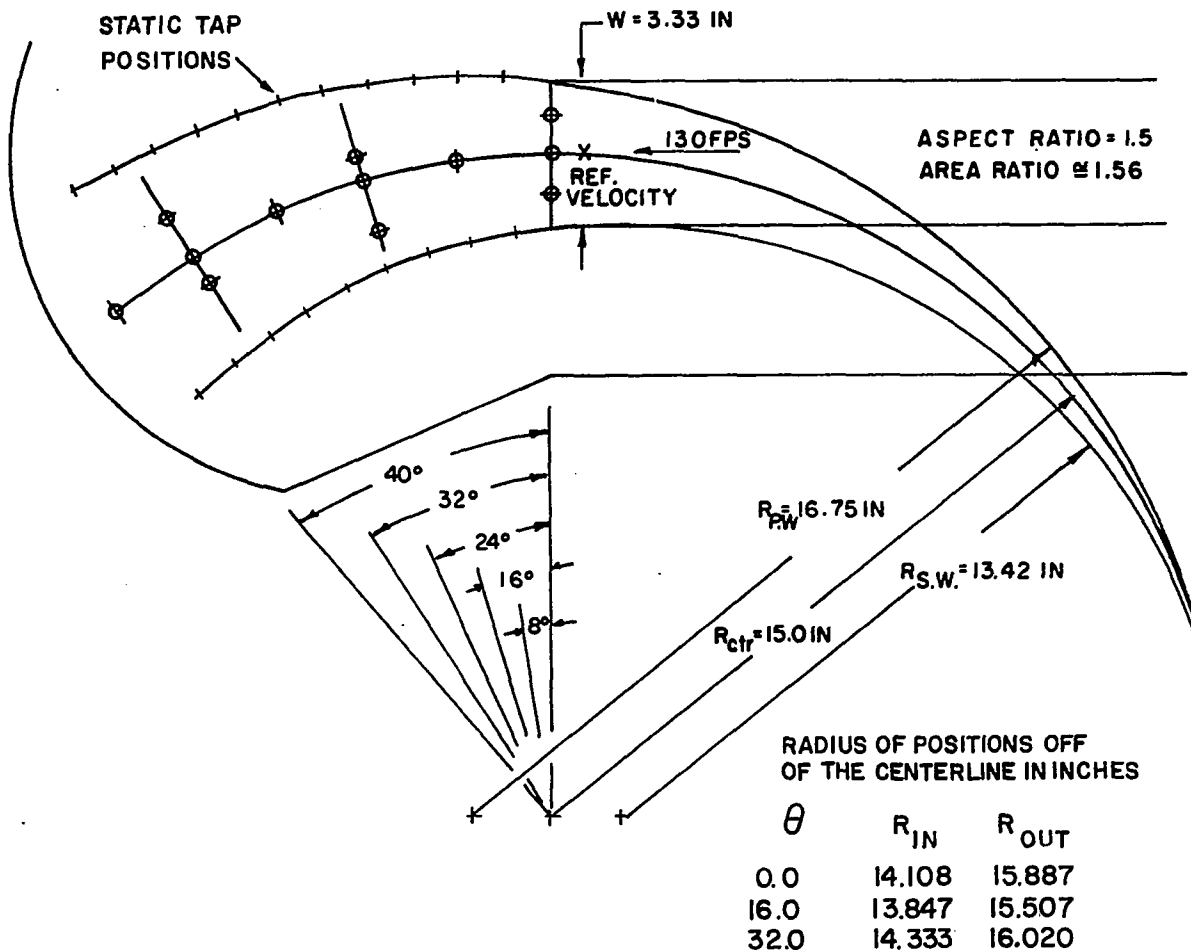


Figure 11. Location of survey positions

indicate the manometer reservoir fluid level. The inclined manometer bank readings completed the list of data procured during each test run.

Each time a test run was conducted all the previously mentioned measured data were recorded on coding forms for later transfer to punched cards. This enabled the data to be reduced by a computer program which is discussed in the next section.

EXPERIMENTAL DATA REDUCTION

This section of the dissertation is concerned with three topics in subsections entitled: Calculation of Basic Flow Variables, Parameter Calculations and Data Uncertainty.

Calculation of Basic Flow Variables

A computer program was developed to transform the experimental data obtained from the read-out devices listed in Table 6 of the Data Acquisition subsection. The equations involved, some pertinent assumptions, and the method of approach are presented at this point.

The data reduction program consists of four basic parts:

- (1) Hot-wire calibration data
- (2) Hot-wire velocity profile data
- (3) Wall static pressure data
- (4) Total pressure survey data.

They are discussed in that order.

Hot-wire calibration data

Hot-wire calibration data reduction involved determining relationships among a modified electrical power parameter, a velocity vector angle with respect to the wires and the magnitude of the mean velocity. Three values for each variable at each data point were obtained and averaged. This method reduces errors in two ways. Transposition of numbers is more readily detected, and more reliable values for varying data are obtained.

Experimentally determined hot-wire calibration values were the following:

- (1) Barometric pressure (in. Hg.)
- (2) Barometer ambient temperature ($^{\circ}$ F)
- (3) Room temperature ($^{\circ}$ F)
- (4) Calibration stream static temperature ($^{\circ}$ F)
- (5) Calibration stream static pressure (in. of H_2O)
- (6) Hot-wire sensor cold resistance (ohms)
- (7) Cable resistance (ohms)
- (8) Overheat ratio (dimensionless)
- (9) Anemometer bridge voltage (volts)
- (10) Calibration angle (degrees)
- (11) Pitot-static probe differential pressure (in. of H_2O).

Each calibration point was measured three times and the respective values were averaged. After the average values were obtained the following parameters were evaluated:

$$\frac{E_b^2 R_s}{R_t^2 (R_{oh} - 1)}, A, B, C, V, \text{ and } n.$$

(The notation used here is the same as that in the Instrumentation Calibration subsection.)

A correction to the barometer reading was obtained by a two-dimensional curve fit using Lagrange polynomials to fit the tabulated correction data for temperature. The correction factor is a function of both temperature and manometer column height. With this value and a constant

correction value for gravity the atmospheric pressure was calculated from the equation

$$P_{atm} = (\text{barometric reading} - \text{temperature correction} - \text{gravity correction}) \\ \times \frac{\text{(specific weight of mercury)}}{12 \times 144}.$$

Specific weight of the manometer fluid was determined from a fitted Lagrange polynomial equation with room temperature the independent variable. Sufficient information had been calculated to allow the calculation of stream static pressure:

$$P_{static} = P_{atm} \times 144.0 + (\text{static tap manometer reading}) \\ \times (\text{specific weight of manometer fluid})/12.0.$$

This calculation allowed evaluation of the air density:

$$\rho_{air} = P_{static} / (53.36 \times \text{static temperature} + 459.688).$$

It should be noted at this point that the assumption was made that the total temperature was essentially equal to the static temperature and only the total temperature reading was obtained.

Finally the velocity was calculated from the expression:

$$V = \left(\frac{2.0 \times 32.174}{\rho_{air}} \text{ (specific weight of manometer fluid)} \right. \\ \left. \times \frac{(\text{Pitot-static probe manometer reading})}{12.0} \right)^{\frac{1}{2}}.$$

Velocity calculations were made for each data point in the calibration set.

The next primary parameter calculated was the modified power parameter. Some intermediate calculations were required first. These involved obtaining the values for various resistances. The sensor resistance, R_s ,

was obtained from the cold resistance, R_c , the probe resistance, R_p , the probe holder resistance, R_{ph} , and the cable resistance, R_{cab} . The cold resistance is a value read from the anemometer resistance bank when negligible current is supplied to the sensor while the sensor is essentially at stream temperature. All other resistance values resulted from direct resistance measurements across the individual part. The sensor resistance expression is

$$R_{s_1} = R_c - (R_p + R_{ph} + R_{cab}) .$$

This is not the sensor resistance which was used in the final expression. To determine the final value, an overheat ratio was required. The overheat ratio, R_{oh} , essentially expresses the magnitude of the temperature difference between the heated wire and the stream temperature. In this work, 1.4 and 1.5 were used. The final sensor resistance was calculated from the expression

$$R_s = R_{s_1} \times R_{oh} .$$

The total resistance, R_t , in the circuit of the anemometer bridge voltage meter was determined by

$$R_t = R_s + R_p + R_{ph} + R_{cab} + \text{bridge leg resistance.}$$

Finally, the combined resistances and the anemometer bridge voltage reading, E_b , were used to calculate the modified power

$$MP = E_b^2 R_s / (R_t^2 [R_{oh} - 1.0]) .$$

As with the velocity, this parameter was determined at every probe angle position and every calibration tunnel pressure setting.

MP and V are normally related through the expression

$$MP = K_1 + K_2 V^N.$$

A short computer program was developed which would determine the value for K_2 and N if a value for K_1 was assumed. The calibration values of $\ln(MP - K_1)$ and $\ln(V)$ were determined from a curve fit using a first order least squares set of equations which produced a set of values for K_2 and N . This process was carried out for several values of K_1 until the resulting equation best fit the calibration data. This technique produced good results but required a separate computer run for the calibration data before any boundary layer data could be processed since the evaluation of the optimum values for the coefficients and exponent was by inspection of the deviation of the predicted MP value from the calibration value. It was found that a second order least squares fit of the data was as accurate and did not require a separate run for the calibration data. It had the form

$$MP = C_1 + C_2 V + C_3 V^2.$$

The probe was positioned at various angle orientations with respect to the mean flow vector for each velocity setting, and a set of modified power readings were calculated for each condition. Letting MP_θ denote the modified power value obtained when a sensor is at an angle theta with respect to the mean flow, a modified power ratio, MPR, was formed with the value MP_{90° as a normalizing factor and the square root of this ratio was obtained

$$MPR = \frac{MP_\theta}{MP_{90}} .$$

Next, the square root of the sine of the corresponding angle was calculated. As will be demonstrated later, these two parameters have nearly a linear relationship for the smaller angle values. A linear least squares fit of the calibration data $MPR^{\frac{1}{2}}$ and $\sin^{\frac{1}{2}}\theta$ was executed for the lower values of $\sin^{\frac{1}{2}}\theta$ and the coefficients were retained for future use. This process was conducted for both wires and at each velocity setting where variable probe angle positions were made.

All the values calculated so far were retained for use in reducing experimental values of MP to corresponding velocities and angles. The previously mentioned parameters were considered semi-permanent data. Recalculation was necessary only if recalibration was necessary.

Hot-wire velocity profile data

Since all the calibration relationships have been obtained, data from a flow field of unknown characteristics could be acquired and reduced to basic flow properties. This part of the program reduced hot-wire anemometer output, both mean and fluctuating data, also reference pressure and temperature data. Pressure and temperature data were processed as explained previously.

Hot-wire anemometer data was taken three times at every probe position. Only mean readings were obtained in the diffuser profile positions. Reasons for only limited fluctuating data are discussed in APPENDIX C. First, an explanation of the procedure for determining the mean velocity and the angles with respect to the sensors is presented.

After the bridge voltage readings were averaged and arranged in the correct array and the pertinent resistances and overheat ratios supplied,

then a modified power parameter was calculated for each data point and each wire. The power parameter value obtained for one wire was designated as the U-wire and a value for the other wire was designated as the V-wire. Again, a Lagrange polynomial was used to determine what is called the equivalent velocity, that is, the velocity which would effect the same power reading if the velocity was normal to the wire rather than being oblique. After determining these two velocities which were denoted as UEQV and VEQV, the first estimate for the total mean velocity, QTOT, was obtained from the expression

$$QTOT^2 = \frac{UEQV^2 + VEQV^2}{1 + k^2}$$

where k is a factor which essentially signifies the contribution to the heat transfer by the velocity component parallel to the wire. k is a weak function of velocity and angle but for the previous calculation it was assumed to be only a function of, L/D , wire length to diameter ratio. The previous equation was derived in APPENDIX C. Upon denoting the angle between the U-wire and the total mean velocity vector as α , and using the mean velocity equation which was derived in APPENDIX C, the sine of the angle was determined

$$\sin \alpha = \left\{ \left[\frac{UEQV}{QTOT}^2 - k^2 \right] / (1-k^2) \right\}^{1/2}.$$

Because of the coordinate system used in APPENDIX C and the assumption that the mean velocity vector was in the same plane as the two sensor wires, the angle β between the V-wire and mean velocity vector was related by

$$\sin \beta = (1.0 - \sin^2 \alpha)^{1/2}.$$

It should be emphasized that the values obtained at this point for QTOT, $\sin \alpha$ and $\sin \beta$ are all normally within five percent of the final value. In an attempt to increase the accuracy of the values for QTOT, $\sin \alpha$ and $\sin \beta$, an iteration scheme based on the type of correlation equations presented by Friehe and Schwarz (26) was applied. Their equations relate the equivalent velocity to the actual velocity and the angle between the actual velocity vector and the wire. In the present work it was found that considerable scatter occurred when correlating with their parameters, but replacing their velocity ratio by a power ratio resulted in a very well-behaved correlation. To be explicit, their correlation parameters were

$$(\sin \alpha)^{\frac{1}{2}} \quad \text{abscissa}$$

$$\left(\frac{UEQV}{QTOT} \right)^{\frac{1}{2}} - (\sin \alpha)^{\frac{1}{2}} \quad \text{ordinate}$$

whereas in this work the correlation parameters were

$$(\sin \alpha)^{\frac{1}{2}} \quad \text{abscissa}$$

$$\left(\frac{MP_{\alpha}}{MP_{90}} \right)^{\frac{1}{2}} \quad \text{ordinate.}$$

MP_{α} is the value of $E_b^2 R_s / (R_t^2 [R_{oh} - 1.0])$ that results when the wire is at an angle of alpha with respect to the mean flow vector. Analogously, what is meant by MP_{90} can be seen. The MP ratio becomes a weak function of velocity at higher velocity magnitudes. Two typical correlation plots are shown in Figure 12. One for a hot-film sensor and the other a hot-wire sensor. As can be seen from the figure, a linear portion exists

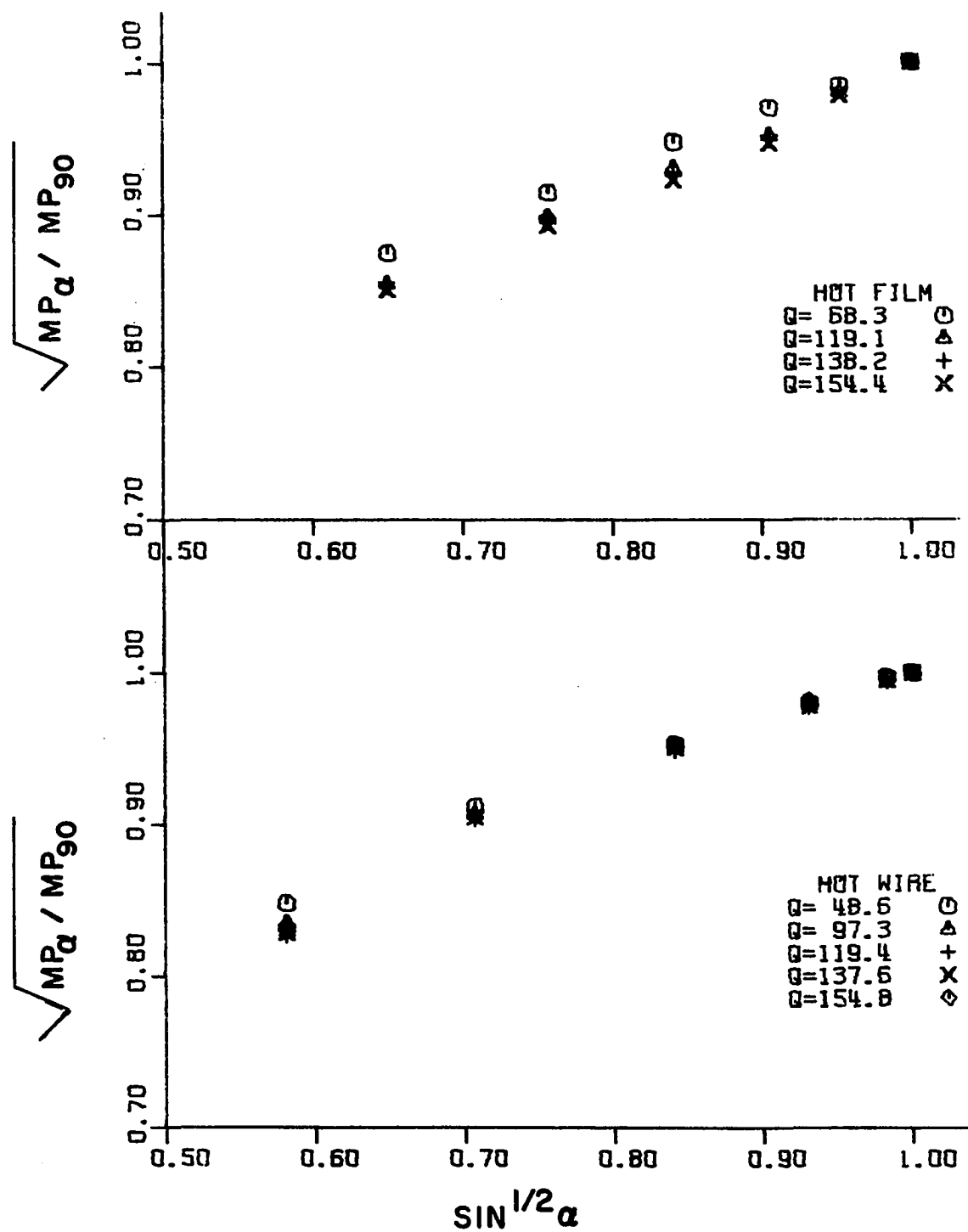


Figure 12. Hot-wire power and angle relationship

primarily for the lower values of alpha. This linear portion was fitted to a first order least squares set of equations and values of the intercept, a, and slope, b, were obtained. This operation was performed for both wires at each velocity value where an angular calibration set was obtained. An array for both a and b was then known as a function of QTOT for both wires. A curve fitting routine was used to find values for a and b at intermediate values of QTOT. Recalling that a first approximation for $\sin \alpha$ and $\sin \beta$ were both known, then the two were compared to determine which had the lowest value. After using the lowest angle value to determine which wire calibration curve to use, the appropriate values for a and b were obtained. With the first approximation for QTOT, the value for MP_{90° was obtained from a second order least squares fit of the calibration data

$$MP_{90^\circ} = C_1 + C_2 (QTOT) + C_3 (QTOT)^2.$$

The second approximation for the sine of the angle was obtained by solving

$$\left(\frac{MP_\alpha}{MP_{90^\circ}} \right)^{\frac{1}{2}} = a + b (\sin \alpha)^{\frac{1}{2}}$$

for $\sin \alpha$, and from the same type of expression for the opposite angle, $\sin \beta$. The angle not determined from the previous equation was calculated from the relationship between the two angles. Using the last calculated values for QTOT, $\sin \alpha$ and $\sin \beta$ a two-dimensional curve fit of the calibration data was performed using QTOT and $\sin \alpha$ as the independent variables in one case to find the modified power ratio for the U-wire and using QTOT and $\sin \beta$ in the other case to find the modified power

ratio for the V-wire. Since values of MP_{α} and MP_{β} were available from the data, then MP_{90} for each wire was found from the following equations:

$$\left(MP_{90} \right)_{U\text{-wire}} = MP_{\alpha} / \left(\frac{MP_{\alpha}}{MP_{90}} \right)_{\text{curve fit value}}$$

and

$$\left(MP_{90} \right)_{V\text{-wire}} = MP_{\beta} / \left(\frac{MP_{\beta}}{MP_{90}} \right)_{\text{curve fit value}}$$

The calibration equation (second order least squares fit) was solved for QTOT and was used to calculate the value of velocity as a function of the above modified power values which produced

$$(QTOT)_{U\text{-wire}} = QTOT-U = -\frac{C_2}{2C_1} - \frac{1}{2} \left\{ \left(\frac{C_2}{C_3} \right)^2 - \frac{4(C_1 - [MP]_{90-U})}{C_3} \right\}^{\frac{1}{2}}$$

$$(QTOT)_{V\text{-wire}} = QTOT-V = -\frac{C_2}{2C_1} - \frac{1}{2} \left\{ \left(\frac{C_2}{C_3} \right)^2 - \frac{4(C_1 - [MP]_{90-V})}{C_3} \right\}^{\frac{1}{2}}.$$

Note that C_2 for the U-wire is not necessarily equal to C_2 for the V-wire. The same for the rest of the coefficients. If QTOT-U was equal to QTOT-V then the correct value for the velocity was considered equal to QTOT-U, if not, the average of QTOT-U and QTOT-V was calculated and the entire process was repeated using the average velocity, iterating until the average velocity from the previous iteration was within 0.05 feet per second of the current iteration average velocity value. The average velocity was used as the convergence criteria because the angle was based on the velocity in the first step of the iteration process and if the angle ceased to change then all other values ceased to change. Normally

only three to four iterations per data point were required. If more than five iterations were required a "dubious value" warning was noted and many times it reflected a bad calibration point or a bad data point.

Having obtained the values for QTOT, alpha and beta the fluctuating data was analyzed if any was available. As was mentioned earlier, only a limited amount of fluctuating data was obtained. It was found that for the type of equations which were derived in APPENDIX C for the fluctuating data reduction, as well as various modifications of the equations, that turbulence intensity values were predicted "correctly" only for the case in which the wires were 45 degrees with respect to the mean velocity vector. "Correctly", in this case, means the value obtained with the split-V probe was within a few percent of the value obtained using a single wire oriented 90 degrees to the flow. Figure 64 in APPENDIX C shows some turbulence distributions across the mating section exit. Since the probe orientation with respect to the mean flow angle at a point could not be changed with the positioning device which was used, then turbulence intensity could be obtained only when the probe was positioned at a point where the flow was 45 degrees with respect to the wire. APPENDIX C contains a hypothesis pertaining to the inability to measure turbulence data at angles other than 45 degrees with respect to the mean flow.

As with the mean parameters, fluctuating data was taken three times at every probe position. An attempt was made to correct the data obtained from directly reading the random noise meters. This process was based

on the premise that all the data must satisfy the following two basic equations:

$$\overline{(e_u + e_v)^2} = \overline{e_u^2} + 2\overline{e_u e_v} + \overline{e_v^2}$$

$$\overline{(e_u - e_v)^2} = \overline{e_u^2} - 2\overline{e_u e_v} + \overline{e_v^2}$$

where e_u denotes the instantaneous fluctuating voltage from the U-wire and e_v the same parameter from the V-wire. Through the use of a correlator in conjunction with two random noise meters the values for $\overline{(e_u + e_v)^2}$, $\overline{(e_u - e_v)^2}$, $\overline{e_u^2}$, and $\overline{e_v^2}$ were obtained experimentally. If both equations were solved for $\overline{e_u e_v}$, then using experimental data to calculate these values was obvious if the readings were correct or not since it takes a unique set of data to produce equal values of $\overline{e_u e_v}$. In general, an average of the individual experimental readings was not sufficient to obtain equal values of $\overline{e_u e_v}$. Various techniques were tried to determine the best way to satisfy the equations so that $\overline{e_u e_v}$ was the same value from either equation, and at the same time to obtain values of $\overline{e_u^2}$, $\overline{e_v^2}$, $\overline{(e_u + e_v)^2}$ and $\overline{(e_u - e_v)^2}$ within their respective scatter bands. The following technique was chosen.

The first step was to obtain an average value for $\overline{4e_u e_v}$,

$$\overline{4e_u e_v} = \frac{1}{3} \sum_{N=1}^3 \overline{(e_u + e_v)_N^2} - \overline{(e_u - e_v)_N^2} .$$

Since $\overline{(e_u - e_v)^2}$ appeared to be the most reproducible, it was obtained from a direct average,

$$\overline{(e_u - e_v)_C^2} = \frac{1}{3} \sum_{N=1}^3 \overline{(e_u - e_v)_N^2} .$$

A corrected value for the sum was obtained from the following relation:

$$\overline{(e_u + e_v)^2}_C = \overline{(e_u - e_v)^2}_C + 4\overline{e_u e_v}.$$

From the above relations and the average values of the experimentally obtained parameters $\overline{e_u^2}$ and $\overline{e_v^2}$ the last two required values were determined as follows:

$$\overline{(e_u^2)}_C = \frac{1}{2} \left\{ \overline{(e_u - e_v)^2}_C + \frac{1}{2} (4\overline{e_u e_v}) - \frac{1}{3} \sum_{N=1}^3 \overline{(e_v^2)}_N + \frac{1}{3} \sum_{N=1}^3 \overline{(e_u^2)}_N \right\}$$

and

$$\overline{(e_v^2)}_C = \overline{(e_u - e_v)^2}_C + \frac{1}{2} (4\overline{e_u e_v}) - \overline{(e_u^2)}_C.$$

Values having the subscript C were used in the turbulence equations but for simplicity the subscript was deleted in the remaining discussion.

The turbulence equations which were used in the data reduction program are as follows:

$$\frac{\overline{e_u^2}}{\Gamma_u^2} = A_u^2 \overline{q_s^2} + C_u^2 \overline{q_t^2} + 2A_u C_u \overline{q_s q_t}$$

$$\frac{\overline{e_v^2}}{\Gamma_v^2} = A_v^2 \overline{q_s^2} + C_v^2 \overline{q_t^2} + 2A_v C_v \overline{q_s q_t}$$

$$\frac{(4\overline{e_u e_v})}{4\Gamma_u \Gamma_v} = A_u A_v \overline{q_s^2} + C_u C_v \overline{q_t^2} - (A_u C_v - A_v C_u) \overline{q_s q_t}$$

where

$$\Gamma_u = \kappa_u A_u^{-1/2}$$

$$\Gamma_v = \kappa_v A_v^{-\frac{1}{2}}$$

$$\kappa_u = \frac{dE_u}{d(UEQV)}$$

$$\kappa_v = \frac{dE_v}{d(VEQV)}$$

$$A_u = 1 - (1 - k_u^2) \cos^2 \alpha$$

$$A_v = 1 - (1 - k_v^2) \cos^2 \beta$$

$$C_u = (1 + k_u^2) \cos \alpha \cos \beta$$

$$C_v = (1 + k_v^2) \cos \alpha \cos \beta .$$

For simplicity, the bars over the α and β variables were deleted but they are understood to be the average values. The complete nomenclature is given in APPENDIX C. These equations were solved simultaneously for $\overline{q_s^2}$, $\overline{q_t^2}$ and $\overline{q_s q_t}$ which are the turbulence in the mean flow direction, the turbulence normal to the mean flow direction and the Reynolds stress respectively. This concludes the hot-wire anemometer data reduction.

Wall static pressure data

Wall pressure data was obtained by reading a bank of manometers. These manometer readings were reduced to pressure readings by the following procedure.

Multiple readings of the manometers were obtained and averaged. The average value was then transformed into a calibrated manometer height by

$$h = h_{std}(I-1) + (h_{std}(I) - h_{std}(I-1)) \frac{[Manometer reading - h_{C-STD}(I-1)]}{[h_{C-STD}(I) - h_{C-STD}(I-1)]}$$

where

- $h_{STD}(I-1)$ = calibration "standard" reading at a value just below the desired value
- $h_{STD}(I)$ = calibration "standard" reading just above the desired value
- $h_{C-STD}(I-1)$ = manometer reading corresponding to $h_{STD}(I-1)$
- $h_{C-STD}(I)$ = manometer reading corresponding to $h_{STD}(I)$.

Since the reservoir level changed, a correction was made for it. One manometer tube in the bank monitored the level change. The value of the water column height was used to determine the pressure was

$$h_{corrected} = h - h_{level}.$$

Pressure was obtained from the following relation

$$P_{wall} = \text{specific weight of manometer fluid} \times \frac{h_{corrected}}{12.0}.$$

The preceding calculations were executed for each manometer tube.

Total pressure survey data

If a total pressure survey was conducted the procedure for determining the pressure was simply

$$P_{total} = P_{ATM} + \frac{(\text{manometer column height})}{12.0}$$

$$\times (\text{specific weight of manometer fluid})$$

where P_{ATM} is atmospheric pressure and was calculated earlier.

After the raw data was transformed into basic properties, various correlating parameters associated with the basic properties were formulated. The subsequent subsection outlines the approaches used to accomplish this task.

Parameter Calculations

The primary parameters calculated in this work were the integral parameters and shape factors. Some of the other parameters are boundary layer thickness, and the limiting line skewing angle.

A computer program was written to calculate the entire set of parameters. All the integral parameters were determined by a summation of trapezoidal areas which were comprised of a dependent parameter and an independent variable derived from the experimental data. Curve fitting, wherever necessary, was done with the use of a second order Lagrange polynomial.

Boundary layer thickness was assumed to be the distance from the wall at which the velocity was 0.995 times the free stream velocity, $Q_{f.s.}$. Free stream velocity was considered the greatest velocity in the profile which was relatively constant over an appreciable distance. It was noticed that the free stream could be found very readily by monitoring the signals on the oscilloscope as an indication of the turbulence level. After determining Q , defined as 0.995 $Q_{f.s.}$, it was used to curve fit for δ , boundary layer thickness.

The skewing angles, α , were determined by curve fitting for the angle at the boundary layer edge using the angles between the mean velocity vector and the u-wire. This angle was then subtracted from all the other angles producing the skewing angle distribution. It was assumed that the limiting line skewing angle, $\alpha_{C.L.}$, was between the free stream velocity vector and a best estimate of the wall collateral layer

velocity vector as determined from velocity polar plots.

Velocity polar plots are plots of the crossflow velocity ratio w/Q against the streamwise velocity ratio u/Q . Crossflow velocity was obtained from the relation

$$w = Q_s \sin \alpha$$

whereas the streamwise velocity was found from the relation

$$u = Q_s \cos \alpha .$$

The integral parameters were obtained from their definitions using the intrinsic coordinate system which resulted in the following:

Streamwise displacement thickness

$$\begin{aligned} \delta_1^* &= \frac{1}{Q} \int_0^\delta (Q - u) d\eta \\ &= \delta \int_0^1 \left(1 - \frac{u}{Q}\right) d(\eta/\delta) \end{aligned}$$

Crossflow displacement thickness

$$\begin{aligned} \delta_2^* &= \frac{1}{Q} \int_0^\delta (0 - w) d\eta \\ &= \delta \int_0^1 -\frac{w}{Q} d(\eta/\delta) \end{aligned}$$

Streamwise momentum thickness

$$\begin{aligned} \theta_{11} &= \frac{1}{Q^2} \int_0^\delta (Q - u) u d\eta \\ &= \delta \int_0^1 \left(1 - \frac{u}{Q}\right) \frac{u}{Q} d(\eta/\delta) \end{aligned}$$

Streamwise interaction momentum thickness

$$\begin{aligned}\theta_{21} &= \frac{1}{Q^2} \int_0^\delta (0 - w) u d\eta \\ &= \delta \int_0^1 \left(-\frac{w}{Q}\right) \frac{u}{Q} d(\eta/\delta)\end{aligned}$$

Crossflow momentum thickness

$$\begin{aligned}\theta_{22} &= \frac{1}{Q^2} \int_0^\delta (0 - w) w d\eta \\ &= \delta \int_0^1 \left(-\frac{w}{Q}\right) \frac{w}{Q} d(\eta/\delta)\end{aligned}$$

Crossflow interaction momentum thickness

$$\begin{aligned}\theta_{12} &= \frac{1}{Q^2} \int_0^\delta (Q - u) w d\eta \\ &= \delta \int_0^1 \left(1 - \frac{u}{Q}\right) \frac{w}{Q} d(\eta/\delta)\end{aligned}$$

It should be noted that $\delta_2^* = \theta_{21} - \theta_{12}$. The shape parameters which were calculated are the following:

Streamwise shape factor

$$H_1 = \delta_1^*/\theta_{11}$$

Crossflow shape factor

$$H_2 = \delta_2^*/\theta_{22} .$$

All other parameters which were calculated were algebraic combinations of the ones previously calculated.

Data Uncertainty

All data obtained during this investigation was considered single sample data. The method presented by Kline and McClintock (44) was used to represent estimated values for the error of the reduced data. They suggest that for single sample observations it is valid to estimate a value for the uncertainty interval associated with a given variable based on certain odds. This estimate is a result of considering possible deviations from the ideal experiment and of experience with the equipment involved. In order to obtain the value closest to the actual value, the uncertainty interval was associated with the arithmetic mean of the observed value. Mathematically this is stated as

$$V = \bar{V} \pm \epsilon \text{ (N to 1)}$$

where

V = true value of the variable

\bar{V} = best estimate of the variable value (arithmetic mean of observed variable values)

ϵ = uncertainty interval of the variable

(N to 1) = odds given that \bar{V} is within $\pm \epsilon$ of V .

Their suggestion for determining a value for ϵ was by using the following equation:

$$\epsilon_G^2 = \left(\frac{\partial G}{\partial x_1} \epsilon_1 \right)^2 + \left(\frac{\partial G}{\partial x_2} \epsilon_2 \right)^2 + \dots + \left(\frac{\partial G}{\partial x_n} \epsilon_n \right)^2 \quad (12)$$

where G is the desired dependent variable and x_n is the n^{th} independent variable. G is expressed as

$$G = G(x_1, x_2, \dots, x_n).$$

Values for the independent uncertainty intervals were based on experience with the specific instrumentation system and a knowledge of possible deviations from ideal conditions. Before formally using the suggested method for determining the uncertainty of a given dependent variable, a review of some observations noted during the experimental work are given. Also, some of the types of errors which were expected are discussed.

Primary interest was placed on determining dimensionless variables which assisted in indicating flow behavior on the end wall of a curved diffuser. Since dimensionless variables were of primary importance, then data with absolute values differing from the actual was still useful. As an illustration, Figure 13 shows a velocity polar plot that has data obtained from dirty wires which resulted in the reference velocity being 5.5 feet per second below the standard value and also data obtained from the same probe after it was cleaned which had a velocity 0.3 feet per second below the standard value. In dimensionless terms these two profiles are quite similar. The standard value for velocity at the reference point was determined through the use of a Pitot-static probe. The majority of velocity profiles that were taken in the configuration with an aspect ratio of 1.5 were repeated at least once. Some were repeated three times in an attempt to obtain the best absolute value for the velocity, but because of uncontrollable conditions some of the profiles presented do not have absolute values within the percentage deviation from the reference values that was desired. Inspection of Figure 13 indicates that at least some confidence can be placed in the dimensionless variables.

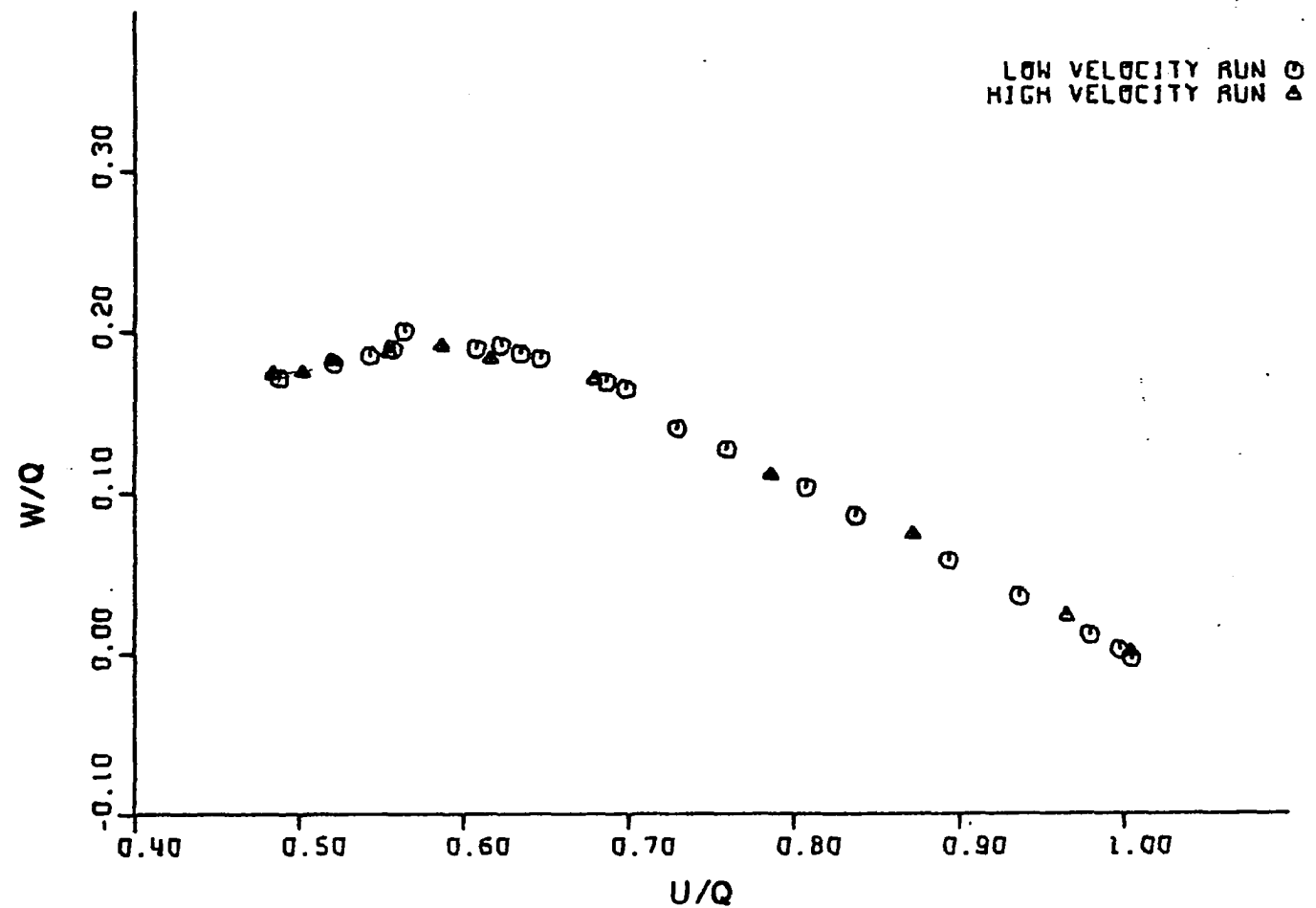


Figure 13. Polar plot comparison at different absolute velocities

In a subsequent portion of this section many of the possible errors encountered in this investigation are enumerated. Some of them will be discussed in more detail at this point. Experience with the particular test system used in this investigation has shown that temperature, wire contamination and aging, and wire configuration changes were the primary causes of deviations from the standard to which the values were compared.

The constant temperature hot-wire anemometer attempts to maintain a given constant resistance in the small wire sensor exposed to an air stream through the use of electronic feedback circuitry which tries to keep the bridge circuit in balance. The driving potential which attempts to change the resistance is a coupled effect among the mass flow rate and the difference between the stream temperature and sensor temperature. If the mass flow rate over the sensor increased, then the cooling effect would be greater and the sensor temperature would decrease, thereby decreasing the resistance and actuating the feedback system which would produce an increased bridge voltage to maintain the pre-selected resistance. If the stream temperature increased then the cooling effect would decrease and the effect would be a decrease in bridge voltage. Another effect is that of wire contamination, as more dirt is accumulated on the wire it tends to act as an insulator which decreases the cooling effect of the mass flow rate and stream temperature resulting in a decrease in the bridge voltage. Wire aging resulted in various effects. After using a wire a period of time it tended to produce a drifting voltage output. Cleaning the wire was useless and when the wire was viewed under a microscope, surface irregularities were seen. One anomaly occurred

during testing with a particular wire which had been used several times. The temperature of the stream was higher than the calibration stream temperature and the wire was slightly contaminated which would normally produce a bridge voltage value less than the calibration value for the same velocity. In this instance the bridge voltage for one sensor had a higher value and the only cause suspected was that the wire sensors had become taut, thereby changing orientation with respect to each other and to the free stream in the reference position.

In an attempt to determine the magnitude of the effect of temperature on the hot-wire measuring system a series of measurements were taken while the stream temperature was varying. Since the temperature of the test cell could not be regulated and thereby, also the stream temperature, the only way stream temperature could be varied over a relatively short time period was to take measurements during the blower warm-up period. Over a given temperature and voltage range and for a particular probe position, it was found that for the U-wire the bridge voltage to stream temperature relationship was $0.00534 \text{ volts}/{}^{\circ}\text{F}$ and $0.00782 \text{ volts}/{}^{\circ}\text{F}$ for the V-wire. Also, it was found for the particular probe and velocity range that a bridge voltage to velocity relationship was $0.00250 \text{ volts/feet per second}$ and $0.00317 \text{ volts/feet per second}$ for the U-wire and V-wire respectively. Fortunately, because of the sensor calibration characteristics, the ratio of bridge voltage to velocity increases for lower velocity ranges as are found in the boundary layer.

A change in room temperature which resulted in a change in the instrumentation cabinet temperature also affected the bridge voltage

readings. On several occasions the hot-wire channels were maintained in the standby condition and allowed to operate over periods of time up to nine hours while the cabinet temperature and standby voltage were monitored. There was some scatter in the data but most of the readings indicated a relationship of standby voltage reading to cabinet temperature readings of $0.08 \text{ volts}/{}^{\circ}\text{F}$ and $0.18 \text{ volts}/{}^{\circ}\text{F}$ for channels one and two respectively. A gross relationship between the standby voltage setting and the bridge voltage reading in the run condition is that a two percent change in the standby resulted in a 0.1 percent change in the bridge voltage.

One of the mechanical problems encountered in the data procurement was that of positioning the probe so that both wires had the same geometrical relationship with respect to the floors. Attempts were made to shim the probe holder so the sensors were both parallel to the floor and after trial and error the least variation from end to end of the sensors was 0.001^+ inches. The majority of the time the probe was rotated about its streamwise axis so that the two wires (sensors) were at the same average distance from the end wall and the end to end variation was approximately 0.002 inches. If one sensor was closer to the wall than the other then erroneous angles and magnitudes of velocity were predicted (especially in the inner layers of the boundary layer) because of the large velocity gradient. Since the data reduction theory was based on both wires sensing the same total velocity then it is more essential to have the two wires the same average distance from the end wall than to keep the probe at zero angle of attack with respect to the end wall.

Probe vibration was originally thought to be the primary defect in the instrumentation system design. As far as could be ascertained, this had negligible effect on the readings. When the probe holder was adjusted in the stream with the sensors near the pressure wall and the end wall at the diffuser exit, the vibration problem was the most acute. Measurements of the peak to peak amplitude of the vibrations in this position were obtained and variations from a mean were on the average ± 0.0117 inches. In data procurement positions the amplitude was approximately ± 0.005 inches. Voltage readings were observed when the probe was in its normal unrestrained condition near the end wall and also when it was restrained to reduce vibration. No discernible difference in readings occurred.

Some of the reasons attributed to errors in measurements for this investigation are the following:

- (1) Geometrical errors
 - a. Flatness of end wall
 - b. Hysteresis in probe positioner
 - c. Crooked sensors
 - d. Vibration
- (2) Environmental errors
 - a. Temperature changes
 - b. Dirt accumulation
 - c. Wire aging and/or corrosion.

Uncertainties for the independent variables or basic variables are presented first and then uncertainties of the dependent variables which were calculated are presented. The uncertainties of the dependent variables

are based on the hypothesis that the wires are clean, not corroded, and that the stream temperature was approximately the same as the calibration stream. All of the data presented does not adhere to this hypothesis but as indicated in a preceding part of this section, the dimensionless quantities are comparable.

Table 7 shows the independent variables, a typical value, and the associated uncertainty. Uncertainties of the dependent variables were determined using Equation 12. Integral parameter uncertainties were approximated by a finite summation replacing the integral. Basic ratios were redefined as a dependent variable and uncertainties were calculated from the resulting expression. For example, the expression used to determine the uncertainty of u/Q was

$$G_1 = \frac{u}{Q} = \frac{Q_s \cos \alpha}{Q} .$$

Some typical values of dependent variables and parameters are shown below with their uncertainty values and the associated odds.

Static pressure

$$P_s = (2039.571 \pm 0.357) \text{ psf} \quad (20 \text{ to } 1)$$

Velocity - Pitot-static probe

$$V = (131.48 \pm 0.217) \text{ fps} \quad (20 \text{ to } 1)$$

Modified power

$$MP = (0.05865 \pm 0.000126) \text{ watts} \quad (20 \text{ to } 1)$$

Velocity - Hot-wire anemometer

$$Q_s = (128.90 \pm 1.22) \text{ fps} \quad (20 \text{ to } 1)$$

Table 7. Uncertainties in basic variables

Independent or basic variable	Typical values	Uncertainty
Radius	(14.000 → 15.000) in.	0.003 in.
Angle	(0.00 → 40.00) deg.	2 min.
Distance from the end wall	(0.000 → 1.000) in.	0.003 in.
Temperature		
a) mercury ther- momter	(80.0 → 90.0) deg. F.	0.2 deg. F.
b) thermocouple	(80.0 → 95.0) deg. F.	1.0 deg. F.
Pressure		
a) manometer read- ings	(-1.40 → 5.50) in. H ₂ O	0.01 in. H ₂ O
b) barometer read- ings	(28.900 → 30.000) in. Hg.	0.005 in. Hg.
Resistance	(6.00 → 10.00) ohms	0.01 ohms
Voltage	(2.00 → 3.000) volts	0.003 volts (Repeatability value)

Angle - Hot-wire anemometer

 β (angle between wire sensor and Q_s)

$$\sin \beta = (0.500 \pm 0.009) \quad (20 \text{ to } 1)$$

β was repeatable between reference velocity checks at the beginning of a run to the end of a run within 0.3 degrees in most cases.

 α (angle between Q_s and Q)

$$\alpha = (18.8 \pm 0.5) \text{ degrees} \quad (20 \text{ to } 1)$$

Streamwise velocity ratio

$$\frac{u}{Q} = (0.7681 \pm 0.0122) \quad (20 \text{ to } 1)$$

Crossflow velocity ratio

$$\frac{w}{Q} = (0.1099 \pm 0.0069) \quad (20 \text{ to } 1)$$

Streamwise velocity ratio (collateral layer edge)

$$\left(\frac{u}{Q}\right)_{C.L.} = (0.5006 \pm 0.0107) \quad (20 \text{ to } 1)$$

Crossflow velocity ratio (collateral layer edge)

$$\left(\frac{w}{Q}\right)_{C.L.} = (0.1707 \pm 0.0094) \quad (20 \text{ to } 1)$$

Triangular crossflow ratio

$$\frac{w_c}{w_{c'}Q} = (0.5910 \pm 0.0193) \quad (20 \text{ to } 1)$$

A particular crossflow ratio

$$\frac{w/Q}{w_{c'}/Q} = (0.5543 \pm 0.0300) \quad (20 \text{ to } 1)$$

Normalized distance from the end wall

$$\eta/\delta = (0.4398 \pm 0.136) \quad (20 \text{ to } 1)$$

Displacement thicknesses

$$\delta_1^* = (0.0819 \pm 0.0018) \text{ inches} \quad (20 \text{ to } 1)$$

$$\delta_2^* = (-0.0337 \pm 0.0008) \text{ inches} \quad (20 \text{ to } 1)$$

Momentum thicknesses

$$\theta_{11} = (0.0533 \pm 0.0010) \text{ inches} \quad (20 \text{ to } 1)$$

$$\theta_{12} = (0.0108 \pm 0.0004) \text{ inches} \quad (20 \text{ to } 1)$$

$$\theta_{21} = (-0.0230 \pm 0.0007) \text{ inches} \quad (20 \text{ to } 1)$$

$$\theta_{22} = (-0.0044 \pm 0.0002) \text{ inches} \quad (20 \text{ to } 1)$$

Streamwise shape factor

$$H_1 = (1.5371 \pm 0.0442) \quad (20 \text{ to } 1)$$

Crossflow shape factor

$$H_2 = (7.6785 \pm 0.3792) \quad (20 \text{ to } 1)$$

ANALYSIS AND DISCUSSION OF DATA

Data obtained in this investigation is presented and briefly discussed. Then additional published data is discussed and compared with the diffuser data. Emphasis is placed on the similarity of integral parameter development, on the basic data trends resulting from geometrical or fluid flow parameter change and on the influence of basic flow variables on boundary layer development. A brief discussion of double-skewed turbulent boundary layers is also presented. Finally, some remarks are made pertaining to velocity models and some new parameters are introduced.

Diffuser Data

Data obtained in a skewed turbulent boundary layer with an adverse pressure gradient is presented as velocity profiles, shape factors and integral parameters. Pressure distribution measurements for both side walls are also given. The data is tabulated in APPENDIX D. The profiles have the following designation:

RRXXP1 = profile number

RR = centerline radius in inches

XX = centerline turning angle in degrees

P = position in reference to the centerline

P = nearest to the pressure wall

C = on the centerline

S = nearest to the suction wall.

These positions coincide with the profile stations shown in Figure 11.

Both streamwise and crossflow velocity normalized with respect to the free stream velocity are shown in Figures 14 through 25 as a function of the normalized distance from the wall. The streamwise velocity profiles are similar in shape to developing two-dimensional turbulent boundary layers over flat plates. It is interesting to note that the streamwise velocity profile at the zero-degree station, Figure 15, and the one at the forty-degree station, Figure 25, are nearly the same over the major portion of the profiles. Likewise the eight-degree station profile, Figure 17, and the thirty-two degree station profile, Figure 23, are nearly the same except near the wall. A comparison of the sixteen-degree profile, Figure 19, and the twenty-four degree profile, Figure 21, shows the same type of similarity. A plot of the shape factors as a function of angle helps support this observation as shown in Figure 26.

Development of the end wall centerline profiles showed decreasingly flatter profiles from the diffuser inlet, Figure 15, to the sixteen-degree station, Figure 19. These profiles showed characteristics of profiles approaching separation. Wall pressure taps distributed on both side walls one inch above the end wall should suggest a qualitative pressure distribution on the end wall. Assuming this to be true, Figure 27 shows a relatively large pressure gradient up to the sixteen degree station compared to the pressure gradient in the rest of the diffuser. This type of pressure distribution would indicate conditions near separation were possible. Upon decreasing the pressure gradient, the velocity profiles should tend to return to a flatter profile. Profiles shown in Figures 21, 23 and 25 developed into increasingly flatter profiles as expected

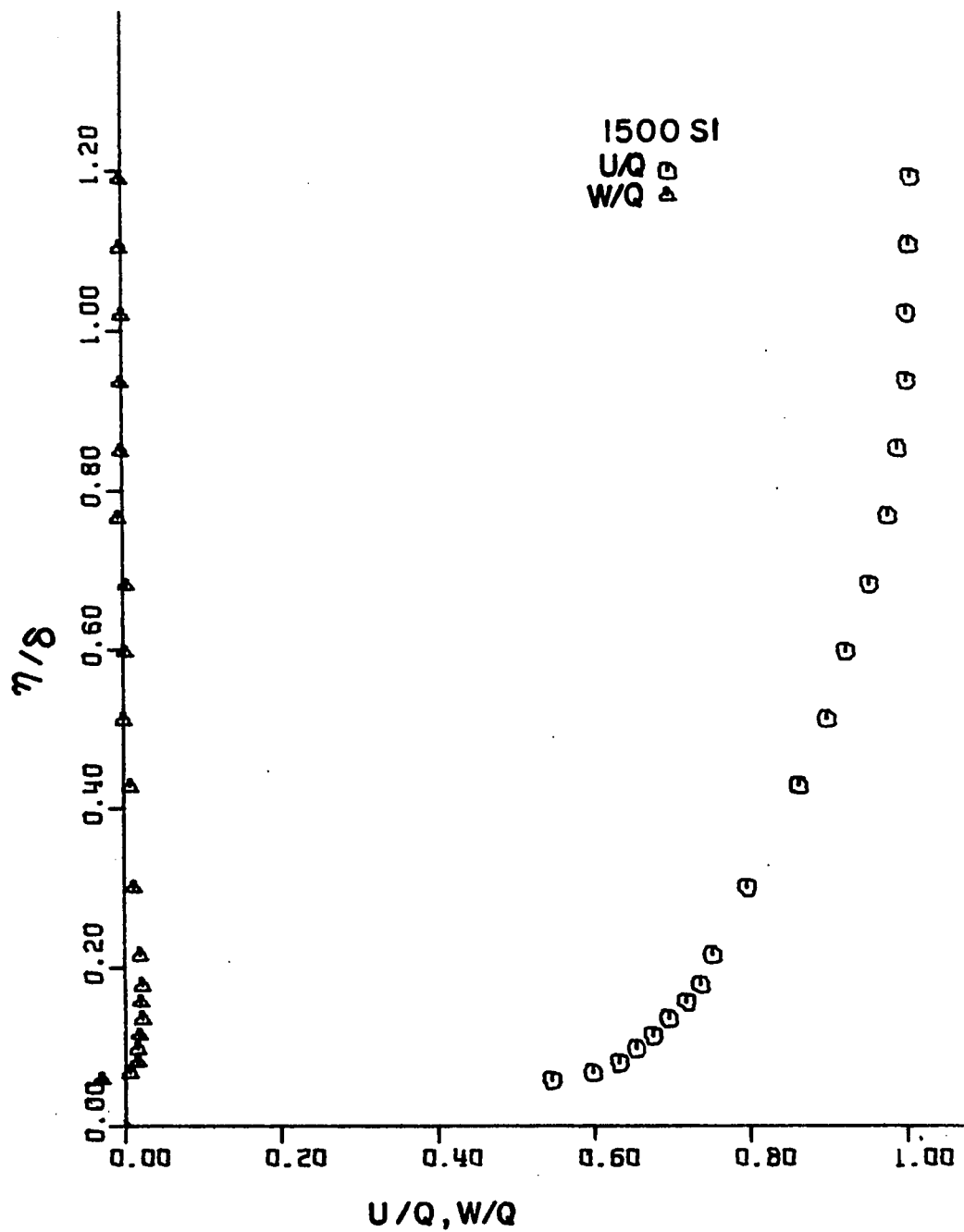


Figure 14. Velocity profiles on the diffuser end wall

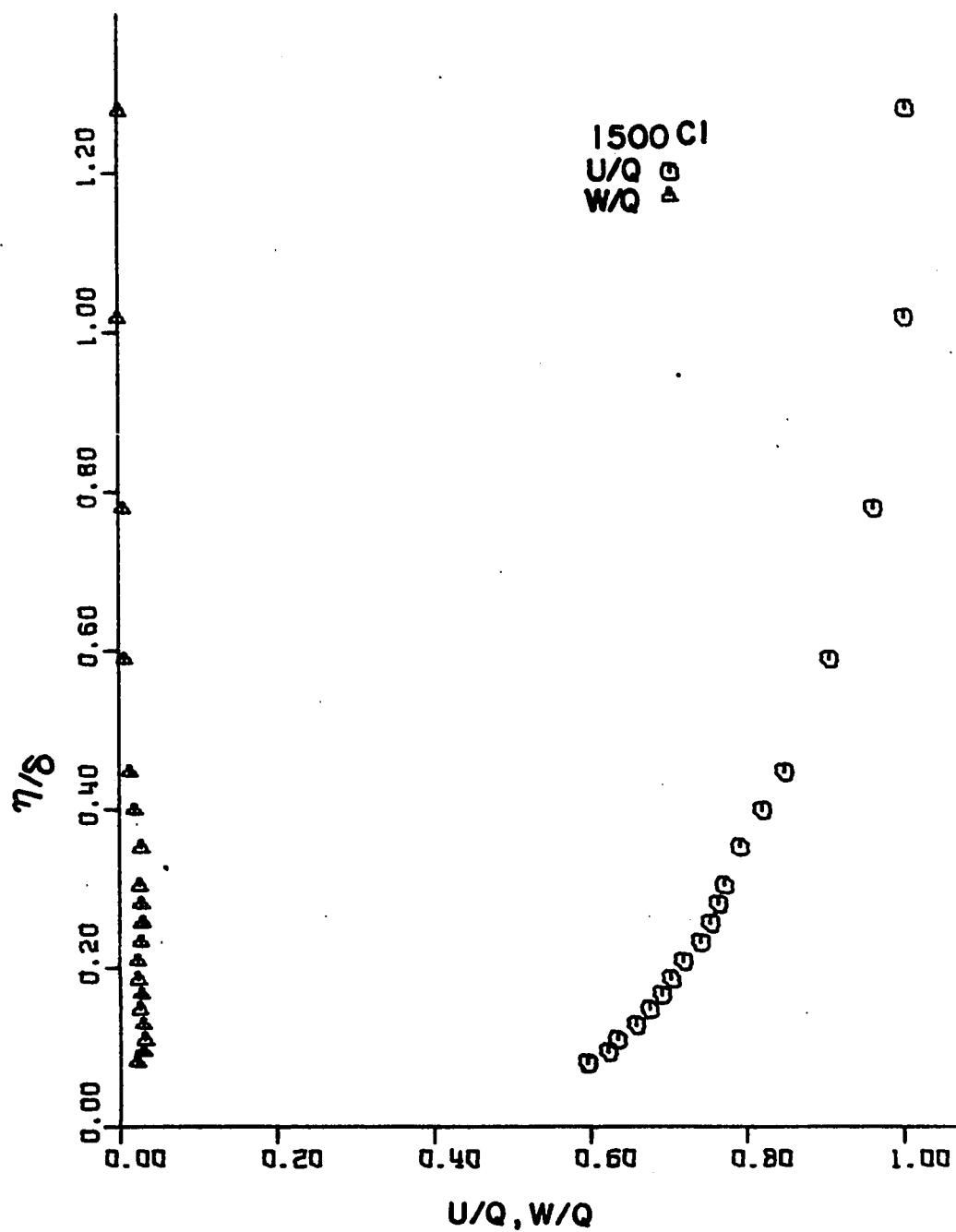


Figure 15. Velocity profiles on the diffuser end wall

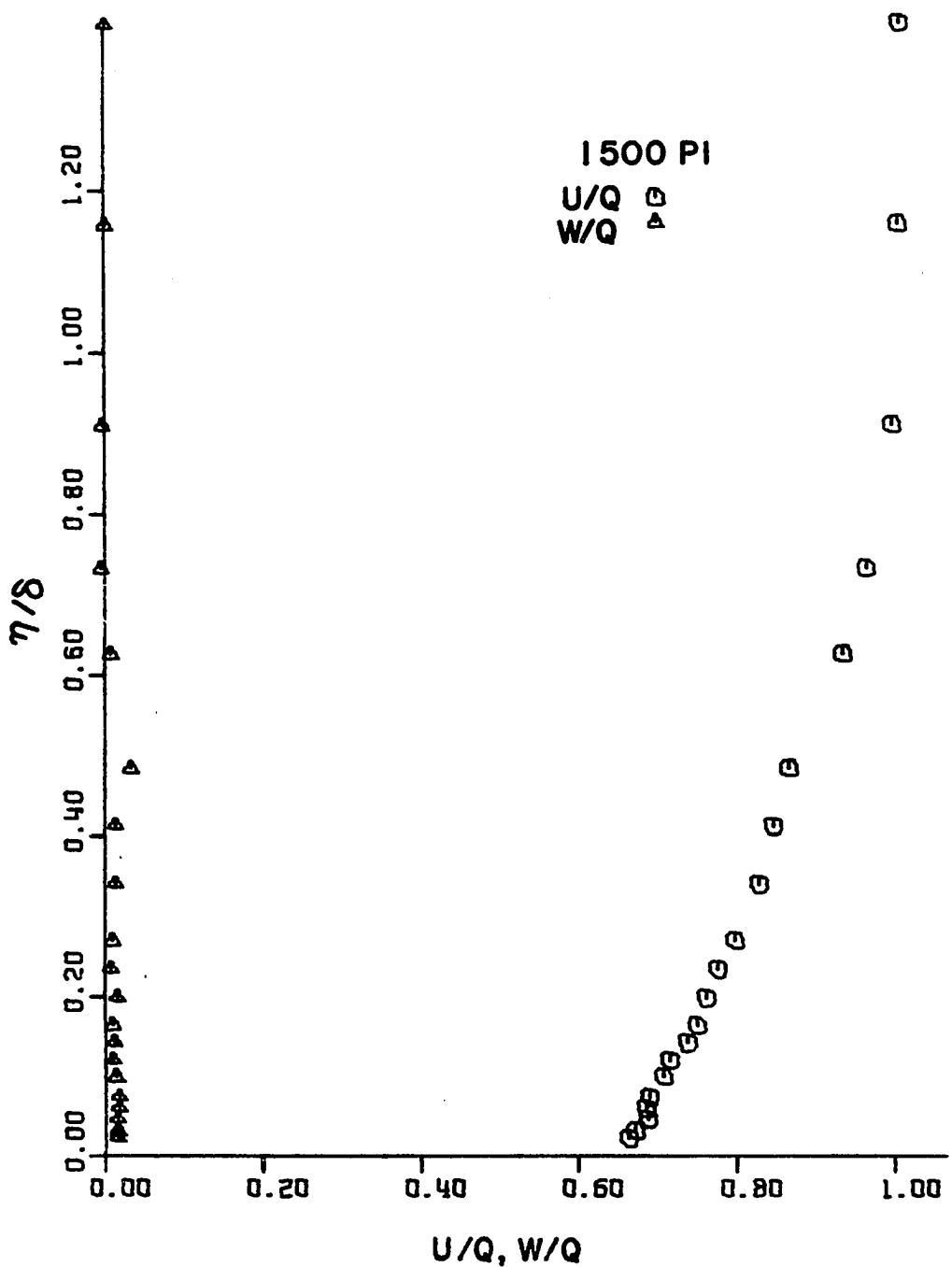


Figure 16. Velocity profiles on the diffuser end wall

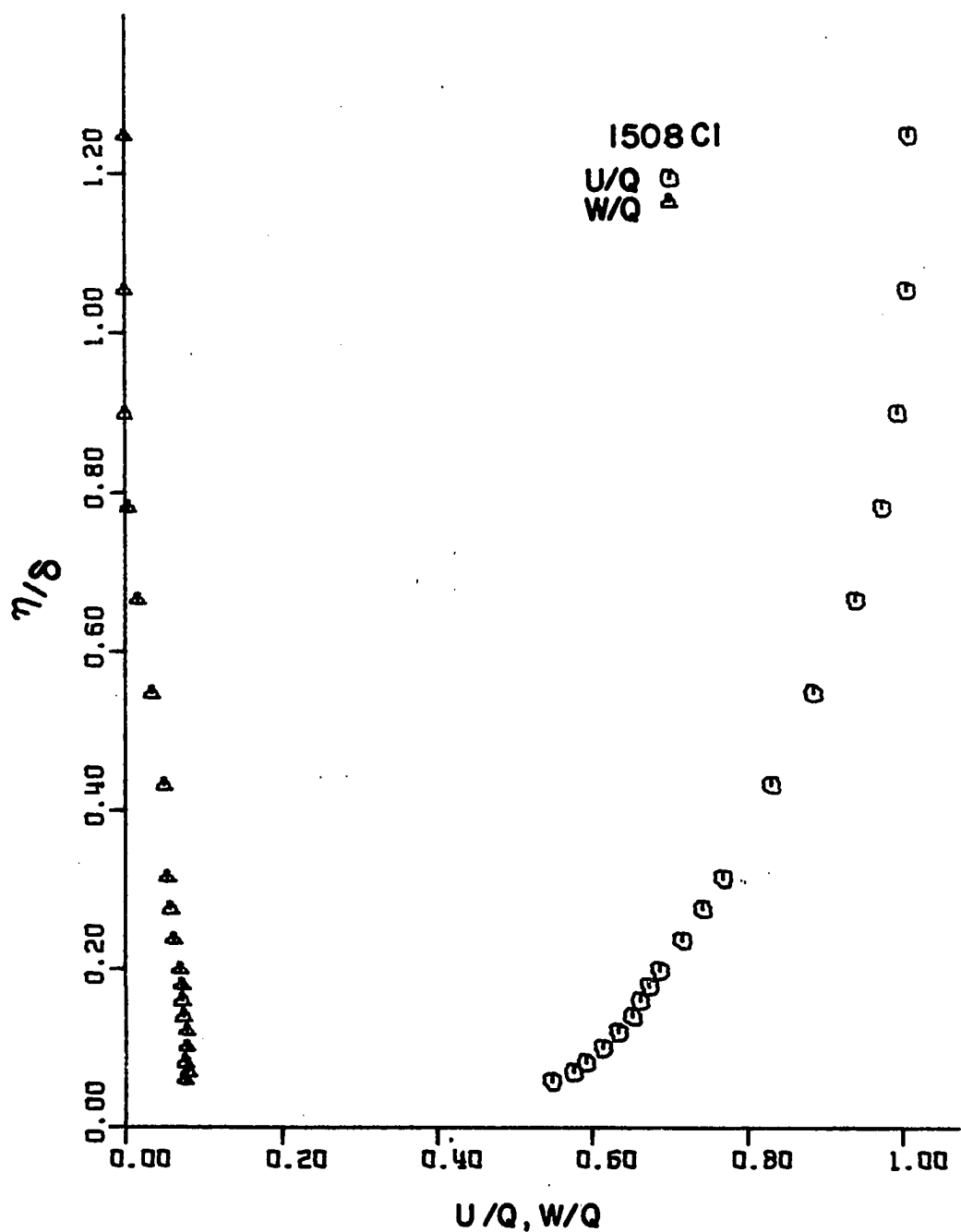


Figure 17. Velocity profiles on the diffuser end wall

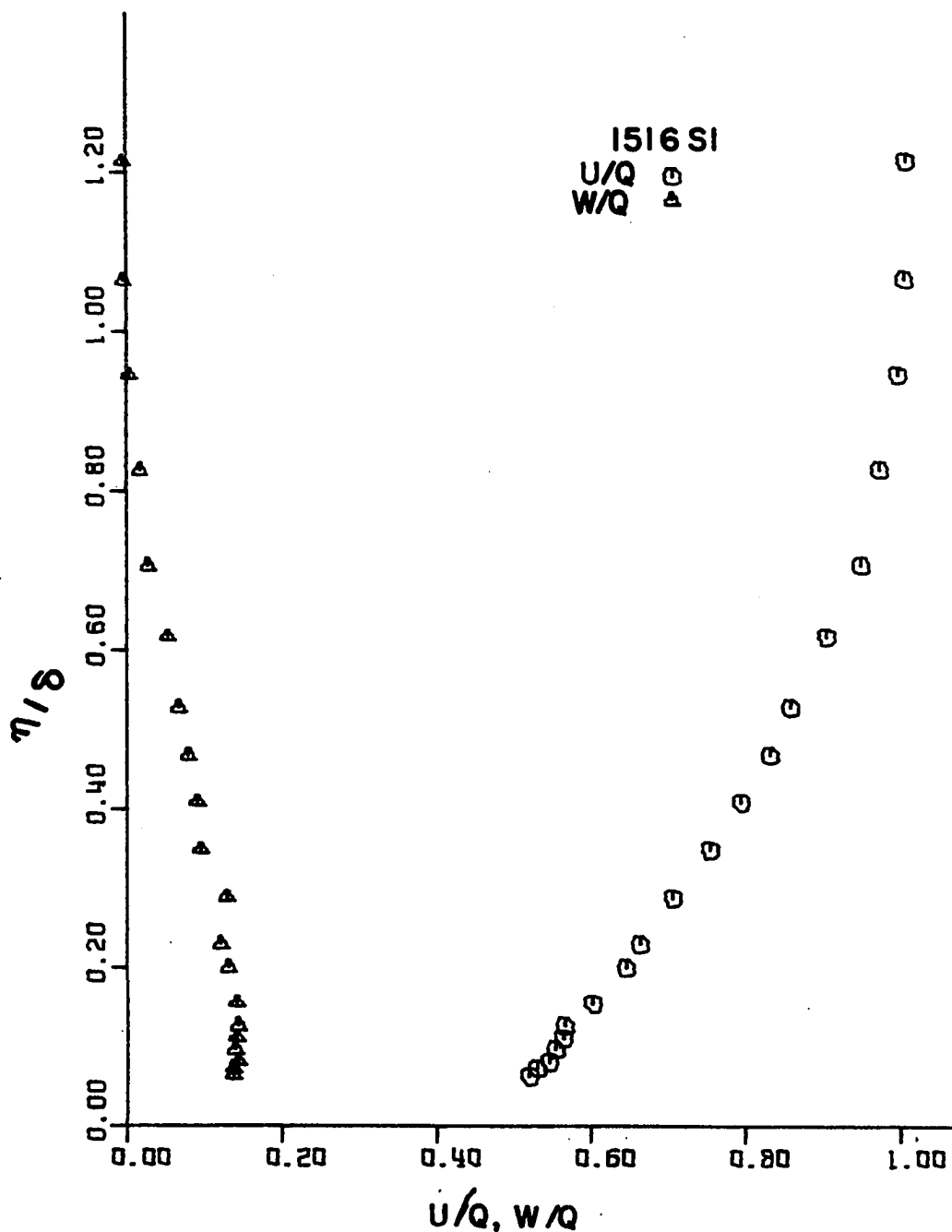


Figure 18. Velocity profiles on the diffuser end wall

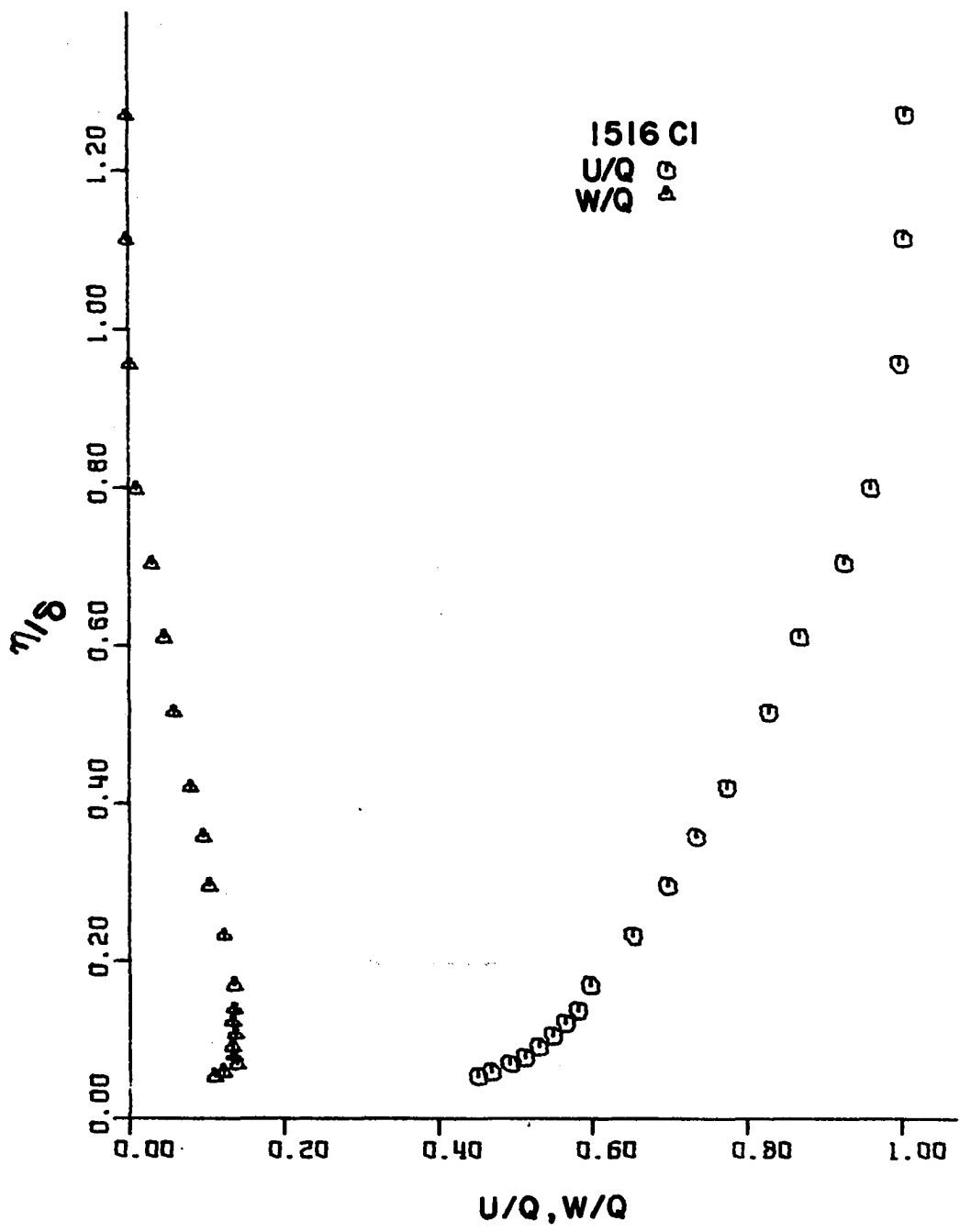


Figure 19. Velocity profiles on the diffuser end wall

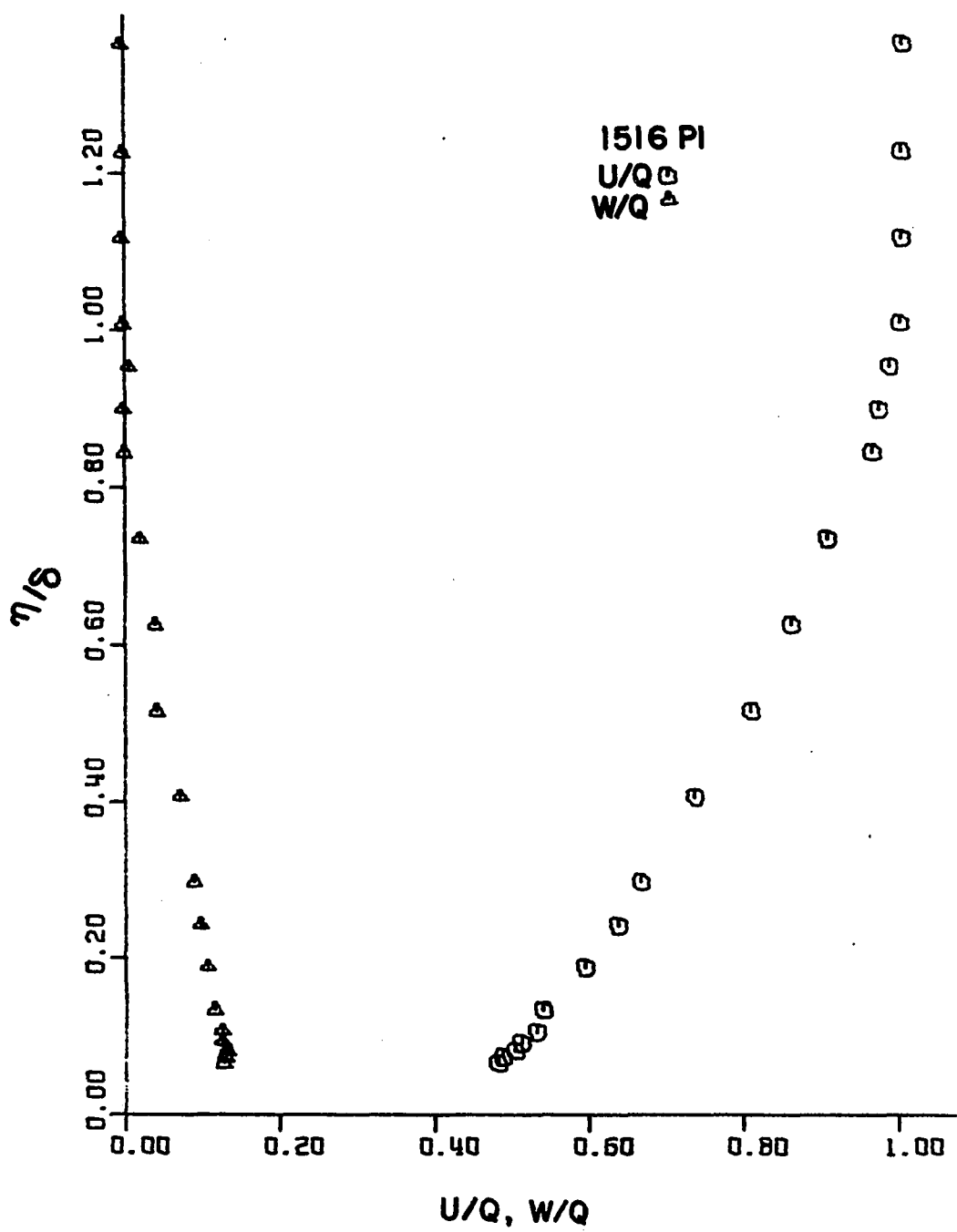


Figure 20. Velocity profiles on the diffuser end wall

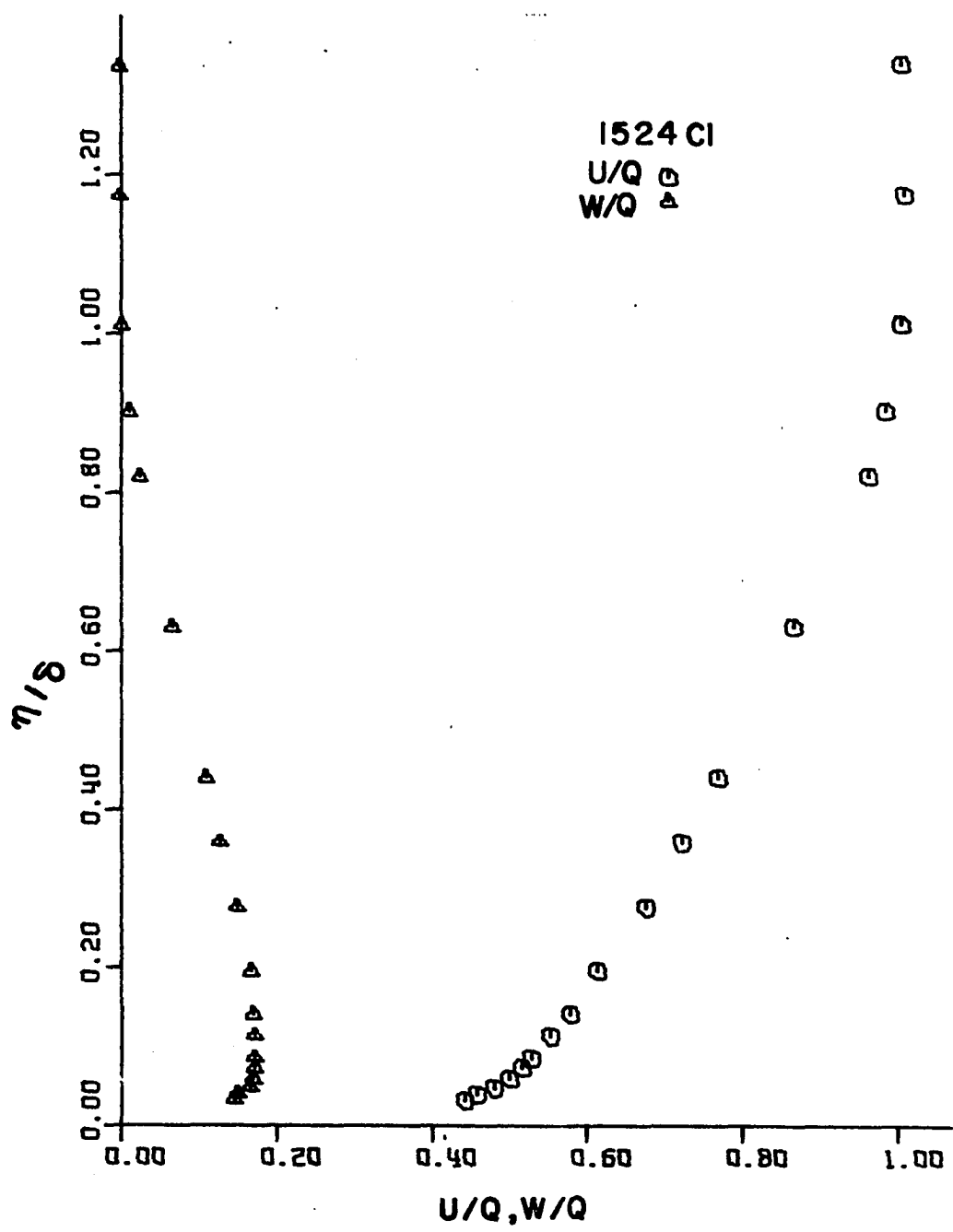


Figure 21. Velocity profiles on the diffuser end wall

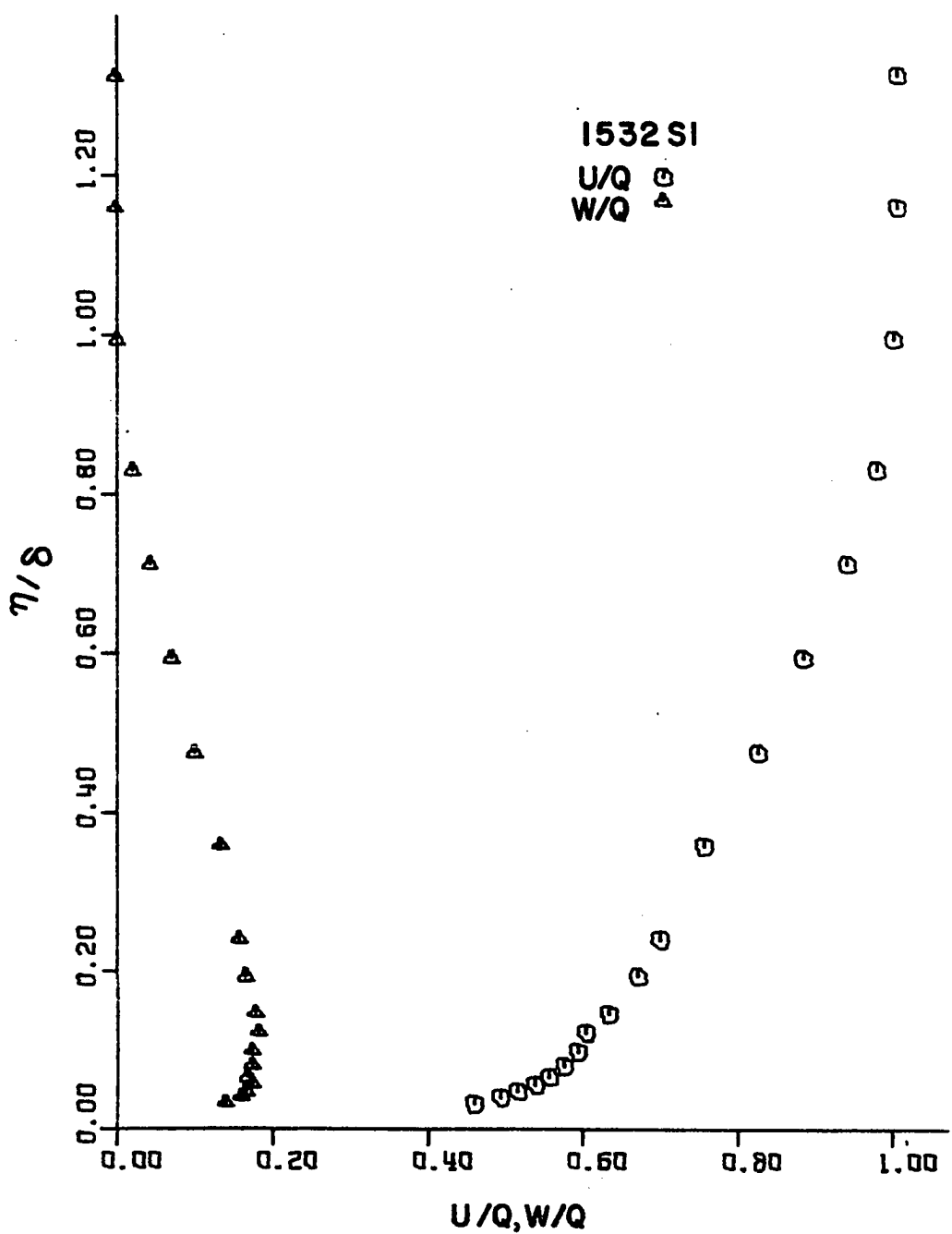


Figure 22. Velocity profiles on the diffuser end wall

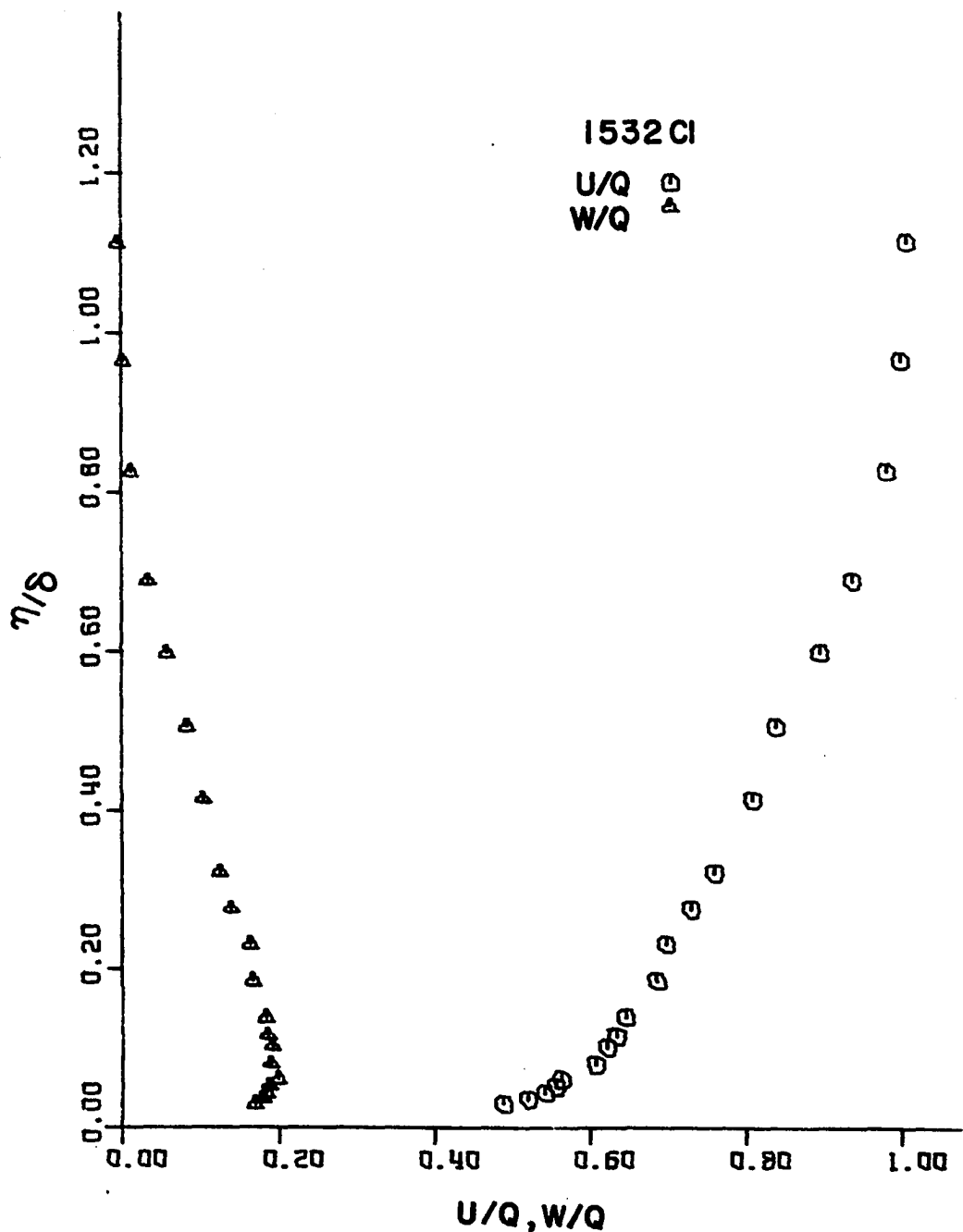


Figure 23. Velocity profiles on the diffuser end wall

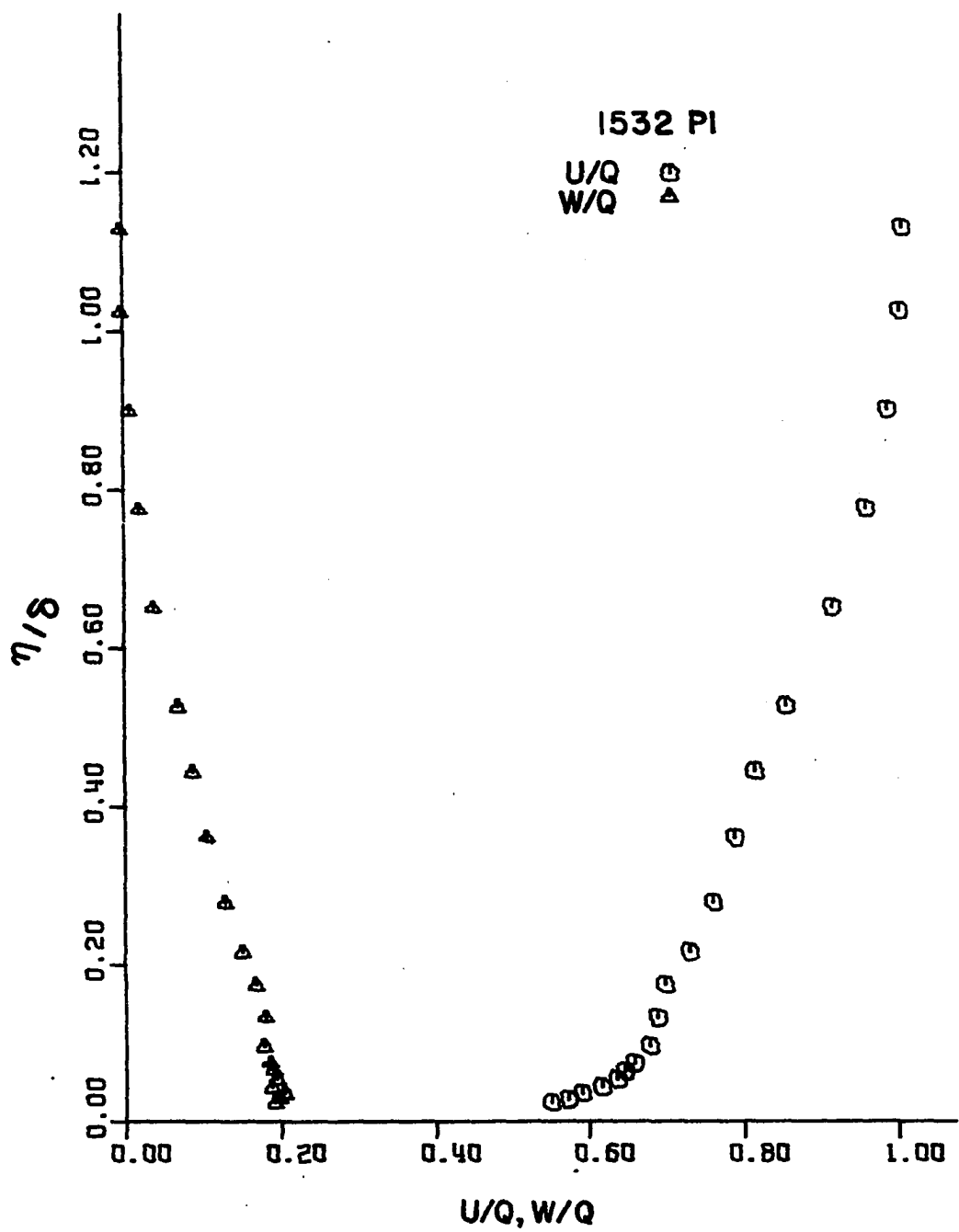


Figure 24. Velocity profiles on the diffuser end wall

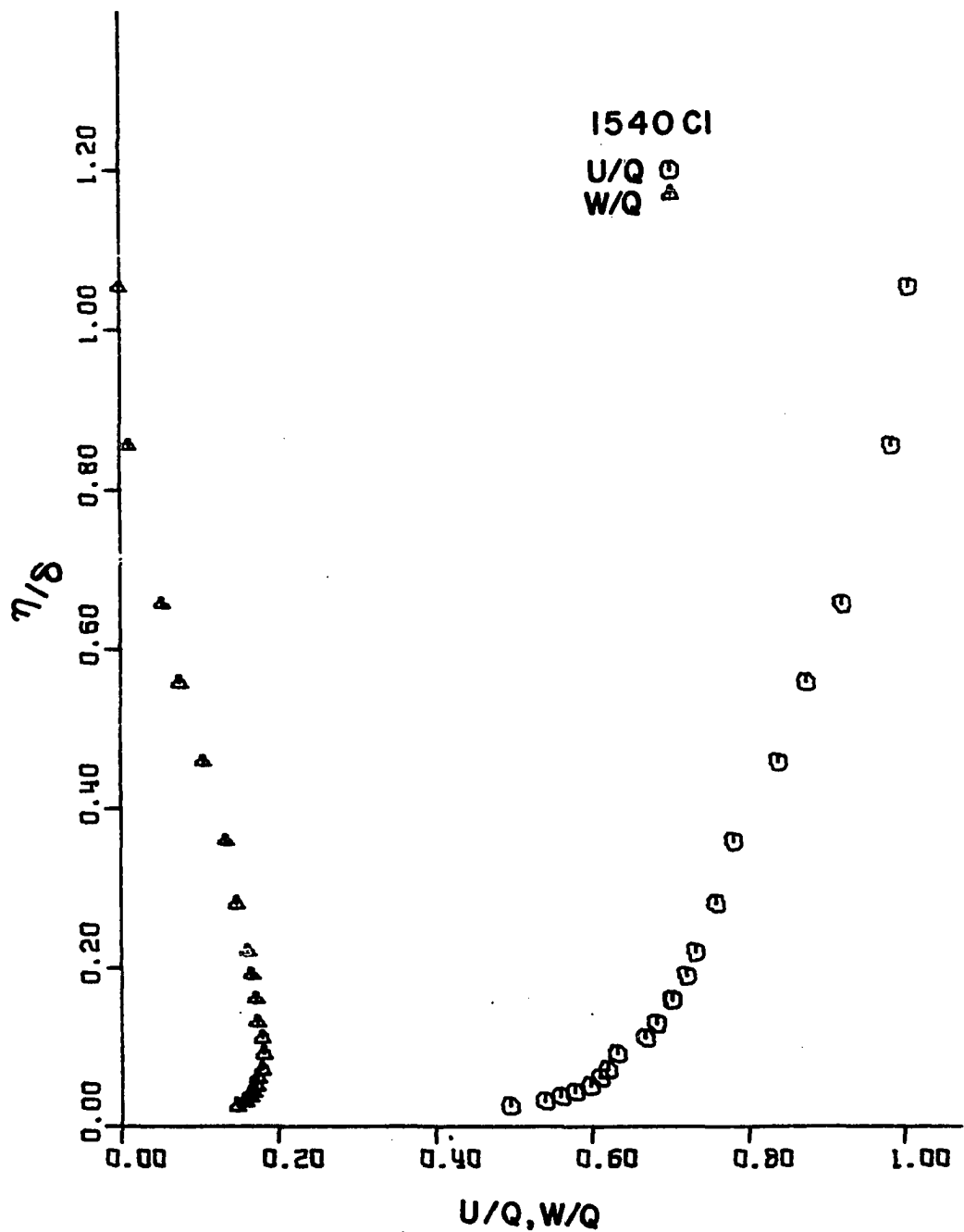


Figure 25. Velocity profiles on the diffuser end wall

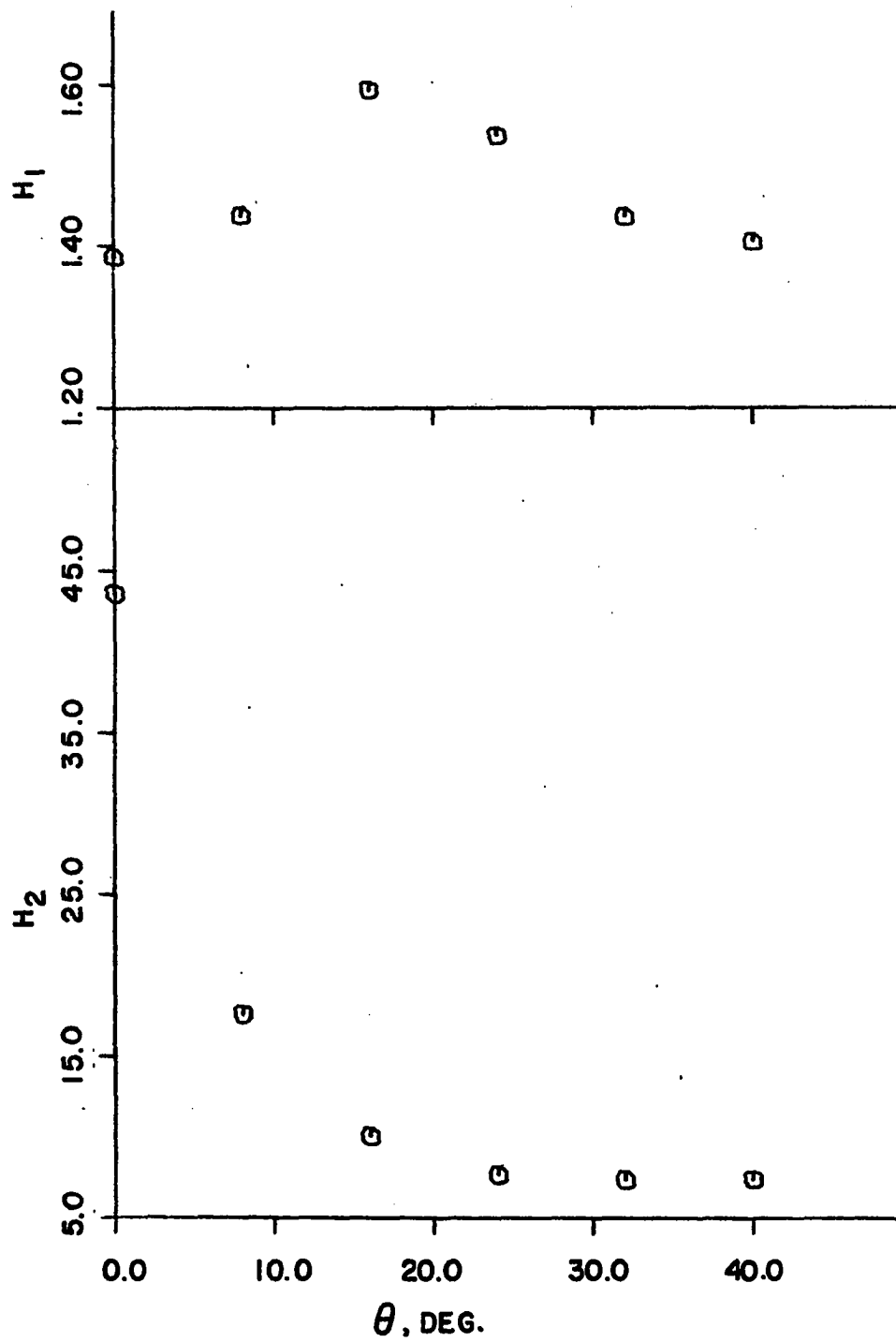


Figure 26. Diffuser end wall centerline shape factor distribution

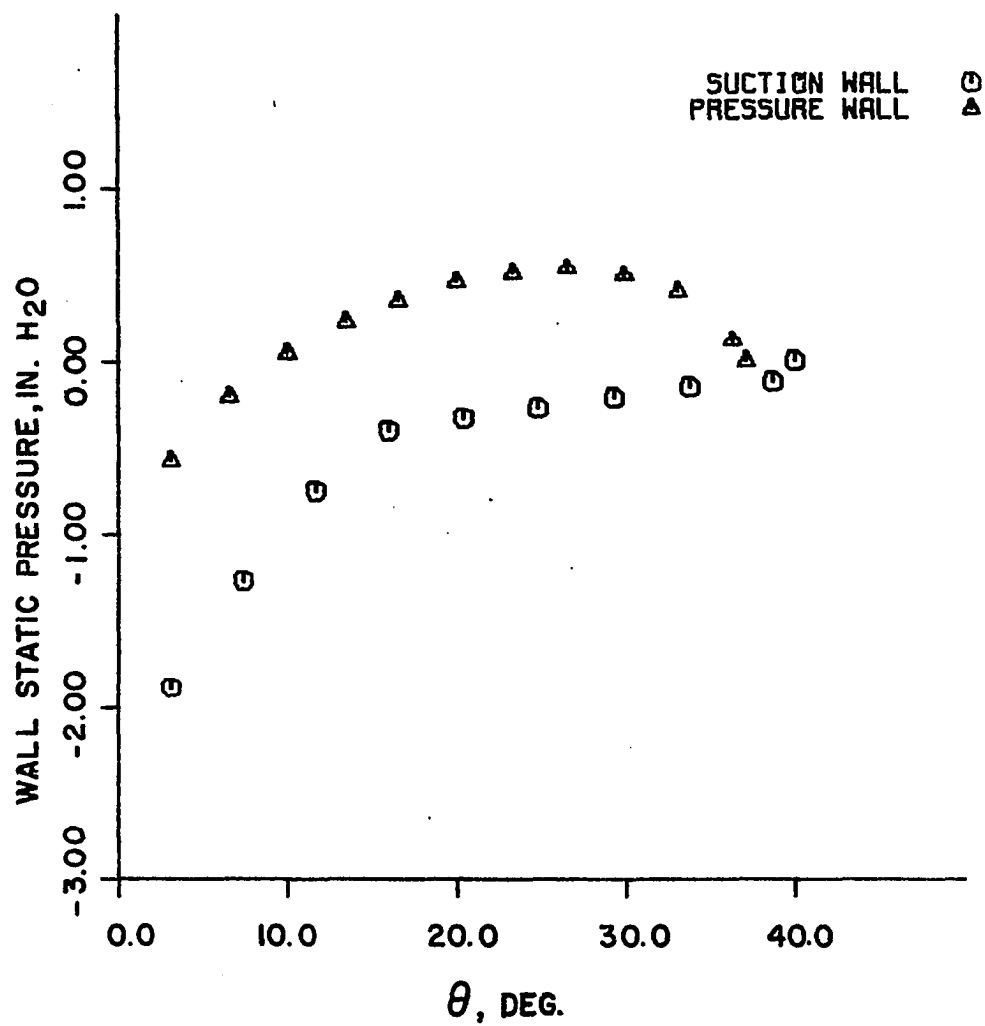


Figure 27. Diffuser side wall pressure distributions

from the pressure distribution. The streamwise shape factor distribution in a straight diffuser is continually increasing contrary to the distribution shown in Figure 26. Possibly it could be explained because of the type of pressure distribution previously discussed.

Crossflow velocity profiles developing along the end wall centerline showed a continual increase in magnitude up to the thirty-two degree station. The rate of increase was greatest near the wall. From the thirty-two degree station to the forty-degree station the crossflow velocity decreased slightly near the wall but increased in regions farther from the wall.

Streamwise profile variations across the diffuser do not show any consistent trends. Crossflow profile distributions across the diffuser at sixteen and thirty-two degrees indicate similar trends. The profiles became increasingly flatter in the maximum crossflow region from the pressure wall profile to the suction wall profile.

Polar velocity plots are fairly reliable representations of velocity distribution in a skewed boundary layer since they depend on the distance from the wall only through the definition of the velocity at the edge of the boundary layer. Errors should be small in determining that particular value even though boundary layer thickness is subject to considerable error. Figures 28, 29 and 30 are polar plots showing the velocity variation across the diffuser. Considerable variation across the diffuser does not occur, at least for the extent of the passage that was surveyed. Polar plot variations across the duct at turning angles of sixteen and thirty-two degrees show an increasingly flatter portion in the profiles

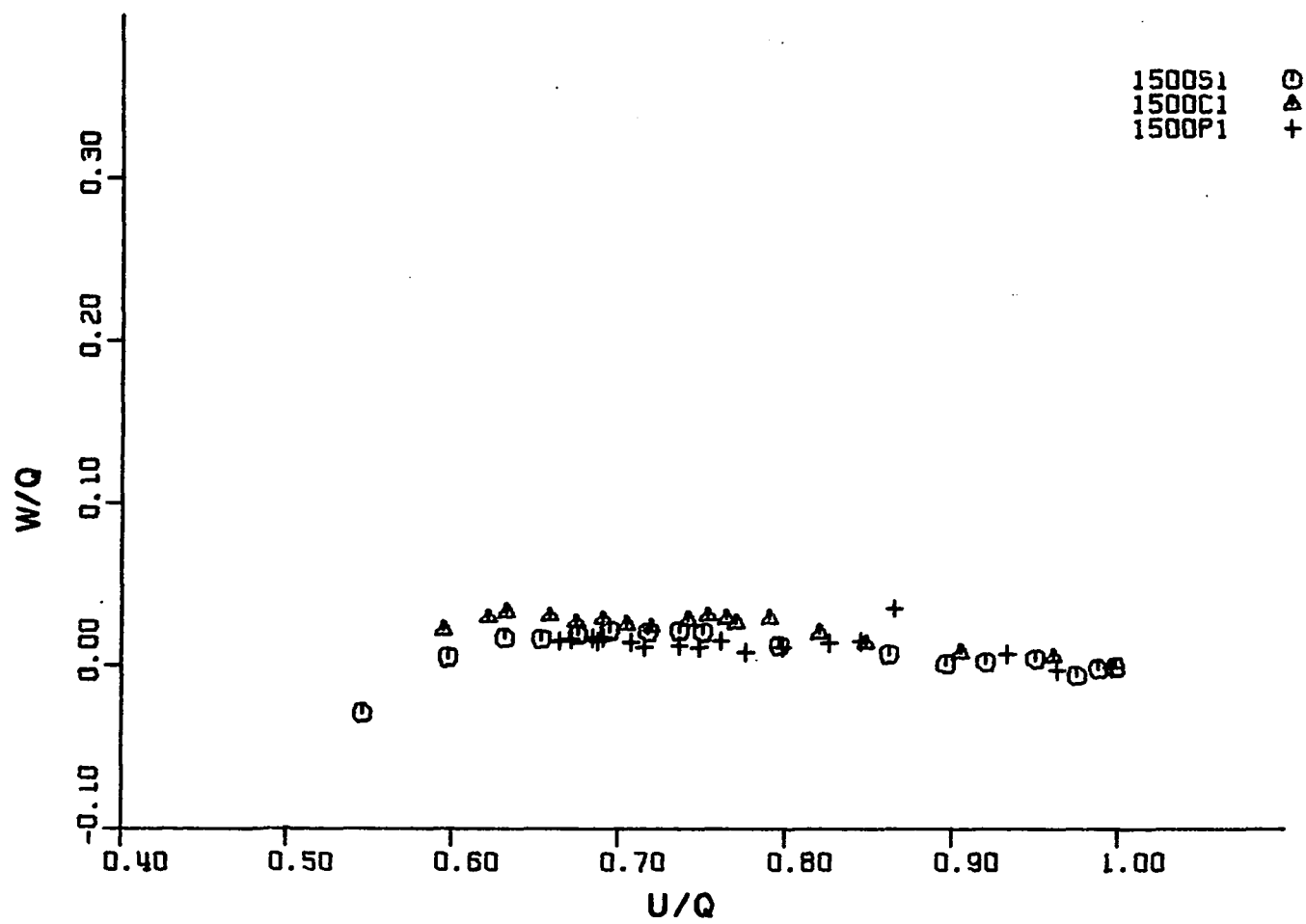


Figure 28. Diffuser velocity polar plot

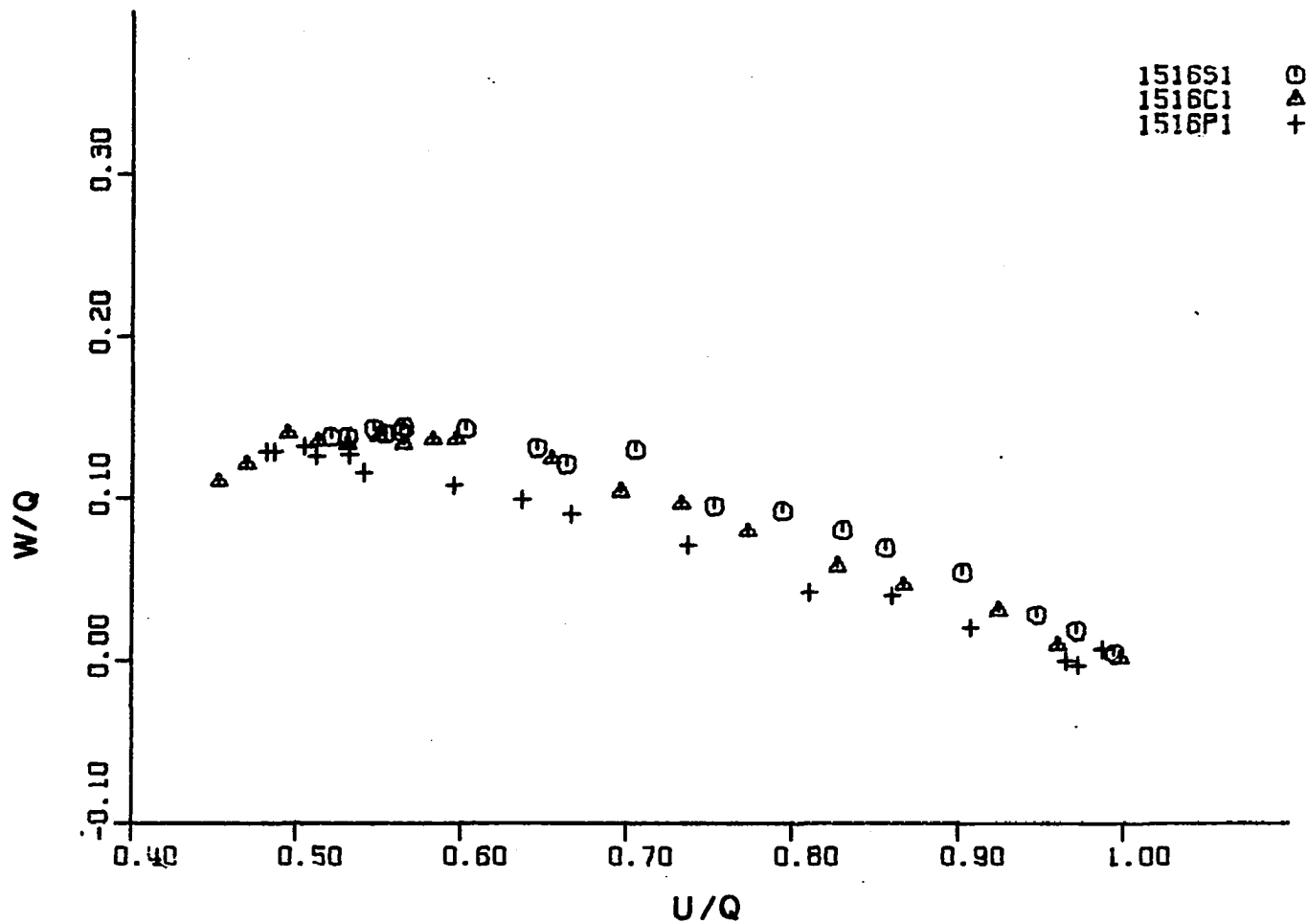


Figure 29. Diffuser velocity polar plot

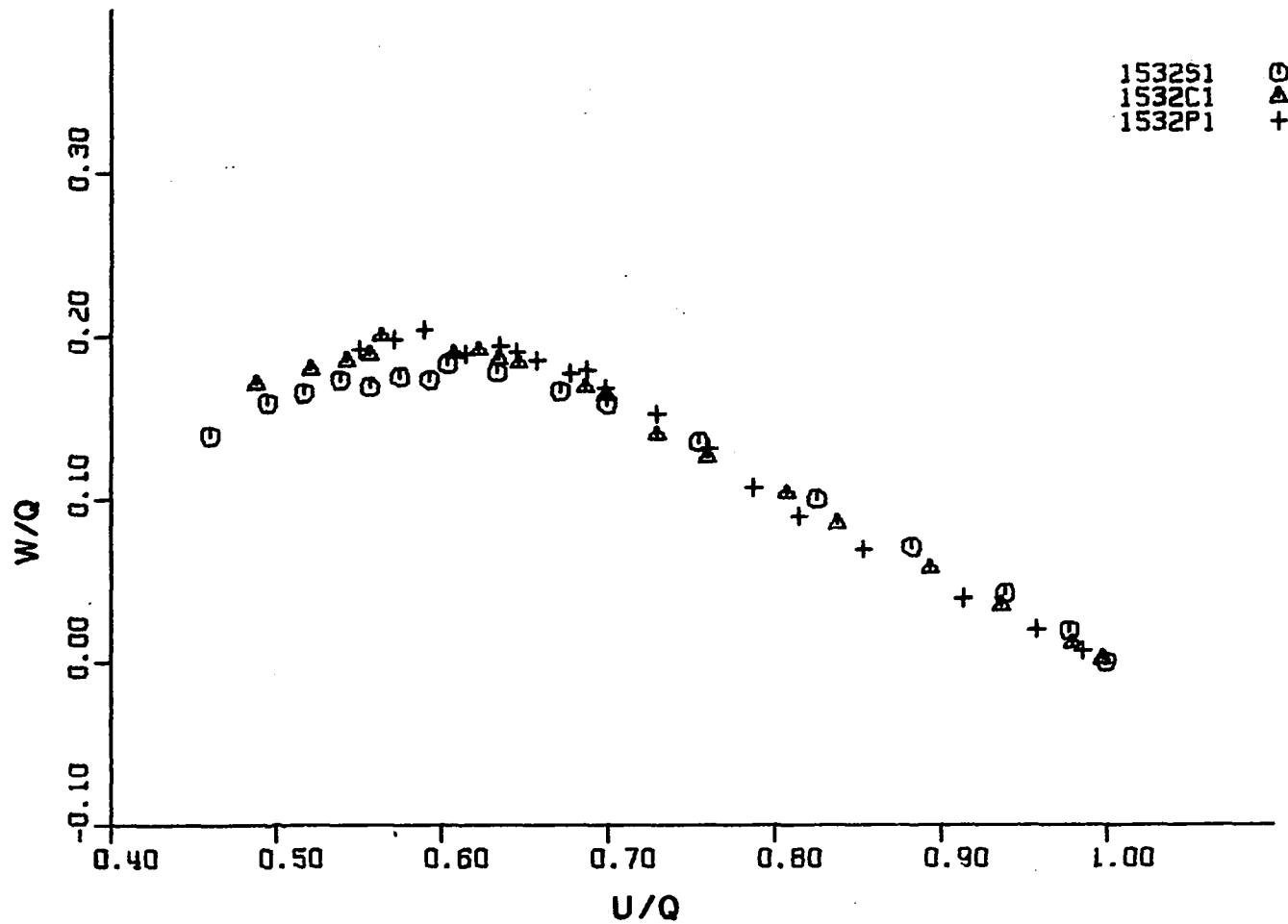


Figure 30. Diffuser velocity polar plot

in the region of maximum crossflow as the suction wall is approached. This same trend was observed for the data Francis (24) published. One set of his profiles is shown in Figure 45. Figure 31 shows the variation of velocity along the end wall centerline from the diffuser throat to the forty degree station. These profiles exhibit relatively straight portions near the edge of the boundary layer and the angles between these and the abscissa of the plot increased as centerline turning angle increased. As was reported by Francis (24), a flat portion in the region of maximum crossflow is evident. Because of the small boundary layer thickness, it was difficult to measure any extent of the collateral region often found near the wall.

Boundary layer thickness, as reported in the Literature Review, is influenced by the pressure gradient and the wall shear stress. Figure 32 shows the distribution of boundary layer thickness along the end wall centerline of the diffuser. A nearly linear distribution results.

Compiled Three-Dimensional Boundary Layer Data

A single set of data is difficult to analyze. A systematically controlled variation in geometrical and fluid flow parameters to determine various interactions would be the ideal approach but would require an extremely long period of study. In lieu of that, data from other sources was used in this case for comparative purposes. Three other sets of data appeared to be the most suitable. Two of these sets were produced by Francis (24) and the other by Pierce and Klinksiek (59). The reasons for choosing these sets were that the test sections used had the

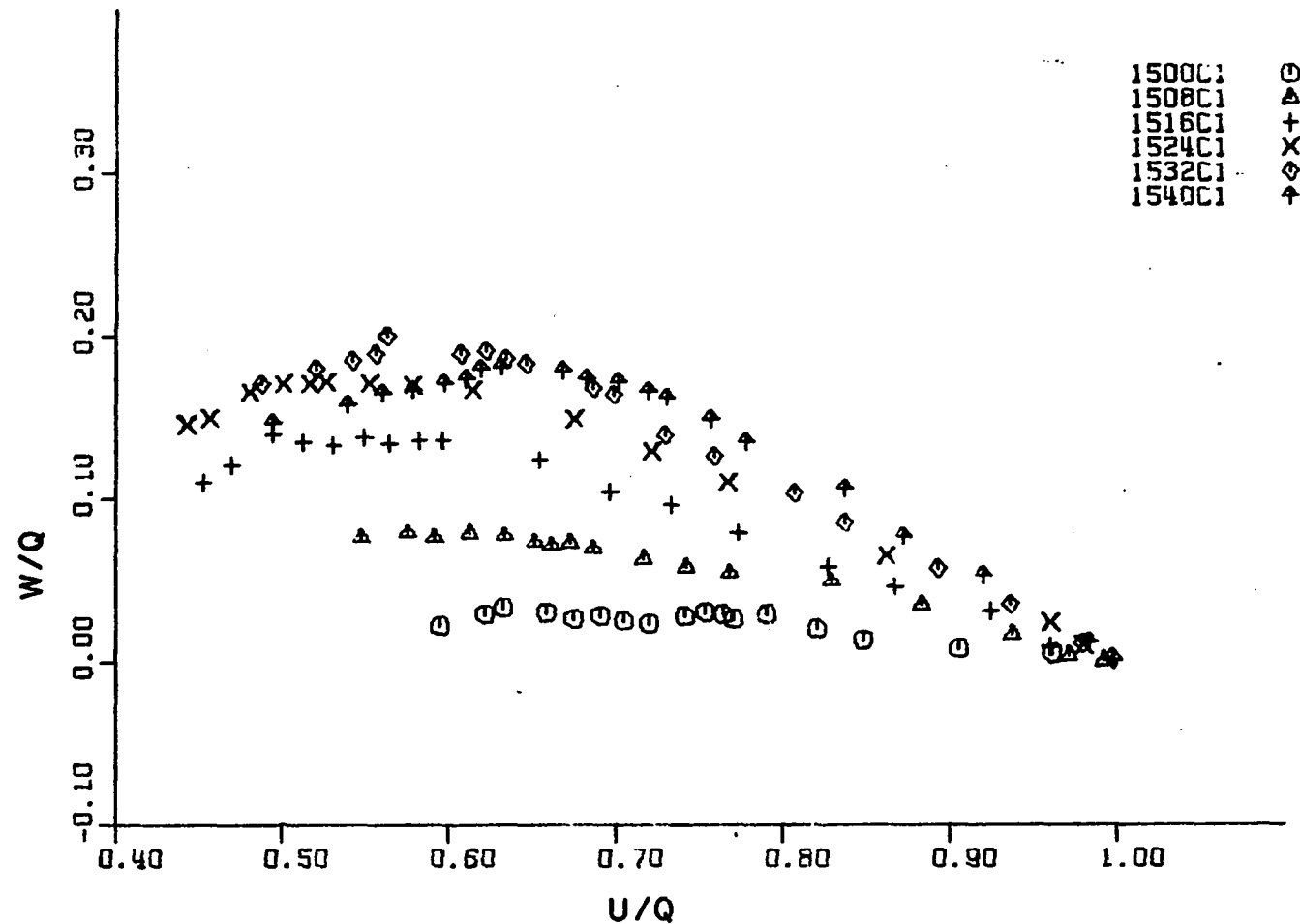


Figure 31. Diffuser velocity polar plot

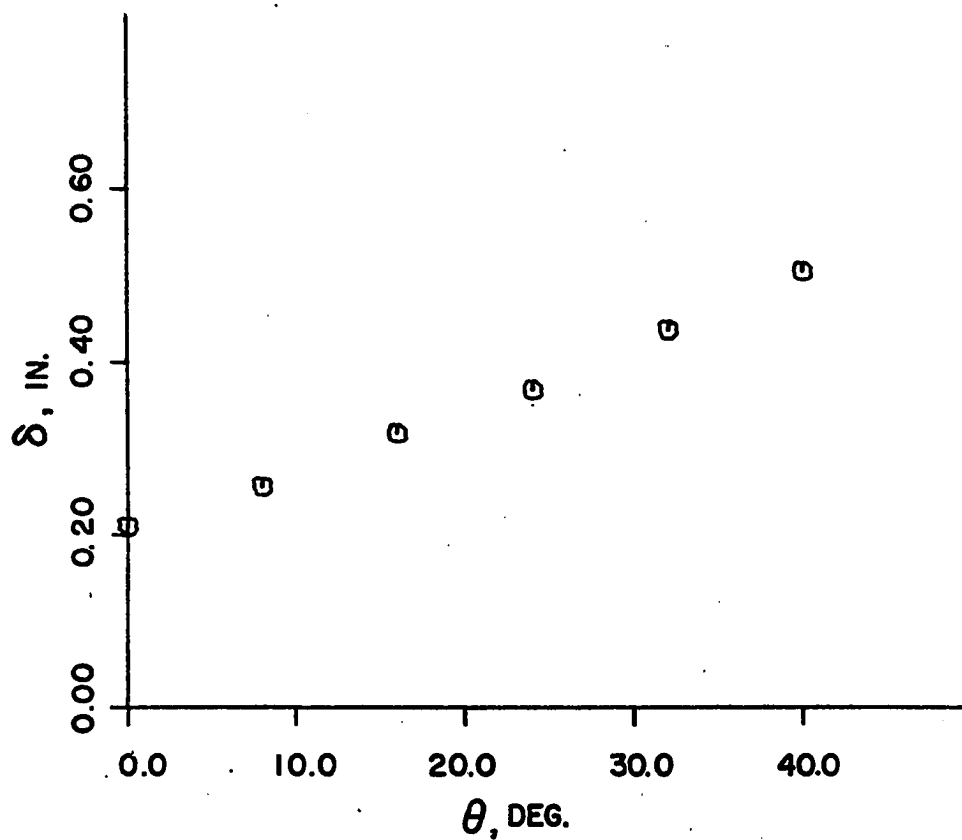


Figure 32. Diffuser end wall centerline boundary layer thickness development

same aspect ratio as the inlet aspect ratio for the present set of data and all had circular arc centerlines. The designation of the data is as follows:

RRXXZZ = profile number

RR = centerline radius of curvature

XX = centerline turning angle

ZZ = investigator

ZZ = 01 → Francis

ZZ = 02 → Pierce and Klinksiek.

The diffuser data designation was previously described for the results of this dissertation.

Table 8 summarizes some of the basic variables for the three test arrangements. Figures 69 and 70 in APPENDIX F are schematic diagrams of the test apparatus involved. Data used in the comparison are also tabulated in APPENDIX F.

As reported in the Literature Review, the most common method used for calculating skewed boundary layer growth is by use of the momentum integral equations. In view of this, various shape factors are presented and discussed. Other parameters are presented in an attempt to show some basic flow behavioral patterns.

When the boundary layer equations are put into integral form, one of the resulting dependent variables is the streamwise momentum thickness which was defined in the parameter calculation subsection. In Figure 33 this parameter is plotted against, θ/θ_{\max} , the ratio of the local centerline turning angle to the maximum centerline turning angle involved in

Table 8. Comparison of experimental geometric and flow variables

Test section configuration	Throat $U/u_{Ft=1}$	Throat δ in.	Throat $\sqrt{u'^2/Q}$ %	Type of air supply	Contraction Ratio	Length from contraction exit to throat in.	Throat cross-section area in. ²	Aspect ratio H/W	Area ratio A_E/A_t
55XX01 60 degree rectangular bend with a 55 inch centerline radius	10.7×10^5	0.63	0.16	Suction	10 to 1 in 13 inches	48.0	150.0	1.5	1.0
25XX01 60 degree rectangular bend with a 25 inch centerline radius	10.7×10^5	0.62	0.16	Suction	10 to 1 in 13 inches	48.0	150.0	1.5	1.0
25XX02 60 degree rectangular bend with a 25 inch centerline radius	5.5×10^5	2.79	----	Suction	9 to 1 in 18 inches	78.7	150.0	1.5	1.0
S 15XXC1 40 degree P rectangular diffusing bend with a 15 inch centerline radius	7.2×10^5	0.21	0.44	Blowing	19.65 to 1 in 36 inches	29.2	16.66	1.5	1.56

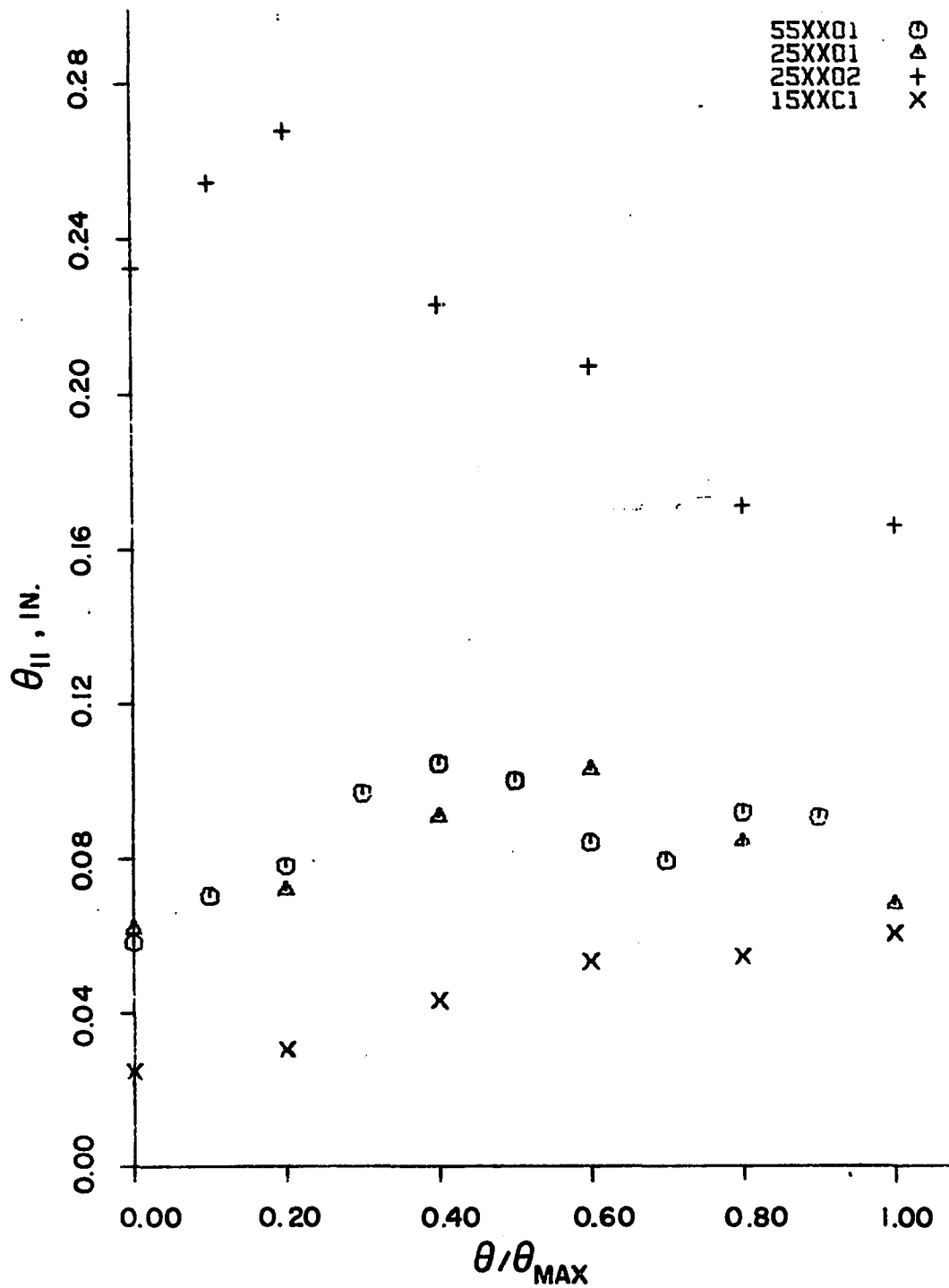


Figure 33. Momentum thickness distribution

the particular test. This ratio is essentially the ratio of the distance over which the boundary layer was formed from the beginning of turning to the termination of the centerline turning angle. It is seen that a large variation of momentum thickness exists between the four sets of data. Each set of data shows an initial increase in momentum thickness and subsequently a decrease except for the diffuser data which continually increases. Data set 55XX01 shows two maximums, contrary to the others. One hypothesis which might explain this phenomenon is that development of the boundary layer occurred over a considerably longer distance for the same centerline turning angle. This greater development distance would allow the limiting streamtube from the pressure side wall to impinge on the suction side wall, roll up into a vortex and spread over a large portion of the duct before the duct turning terminated. The vortex would induce a different crossflow distribution and because of continuity the streamwise velocity distribution near the wall would change, thereby causing a variation in the momentum thickness value. The other configurations would probably result in a vortex roll-up but the distance from the point of impingement on the suction wall to the end of the curved section would be insufficient to allow interaction between the spreading vortex and the centerline boundary layer. An experimental study would be required to determine the validity of this hypothesis.

A parameter which is used in two-dimensional boundary layer study to indicate the proximity of separation is the streamwise shape factor, H_1 . A value of 1.8 is considered to indicate separation. Streamwise shape factor is presented in Figure 34 as a function of the normalized

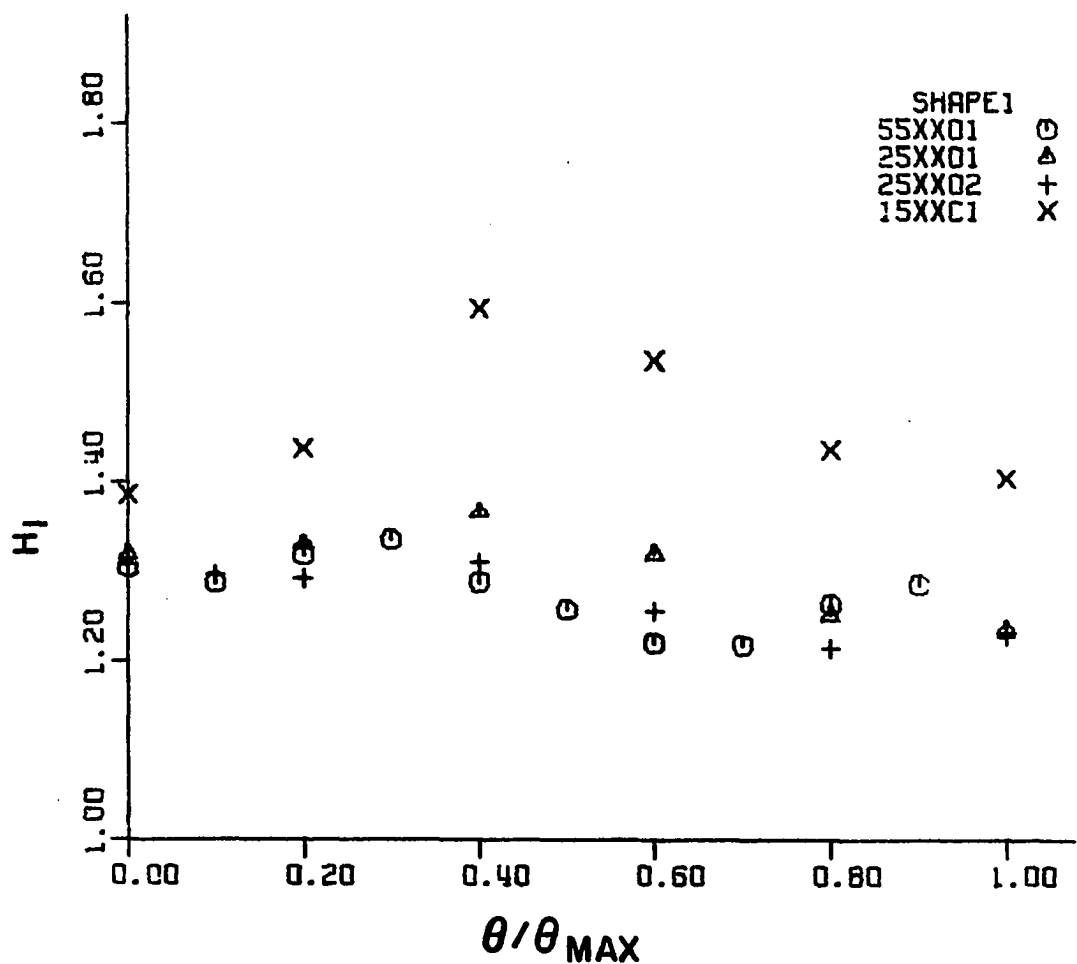


Figure 34. Streamwise shape factor development

centerline turning angle. Again the relatively short test sections showed one distinct maximum value whereas the 55XX01 distribution had two distinct peaks. Even though there was a large variation in the streamwise momentum thickness, the shape factors are in a much tighter band except for the diffuser data where a higher shape factor would be expected.

In Figure 35, the crossflow shape factor distribution appears to be definitely influenced by the geometrical shape of the test section. Except for the initial values of the shape factor at the beginning of curvature, tests 25XX01 and 25XX02 are almost identical in distribution. If Table 8 is consulted, it is seen that Reynolds number between the two tests are different by a factor of almost two and boundary layer thickness differs by greater than a factor of four. The geometrical shape of the test section walls was the only point of similarity between the two tests. Crossflow pressure distributions are primarily dictated by the confining passage and pressure is normally the primary skewing driving potential. The diffuser shape factor distribution is somewhat similar in shape but of different magnitude. Although pressure was the primary skewing driving potential, the shape factor data of test 55XX01 indicates other influences are to be considered such as influence from the corner vortex.

Even though boundary layer thickness did not appear to affect the crossflow shape factor, it does have an influence on the momentum thicknesses and the skewing angles. A thick boundary layer appears to affect

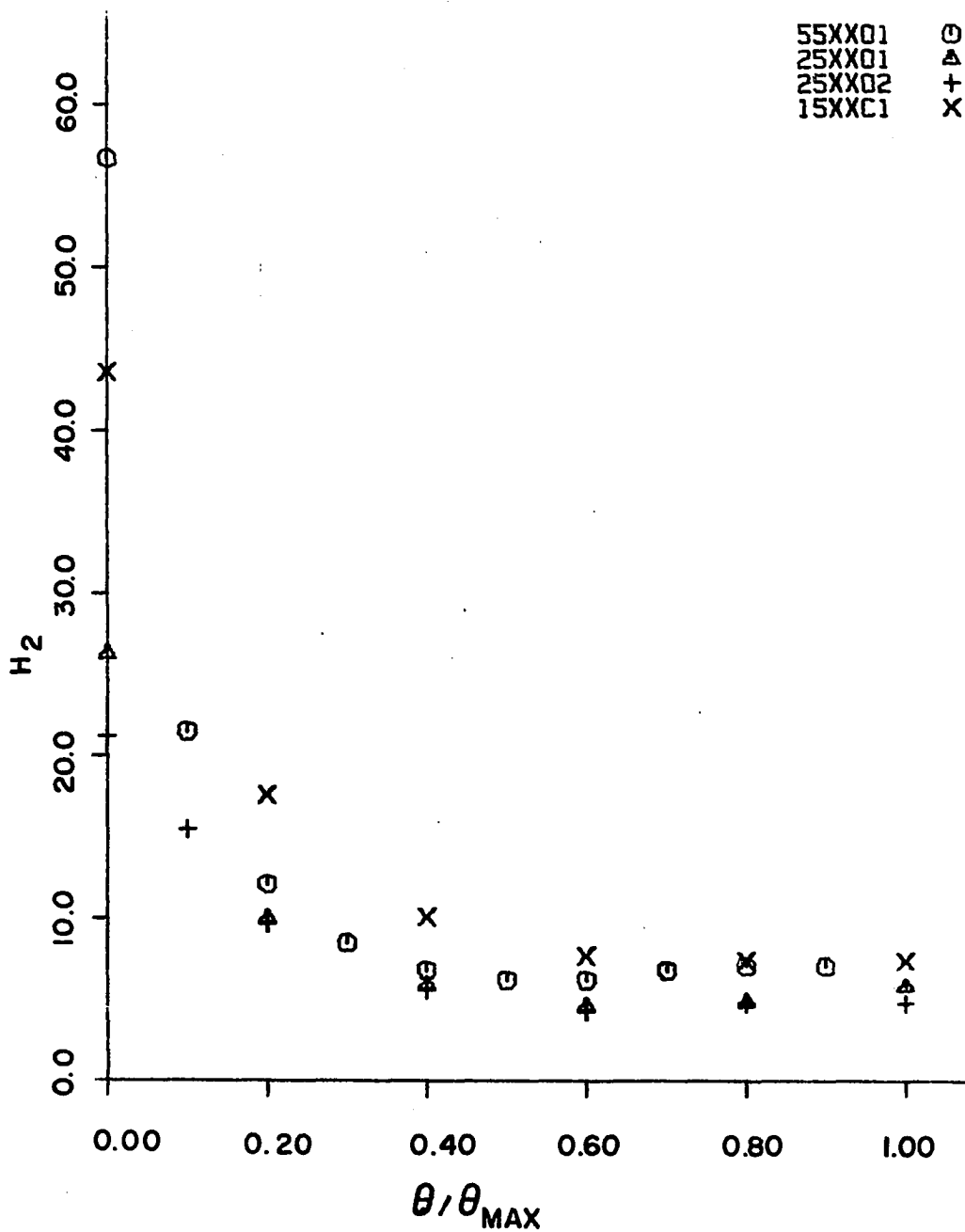


Figure 35. Crossflow shape factor development

the momentum thickness directly as indicated by the following equations:

$$\theta_{11} = \frac{1}{Q^2} \int_0^\delta (U-u) u d\eta = \text{streamwise momentum thickness for an incompressible fluid}$$

$Q = U$ for an intrinsic coordinate system.

Let

$$\Gamma = \eta/\delta$$

$$d\Gamma = \frac{d\eta}{\delta}$$

therefore

$$\theta_{11} = \delta \int_0^1 \left(1 - \frac{u}{Q}\right) \frac{u}{Q} d(\eta/\delta) . \quad (13)$$

Boundary layers having exactly similar streamwise velocity profiles would have a momentum thickness directly proportional to the boundary layer thickness. Since skewing angles are hypothesized to be directly dependent on the local momentum of the fluid, then the more the momentum deficit the greater the skewing angle. Momentum thickness is an indication of the momentum deficit in a boundary layer. The greater the momentum deficit the higher the momentum thickness value which implies thick boundary layers would result in higher skewing angles. A comparison of Figures 36 and 37 support this hypothesis, but skewing angle is not a function of boundary layer thickness alone as is discussed later. Figure 36 shows the distribution of the boundary layer thickness along each test section end wall centerline. Because the boundary layer development distances in the test sections were different for each test, except for 25XX01 and 25XX02, then a comparison of magnitude changes are inconsequential but the trends are significant. Test 25XX02 had a different

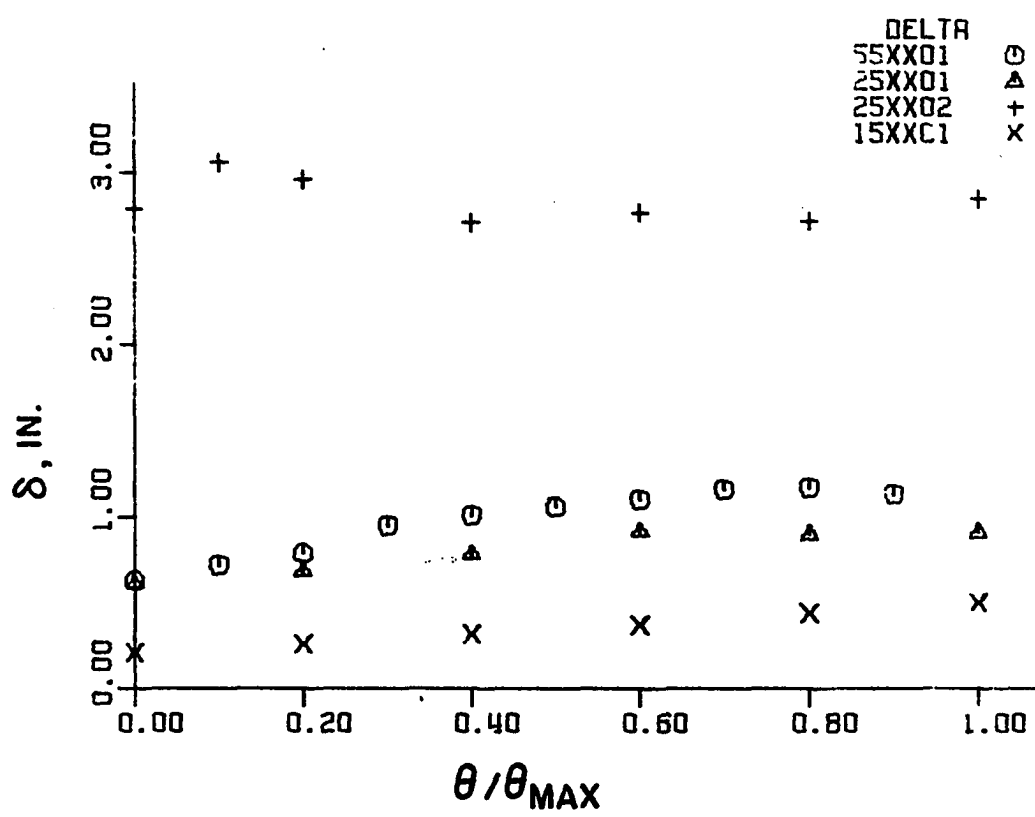


Figure 36. Boundary layer thickness variation along the end-wall centerline

distribution from the other tests in that boundary layer thickness decayed after an initial increase near the beginning of the curve. Since this test had a thick boundary layer then possibly the large amount of skewing decreased the boundary layer thickness faster than free stream air could be entrained to increase the thickness.

Other factors besides the previously mentioned ones influence the magnitude of the skewing angle in the boundary layer. An important one is the radius of curvature of the free stream streamline. Equation 5 reduces to

$$-\frac{\bar{u}^2}{h_1 h_3} \frac{\partial h_1}{\partial \xi} = -\frac{1}{\rho h_3} \frac{\partial \bar{P}}{\partial \xi}$$

if viscosity is neglected and an intrinsic coordinate system is used.

The term

$$-\frac{1}{h_1 h_3} \frac{\partial h_1}{\partial \xi}$$

is the reciprocal of the radius of curvature of the streamline in the plane of the surface over which the boundary layer forms. The equation indicates that for the same velocity, the pressure gradient would increase for a decreasing radius of curvature. A higher pressure gradient would result in greater skewing angles. Figure 37 shows the distribution of the skewing angle of the limiting streamline along the duct centerline. The difference between 55XX01 and 25XX01 is an indication of the radius of curvature effect and the difference between 25XX01 and 25XX02 indicates the boundary layer thickness effect. The diffuser centerline has a small radius of curvature, but also a small boundary layer thickness which has a compensating effect. If the skewing angles were plotted against the

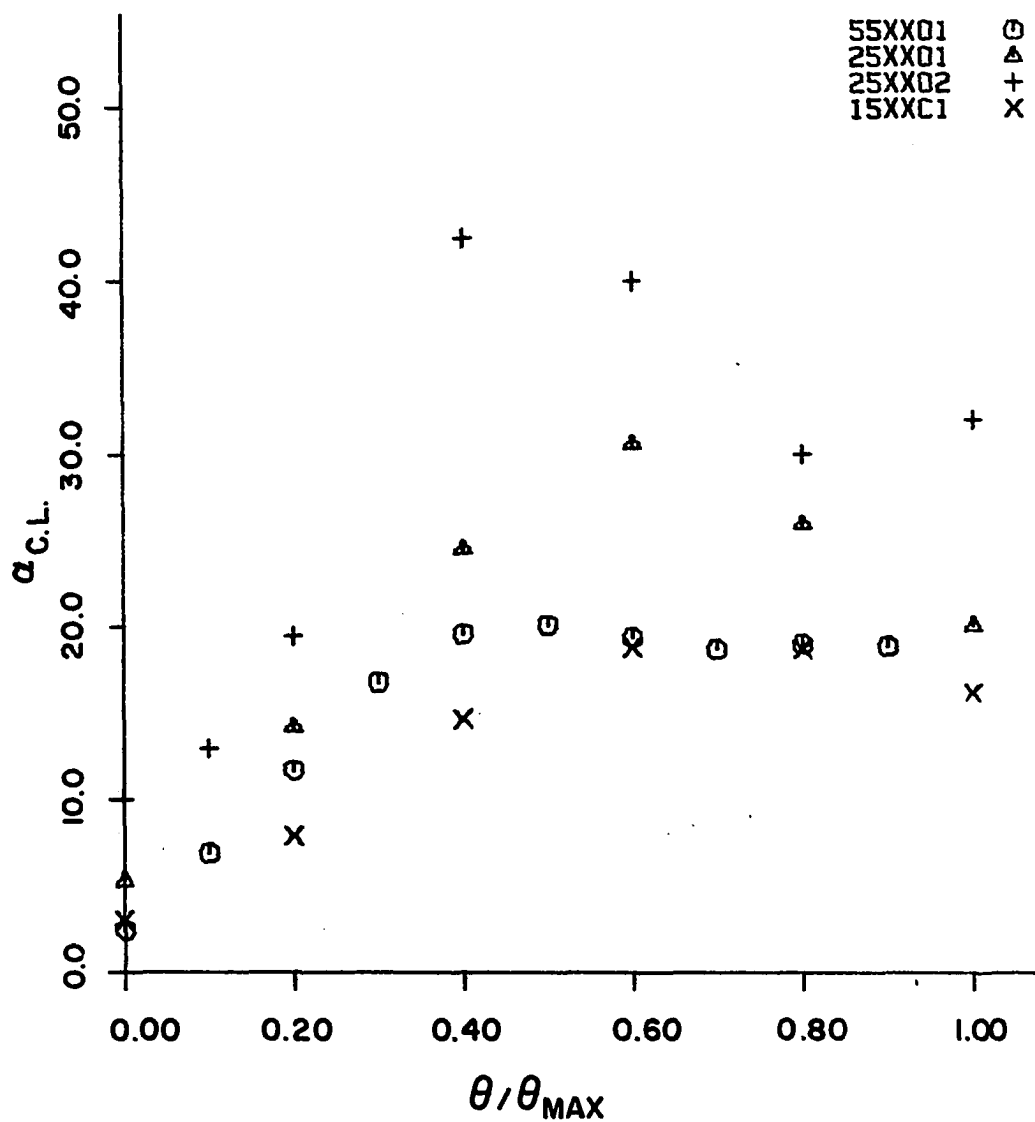


Figure 37. Collateral layer skewing angle distribution

distance along the centerlines, the maximum diffuser skewing angle would effectively coincide with θ/θ_{\max} of 0.25 for the 25XX01 and 25XX02 tests.

On this basis the rate of change of the diffuser skewing angle would be comparable to the 25XX02 case, which possibly indicates the effect of the adverse streamwise pressure gradient.

As mentioned earlier, the boundary layer thickness and momentum thickness both were important in determining the behavior of the skewing action. A combination of these two terms might produce a valid shape factor. In reference to Equation 13, it appears logical to divide the momentum thickness by the boundary layer thickness to obtain a trial parameter. The resulting ratio would indicate the deviation from similar profiles during development, or in other words the ratio would be constant if similar profiles existed. Also, this parameter might replace the momentum thickness as a dependent variable in the momentum integral equations by integrating between the limits of 0 to 1 with n/δ being the independent variable. Streamwise momentum thickness divided by the boundary layer thickness is plotted against the normalized centerline turning angle in Figure 38 which indicates that a distribution trend is established for the relatively short test sections but a double peak occurs in the 55XX01 case.

In an attempt to gain information about some mechanisms in skewed turbulent boundary layers, some velocity polar plots showing the development of reversed skewing were examined. These data were obtained by Pierce and Klinksiek (59) in the downstream curved section from configuration 25XX02 and is shown in Figure 70. A definite trend in the skewing

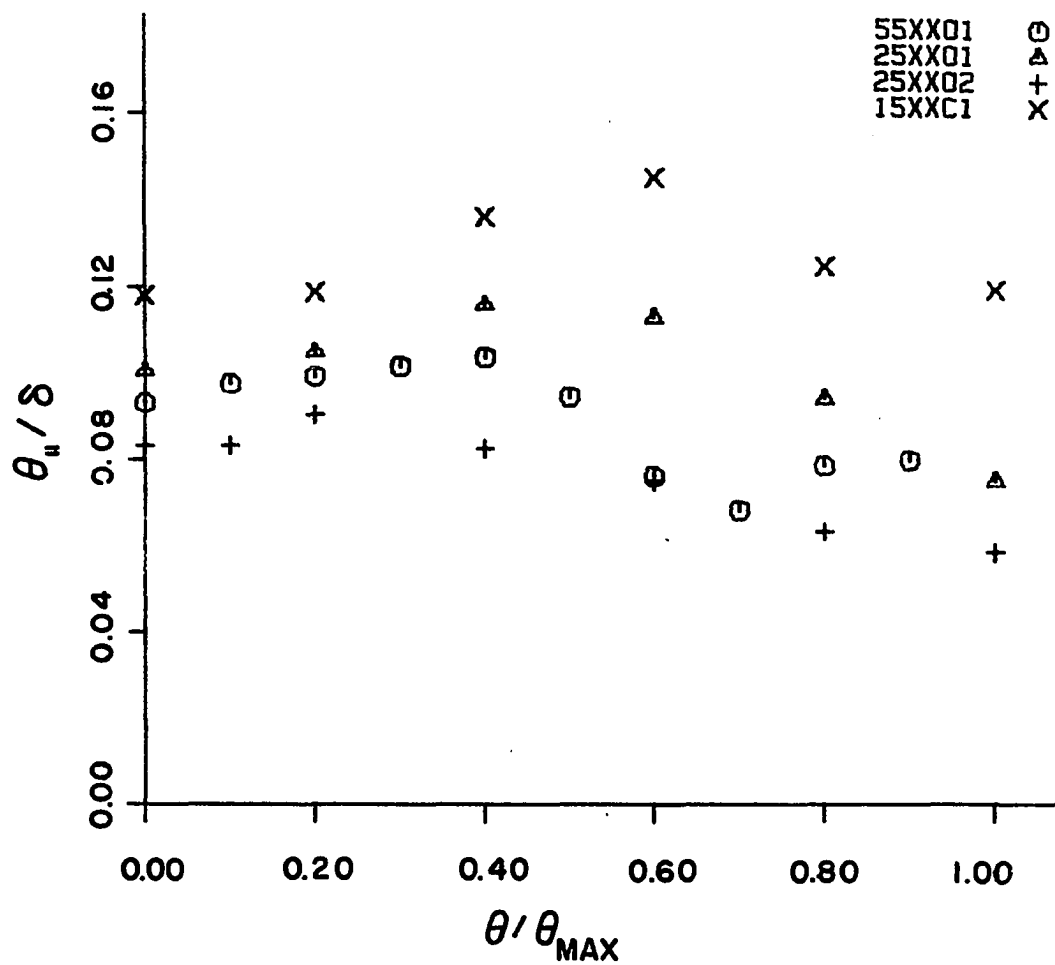


Figure 38. Combined momentum thickness-boundary layer thickness parameter

propagation appeared which prompted a similar investigation in single skewed profiles. A discussion of the double skewing propagation trend is presented in a subsequent subsection. In essence, normalized streamwise velocity and normalized crossflow velocity appeared to have a linear variation with respect to the turning angle. A search for a readily recognizable point which showed the propagation of the single skewed profiles was made. The point at the edge of the wall collateral layer was the most consistent, although in some cases it was difficult to distinguish. The streamwise velocity ratio at the edge of the collateral layer is designated as $(u/Q)_{C.L.}$ and that for the crossflow as $(w/Q)_{C.L.}$. By inspecting Figures 39 through 42 and comparing the variation of $(u/Q)_{C.L.}$ with the streamwise shape factor it is seen that for the respective tests the trends of the two parameters are inverse to each other. Possibly the collateral layer near the wall governs the shape of the entire boundary layer. In recalling some of the discussion in the Literature Review it seems plausible that the inner layers could play an active part in the structure of the outer regions. A value of y^+ would be informative as to the region in which the collateral layer edge was located. Unfortunately as reported by Pierce and Krommenhoek (60) values of the wall shear stress predicted by various two-dimensional methods could be in error by 15 percent or more when applying them to three-dimensional boundary layers. Since y^+ values depend on the wall shear stress then unreliable results would occur. Also it is not known whether the two-dimensional criteria for boundary layer region designation would be valid for three-dimensional boundary layers. In place of y^+ values,

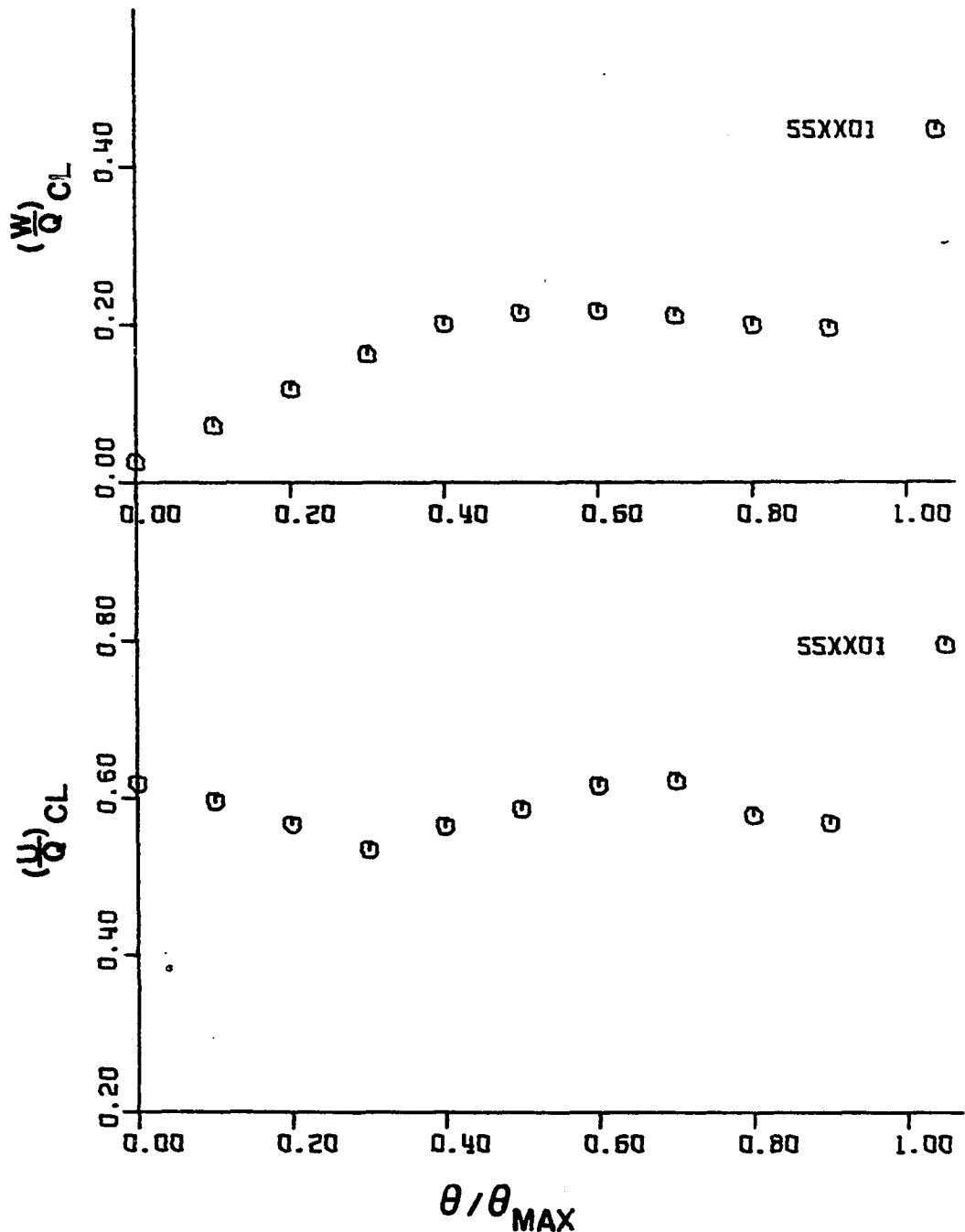


Figure 39. Velocity ratio variation at the edge of the wall collateral layer along the end wall duct centerline

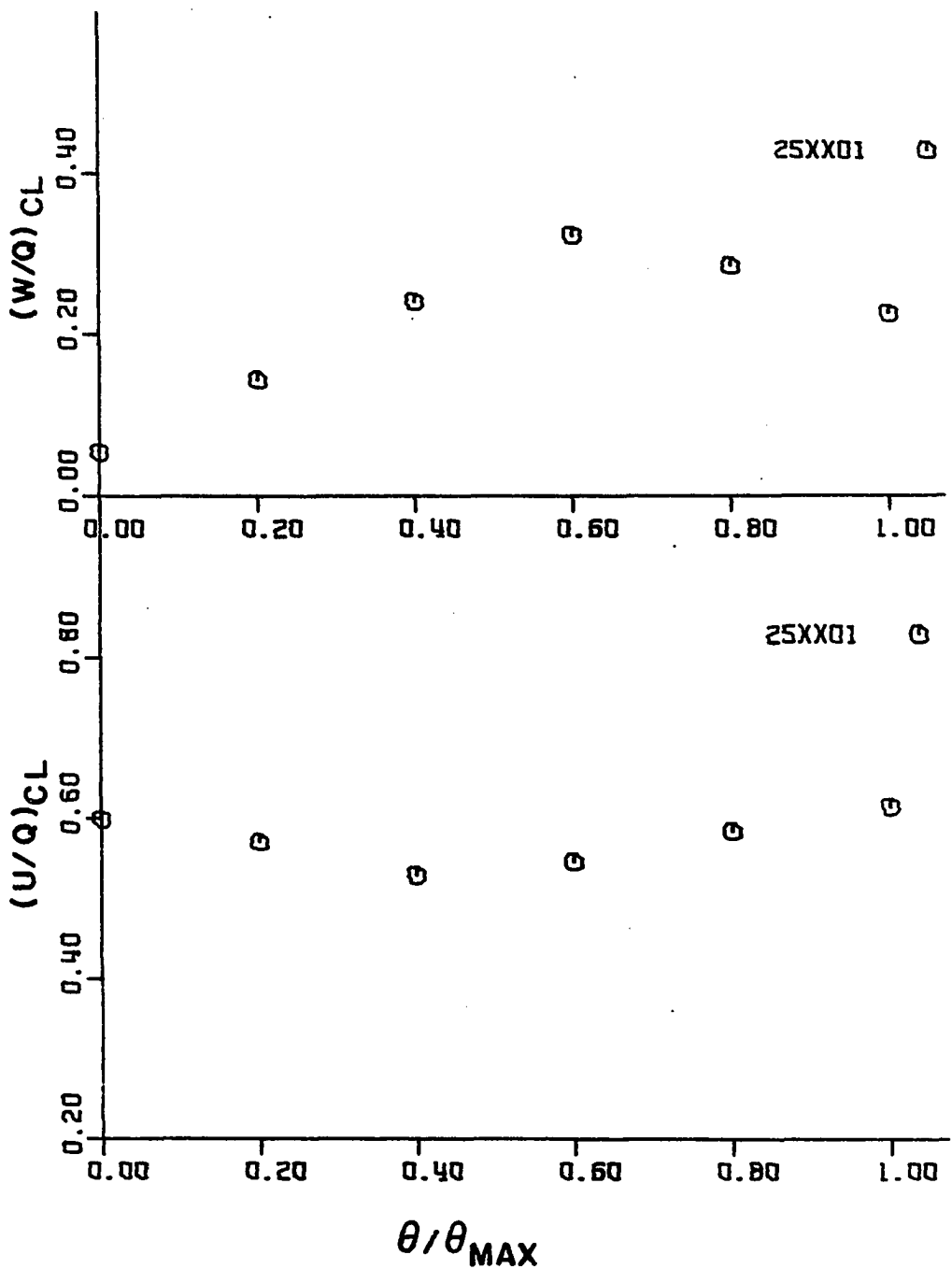


Figure 40. Velocity ratio variation at the edge of the wall collateral layer along the end wall duct centerline

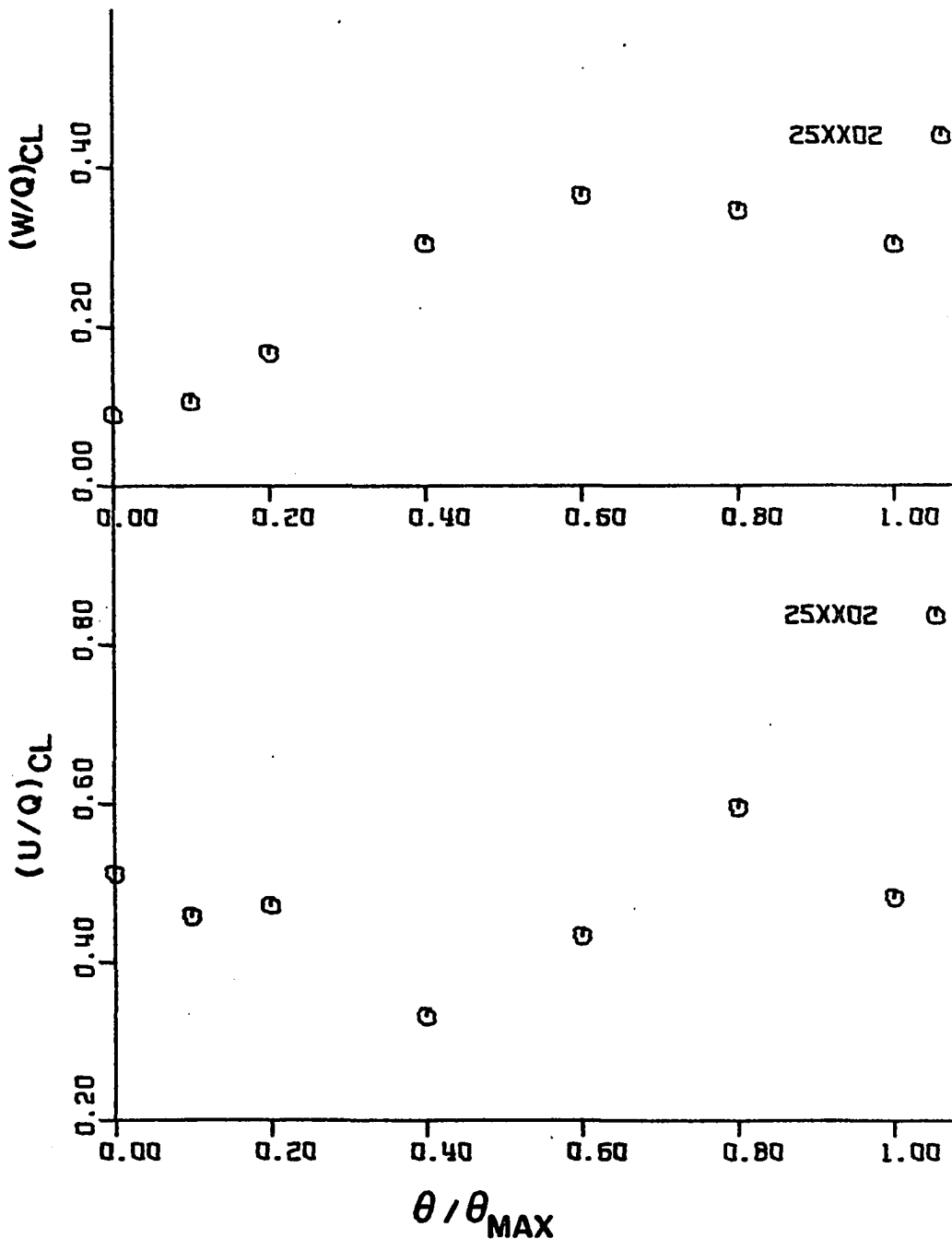


Figure 41. Velocity ratio variation at the edge of the wall collateral layer along the end wall duct centerline

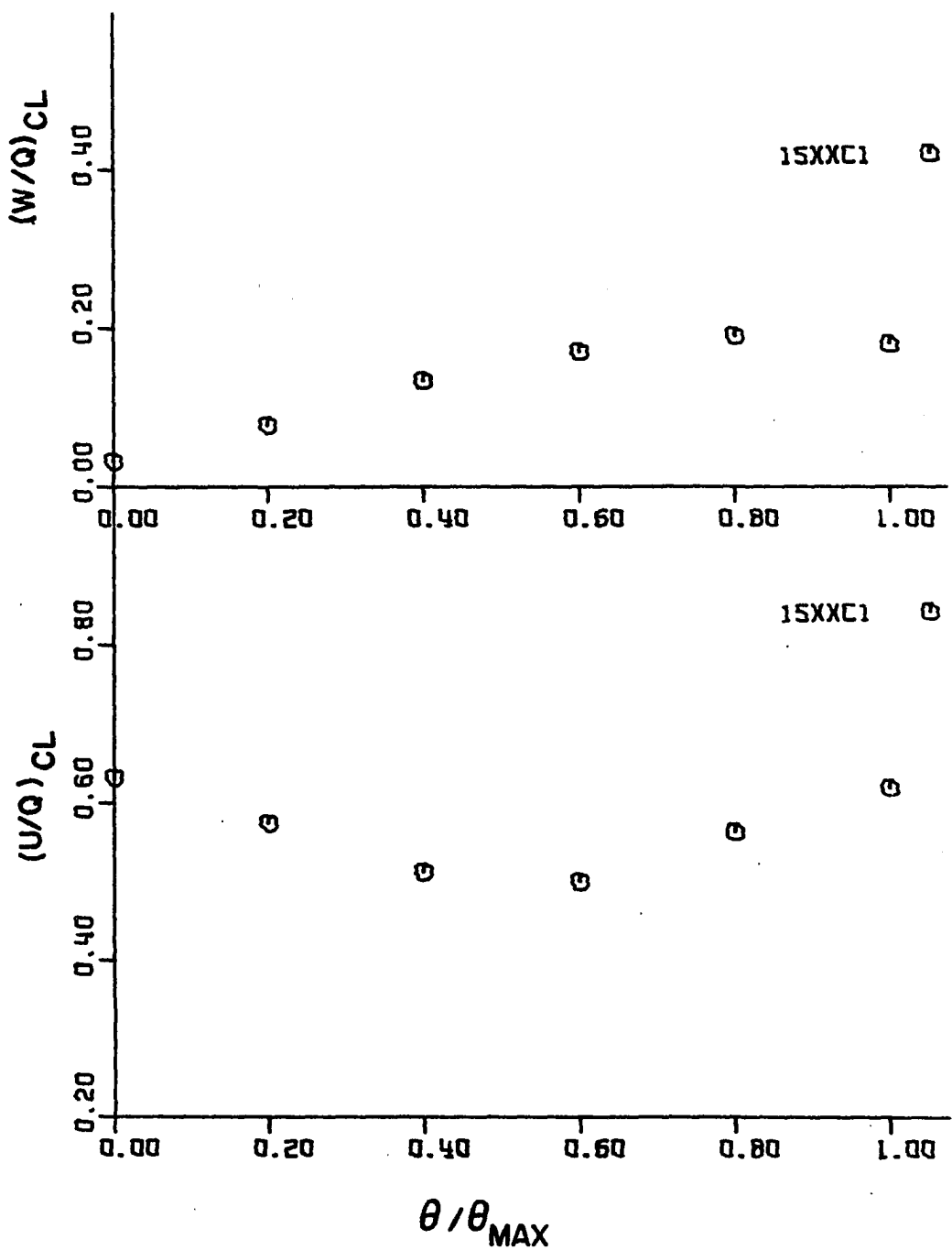


Figure 42. Velocity ratio variation at the edge of the wall collateral layer along the end wall duct centerline

a physical picture of the relationship between the collateral layer edge and the position in the boundary layer is presented as a plot of $(n/\delta)_{C.L.}$ and centerline turning angle as shown in Figure 43. As can be seen by the figure the collateral boundary layer edge is normally located at a small percentage of the boundary layer thickness.

Returning to Figures 39 through 42 with our attention on the cross-flow velocity ratio, a consistent trend is present in every profile. Because of the similarity between the curves of 25XX01 and 25XX02, it would seem justified to hypothesize that the primary influence on $(w/Q)_{C.L.}$ was due to the pressure gradient.

A typical characteristic of many velocity polar plots in partially developed skewed boundary layers is the flat portion from the edge of the wall collateral region which extends a varied distance towards the boundary layer edge. This prevails more in the curved duct profiles but is also apparent in some of the data of Kuethe, et al. (47), Johnston (39), and Hornung and Joubert (36). It was first believed that this flat portion was a result of the down-wash of fluid off the pressure wall onto the end wall and its mixture with the end wall boundary layer. This theory was given by Francis and Pierce (25) for the reason that anomalous turbulence profiles existed in the skewed boundary layer profiles. After studying their data, it was noticed that the anomalous turbulence profiles coincided with the velocity polar profiles having noticeable flat portions in the maximum crossflow region as shown in Figure 44. As discussed in the Literature Review, high turbulence tends to flatten velocity profiles through the mixing action. This supports the correlation between

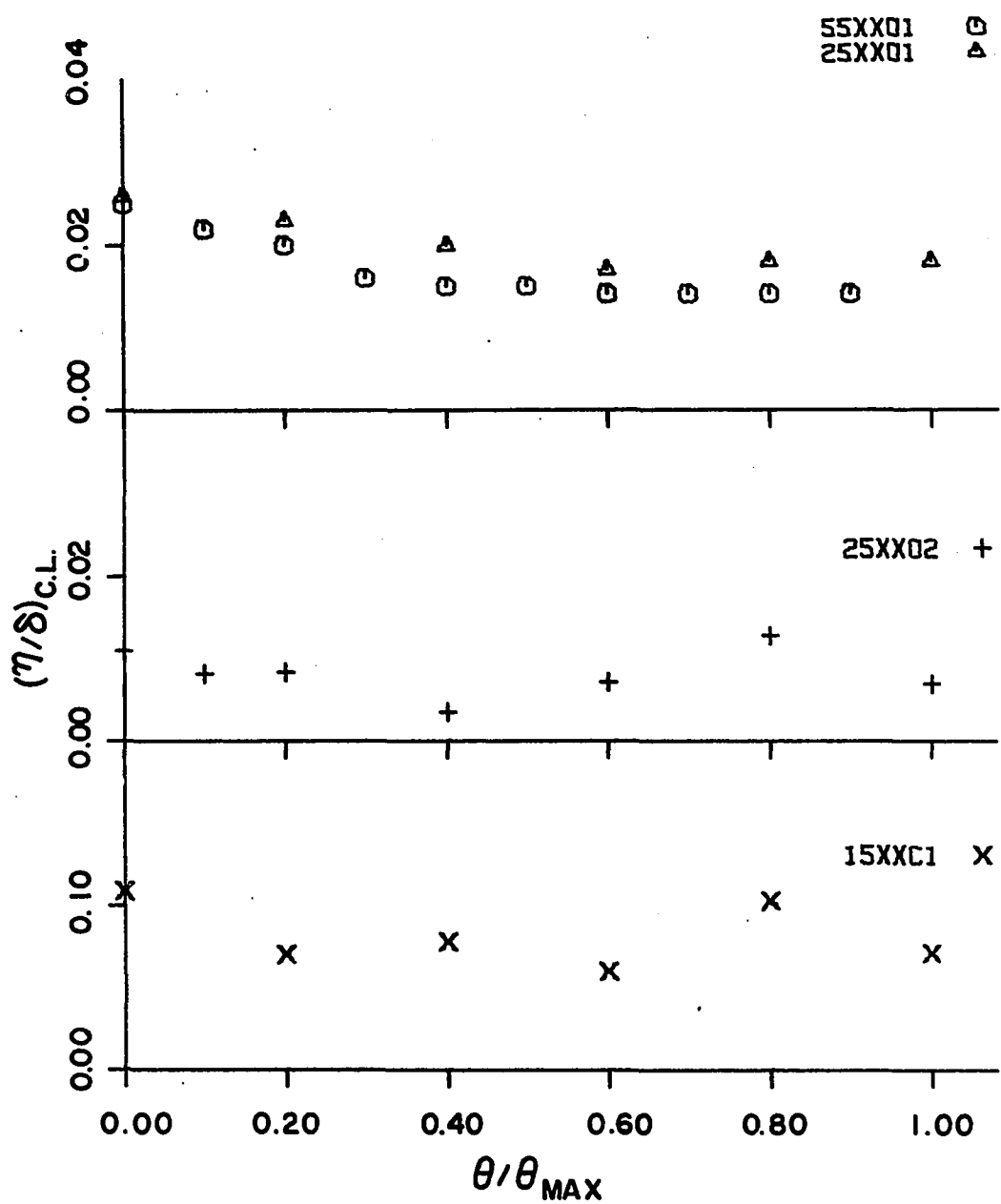


Figure 43. Position of the wall collateral layer edge with respect to the end wall

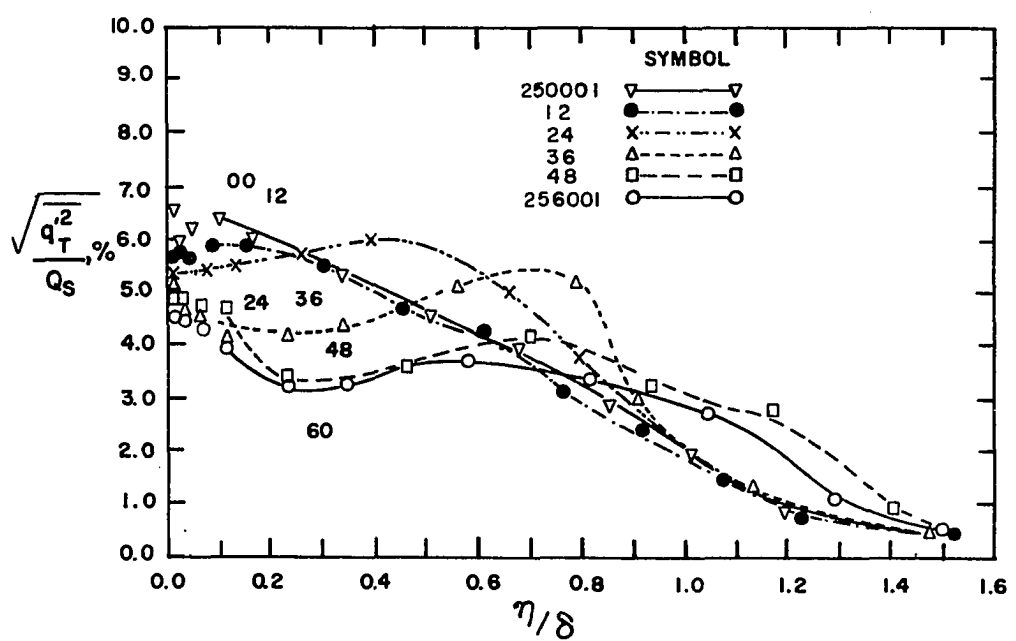
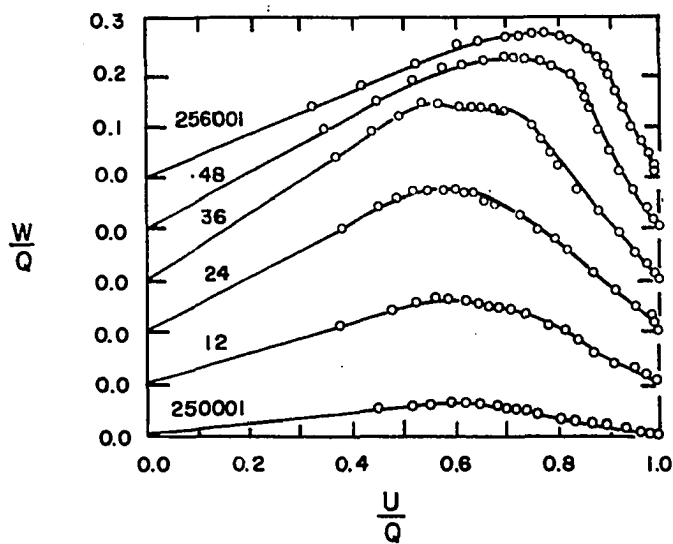


Figure 44. Comparison of velocity polar plot profiles with corresponding turbulence intensity profiles

the flat portion in the polar plots and the anomalous turbulence profiles. If the correlation between the anomalous turbulence profiles and the flat portion is universally accepted then the fluid down-wash theory is dubious since velocity polar profiles, Figure 45, near the pressure wall do not exhibit the flat portion. It would seem reasonable that if the fluid down-wash was the primary source of turbulence excitation it would have its greatest effect near the pressure wall and decay as it propagated into the midstream. The mechanism involved in developing this flat portion in the velocity polar plot is not completely understood.

Remarks on a Double-Skewed Turbulent Boundary Layer

Concentration on single skewed boundary layers has been the approach up to now, but a few remarks pertaining to the development of the double-skewed profile might be of assistance in understanding single skewed boundary layers. Also, a look at the double skewing could possibly suggest a method for predicting the behavior of boundary layer development for a particular case. As mentioned in the Literature Review, double skewing is a result of an inflection point in the free stream streamlines. Pierce and Klinksiek (59) arranged a set of ducting to accomplish this, as is shown in Figure 70. The resulting velocity polar plots are presented in Figure 46 which show the development of the double-skewed boundary layer. Profiles were taken every three degrees on the centerline of the test section end wall which had a centerline radius of fifty-five inches.

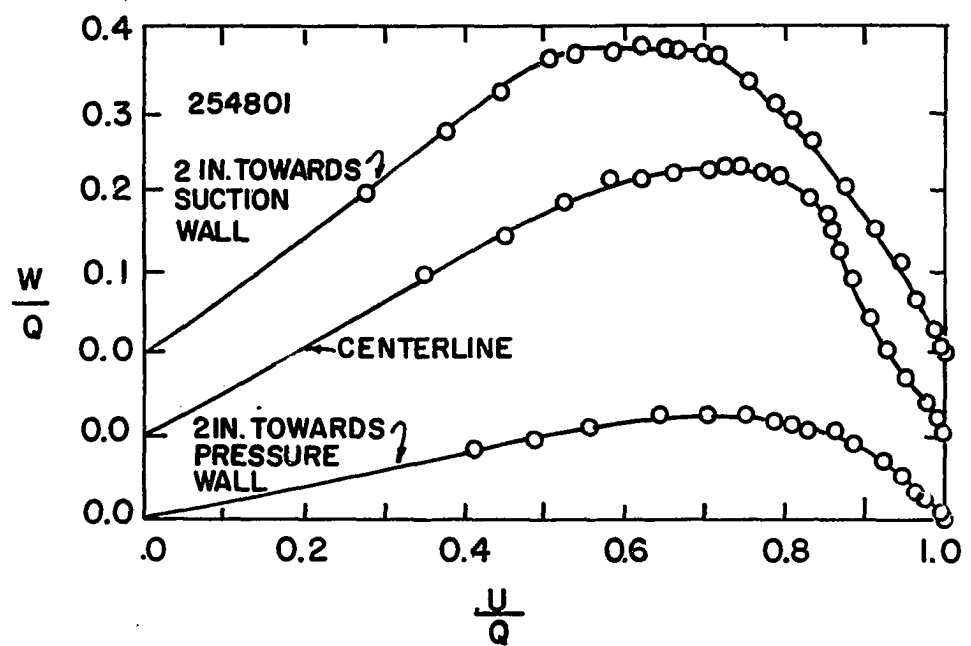


Figure 45. A radial variation of velocity polar plot profiles

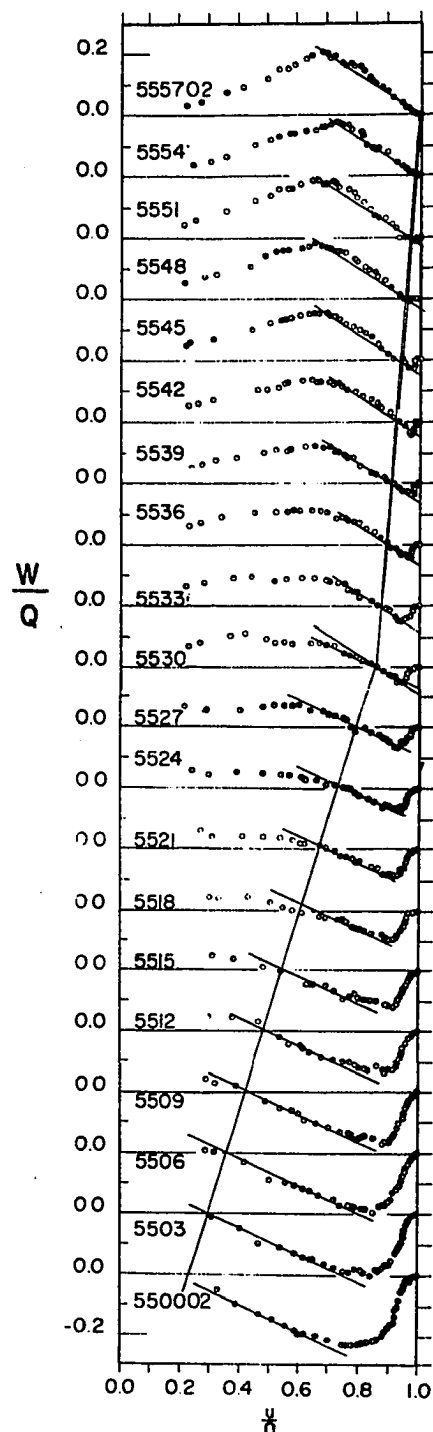


Figure 46. A development of a double-skewed turbulent boundary layer velocity profile

As can be seen by the line extending from the zero-degree profile to the thirty-degree profile and then extending at a different angle to the fifty-seven degree profile that propagation of skewing is nearly linear with respect to the streamwise velocity component and the angle of turn. This could be approximated as

$$\left(\frac{u}{Q}\right) = a_1 + b_1 \theta \quad 0^\circ \leq \theta \leq 30^\circ \\ \frac{w}{Q} = 0$$

$$\left(\frac{u}{Q}\right) = a_2 + b_2 \theta \quad 30^\circ \leq \theta \leq 60^\circ \\ \frac{w}{Q} = 0$$

Such a relationship might be extended to other parts of the boundary layer since the lines along the data are parallel to each other from zero degrees to thirty degrees and again from thirty degrees to fifty-seven degrees. Because the lines are straight and parallel then at least parts of the boundary layer have a linear development of the cross-flow velocity with respect to the turning angle. This could be formulated as

$$\frac{w}{Q} = d_1 + d_2 \left(\frac{u}{Q}\right).$$

For

$$\frac{w}{Q} = 0$$

the expression becomes

$$d_1 + d_2 \left(\frac{u}{Q}\right) = 0 \\ \frac{w}{Q} = 0$$

or

$$d_1 + d_2 (a_1 + b_1 \theta) = 0$$

which results in

$$\frac{w}{Q} = d_2 \left(\frac{u}{Q} - a_1 - b_1 \theta \right).$$

Since the slope of the polar plots change at a turning angle of thirty degrees, which is half of the turning angle, then d_2 is probably a function of the pressure gradient and its direction with respect to the free stream as well as a function of the wall shear stress and its direction. Velocity variation in the streamwise and radial directions in the core of curved channel flow is associated with a pressure gradient both in the radial and streamwise direction. This changes the total pressure gradient direction as the flow proceeds through the curve. Since the straight parallel lines in Figure 46 are in the outer portion where the pressure gradient is usually considered of primary importance, then it would be indicated that the pressure gradient and its direction would merit further consideration. More information is required before determining the influence of the wall shear stress and pressure gradient direction on the skewing action in the boundary layer.

Remarks on Velocity Profile Models

A subsection in the Literature Review was devoted to velocity profile models and their characteristics. A preliminary conclusion was that the methods presently available are inadequate to predict the velocity in a very broad range of conditions. To compare the present data with the various models appeared to be of little value in view of the previous

comparisons, so it was not attempted.

The Law of the Wall had been reported to be invalid in most three-dimensional flows. This would tend to preclude the use of Coles' model directly. A cursory look at many velocity polar profiles indicates Johnston's triangular model was valid, at most, during the early development of a skewed boundary layer. In general, all information points to the need of a new, more general velocity model or a boundary layer calculation method which circumvents a direct need for velocity models.

Neither has been accomplished in this work but a few new parameters will be presented and discussed which might help lead to a velocity model.

Earlier in this section it was observed that the crossflow velocity at the edge of the wall collateral layer, $(w/Q)_{C.L.}$, indicated a consistent trend for each set of data presented. Because of this, $(w/Q)_{C.L.}$ has possibilities as a normalizing parameter with some similarity qualities. If this quantity was divided into the actual crossflow velocity at all points in the profile a multitude of distributions would result. Since most known velocity polar profiles initially had a triangular shape and developed in various ways from that configuration, possibly a triangular distribution could be basic to the three-dimensional flow and an additional distribution added to it to complete the profile. This type of correlation would be analogous to the Law of the Wall in two-dimensional flow which is added to a wake distribution to describe the complete profile. Of course, no law was expected since the formulation did not include significant basic variables, such as shearing stress or some form of it. An insufficient amount of shear stress data in three-

dimensional flow appears to be one of the primary factors in not developing more reliable velocity models. Figure 47 shows the model used to formulate the triangular distribution. A straight line is drawn connecting the edge of the wall collateral layer to the edge of the boundary layer. Using geometrical relationships the crossflow velocity at the edge of the wall collateral layer is expressed as

$$\left(\frac{w}{Q}\right)_{C.L.} = \frac{1.0}{\cot \alpha_{max} + \cot \beta'}$$

and the crossflow velocity corresponding to the triangular distribution at any value of η/δ is expressed as

$$\frac{w_c}{Q} = \frac{1.0}{\cot \alpha + \cot \beta'} .$$

The ratio of the two is simply

$$\frac{\frac{w_c}{Q}}{\left(\frac{w}{Q}\right)_{C.L.}} = \frac{w_c}{w_{CL}} = \frac{\cot \alpha_{max} + \cot \beta'}{\cot \alpha + \cot \beta'}$$

and is seen to be a ratio of trigonometric functions alone. This function is plotted against η/δ for the four sets of data that have been previously discussed and is presented as Figures 48 through 51. If curves for turning angles less than or equal to twelve degrees were eliminated from Figures 48 and 49, the remaining curves from both figures would lie in a relatively narrow band. Figure 50 shows considerably more scatter than the previous two sets. A trend more similar to the other two sets would be obtained by replacing δ with the distance to the edge of the crossflow boundary layer. The diffuser data indicated a straighter distribution of the function but was on the same order of magnitude as 55XX01 and

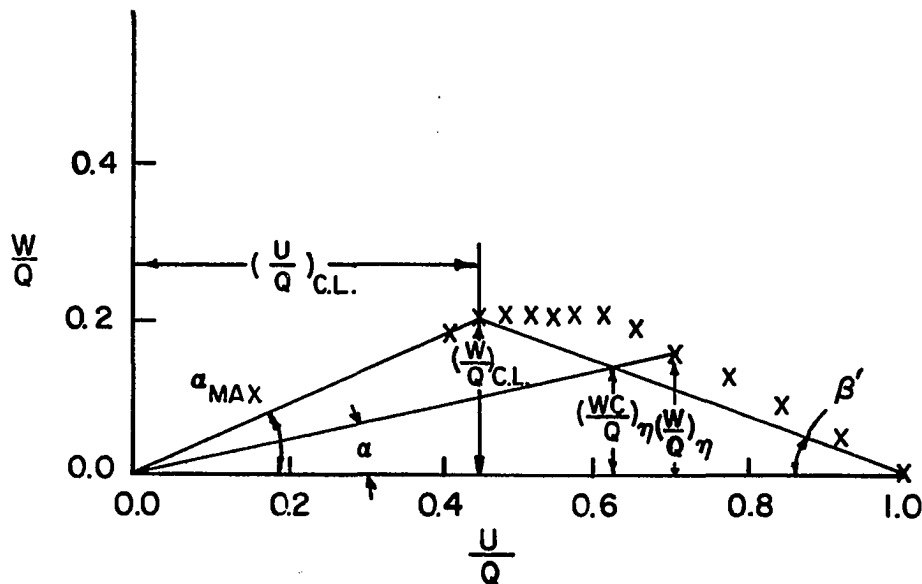


Figure 47. Model of the triangular distribution

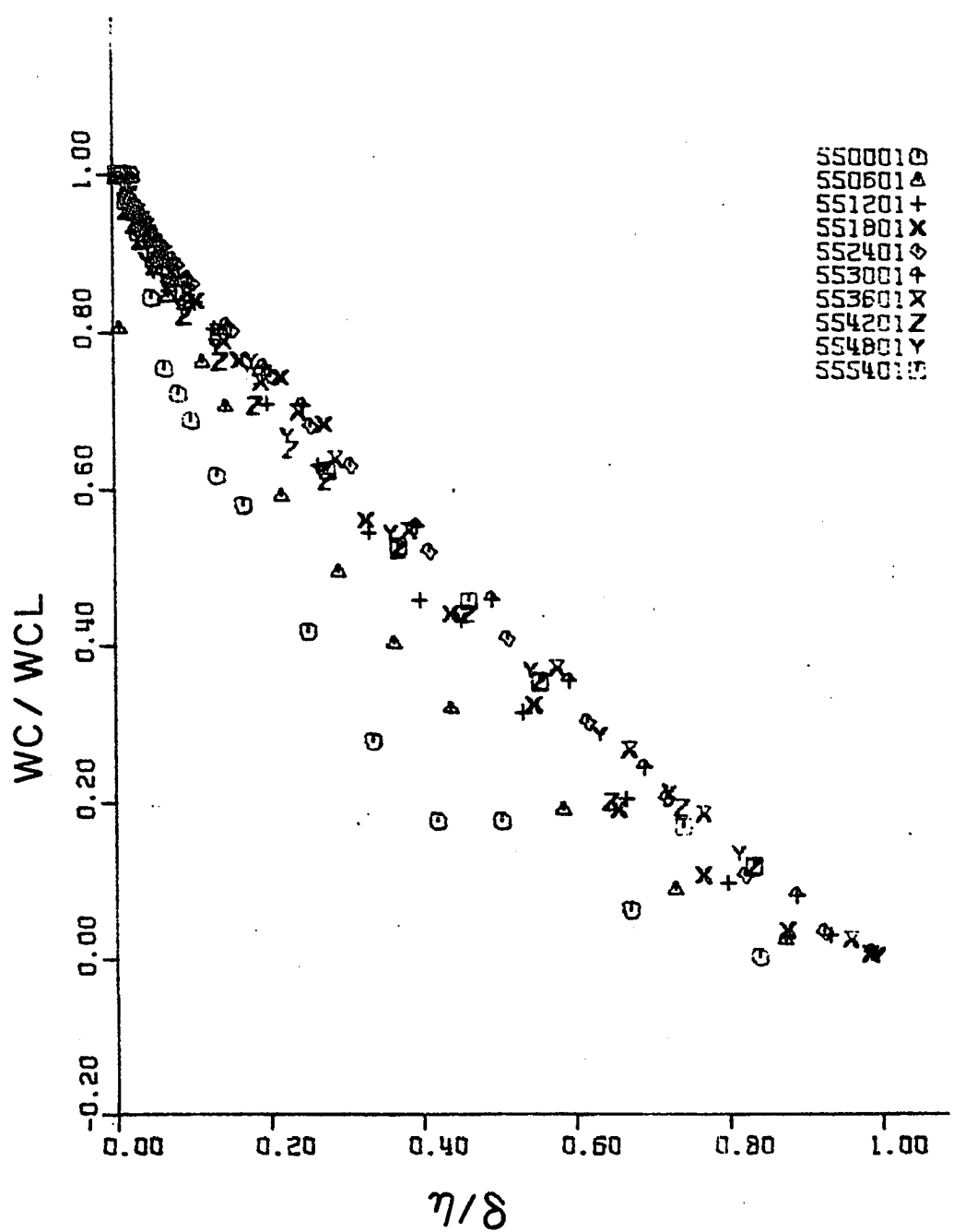


Figure 48. Triangular distribution correlation

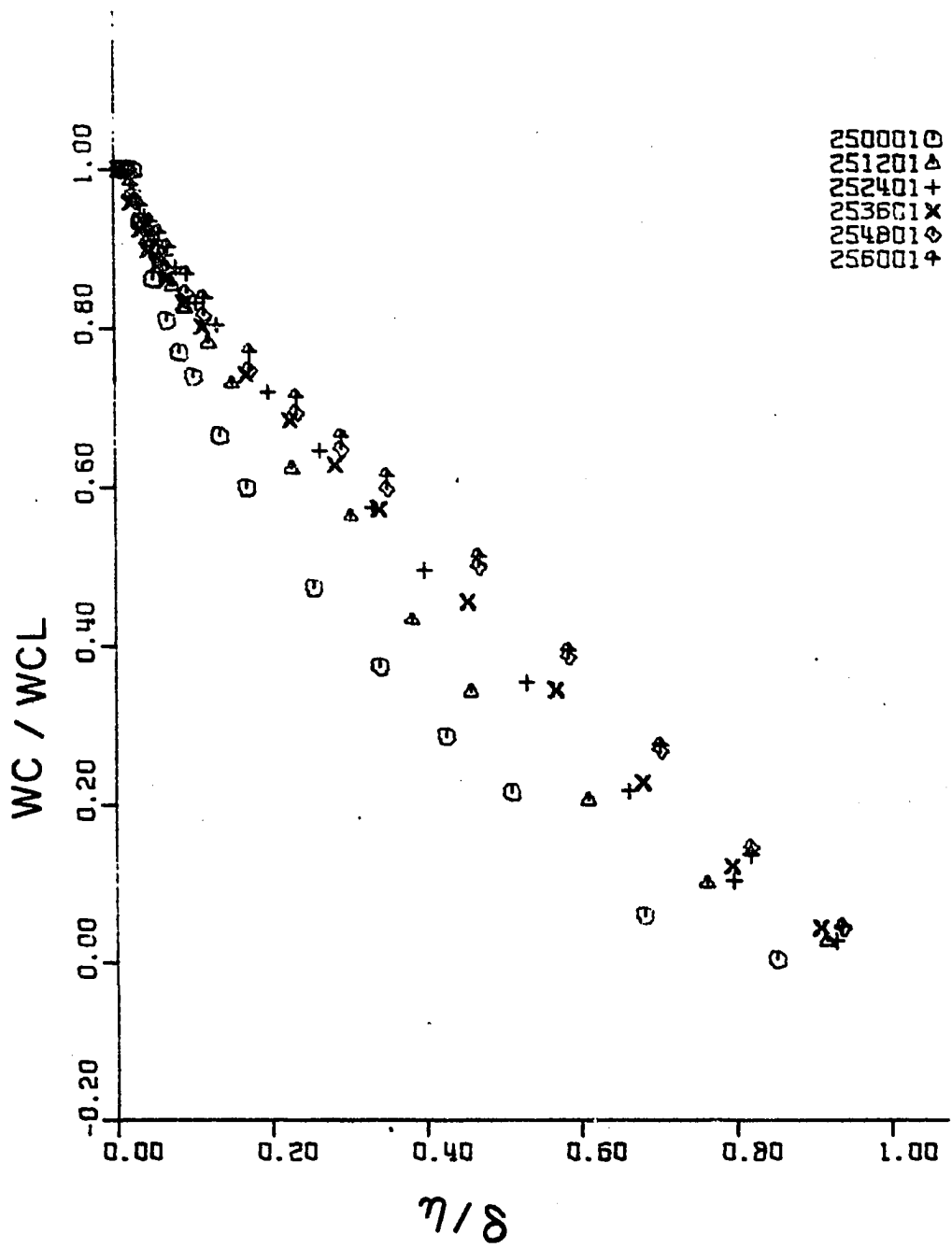


Figure 49. Triangular distribution correlation

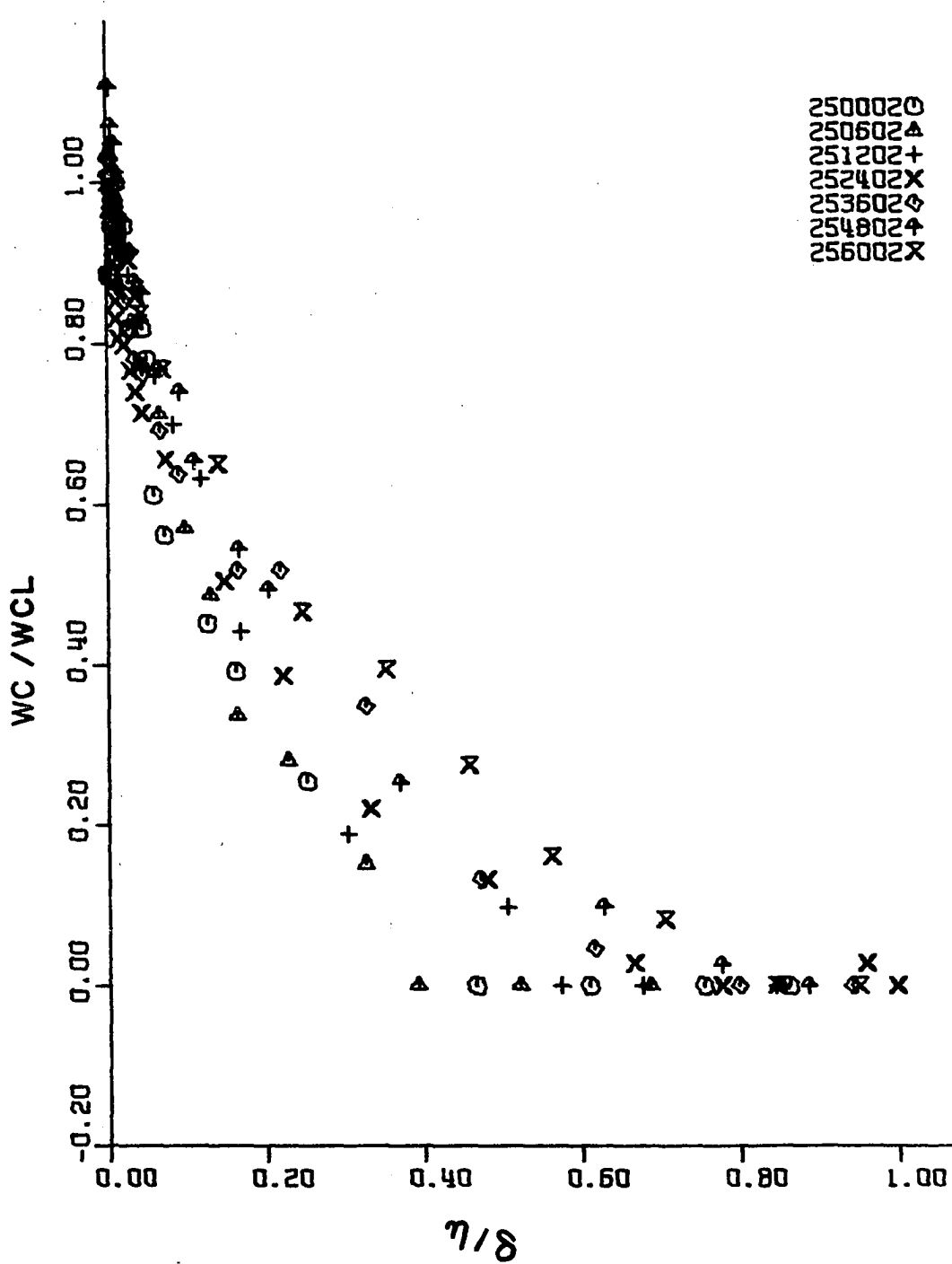


Figure 50. Triangular distribution correlation

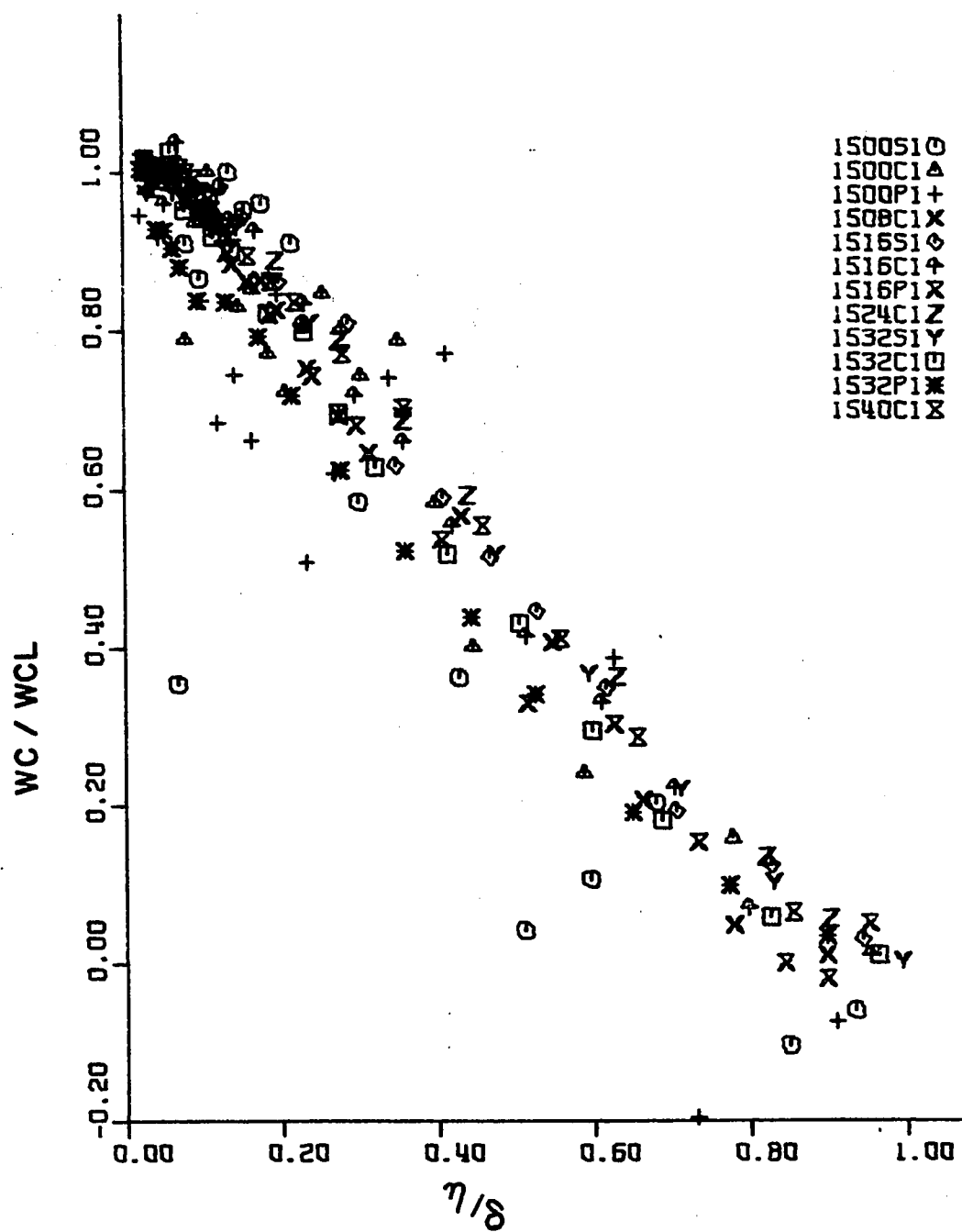


Figure 51. Triangular distribution correlation

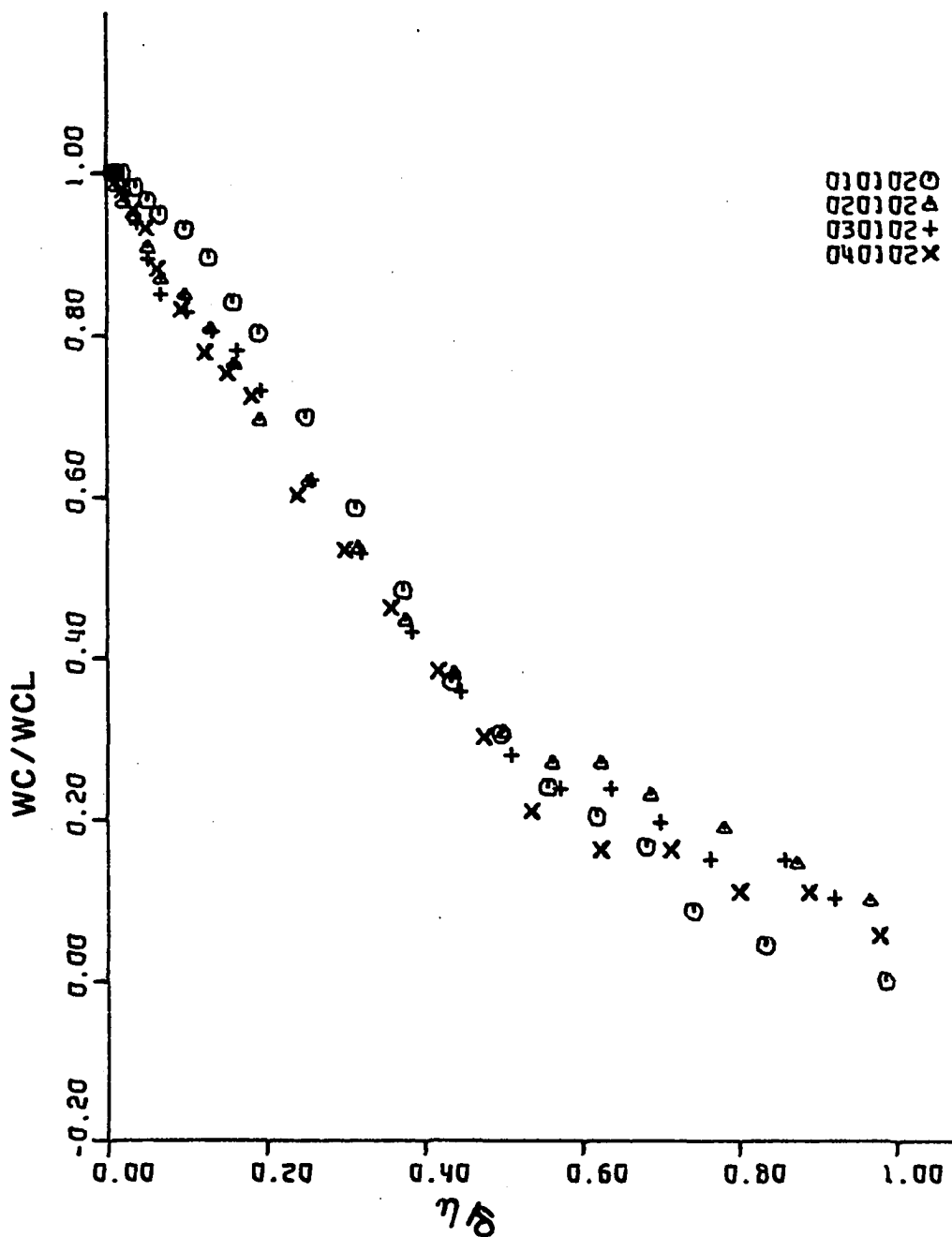


Figure 52. Triangular distribution correlation

25XX01. A much tighter band of data results if only the centerline profiles are exhibited. It was suspected that since each set of data was fairly consistent within itself, then the magnitudes of boundary layer thickness, Reynolds number, pressure gradient, shear stress, and the directions of the latter two are of prime importance. Sets of data having all this information were sought and the result of the search revealed only one set, that of Pierce and Krommenhoek (60). APPENDIX F contains a schematic diagram of their test section, Figure 71, and data used from their work is tabulated in Tables 18 through 21. As can be seen from Table 18, they had a range of Reynolds numbers, a range of pressure gradients and wall shear stress values. The direction of the wall shear stress varied but the direction of VP with respect to the free stream was essentially constant for every test run. Figure 52 consists of a plot of the same parameters as in Figures 48 through 51 and except for the larger values of η/δ a fairly tight band is exhibited. This data tends to suggest that the pressure gradient direction with respect to the free stream is one of the primary parameters to be considered in formulating a velocity model. This might also explain part of the reason for the discrepancy between the profiles at lower values of centerline turning compared to the ones at higher values. It could also explain the distinct variation in slope in the diffuser correlation curves.

Subsequently, it was noticed that the parameter w_c/w_{CL} would be equivalent to the defect parameter of Hornung and Joubert (36) if the velocity polar plot actually possessed a triangular shape. Their parameter was the ratio of the magnitude of the vector connecting the tip of

an arbitrary boundary layer velocity to the tip of the free stream velocity vector divided by the magnitude of the velocity vector which connects the tip of the velocity vector at the edge of the wall collateral layer to the tip of the free stream velocity vector. Since their measured velocity polar plots were almost triangular in shape, then their parameter plotted against η/δ should exhibit a similar shape to the ones presented in this work. Their Figure 17 shows this trend.

A modification to the previous approach to determine a crossflow parameter was made to obtain an expression entirely in terms of the actual velocity ratios. Figure 53 shows the geometrical relationship used to do this. Again using trigonometrical relations the value of $w/c'/Q$ is represented by

$$\frac{w/c'}{Q} = \frac{1}{\cot \alpha_{max} + \cot \beta''}$$

where

$$\cot \beta'' = \frac{1 - w/Q}{w/Q} .$$

If this complete expression is divided into w/Q and rearranged the result is

$$\frac{w/Q}{w/c'/Q} = \frac{w}{Q} \cot \alpha_{C.L.} + (1 - u/Q) = \frac{w}{Q\varepsilon} + (1 - u/Q) .$$

This expression would also be equivalent to Hornung and Jouberts defect parameter for actual triangular distributions. This parameter is plotted against η/δ in Figures 54 through 58. The distributions are quite similar to the previous parameter except for test 25XX02 in which a vast improvement was made on the scatter of the plots. If this particular

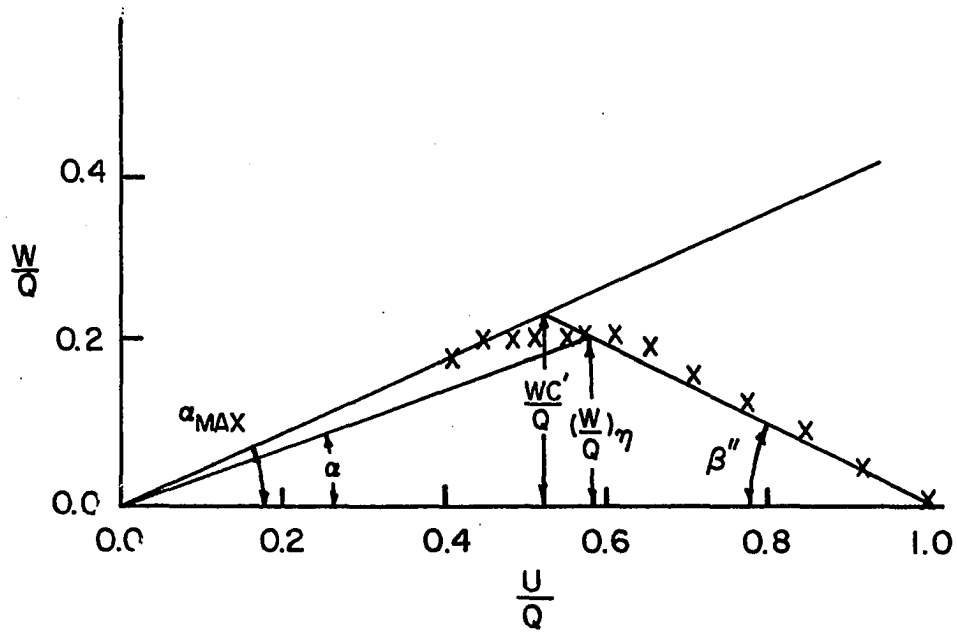


Figure 53. Model for a particular crossflow velocity ratio

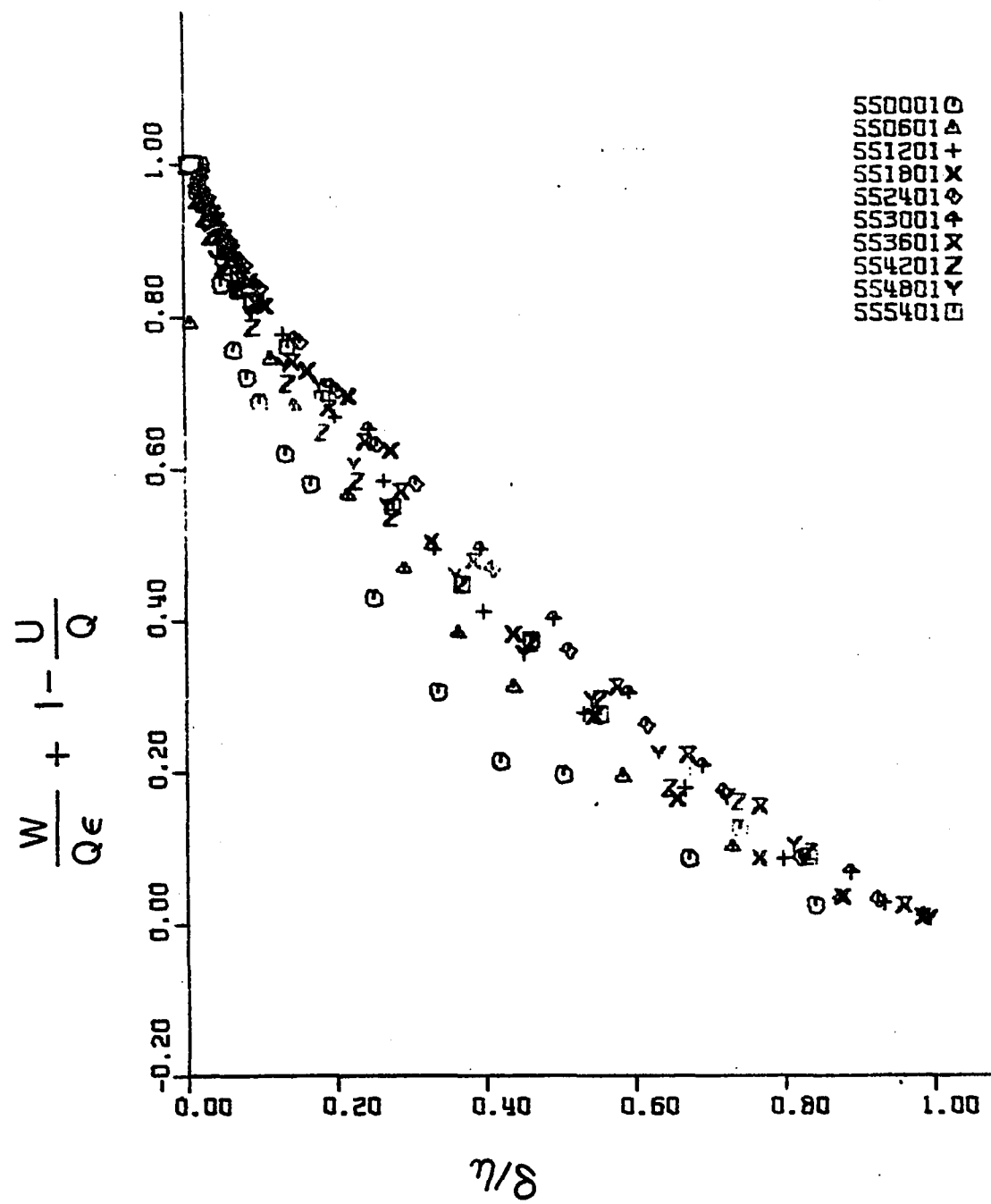


Figure 54. A particular crossflow correlation

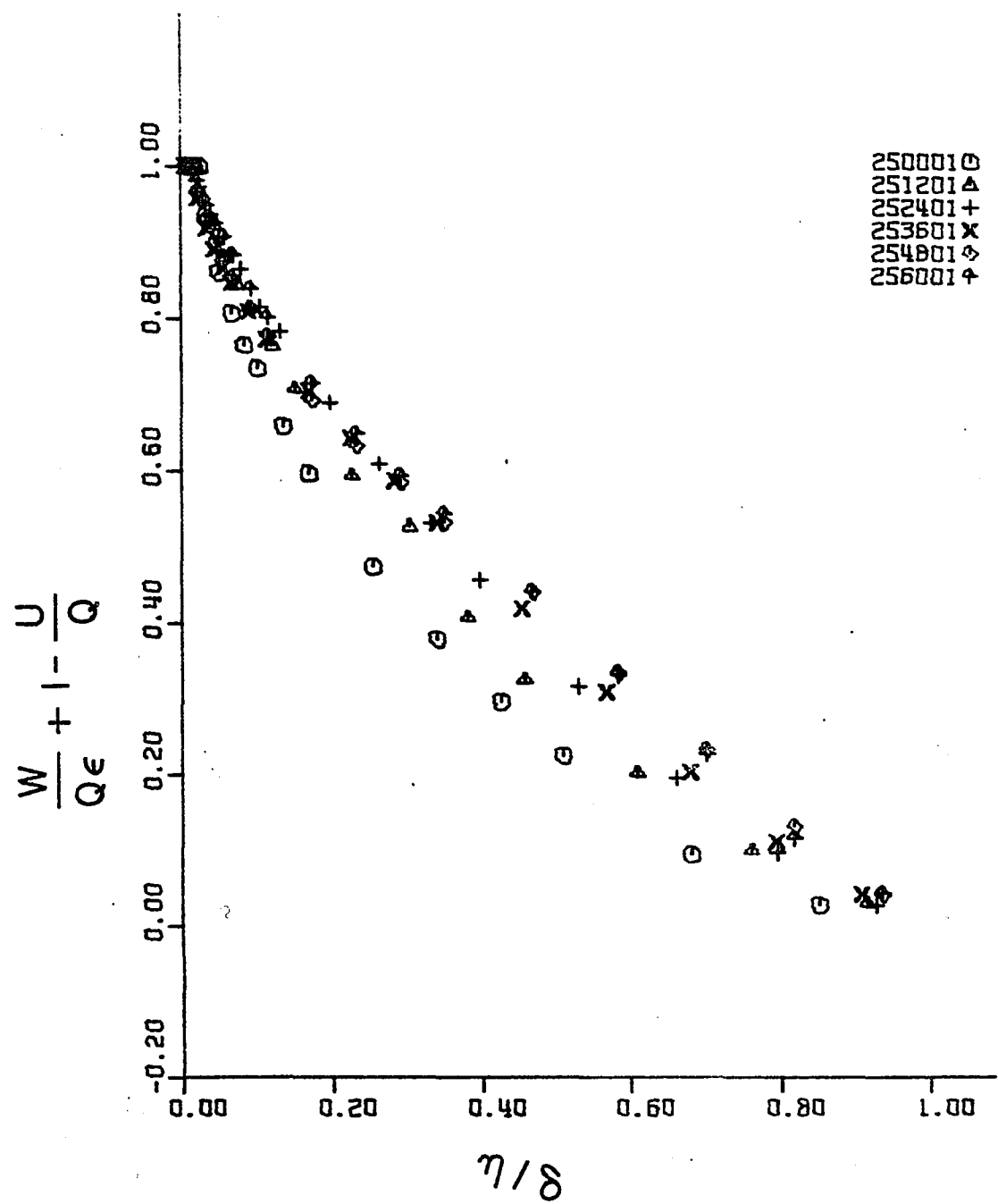


Figure 55. A particular crossflow correlation

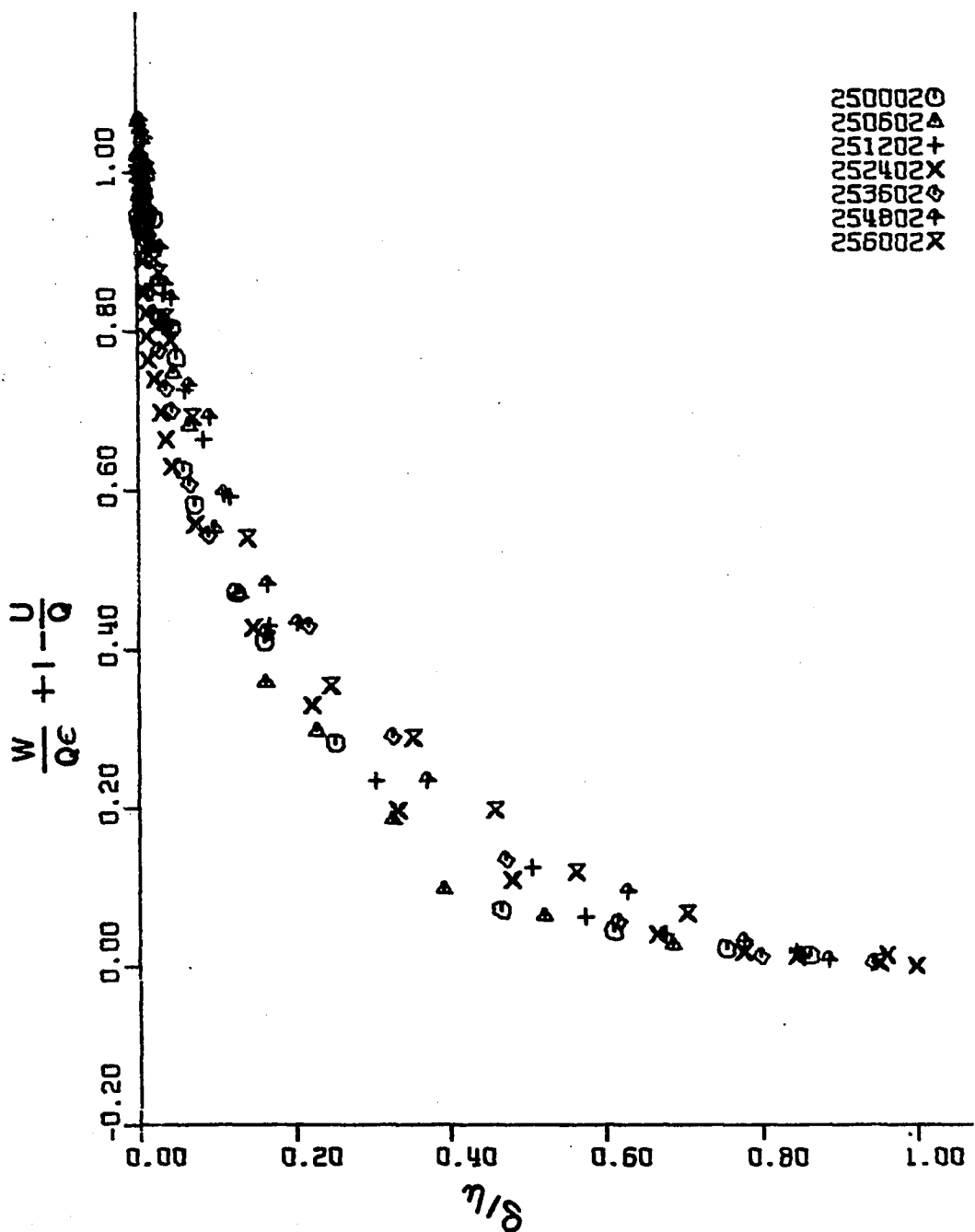


Figure 56. A particular crossflow correlation

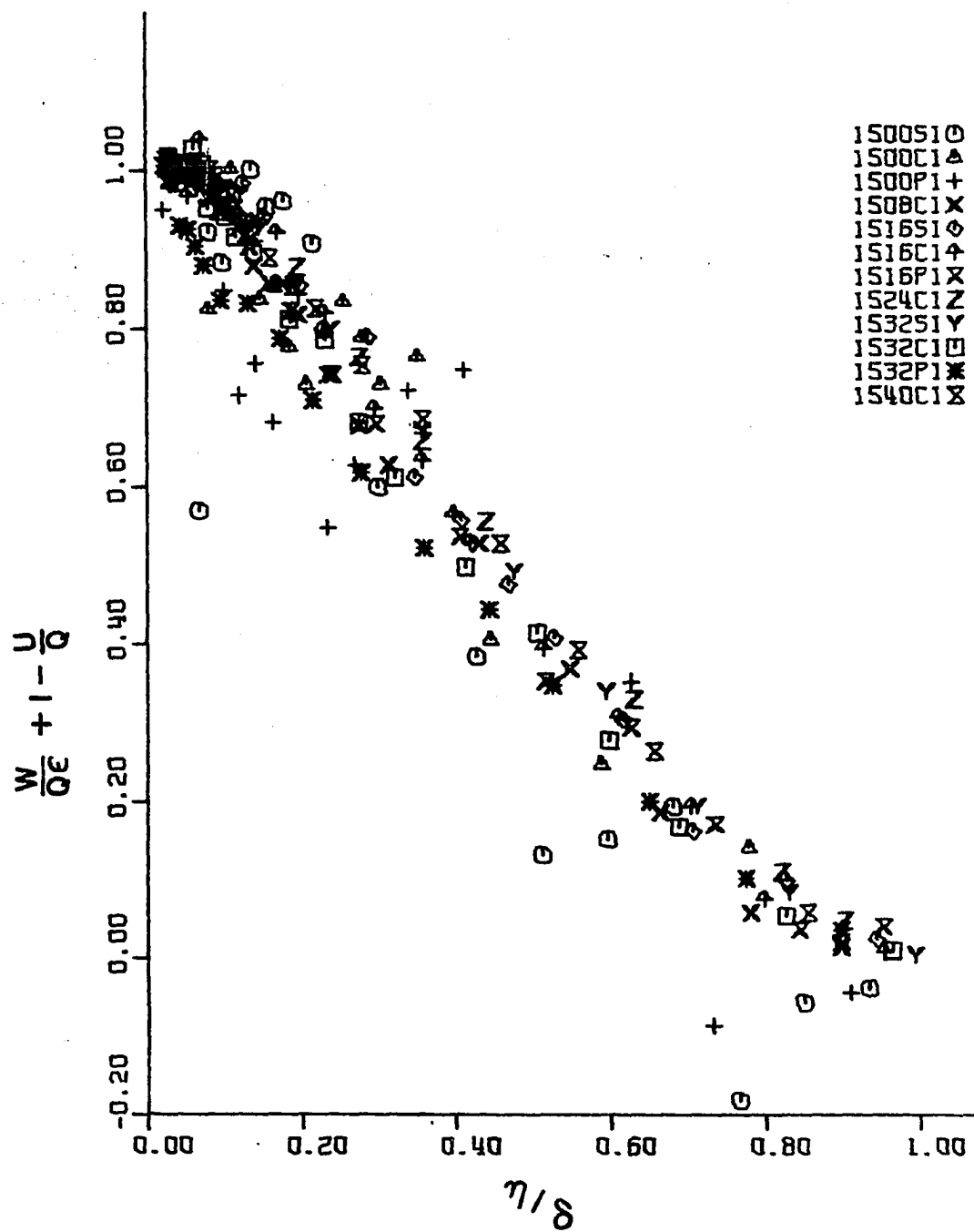


Figure 57. A particular crossflow correlation

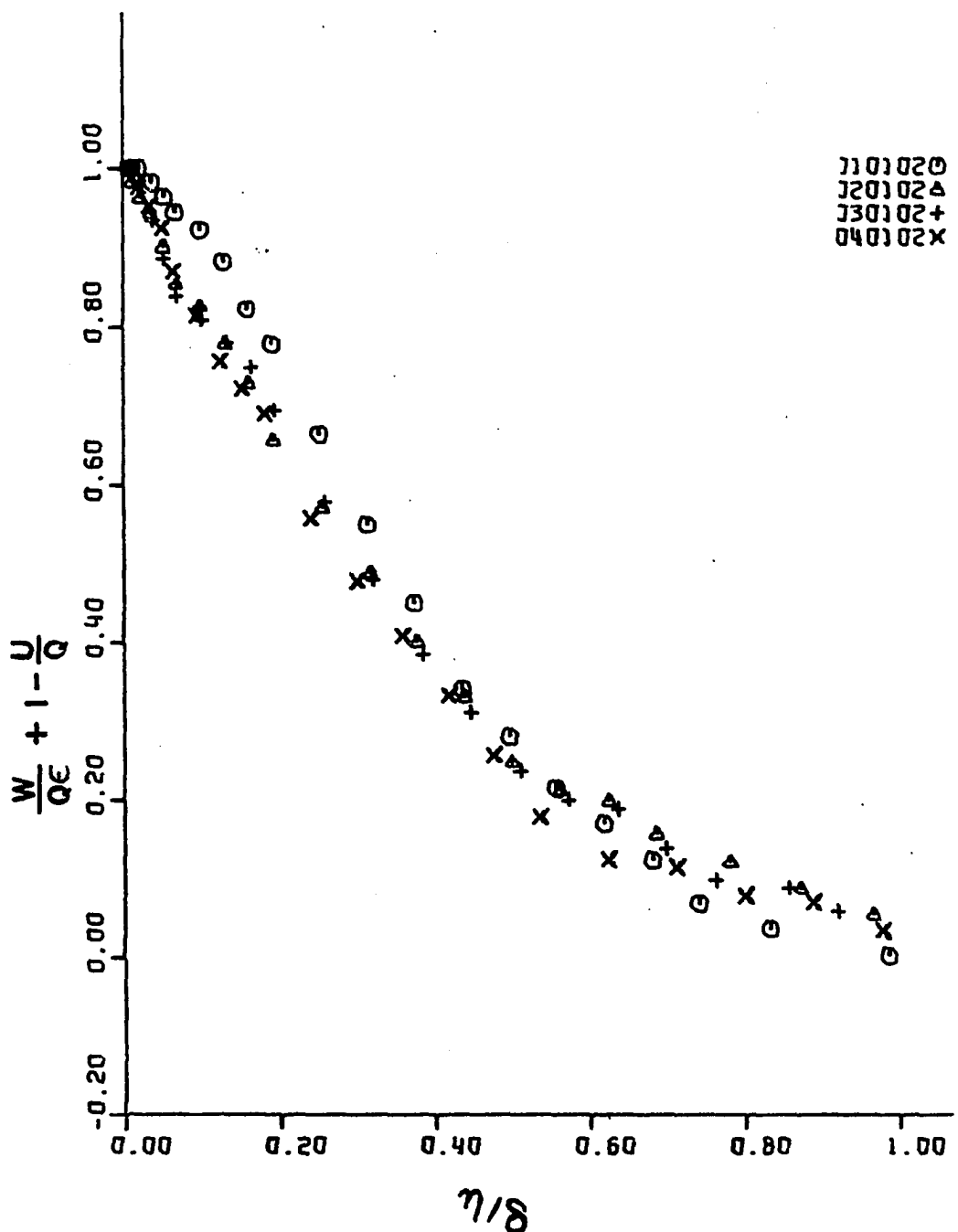


Figure 58. A particular crossflow correlation

relationship could be more universally correlated using the form

$$\frac{w}{Q} \cot \alpha_{\max} + (1-u/Q) = f(n/\delta, \tau_{\text{wall}}, \nabla P)$$

then it could serve as an auxiliary equation in conjunction with the boundary layer equations in an attempt to numerically solve the set of governing equations.

Considerable work remains in order to obtain a velocity model for three-dimensional turbulent boundary layers. Data containing pressure gradient and shear stress data along with the developing velocity profiles are required before significant advancement can be made.

CONCLUSIONS

The test section, which had movable side walls, appeared to function as designed and there was no particular difficulty in adjusting the side walls to a desired configuration. Sealing was no problem for the particular pressures which occurred in the present tests. At any point where a leak was detected it was found that rubber cement sufficed as a sealer and easily rubbed off after the walls were moved to a new location. The versatility of the test section should allow it to be used for many future experimental investigations.

All facets of the data procurement technique developed in this investigation were satisfactory except for the turbulence measurements. At present, this author is not aware of any acceptable method of measuring Reynolds stresses in three-dimensional flow. It would be a significant contribution to develop one.

Data obtained in the diffusing passage did not show any gross abnormalities when compared to data from larger passages. At least for the positions surveyed in the diffuser it seemed plausible to conclude that the wall influence was not any more acute than for the data obtained in larger ducts.

Diffuser data velocity polar plots show that the flat portion in the maximum crossflow region is evident earlier in the development of the boundary layer than for ducts without pressure gradients. Since the pressure gradient across the duct is highest near the beginning turning angle and then decreases, it appears the flat portion in the velocity polar

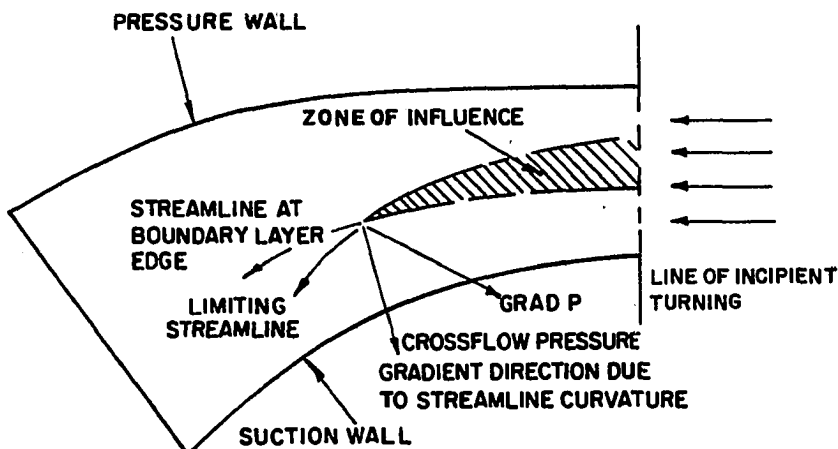
plot is more a pressure gradient effect than a wall effect.

Based on two-dimensional boundary layer data, it seemed feasible to expect the diffuser data to indicate a faster boundary layer growth. As expected, the boundary layer growth in three-dimensional boundary layers with streamwise adverse pressure gradients grew at a higher rate than ones in negligible streamwise pressure gradients. In comparison, on a development length basis, the diffuser boundary layer grew at twice the rate of the data of Francis (24).

After comparing the data of various experimental investigations it appeared that the size of the boundary layer at the position of beginning curvature and also the shape of the initial profile had a definite significance in the development of the three-dimensional boundary layer as it was subjected to a crossflow pressure gradient. Another indication from the data was that the magnitude and direction of VP is a controlling factor in the shape and development of the skewed turbulent boundary layer. This in essence indicates that duct geometry is one of the primary controlling factors. The radius of centerline curvature and the turning angle influence the development of the turbulent skewed boundary layer by varying the magnitude of the pressure gradient across the duct and through the development of the free stream velocity profile across the duct. Variation in the gross behavior, that is the variation of the shape factors, seemed to correlate quite well with the variations of the magnitude and direction of the velocity vector at the edge of the wall collateral layer even though it is normally located at a distance from the wall which is a small percent of the total boundary layer thickness.

Two parameters were introduced which were primarily based on cross-flow velocity ratios. These parameters, when plotted against η/δ , would correlate the boundary layer development fairly well for each test section but varied considerably for data from a variety of test sections. More parameters are required in the correlation function in order to make all the data coalesce. If three-dimensional turbulent boundary layer correlation parameters have any resemblance to those for two-dimensional layers, then some variable which is a function of wall shear stress would be required. Unfortunately, there is no experimental shear stress data available from three-dimensional turbulent boundary layers as they develop in a curved duct. Shear stress data along with pressure gradient under these conditions would be a welcome contribution.

Insufficient data exists to develop a complete hypothesis on the mechanisms of a three-dimensional boundary layer. The available data suggests that the skewed boundary layer profile at a given location has a history from a zone as shown in Figure 59. This zone might be thought of as a ribbon with its width having a non-linear surface stretching from the end wall towards the suction wall up to the boundary layer edge. As it moves down the duct its particles converge and the ribbon becomes vertical to the wall at a given location but its direction is not constant. Proceeding from the vertical position, the edge of the ribbon at the end wall is now on the suction side of the free stream edge and the width of the ribbon is stretched. At the location where the ribbon was vertical to the surface (end wall) a velocity polar plot representing the relative propagation of the fibers of the ribbon might look like the one



TOP VIEW OF CURVED DUCT

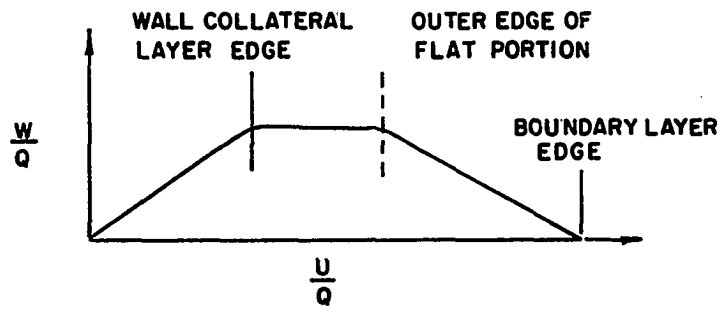


Figure 59. Boundary layer characteristics in a curved duct

in Figure 59. From the end wall to the edge of the wall collateral layer the ribbon would have the same direction and since it is generally close to the wall it might be influenced greatly, as in two-dimensional flow, by the streak breakups which are ejected from the viscous sublayer. Perhaps the energy obtained from the breakups is the reason this portion of the boundary layer is collateral. A flat portion in the polar plot sometimes exists immediately above the wall collateral layer. This portion of the boundary layer appears to have a significant influence from the magnitude and direction of VP. In addition, this area has higher turbulence which could be due to the rate of change of skewing. The rate of change in skewing would in part be a function of the pressure gradient and its direction. It is very difficult to conceive what mechanism would cause the cross flow to remain constant in velocity over a portion of the boundary layer while the streamwise velocity is increasing. The remainder of the boundary layer would require some unique balance between the shearing stress, pressure gradient and momentum of the fluid to maintain a quasi-linear relation between the cross flow velocity and the streamwise velocity.

LITERATURE CITED

1. Ashkenas, H. and Riddell, F. R. Investigation of the turbulent boundary layer on a yawed flat plate. U.S. National Advisory Committee for Aeronautics Technical Note 3383. 1955.
2. Blackman, D. and Joubert, P. N. The three-dimensional turbulent boundary layer. Royal Aeronautical Society Journal 64: 692-694. 1961.
3. Bradshaw, P. The effect of wind tunnel screens on nominally two-dimensional boundary layers. Journal of Fluid Mechanics 22: 679-687. 1965.
4. Bradshaw, P. "Inactive" motion and pressure fluctuations in turbulent boundary layers. Journal of Fluid Mechanics 30: 241-258. 1967.
5. Bradshaw, P. The turbulence structure of equilibrium boundary layers. Journal of Fluid Mechanics 29: 625-645. 1967.
6. Bradshaw, P. Turbulent boundary layers. The Aeronautical Journal of the Royal Aeronautical Society 72: 451-459. 1968.
7. Bradshaw, P., Ferriss, D. H. and Atwell, N. P. Calculation of boundary layer development using the turbulent energy equation. Journal of Fluid Mechanics 28: 593-616. 1967.
8. Bull, M. K. Wall pressure fluctuations associated with subsonic turbulent boundary layer flow. Journal of Fluid Mechanics 28: 719-754. 1967.
9. Carmichael, A. D. An approach to three-dimensional turbulent boundary layers. American Society of Mechanical Engineers Paper 66-WA/GT-10. New York, New York, The Society. 1966.
10. Champagne, F. H. and Sleicher, C. A. Turbulence measurements with inclined hot-wires. Part 2. Hot-wire response equations. Journal of Fluid Mechanics 28: 177-182. 1967.
11. Champagne, F. H., Sleicher, C. A. and Wehrmann, O. H. Turbulence measurements with inclined hot-wires. Part 1. Heat transfer experiments with inclined hot-wires. Journal of Fluid Mechanics 28: 153-175. 1967.
12. Clark, J. A. A study of incompressible turbulent boundary layers in channel flow. American Society of Mechanical Engineers Transactions, Series D: Journal of Basic Engineering 90: 455-468. 1968.

13. Clauser, F. H. The turbulent boundary layer. In Dryden, H. L., Von Karman, T. and Kuerti, G., editors. Advances in applied mechanics. Vol. 4. Pp. 1-51. New York, New York, Academic Press, Inc. 1956.
14. Clauser, F. H. Turbulent boundary layers in adverse pressure gradients. Journal of the Aeronautical Sciences 21: 91-108. 1954.
15. Coles, D. Discussion. American Society of Mechanical Engineers Transactions, Series D: Journal of Basic Engineering 82: 246-247. 1960.
16. Coles, D. The law of the wake in the turbulent boundary layer. Journal of Fluid Mechanics 1: 191-226. 1956.
17. Coles, D. and Hirst, E. A., editors. Computation of turbulent boundary layers. Vol. 2. Compiled data. AFOSR-IFP-Stanford Conference Proceedings. 1968.
18. Cooke, J. C. Three-dimensional turbulent boundary layers. Great Britain Aeronautical Research Council Current Paper No. 635. 1961.
19. Cumpsty, N. A. and Head, M. R. The calculation of three-dimensional turbulent boundary layers. Part 1: Flow over the rear of an infinite swept wing. Aeronautical Quarterly 18: 55-84. 1967.
20. Eichelbrenner, E. A. La Couche limite tridimensionnelle en regime turbulent d'un fluide compressible: cas de la paroi athermane. North Atlantic Treaty Organization, Advisory Group for Aerospace Research and Development. AGARDograph 97, Part 2. 1965.
21. Eichelbrenner, E. A. and Peube, J-L. The role of S-shaped crossflow profiles in three-dimensional boundary layer theory. U.S. Navy European Research Contracts, ONR Contract NG2558-4460. Defense Documentation Center, Defense Supply Agency, AD 650-953. 1966.
22. Eichelbrenner, E. A. and Peube, J-L. Theoretical and experimental investigations on three-dimensional (laminar and turbulent) boundary layers, in particular on problems of transition, separation and reattachment. U.S. Navy European Research Contracts, ONR Contract N 62558-3862. Defense Documentation Center, Defense Supply Agency, AD 650-952. 1966.
23. Fox, R. W. and Kline, S. J. Flow regimes in curved subsonic diffusers. American Society of Mechanical Engineers Transactions, Series D: Journal of Basic Engineering 84: 303-316. 1962.

24. Francis, G. P. Incompressible flow of the three-dimensional turbulent boundary layer on the floor of curved channels. Unpublished Ph.D. thesis. Ithaca, New York, Library, Cornell University. 1965.
25. Francis, G. P. and Pierce, F. J. An experimental study of skewed turbulent boundary layers in low speed flows. American Society of Mechanical Engineers Paper 66 WA/FE-2. New York, New York, The Society. 1966.
26. Friehe, C. A. and Schwarz, W. H. Deviations from the cosine law for yawed cylindrical anemometer sensors. American Society of Mechanical Engineers Transactions, Series E: Journal of Applied Mechanics 35: 655-662. 1968.
27. Gersten, K. Corner interference effects. North Atlantic Treaty Organization, Advisory Group for Research and Development. AGARD Report 299. 1959.
28. Gessner, F. B. and Jones, J. B. On some aspects of fully developed turbulent flow in rectangular channels. Journal of Fluid Mechanics 23: 689-713. 1965.
29. Goldberg, P. Upstream history and apparent stress in turbulent boundary layers. Massachusetts Institute of Technology Gas Turbine Laboratory Report No. 85. May 1966.
30. Goldstein, S. Modern developments in fluid dynamics. Vol. 2. Oxford, England, Clarendon Press. 1938.
31. Gruschwitz, E. Turbulence reibungsschichten mit sekundarstromung. Ingenieur-Archiv 6: 355-365. 1935.
32. Herring, H. J. and Norbury, J. F. Some experiments on equilibrium turbulent boundary layers in favorable pressure gradients. Journal of Fluid Mechanics 27: 541-549. 1967.
33. Horlock, J. H. Discussion. In Sovran, G., editor. Fluid mechanics of internal flow. P. 237. New York, New York, Elsevier Publishing Company. 1967.
34. Horlock, J. H., Louis, J. F., Percival, P. M. E. and Lakshminarayana, B. Wall stall in compressor cascades. American Society of Mechanical Engineers Transactions, Series D: Journal of Basic Engineering 88: 637-648. 1966.
35. Horlock, J. H., Norbury, J. F. and Cooke, J. C. Three-dimensional boundary layers: A report on Euromech 2. Journal of Fluid Mechanics, Part 2, 27: 369-380. 1967.

36. Hornung, H. G. and Joubert, P. N. The mean velocity profile in three-dimensional turbulent boundary layers. *Journal of Fluid Mechanics*, Part 3, 15: 368-384. 1963.
37. Johnston, J. P. Discussion. *American Society of Mechanical Engineers Transactions, Series D: Journal of Basic Engineering* 81: 303. 1959.
38. Johnston, J. P. Discussion. *Fluid mechanics of internal flow*. In Sovran, G., editor. Pp. 230-235. New York, New York, Elsevier Publishing Company. 1967.
39. Johnston, J. P. On the three-dimensional turbulent boundary layer generated by secondary flow. *American Society of Mechanical Engineers Transactions Series D: Journal of Basic Engineering* 82: 233-246. 1960. Also available as Three-dimensional turbulent boundary layer. Massachusetts Institute of Technology Gas Turbine Laboratory Report No. 39. 1957.
40. Joubert, P. N., Perry, A. E. and Brown, K. C. Critical review and current developments in three-dimensional turbulent boundary layers. In Sovran, G., editor. *Fluid mechanics of internal flow*. Pp. 210-237. New York, New York, Elsevier Publishing Company. 1967.
41. Kline, S. J. *Similitude and approximation theory*. New York, New York, McGraw-Hill Book Company, Inc. 1965.
42. Kline, S. J. Some remarks on turbulent shear flows. *Proceedings of the Institution of Mechanical Engineers* 180: 222-244. 1966.
43. Kline, S. J., Abbott, D. E. and Fox, R. W. Optimum design of straight-walled diffusers. *American Society of Mechanical Engineers Transactions, Series D: Journal of Basic Engineering* 81: 321-331. 1959.
44. Kline, S. J. and McClintock, F. A. Describing uncertainties in single sample experiments. *Mechanical Engineering* 75: 3-8. 1953.
45. Kline, S. J., Reynolds, W. C., Schraub, F. A. and Runstadler, P. W. The structure of turbulent boundary layers. *Journal of Fluid Mechanics* 30: 741-773. 1967.
46. Knudsen, J. G. and Katz, D. L. *Fluid dynamics and heat transfer*. New York, New York, McGraw-Hill Book Company, Inc. 1958.
47. Kuethe, A. M., McKee, P. G. and Curry, W. H. Measurements in the boundary layer of a yawed wing. U.S. National Advisory Committee for Aeronautics Technical Note 1946. 1949.

48. Mager, A. Generalization of boundary layer momentum integral equations to three-dimensional flows including those of a rotating system. U.S. National Advisory Committee for Aeronautics Report 1067. 1952.
49. McDonald, H. The departure from equilibrium of turbulent boundary layers. The Aeronautical Quarterly 19: 1-19. 1968.
50. Mellor, G. L. The effects of pressure gradients on turbulent flow near a smooth wall. Journal of Fluid Mechanics 24: 255-274. 1966.
51. Mellor, G. L. Incompressible, turbulent boundary layers with arbitrary pressure gradients and divergent or convergent cross flows. American Institute of Aeronautics and Astronautics Journal 5: 1570-1579. 1967.
52. Milne-Thomson, L. M. Theoretical hydrodynamics. 4th edition. New York, New York, The MacMillan Company. 1960.
53. Nelson, W. G. Skewed turbulent boundary layers. Massachusetts Institute of Technology Gas Turbine Laboratory Report No. 55. 1959.
54. Perry, A. E., Bell, J. B. and Joubert, P. N. Velocity and temperature profiles in adverse pressure gradient turbulent boundary layers. Journal of Fluid Mechanics 25: 299-320. 1966.
55. Perry, A. E. and Joubert, P. N. A three-dimensional turbulent boundary layer. Journal of Fluid Mechanics 22: 285-304. 1965.
56. Phillips, O. M. The maintenance of Reynolds stress in turbulent shear flow. Journal of Fluid Mechanics 27: 131-144. 1967.
57. Pierce, F. J. The law of the wake and plane of symmetry flows in three-dimensional turbulent boundary layers. American Society of Mechanical Engineers Transactions, Series D: Journal of Basic Engineering 88: 101-108. 1966.
58. Pierce, F. J. The turbulent flow at the plane of symmetry of a collateral three-dimensional boundary layer. American Society of Mechanical Engineers Transactions, Series D: Journal of Basic Engineering 86: 227-233. 1964.
59. Pierce, F. J. and Klinksiek, W. F. Secondary flow reversal and velocity profile models in a three-dimensional turbulent boundary layer. Interim Technical Report No. 1. Department of the Army Project No. 20014501B33G, USARO-D Project No. 6858E. 1968. Also Klinksiek, W. F. and Pierce, F. T. Simultaneous lateral skewing in a three-dimensional turbulent boundary layer flow. American Society of Mechanical Engineers Paper No. 69-FE-24. 1969.

60. Pierce, F. J. and Krommenhoek, D. H. Wall shear stress diagnostics in three-dimensional turbulent boundary layers. Interim Technical Report No. 2. Department of the Army Project No. 20014501B33G, USARO-D Project No. 6858E. 1968.
61. Pletcher, R. H. An investigation of secondary flow in the entrance section of a straight rectangular duct. Unpublished M.S. thesis. Ithaca, New York, Library, Cornell University. 1962.
62. Rouse, H. Advanced mechanics of fluids. New York, New York, John Wiley and Sons, Inc. 1959.
63. Rouse, H. and Hassan, M. M. Cavitation-free inlets and contractions. Mechanical Engineering 71: 213-218. 1949.
64. Sagi, C. J. and Johnston, J. P. The design and performance of two-dimensional, curved diffusers. American Society of Mechanical Engineers Transactions, Series D: Journal of Basic Engineering 89: 715-731. 1967.
65. Sandborn, V. A. Metrology of fluid mechanics. Colorado State University, Report CER66VAS32. 1966.
66. Sandborn, V. A. and Slogar, R. J. Study of the momentum distribution of turbulent boundary layers in adverse pressure gradients. U.S. National Advisory Committee for Aeronautics Technical Note 3264. 1955.
67. Schlichting, H. Boundary layer theory. 4th edition. New York, New York, McGraw-Hill Book Company, Inc. 1960.
68. Schubert, G. and Corcos, G. M. The dynamics of turbulence near a wall according to a linear model. Journal of Fluid Mechanics 29: 113-135. 1967.
69. Sherman, F. S. Introduction to three-dimensional boundary layers. The RAND Corporation Memorandum RM-4843-PR. 1968.
70. Smith, P. D. Calculation methods for three-dimensional turbulent boundary layers. Aeronautical Research Council, Reports and Memoranda No. 3523. 1968.
71. Spalding, D. B. Theories of the turbulent boundary layer. Applied Mechanics Reviews 20: 735-740. 1967.
72. Squire, H. B. and Winter, K. G. The secondary flow in a cascade of airfoils in a nonuniform stream. Journal of Aeronautical Sciences 18: 271-277. 1951.

73. Sternberg, J. The three-dimensional structure of the viscous sublayer. North Atlantic Treaty Organization, Advisory Group for Aerospace Research and Development. AGARDograph 97, Part 1. 1965.
74. Taylor, E. S. The skewed boundary layer. American Society of Mechanical Engineers Transactions, Series D: Journal of Basic Engineering 81: 297-304. 1959.
75. Thermo-Systems Incorporated. Hot-film and hot-wire anemometry theory and application bulletin TB5. St. Paul, Minnesota, Thermo-Systems Incorporated. ca. 1967.
76. Townsend, A. A. The properties of equilibrium boundary layers. Journal of Fluid Mechanics 1: 561-573. 1956.
77. Tracy, H. J. Turbulent flow in a three-dimensional channel. Proceedings of American Society of Civil Engineering: Journal of the Hydraulics Division HY6: 9-35. 1965.
78. Tritton, D. J. Some new correlation measurements in a turbulent boundary layer. Journal of Fluid Mechanics 28: 439-462. 1967.

ACKNOWLEDGMENTS

Thanks are expressed to Dr. Ernest W. Anderson, Professor Robert C. Fellinger, Dr. James D. Iversen, Dr. Robert J. Lambert, and Dr. George K. Serovy for serving as the author's graduate study committee.

The guidance and help given by Dr. Serovy as director of the research resulting in this dissertation is gratefully acknowledged.

Financial support received during the course of study from the Chrysler Fellowship, Ford Foundation Forgivable Loan, Iowa State University Engineering Research Institute and the Iowa State University Department of Mechanical Engineering is greatly appreciated.

The author is grateful for the cooperation and help given by Mr. Leon Girard and his machinists, and by Mr. John Siegfried during the development and construction of the test apparatus. Special thanks are due Mr. Clifford Osam for his willing assistance during the entire experimental phase of this dissertation.

Gratitude goes to the author's wife for typing the manuscript. In addition, the author is deeply indebted to his wife and children for their understanding and encouragement throughout the entire graduate program.

APPENDIX A. SELECTED VELOCITY
MODELS FOR THREE-DIMENSIONAL TURBULENT BOUNDARY LAYERS

Polynomial Models

1. Prandtl's suggested relationship

$$\frac{u}{Q} = \Gamma(\eta/\delta, K, \lambda)$$

$$\frac{w}{Q} = \epsilon \Lambda(\eta/\delta, K, \lambda)$$

where $\epsilon = \tan \alpha_w$

α_w = angle between Q and the wall shear vector

η = distance normal to the surface

δ = boundary layer thickness

K, λ = shape factors

2. Mager's (48) model

$$\frac{u}{Q} = (\eta/\delta)^{\frac{1}{7}}$$

$$\frac{w}{Q} = \epsilon \left[1 - (\eta/\delta)^2 \right] (\eta/\delta)^{\frac{1}{7}}$$

3. Cooke's (18) model

$$\frac{u}{Q} = (\eta/\delta)^{(H_1-1)/2}$$

$$\frac{w}{Q} = \epsilon \left[(\eta/\delta)^{(H_1-1)/2} \right] \left[1 - (\eta/\delta)^2 \right]$$

4. Eichelbrenner and Peube's (21) model

$$\frac{u}{Q} = (\eta/\delta)^m$$

$$\frac{w}{Q} = B \left[\frac{u}{Q} - 6\left(\frac{u}{Q}\right)^3 + 8\left(\frac{u}{Q}\right)^4 - 3\left(\frac{u}{Q}\right)^5 \right]$$

$$- C \left[4\left(\frac{u}{Q}\right)^3 - 7\left(\frac{u}{Q}\right)^4 + 3\left(\frac{u}{Q}\right)^5 \right]$$

where $B = e \left[\frac{\partial \left(\frac{w}{Q} \right)}{\partial \left(\frac{u}{Q} \right)} \right]_{\frac{u}{Q}=0}$

$$C = \lim_{\frac{u}{Q} \rightarrow 1} \left(\frac{\frac{w}{Q}}{\frac{u}{Q}-1} \right) = \left. \frac{\partial^3 \left(\frac{w}{Q} \right)}{\partial \left(\frac{u}{Q} \right)^3} \right|_{\frac{u}{Q}=1}$$

5. Smith's (70) model

$$\frac{u}{Q} = (\eta/\delta)^{(H_1-1)/2}$$

$$\frac{w}{Q} = e \left[\frac{u}{Q} - 3\left(\frac{u}{Q}\right)^2 + 3\left(\frac{u}{Q}\right)^3 - \left(\frac{u}{Q}\right)^4 \right]$$

$$- e \left[3\left(\frac{u}{Q}\right)^2 - 5\left(\frac{u}{Q}\right)^3 + 2\left(\frac{u}{Q}\right)^4 \right]$$

where $e = \left. \frac{\frac{\partial \left(\frac{w}{Q} \right)}{\partial \left(\frac{u}{Q} \right)}}{\frac{\partial \left(\frac{u}{Q} \right)}{\partial \left(\frac{u}{Q} \right)}} \right|_{\frac{u}{Q}=1}$

Wake Models

1. Coles' (16) model

$$\vec{q} = \vec{q}_{ss} + \vec{q}_w = \vec{q}^* \left[\frac{1}{K_1} \ln(\eta q^*/v) + K_2 \right] + \frac{\Pi}{K_1} \vec{q}^* w(n/\delta)$$

where \vec{q}^* = friction velocity vector (assumed to be in the direction of the wall shear stress) $\tau_w = \rho q^* q^*$

K_1 = universal constant ≈ 0.41

K_2 = universal constant ≈ 5.0

Π = tensor profile parameter (a function of two space coordinates)

$w(n/\delta)$ = wake function

q_{ss} = total velocity component in the shear stress direction

q_w = total velocity component in the wake direction

2. Nelson's (53) model

$$\vec{q} - \vec{Q} = \frac{\vec{e}_o}{K_1} q^* F_1 (n/\delta) + \frac{\vec{e}_w}{K_1} q^* F_2 (n/\delta)$$

where \vec{Q} = free stream velocity vector

\vec{e}_o = unit vector in the shear stress direction
(assumed to be in the limiting streamline direction)

\vec{e}_w = unit vector in the wake direction (assumed to be along the line comprised of the velocity vector tips in a triangular polar plot)

for $F_1(\eta/\delta) = \ln(\eta/\delta) + 2.04$

$$0 < \eta/\delta \leq 0.0478$$

$$F_1(\eta/\delta) = -\exp(1 - 20.905 (\eta/\delta))$$

for $0.0478 < \eta/\delta \leq \infty$

$$F_2(\eta/\delta) = -\exp(-4.54783 (\eta/\delta)^2)$$

Triangular Velocity Model

Johnston's (39) model

$$\frac{w}{Q} = \epsilon \left[u/Q \right] \quad \text{for the triangular portion near the wall (I)}$$

$$\frac{w}{Q} = A \left[1 - u/Q \right] \quad \text{for the triangular portion near the free stream (II)}$$

where $\frac{\epsilon}{A} = 0.1 \left[(1 + \epsilon^2)^{\frac{1}{4}} / \sqrt{C_{fx}} \right] - 1.0$

$$A = -2Q^2 \int_0^\alpha \frac{d\alpha}{Q^2} \quad (\text{if } Q \text{ is constant, } A = -2\alpha)$$

C_{fx} = skin friction in the free stream direction

α = angle of main flow turning with respect to a fixed direction

Hybrid Models

1. Perry and Joubert's (55) model

Inner profile

$$\frac{U_R}{q^*} = \frac{1}{K} \ln(\eta q^*/v) + A$$

Outer profile

$$\frac{\vec{Q} - \vec{q}}{q^*} = \frac{(U_\infty - u)}{q_\infty} \vec{\Pi}'(\xi, \zeta)$$

where U_R = length of arc at the apex of a velocity polar plot A = parameter influenced by surface roughness U_∞ = upstream 2-D free stream velocity u = upstream 2-D boundary layer velocity $\vec{\Pi}'(\xi, \zeta)$ = a vector depending on free stream flow conditions

2. Joubert, Perry and Brown's (40) model

Inner flow (logarithmic law of wall)

$$\frac{U_R}{q^*} = \frac{1}{K} \ln \left(\frac{\eta q^*}{v} \right) + A - \frac{\Delta u_2}{q^*} \left(\frac{k q^*}{v} \right)$$

Intermediate flow (half power law)

$$\frac{U_R}{q^*} = C \left(\frac{1}{\rho} \frac{dp}{d\xi} \frac{\eta}{(q^*)^2} \right)^{\frac{1}{2}} + \frac{\Delta u_1}{q^*} \left(\frac{[q^*]^3}{v} / \frac{1}{\rho} \frac{dp}{d\xi} \right)$$

$$- \frac{\Delta u_2}{q^*} (k q^* / v)$$

Outer flow

$$\frac{\vec{q} - \vec{q}}{q^*} = \frac{(U_\infty - u)}{q_\infty^*} \vec{n}(\xi, \zeta)$$

where Δu_1 = slip velocity at the wall

Δu_2 = slip velocity function, a function of roughness

Note: Brackets behind $\frac{\Delta u_2}{q^*}$ and $\frac{\Delta u_1}{q^*}$ implies
functional dependence.

k = roughness scale

C = universal constant.

APPENDIX B. TURBULENT FLOW EQUATIONS

This Appendix presents the general coordinate system which are used in the development of the governing equations, some relationships and remarks pertaining to averaging fluctuating terms and finally one method of developing the equations of motion and continuity equation in terms of curvilinear coordinates using general scale factors.

Coordinate System

As was mentioned in the Literature Review Section, the intrinsic or natural coordinate system is advocated when working with skewed boundary layers. One of the advantages for using this system is that only one velocity component exists at the edge of the boundary layer. This fact is used in finding values for scale factors and an order of magnitude for the pressure term. Designation of the particular coordinates is as follows:

ξ - represents the coordinate in the direction of the free stream velocity (the coordinate which is tangent to the streamline at the edge of a boundary layer).

η - represents the coordinate perpendicular to ξ (assumed to be approximately normal to the surface over which the boundary layer is developing).

ζ - represents the coordinate perpendicular to both ξ and η in the "crossflow" direction.

Velocity designations will have the notation of u , v , and w which are the instantaneous velocity components in the ξ , η and ζ direction

respectively. If \vec{e}_1 , \vec{e}_2 and \vec{e}_3 are the curvilinear coordinate unit vectors, then the total velocity relationship is

$$\vec{Q} = u \vec{e}_1 + v \vec{e}_2 + w \vec{e}_3. \quad (\text{B-1})$$

Figure 60 depicts the coordinate relationships and shows the definitions of the unit vectors and the scale factors h_1 , h_2 and h_3 which are sometimes called "length stretching factors" to imply their function.

Some vector relationships will be required to obtain the format most suited for similarity analysis. The following relationships can be found in Milne-Thomson (52) which are in terms of the orthogonal coordinate system as shown in Figure 60.

$$\nabla(\) = \frac{1}{h_1} \frac{\partial(\)}{\partial \xi} \vec{e}_1 + \frac{\partial(\)}{\partial \eta} \vec{e}_2 + \frac{1}{h_3} \frac{\partial(\)}{\partial \zeta} \vec{e}_3 \quad (\text{B-2})$$

$$\nabla^2(\) = \frac{1}{h_1 h_2 h_3} \left\{ \frac{\partial}{\partial \xi} \left(\frac{h_2 h_3}{h_1} \frac{\partial(\)}{\partial \xi} \right) + \frac{\partial}{\partial \eta} \left(\frac{h_1 h_3}{h_2} \frac{\partial(\)}{\partial \eta} \right) + \frac{\partial}{\partial \zeta} \left(\frac{h_1 h_2}{h_3} \frac{\partial(\)}{\partial \zeta} \right) \right\} \quad (\text{B-3})$$

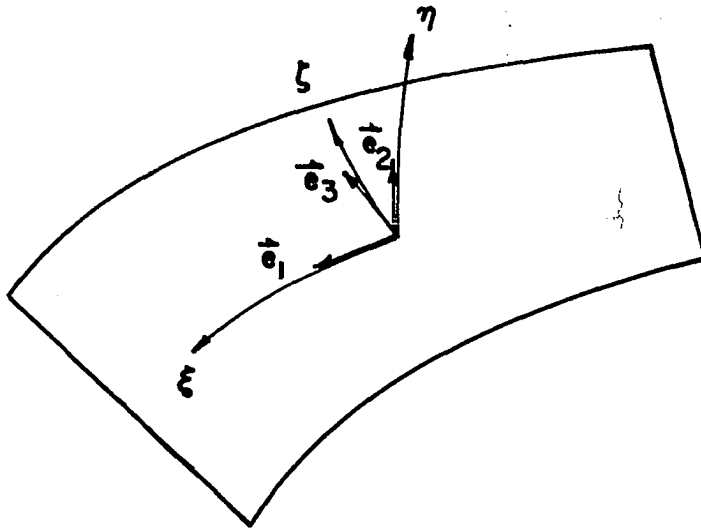
$$\nabla \vec{Q} = \vec{\Omega} = \frac{1}{h_1 h_2 h_3} \begin{vmatrix} h_1 \vec{e}_1 & h_2 \vec{e}_2 & h_3 \vec{e}_3 \\ \frac{\partial}{\partial \xi} & \frac{\partial}{\partial \eta} & \frac{\partial}{\partial \zeta} \\ h_1 u & h_2 v & h_3 w \end{vmatrix} \quad (\text{B-4})$$

If we let

$$\vec{\Omega} = \Omega_1 \vec{e}_1 + \Omega_2 \vec{e}_2 + \Omega_3 \vec{e}_3$$

then

$$\vec{Q}_x (\nabla \vec{Q}) = \vec{Q}_x \vec{\Omega} = \frac{1}{h_1 h_2 h_3} \begin{vmatrix} h_1 \vec{e}_1 & h_2 \vec{e}_2 & h_3 \vec{e}_3 \\ h_1 u & h_2 v & h_3 w \\ h_1 \Omega_1 & h_2 \Omega_2 & h_3 \Omega_3 \end{vmatrix}. \quad (\text{B-5})$$



Curvilinear coordinates ξ, η, ζ

$$\text{Curvilinear unit vectors } \vec{e}_1 = \frac{1}{h_1} \frac{\partial \vec{r}}{\partial \xi}$$

$$\vec{e}_2 = \frac{1}{h_2} \frac{\partial \vec{r}}{\partial \eta}$$

$$\vec{e}_3 = \frac{1}{h_3} \frac{\partial \vec{r}}{\partial \zeta}$$

Scale factors

$$h_1 = \left\{ \left(\frac{\partial x}{\partial \xi} \right)^2 + \left(\frac{\partial y}{\partial \xi} \right)^2 + \left(\frac{\partial z}{\partial \xi} \right)^2 \right\}^{1/2}$$

$$h_2 = \left\{ \left(\frac{\partial x}{\partial \eta} \right)^2 + \left(\frac{\partial y}{\partial \eta} \right)^2 + \left(\frac{\partial z}{\partial \eta} \right)^2 \right\}^{1/2}$$

$$h_3 = \left\{ \left(\frac{\partial x}{\partial \zeta} \right)^2 + \left(\frac{\partial y}{\partial \zeta} \right)^2 + \left(\frac{\partial z}{\partial \zeta} \right)^2 \right\}^{1/2}$$

Figure 60. Orthogonal curvilinear coordinates

Governing Equations

A primary equation used to analytically describe the boundary layer characteristics is obtained through an order of magnitude analysis of the Navier-Stokes equations. A derivation of the Navier-Stokes equations can be found in many texts, for example Schlichting (67) and Rouse (62), and the final form in Cartesian tensor notation is:

$$\rho \left[\frac{\partial q_i}{\partial t} + q_j \frac{\partial q_i}{\partial x_j} \right] = - \frac{\partial P}{\partial x_i} + F_i + \frac{\partial}{\partial x_j} \left[\mu \left(\frac{\partial q_i}{\partial x_j} + \frac{\partial q_j}{\partial x_i} \right) \right] + \frac{\partial}{\partial x_i} \left(\lambda \frac{\partial q_k}{\partial x_k} \right) \quad (B-6)$$

where

ρ = fluid density

t = time

q = any of the three velocity components dictated by its subscript

x = any of the three coordinates dictated by its subscript

P = thermodynamic pressure

F = body force density in the direction dictated by its subscript

μ = fluid viscosity

λ = second coefficient of viscosity (bulk viscosity).

The equation as presented is valid for a compressible, variable viscosity, isotropic, continuous Newtonian fluid. In order to simplify the equation it will be assumed that the fluid encountered in this work is incompressible, has constant viscosity, the mean-flow is steady and that body forces are negligible. The equation then reduces to

$$\rho q_j \frac{\partial q_i}{\partial x_j} = - \frac{\partial P}{\partial x_i} + \mu \frac{\partial}{\partial x_j} \left(\frac{\partial q_i}{\partial x_j} + \frac{\partial q_j}{\partial x_i} \right). \quad (B-7)$$

Converting the Navier-Stokes equation from Cartesian coordinates to orthogonal curvilinear coordinates is accomplished from the vector form of Equation B-7 which is

$$\rho (\vec{Q} \cdot \nabla) \vec{Q} = - \nabla P - \mu \nabla \times (\nabla \times \vec{Q}) \quad (B-8)$$

where

$$\vec{Q} = q_1 \vec{i} + q_2 \vec{j} + q_3 \vec{k}$$

or $Q = \left(q_1^2 + q_2^2 + q_3^2 \right)^{1/2}.$

The vector expression on the left side of equation B-8 does not lend itself to conversion from Cartesian to orthogonal curvilinear coordinates because derivatives of the unit vectors in the curvilinear coordinate system appear in the expansion process. This does not present a problem if the unit vectors are known explicitly as in cylindrical or spherical coordinates but if the derivation is to remain general then expressions for the second derivatives of the Cartesian components (x, y, z) with respect to the curvilinear components must be determined as a function of only the scale factors and the curvilinear coordinates. Rouse (62) has these values tabulated but, nevertheless, the nine unit vector derivatives expand into thirty-six terms. To circumvent this problem a vector identity for the left hand side of Equation B-8 is obtained and the expansion is accomplished from the new form. The vector identity

$$(\vec{Q} \cdot \nabla) \vec{Q} = \nabla \left(\frac{Q^2}{2} \right) - \vec{Q} \times (\nabla \times \vec{Q}) \quad (B-9)$$

is found in Schlichting (67) for one. Because we have assumed the fluid to be incompressible another vector identity will simplify the equation further. This identity is

$$\nabla \times (\nabla \times \vec{Q}) = \nabla(\nabla \cdot \vec{Q}) - \nabla^2 \vec{Q}$$

and since $\nabla \cdot \vec{Q} = 0$ for incompressible flow it reduces to

$$\nabla \times (\nabla \times \vec{Q}) = -\nabla^2 \vec{Q}. \quad (B-10)$$

Using Equations B-8, B-9 and B-10 the final form of the Navier-Stokes equation from which conversion to curvilinear coordinates will take place is

$$\rho \left(\nabla(Q^2/2) - \vec{Q} \times (\nabla \times \vec{Q}) \right) = -\nabla P + \mu \nabla^2 \vec{Q}. \quad (B-11)$$

Equation B-11 is the total vector equation and to put it in more amenable terms, that is, express it as three equations in the ξ , η and ζ directions, a dot product of the unit vectors and the quantities in Equation B-11 are taken.

The ξ direction equation will be developed by separately looking at the four terms in Equation B-11. Through the use of Equations B-1 and B-2 the first term of the Navier-Stokes equation can be written as

$$\nabla \left(\frac{Q^2}{2} \right) \cdot \vec{e}_1 = \frac{1}{h_1} \frac{\partial}{\partial \xi} \left(\frac{Q^2}{2} \right) = \frac{1}{h_1} \left(u \frac{\partial u}{\partial \xi} + v \frac{\partial u}{\partial \xi} + w \frac{\partial u}{\partial \xi} \right). \quad (B-12)$$

Using Equations B-1, B-4 and B-5 the second term becomes

$$\begin{aligned}
 [\vec{Q} \times (\nabla \times \vec{Q})] \cdot \vec{e}_1 &= \frac{1}{h_1 h_2 h_3} \left\{ h_2 h_3 v \Omega_3 - h_2 h_3 w \Omega_2 \right\} h_1 \\
 &= v \left\{ \frac{1}{h_1 h_2} \left[\frac{\partial}{\partial \xi} (h_2 v) - \frac{\partial}{\partial \eta} (h_1 u) \right] \right\} \\
 &\quad + w \left\{ \frac{1}{h_1 h_3} \left[\frac{\partial}{\partial \xi} (h_3 w) - \frac{\partial}{\partial \zeta} (h_1 u) \right] \right\}. \tag{B-13}
 \end{aligned}$$

Next to the last term, the pressure term, is found by use of Equation B-2 and results in

$$\nabla P \cdot \vec{e}_1 = \frac{1}{h_1} \frac{\partial P}{\partial \xi}. \tag{B-14}$$

Finally, the last term is converted using Equation B-3 and yields the following relation

$$v^2 \vec{Q} \cdot \vec{e}_1 = \frac{1}{h_1 h_2 h_3} \left\{ \frac{\partial}{\partial \xi} \left(\frac{h_2 h_3}{h_1} \frac{\partial u}{\partial \xi} \right) + \frac{\partial}{\partial \eta} \left(\frac{h_1 h_3}{h_2} \frac{\partial u}{\partial \eta} \right) + \frac{\partial}{\partial \zeta} \left(\frac{h_1 h_2}{h_3} \frac{\partial u}{\partial \zeta} \right) \right\}. \tag{B-15}$$

Noting that upon expansion of Equation B-13, the terms $\frac{v}{h_1} \frac{\partial v}{\partial \xi}$ and $\frac{w}{h_1} \frac{\partial w}{\partial \xi}$ appear which will cancel two terms in Equation B-12 when the correct sign is applied corresponding to Equation B-11 and then rearranging terms the final form of the Navier-Stokes equation in the ξ -direction can be obtained. One can similarly obtain the equations for the η and ζ -directions. The three equations are as follows:

ξ -direction

$$\rho \left\{ \frac{u}{h_1} \frac{\partial u}{\partial \xi} + \frac{v}{h_2} \frac{\partial u}{\partial \eta} + \frac{w}{h_3} \frac{\partial u}{\partial \zeta} - \frac{v}{h_1 h_2} \left[v \frac{\partial h_2}{\partial \xi} - u \frac{\partial h_1}{\partial \eta} \right] - \frac{w}{h_1 h_3} \left[w \frac{\partial h_3}{\partial \xi} - u \frac{\partial h_1}{\partial \zeta} \right] \right\} = \\ - \frac{1}{h_1} \frac{\partial p}{\partial \xi} + \frac{\mu}{h_1 h_2 h_3} \left\{ \frac{\partial}{\partial \xi} \left(\frac{h_2 h_3}{h_1} \frac{\partial u}{\partial \xi} \right) + \frac{\partial}{\partial \eta} \left(\frac{h_1 h_3}{h_2} \frac{\partial u}{\partial \eta} \right) + \frac{\partial}{\partial \zeta} \left(\frac{h_1 h_2}{h_3} \frac{\partial u}{\partial \zeta} \right) \right\} \quad (B-16)$$

η -direction

$$\rho \left\{ \frac{u}{h_1} \frac{\partial v}{\partial \xi} + \frac{v}{h_2} \frac{\partial v}{\partial \eta} + \frac{w}{h_3} \frac{\partial v}{\partial \zeta} - \frac{u}{h_1 h_2} \left[u \frac{\partial h_1}{\partial \eta} - v \frac{\partial h_2}{\partial \xi} \right] - \frac{w}{h_2 h_3} \left[w \frac{\partial h_3}{\partial \eta} - v \frac{\partial h_2}{\partial \zeta} \right] \right\} = \\ - \frac{1}{h_2} \frac{\partial p}{\partial \eta} + \frac{\mu}{h_1 h_2 h_3} \left\{ \frac{\partial}{\partial \xi} \left(\frac{h_2 h_3}{h_1} \frac{\partial v}{\partial \xi} \right) + \frac{\partial}{\partial \eta} \left(\frac{h_1 h_3}{h_2} \frac{\partial v}{\partial \eta} \right) + \frac{\partial}{\partial \zeta} \left(\frac{h_1 h_2}{h_3} \frac{\partial v}{\partial \zeta} \right) \right\} \quad (B-17)$$

ζ -direction

$$\rho \left\{ \frac{u}{h_1} \frac{\partial w}{\partial \xi} + \frac{v}{h_2} \frac{\partial w}{\partial \eta} + \frac{w}{h_3} \frac{\partial w}{\partial \zeta} - \frac{u}{h_1 h_3} \left[u \frac{\partial h_1}{\partial \zeta} - w \frac{\partial h_3}{\partial \xi} \right] - \frac{v}{h_2 h_3} \left[v \frac{\partial h_2}{\partial \zeta} - w \frac{\partial h_3}{\partial \eta} \right] \right\} = \\ - \frac{1}{h_3} \frac{\partial p}{\partial \zeta} + \frac{\mu}{h_1 h_2 h_3} \left\{ \frac{\partial}{\partial \xi} \left(\frac{h_2 h_3}{h_1} \frac{\partial w}{\partial \xi} \right) + \frac{\partial}{\partial \eta} \left(\frac{h_1 h_3}{h_2} \frac{\partial w}{\partial \eta} \right) + \frac{\partial}{\partial \zeta} \left(\frac{h_1 h_2}{h_3} \frac{\partial w}{\partial \zeta} \right) \right\} \quad (B-18)$$

The remaining governing equation is the continuity equation. One method of obtaining it in curvilinear coordinates is to derive it using the law of conservation of mass in conjunction with a control volume with elemental sides of $h_1 \Delta\xi$, $h_2 \Delta\eta$, and $h_3 \Delta\zeta$. Assuming steady and incompressible flow the continuity equation becomes

$$\frac{1}{h_1 h_2 h_3} \left\{ \frac{\partial}{\partial \xi} (uh_2 h_3) + \frac{\partial}{\partial \eta} (vh_1 h_3) + \frac{\partial}{\partial \zeta} (wh_1 h_2) \right\} = 0 . \quad (B-19)$$

Averaging of Fluctuating Variables

In order to approximate the instantaneous properties in fluid flow systems the instantaneous value is expressed as the sum of a time average component and a fluctuating component. Using the notation of Schlichting (67) and some rules he presented, the relations for instantaneous and time averaged values will be given.

Let f and g be dependent variables and let s denote any space or time independent variable. In addition, let T denote a sufficiently long time period so the mean values are independent of time, that is, if a longer time period was involved in determining the mean value the value would remain unchanged. This assumption restricts the analysis to steady flow in the mean. This could be relaxed by assuming that T denote a time period which is large in comparison to the time required for turbulent oscillations but small enough to neglect changes in the mean. Graphical representations of these two types of flow are shown in Figure 61. The mathematical relationships between the instantaneous, mean and fluctuating values for a dependent variable are as follows:

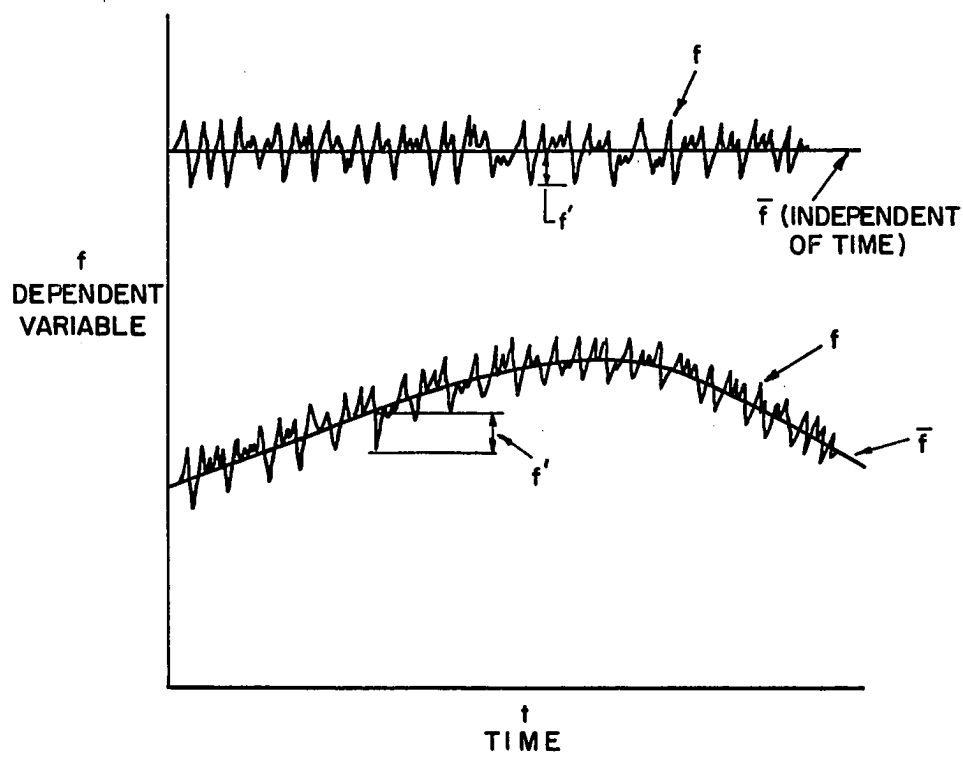


Figure 61. Oscillations of a variable about a mean value

$$f = \bar{f} + f'$$

f = instantaneous value

\bar{f} = mean value

f' = fluctuating value

$$\bar{f} = \frac{1}{T} \int_{t_0}^{t_0+T} f dt$$

From the previous equations it is seen that $\bar{f}' = 0$. This can be shown in the following way. Take the time average of the equation for f ,

$$\frac{1}{T} \int_{t_0}^{t_0+T} f dt = \frac{1}{T} \int_{t_0}^{t_0+T} \bar{f} dt + \frac{1}{T} \int_{t_0}^{t_0+T} f' dt$$

$$\bar{f} = \bar{\bar{f}} + \bar{f}'$$

but $\bar{\bar{f}} = \bar{f}$ since it is independent of the time period which results in $\bar{f}' = 0$.

Some of the operating rules which are required to formulate the boundary layer equations in terms of average values are:

$$\overline{\overline{f}} = \bar{f}$$

$$\overline{\overline{f + g}} = \bar{f} + \bar{g}$$

$$\overline{\overline{f \cdot g}} = \bar{f} \cdot \bar{g}$$

$$\overline{\frac{\partial f}{\partial s}} = \frac{\partial \bar{f}}{\partial s}$$

$$\overline{\int f ds} = \int \bar{f} ds$$

APPENDIX C. HOT-WIRE INSTRUMENTATION

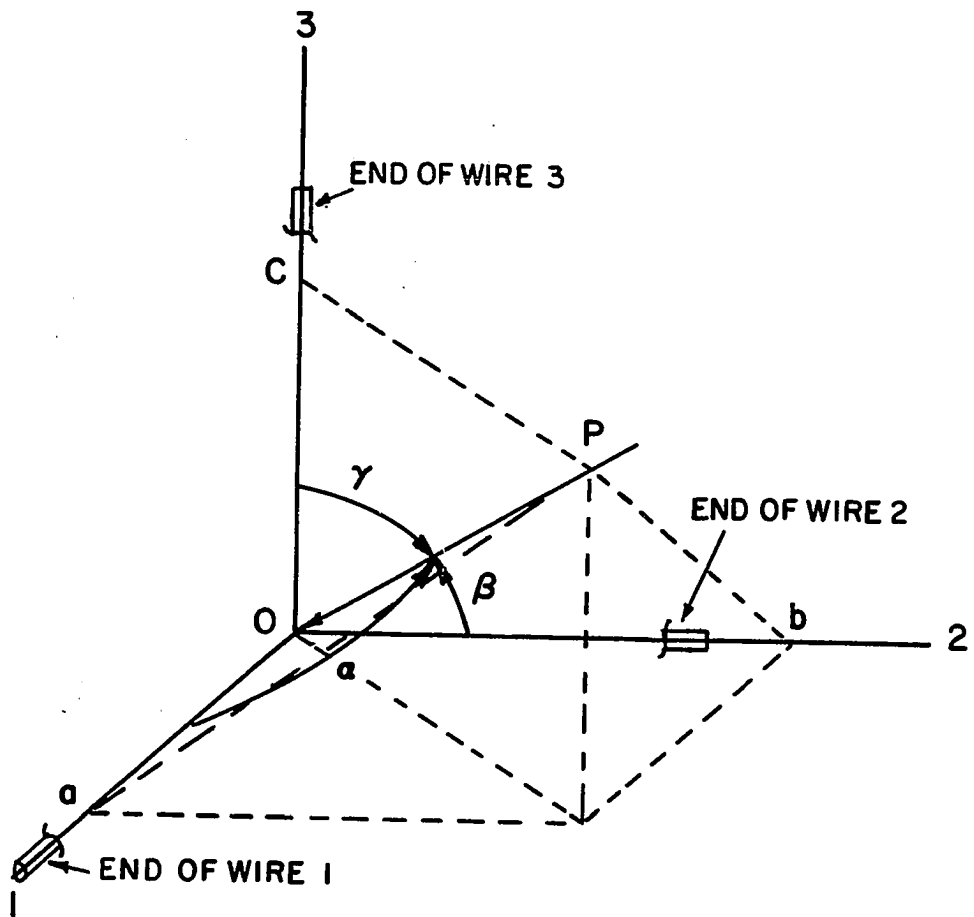
The experimental results reported are dependent on both the data procurement technique and the associated theoretical model. This Appendix develops the pertinent mathematical models and discusses the design of the probes.

Hot-Wire Equations

A set of equations assumed to be valid for three-dimensional flow was developed in terms of instantaneous variables and converted to mean and fluctuating variables allowing the equations to be separated into two sets. Finally the equations were reduced to a set which is valid for the mean velocity vector oriented in the plane of two wires. Before developing the equations, a set of coordinates and nomenclature was required.

Coordinate system and nomenclature

The hot-wire responds to the total instantaneous velocity but the magnitude of the response is dependent on the orientation of the wire with respect to the flow. In order to have the angle between the total velocity vector and each orthogonal coordinate be the total angle, a polar space coordinate system was adopted. Figure 62 shows the coordinate system which is considered coincident with the wire orientation (wires are parallel to the coordinate axes). Polar space coordinates were first made known to this author for this type of analysis through a suggestion in Thermo-Systems Incorporated (75). Since the



$$(0-P)^2 = (0-a)^2 + (0-b)^2 + (0-c)^2$$

$$\cos^2 \alpha + \cos^2 \beta + \cos^2 \gamma = 1$$

$$\alpha = \cos^{-1} \left\{ \frac{(0-a)}{(0-P)} \right\}$$

$$\beta = \cos^{-1} \left\{ \frac{(0-b)}{(0-P)} \right\}$$

$$\gamma = \cos^{-1} \left\{ \frac{(0-c)}{(0-P)} \right\}$$

Figure 62. Polar space coordinate system

instantaneous and mean velocity vectors are in general not oriented in the same way with respect to each wire a distinction was made by the following nomenclature:

Q_I = instantaneous velocity

α, β, γ = instantaneous angles between Q_I and the wires

Q_S = mean velocity

$\bar{\alpha}, \bar{\beta}, \bar{\gamma}$ = mean angles between Q_S and the wires.

The instantaneous velocity was defined in terms of the mean and fluctuating velocities as

$$Q_I^2 = (Q_S \pm q_s)^2 + q_n^2 + q_t^2$$

where

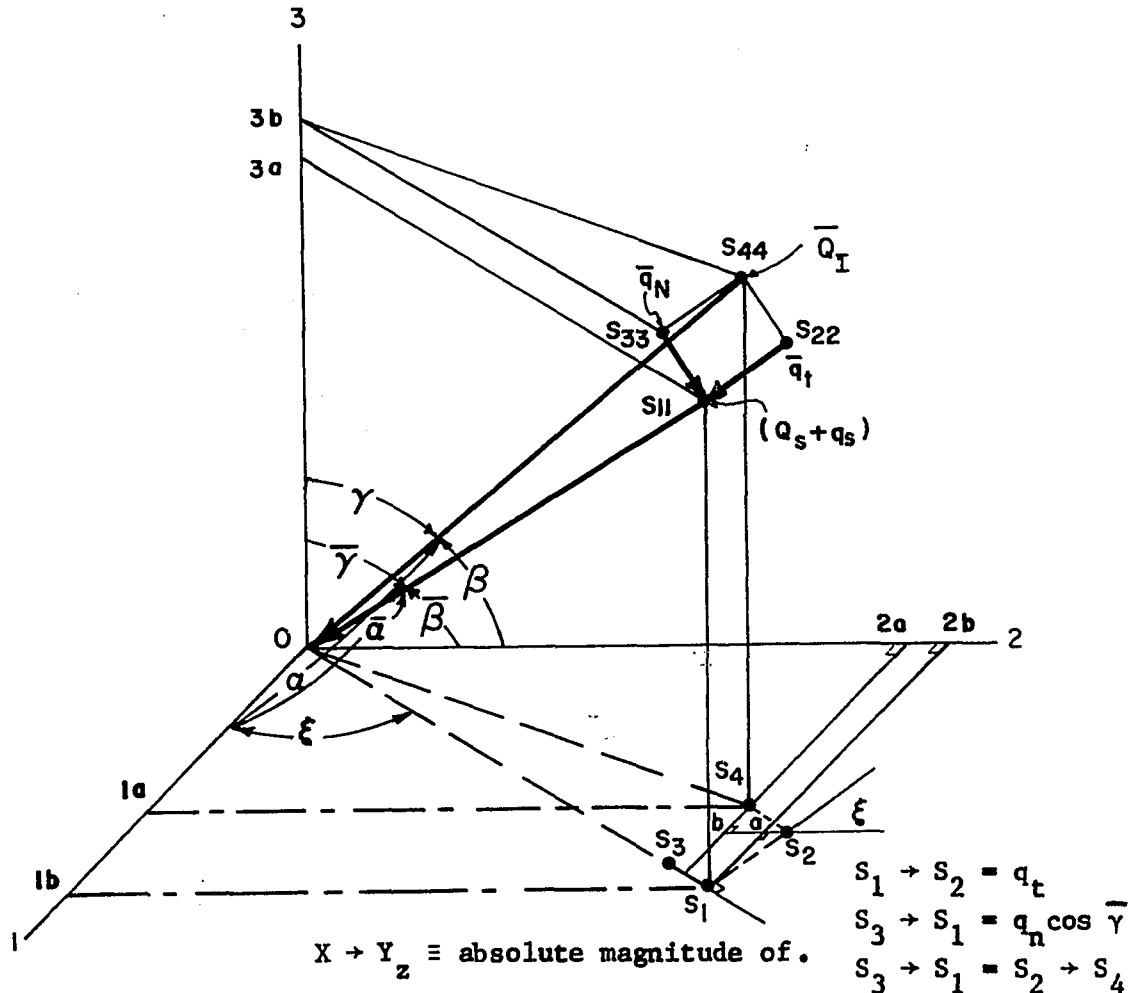
q_s = fluctuating velocity component in the mean flow direction

q_t = fluctuating velocity component in a plane parallel to the 0-1-2 plane in Figure 62 and perpendicular to q_s

q_n = fluctuating velocity component perpendicular to both q_s and q_t .

Figure 63 shows the geometrical relationship between instantaneous, mean and fluctuating quantities. A sign convention was adopted based on the mean velocity component and fluctuating components perpendicular to the wire in question. If the perpendicular components are in the same direction as the mean velocity component, then they are considered positive in sign. For the particular orientation shown in Figure 63 the fluctuating quantities have the following signs:

$$3a \rightarrow 3b = q_n \sin \gamma$$



$$0 \rightarrow 1a = Q_I \cos \alpha$$

$$0 \rightarrow S_{11} = q_s + q_t$$

$$0 \rightarrow 1b = (Q_s + q_s) \cos \bar{\alpha}$$

$$0 \rightarrow S_1 = (Q_s + q_s) \sin \bar{\gamma}$$

$$0 \rightarrow 2a = Q_I \cos \beta$$

$$\sin \xi = \frac{(Q_s + q_s) \cos \bar{\beta}}{(Q_s + q_s) \sin \bar{\gamma}} = \frac{\cos \bar{\beta}}{\sin \bar{\gamma}}$$

$$0 \rightarrow 2b = (Q_s + q_s) \cos \bar{\beta}$$

$$\cos \xi = \frac{\cos \bar{\alpha}}{\sin \bar{\gamma}}$$

$$0 \rightarrow 3b = Q_I \cos \gamma$$

$$0 \rightarrow 3a = (Q_s + q_s) \cos \bar{\gamma}$$

Figure 63. Velocity vectors and geometrical relationships

Wire 1

- (a) q_s is (+)
- (b) q_t is (+)
- (c) q_N is (-)

Wire 2

- (a) q_s is (+)
- (b) q_t is (-)
- (c) q_N is (-)

Wire 3

- (a) q_s is (+)
- (b) q_t is (+)
- (c) q_N is (-).

In the case of wire 3 the q_t component is positive because it will always add to the cooling effect of the wire since it is perpendicular to both the wire and to the mean velocity component.

Instantaneous equations

Champagne et al. (11) made a study of the heat transfer relationship with respect to an inclined wire. From the study the instantaneous relationship

$$U_I^2 = Q_I^2 (\sin^2 \alpha + k^2 \cos^2 \alpha) \quad (C-1)$$

was developed (in terms of the nomenclature used in this work). The expression shows that cooling of the wire results from the velocity

component perpendicular to the wire and from a weighted portion of the velocity component parallel to the wire. They claimed the weighting factor "k" is primarily a function of the length to diameter ratio of the wire and independent of the angle between the velocity vector and the wire. More is said about "k" in a subsequent paragraph. U is defined as the equivalent cooling velocity and may be thought of as the velocity which would result from a calibration curve of electrical power versus velocity for a wire perpendicular to the mean velocity vector if the magnitude of the electrical power from an inclined wire is used in conjunction with the calibration curve.

Another proposed instantaneous equation was developed by Friehe and Schwarz (26). Since $U = Q_I$ at $\alpha = 90^\circ$, then one form of their equation is

$$U^2 = Q_I^2 \left(1 - b \left[1 - \sin^{\frac{1}{2}} \alpha \right] \right)^4. \quad (C-2)$$

Friehe and Schwarz showed that k in Equation C-1 and b in Equation C-2 are related by

$$k^2 = \tan^2 \alpha \left\{ \left(b + \frac{1 - b}{\sin^{\frac{1}{2}} \alpha} \right)^4 - 1 \right\} \quad (C-3)$$

so that k is a function of angle, contrary to what was reported by Champagne et al. (11).

Because of the type of relationship between the instantaneous, mean and fluctuating velocity components it is not possible to obtain the mean angles as a function of the instantaneous angles alone. A method of overcoming this difficulty is to determine products of the instantaneous velocity and trigonometric functions in terms of the mean and

fluctuating velocities and the mean trigonometric functions. This was done by Champagne for a single wire. The present approach was different in that the components were determined by a different technique and three wires were analyzed concurrently in place of one. If sensors one, two and three are represented by lines 0-1, 0-2 and 0-3 respectively in Figure 63 and the instantaneous relationships for the three sensors are respectively

$$U^2 = Q_I^2 + (k_1^2 - 1) Q_I^2 \cos^2 \alpha \quad (C-4)$$

$$V^2 = Q_I^2 + (k_2^2 - 1) Q_I^2 \cos^2 \beta \quad (C-5)$$

$$W^2 = Q_I^2 + (k_3^2 - 1) Q_I^2 \cos^2 \gamma \quad (C-6)$$

then only three products of instantaneous velocities and trigonometric functions are required.

As is noted in Figure 63, $Q_I \cos \alpha$ is represented by 0-1a and $(Q_s + q_s) \cos \bar{\alpha}$ by 0-1b. For the particular orientation of the vectors it is therefore seen that

$$Q_I \cos \alpha = (Q_s + q_s) \cos \bar{\alpha} - (lb - 1a)$$

$$\text{where } (lb - 1a) = (S_1 - a) + (b - S_4)$$

$$= q_t \sin \xi + q_n \cos \bar{\gamma} \cos \xi$$

$$= q_t \frac{\cos \bar{\beta}}{\sin \bar{\gamma}} + q_n \frac{\cos \bar{\gamma} \cos \bar{\alpha}}{\sin \bar{\gamma}}$$

which results in

$$Q_I \cos \alpha = (Q_s + q_s) \cos \bar{\alpha} - q_t \frac{\cos \bar{\beta}}{\sin \bar{\gamma}} - q_n \frac{\cos \bar{\gamma} \cos \bar{\alpha}}{\sin \bar{\gamma}} . \quad (C-7)$$

Similarly,

$$Q_I \cos \beta = (Q_s + q_s) \cos \bar{\beta} + q_t \frac{\cos \bar{\alpha}}{\sin \bar{\gamma}} - q_n \frac{\cos \bar{\gamma} \cos \bar{\beta}}{\sin \bar{\gamma}} \quad (C-8)$$

and

$$Q_I \cos \gamma = (Q_s + q_s) \cos \bar{\gamma} + q_n \sin \bar{\gamma} . \quad (C-9)$$

It should be noted that if the instantaneous velocity changes orientation with respect to the mean vector, the signs of the fluctuating terms change accordingly. To be general, the signs of the fluctuating quantities should be \pm .

Using the definition of Q_I and Equations C-7, C-8 and C-9, Equations C-4, C-5 and C-6 become:

$$\begin{aligned} U^2 &= Q_s^2 \pm 2q_s Q_s + q_s^2 + q_t^2 + q_n^2 - (1 - k_1^2) \left\{ Q_s^2 \cos^2 \bar{\alpha} \pm 2q_s Q_s \cos^2 \bar{\alpha} \right. \\ &\quad + q_s^2 \cos^2 \bar{\alpha} + q_t^2 \frac{\cos^2 \bar{\beta}}{\sin^2 \bar{\gamma}} + q_n^2 \frac{\cos^2 \bar{\gamma} \cos^2 \bar{\alpha}}{\sin^2 \bar{\gamma}} \pm 2q_t Q_s \frac{\cos \bar{\alpha} \cos \bar{\beta}}{\sin \bar{\gamma}} \\ &\quad \pm 2q_n Q_s \frac{\cos^2 \bar{\alpha} \cos \bar{\gamma}}{\sin \bar{\gamma}} \pm 2q_s q_t \frac{\cos \bar{\alpha} \cos \bar{\beta}}{\sin \bar{\gamma}} \pm 2q_s q_n \frac{\cos^2 \bar{\alpha} \cos \bar{\gamma}}{\sin \bar{\gamma}} \\ &\quad \left. \pm q_t q_n \frac{\cos \bar{\gamma} \cos \bar{\alpha} \cos \bar{\beta}}{\sin^2 \bar{\gamma}} \right\} \end{aligned} \quad (C-10)$$

$$\begin{aligned}
 v^2 = Q_s^2 & \pm 2q_s Q_s + q_s^2 + q_t^2 + q_n^2 - (1 - k_2^2) \left\{ Q_s^2 \cos^2 \bar{\beta} \pm 2q_s Q_s \cos^2 \bar{\beta} \right. \\
 & + q_s^2 \cos^2 \bar{\beta} + q_t^2 \frac{\cos^2 \bar{\alpha}}{\sin^2 \bar{\gamma}} + q_n^2 \frac{\cos^2 \bar{\gamma} \cos^2 \bar{\alpha}}{\sin^2 \bar{\gamma}} \pm 2q_t Q_s \frac{\cos \bar{\beta} \cos \bar{\alpha}}{\sin \bar{\gamma}} \\
 & \pm 2q_n Q_s \frac{\cos^2 \bar{\beta} \cos \bar{\gamma}}{\sin \bar{\gamma}} \pm 2q_s q_t \frac{\cos \bar{\beta} \cos \bar{\alpha}}{\sin \bar{\gamma}} \pm 2q_s q_n \frac{\cos^2 \bar{\beta} \cos \bar{\gamma}}{\sin \bar{\gamma}} \\
 & \left. \pm 2q_t q_n \frac{\cos \bar{\gamma} \cos \bar{\alpha} \cos \bar{\beta}}{\sin^2 \bar{\gamma}} \right\} \tag{C-11}
 \end{aligned}$$

$$\begin{aligned}
 w^2 = Q_s^2 & \pm 2q_s Q_s + q_s^2 + q_t^2 + q_n^2 - (1 - k_3^2) \left\{ Q_s^2 \cos^2 \bar{\gamma} \pm 2q_s Q_s \cos^2 \bar{\gamma} \right. \\
 & + q_s^2 \cos^2 \bar{\gamma} + q_n^2 \sin^2 \bar{\gamma} \pm 2q_n Q_s \sin \bar{\gamma} \cos \bar{\gamma} \pm 2q_s q_n \sin \bar{\gamma} \cos \bar{\gamma} \left. \right\} \tag{C-12}
 \end{aligned}$$

If it is assumed that the turbulence level is low, that is $q_s/Q_s \ll 1$, $q_t/Q_s \ll 1$ and $q_n/Q_s \ll 1$, then Equations C-10, C-11 and C-12 can be reduced and rearranged to yield

$$\begin{aligned}
 v^2 = Q_s^2 & \left(1 - (1 - k_1^2) \cos^2 \bar{\alpha} \right) \pm 2q_s Q_s - (1 - k_1^2) \left\{ \pm 2q_s Q_s \cos^2 \bar{\alpha} \right. \\
 & \pm 2q_t Q_s \frac{\cos \bar{\alpha} \cos \bar{\beta}}{\sin \bar{\gamma}} \pm 2q_n Q_s \frac{\cos^2 \bar{\alpha} \cos \bar{\gamma}}{\sin \bar{\gamma}} \left. \right\} \tag{C-13}
 \end{aligned}$$

$$v^2 = Q_s^2 \left(1 - (1 - k_2^2) \cos^2 \bar{\beta} \right) \pm 2q_s Q_s - (1 - k_2^2) \left\{ \begin{array}{l} \pm 2q_s Q_s \cos^2 \bar{\beta} \\ \pm 2q_s Q_s \frac{\cos \bar{\alpha} \cos \bar{\beta}}{\sin \bar{\gamma}} \pm 2q_n Q_s \frac{\cos^2 \bar{\beta} \cos \bar{\gamma}}{\sin \bar{\gamma}} \end{array} \right\} \quad (C-14)$$

$$w^2 = Q_s^2 \left(1 - (1 - k_3^2) \cos^2 \bar{\gamma} \right) \pm 2q_s Q_s - (1 - k_3^2) \left\{ \begin{array}{l} \pm 2q_s Q_s \cos^2 \bar{\gamma} \\ \pm 2q_n Q_s \sin \bar{\gamma} \cos \bar{\gamma} \end{array} \right\} . \quad (C-15)$$

In the following an approach using simpler equations is presented and an analogy is drawn to obtain the equations actually used in this investigation in their final form. First, more nomenclature is needed, then a form of the binomial series is presented. Assume that \bar{U} is the mean velocity and u is the fluctuating velocity, therefore

$$U = \bar{U} + u \quad (C-16)$$

or

$$U^2 = \bar{U}^2 + 2u\bar{U} + u^2 . \quad (C-17)$$

Following the procedure used to obtain Equations C-13, C-14 and C-15, only terms of higher orders of magnitude were retained based on the assumption that $u/U \ll 1$. Of course this approach would not be necessary if Equation C-16 was the only important one, but the approach is supported when it is observed that the present method results in the same equations as the expansion of one term of King's equation using Equation

C-16 directly. King's equation was assumed to be valid. For constant density and viscosity it can be written as

$$\begin{aligned} K_1 E^2 &= K_2 + K_3 U^N \\ &= K_2 + K_3 (U^2)^{N/2}. \end{aligned} \quad (C-18)$$

K_1 is equal to $R_s / (R_T^2 (R_{oh} - 1.0))$ and K_2 and K_3 are defined on page 91. Also, it was assumed that the voltage, E , can be expressed as the sum of the mean voltage, \bar{E} , and the fluctuating voltage, e . With the use of the approximate form of Equation C-17, Equation C-18 becomes

$$K_1 (\bar{E}^2 + 2e\bar{E} + e^2) = K_2 + K_3 (\bar{U}^2 + 2u\bar{U})^{N/2}.$$

Factoring a \bar{U}^2 from the last term results in

$$K_1 (\bar{E}^2 + 2e\bar{E} + e^2) = K_2 + K_3 \bar{U}^N \left(1 + \frac{2u}{\bar{U}}\right)^{N/2} \quad (C-19)$$

The binomial series is expressed as

$$(1 \pm X)^M = 1 \pm MX + \frac{M(M-1)}{2!} X^2 \pm \frac{M(M-1)(M-2)}{3!} X^3 + \dots \text{etc.}$$

$$\text{for } X^2 < 1. \quad (C-20)$$

Letting $X = \frac{2u}{\bar{U}}$ and $m = N/2$, then Equation C-19 can be written as

$$\begin{aligned} K_1 (\bar{E}^2 + 2e\bar{E} + e^2) &= K_2 + K_3 \bar{U}^N \left\{ 1 + \frac{N}{2} \left(\frac{2u}{\bar{U}}\right) + \frac{1N}{2!2} \left(\frac{N}{2} - 1\right) \left(\frac{2u}{\bar{U}}\right)^2 \right. \\ &\quad \left. + \frac{1}{3!} \frac{N}{2} \left(\frac{N}{2} - 1\right) \left(\frac{N}{2} - 2\right) \left(\frac{2u}{\bar{U}}\right)^2 + \dots \right\}. \end{aligned}$$

Assuming $e/\bar{E} \ll 1$ and neglecting second order terms in both voltage and velocity yields

$$K_1 \bar{E}^2 \left(1 + \frac{2e}{\bar{E}} \right) = K_2 + K_3 \bar{U}^N \left\{ 1 + N \frac{u}{\bar{U}} \right\}. \quad (C-21)$$

Assuming that e and u are positive as often as negative over a sufficient time period means that integrating Equation C-21 with respect to time results in

$$K_1 \bar{E}^2 = K_2 + K_3 \bar{U}^N. \quad (C-22)$$

This is the mathematical model for the mean voltage and mean velocity for a single hot-wire. Turbulence intensity is defined as the root-mean-square (RMS) of the fluctuating velocity. Subtracting Equations C-22 from C-21 results in the fluctuating voltage and velocity relationship:

$$2K_1 \bar{E} e = NK_3 u \bar{U}^{(N-1)}.$$

Both sides are squared and integrated with respect to time

$$(2K_1 \bar{E})^2 \int_{t_o}^{t_o+T} e^2 dt = \left(NK_3 \bar{U}^{N-1} \right)^2 \int_{t_o}^{t_o+T} u^2 dt$$

and the square root is taken to obtain the RMS values. Time averaged fluctuating quantities are indicated with a bar over the squared quantity.

$$2K_1 \bar{E} \sqrt{\bar{e}^2} = NK_3 \bar{U}^N \sqrt{\frac{\bar{u}^2}{\bar{U}^2}} \quad (C-23)$$

A direct analogy can now be made by defining terms in Equations C-13, C-14 and C-15 as:

$$\bar{U}^2 = Q_s^2 \left(1 - (1-k_1^2) \cos^2 \bar{\alpha} \right) \quad (C-24)$$

$$\pm 2u\bar{U} = 2Q_s \left[\pm q_s - (1 - k_1^2) \left\{ \pm q_s \cos^2 \bar{\alpha} \pm q_t \frac{\cos \bar{\alpha} \cos \beta}{\sin \bar{\gamma}} \right. \right. \\ \left. \left. \pm q_n \frac{\cos^2 \bar{\alpha} \cos \bar{\gamma}}{\sin \bar{\gamma}} \right\} \right] \quad (C-25)$$

$$\bar{V}^2 = Q_s^2 \left(1 - (1-k_2^2) \cos^2 \bar{\beta} \right) \quad (C-26)$$

$$\pm 2v\bar{V} = 2Q_s \left[\pm q_s - (1 - k_2^2) \left\{ \pm q_s \cos^2 \bar{\beta} \pm q_t \frac{\cos \bar{\alpha} \cos \bar{\beta}}{\sin \bar{\gamma}} \right. \right. \\ \left. \left. \pm \frac{\cos^2 \bar{\beta} \cos \bar{\gamma}}{\sin \bar{\gamma}} \right\} \right] \quad (C-27)$$

$$\bar{W}^2 = Q_s^2 \left(1 - (1-k_3^2) \cos^2 \bar{\gamma} \right) \quad (C-28)$$

$$\pm 2w\bar{W} = 2Q_s \left[\pm q_s - (1 - k_3^2) \left\{ \pm q_s \cos^2 \bar{\gamma} \right. \right. \\ \left. \left. \pm q_n \sin \bar{\gamma} \cos \bar{\gamma} \right\} \right] \quad (C-29)$$

Mean velocity relationships

With a relationship such as C-22, \bar{U} , \bar{V} and \bar{W} can be obtained from measurements in conjunction with wire calibration curves. If $k_1 = k_2 = k_3$, then by adding Equations C-24, C-26 and C-28 and rearranging terms the result is

$$\bar{U}^2 + \bar{V}^2 + \bar{W}^2 = Q_s^2 \left\{ 3 - (1-k^2) \left[\cos^2 \bar{\alpha} + \cos^2 \bar{\beta} + \cos^2 \bar{\gamma} \right] \right\}.$$

Recalling that by definition of the coordinate system

$$\cos^2 \bar{\alpha} + \cos^2 \bar{\beta} + \cos^2 \bar{\gamma} = 1$$

and by solving for Q_s the relationship arrived at is

$$Q_s = \frac{\sqrt{\bar{U}^2 + \bar{V}^2 + \bar{W}^2}}{\sqrt{2 + k^2}} . \quad (C-30)$$

The same technique was suggested as a means for finding instantaneous velocities in three-dimensional flow in Thermo-Systems Incorporated (75) but no reference or further work on the subject was seen at that time.

Subsequently, the two-dimensional version of Equation C-30 was found to yield velocities differing from values obtained by use of a Pitot-static probe and they varied depending on the angle with respect to the velocity vector and the sensors. As a result this equation was used only as a starting value for an iterative solution. Equation C-2 written in terms of the mean values $\bar{U}^2 = Q_s^2 (1 - b [1 - \sin^2 \bar{\alpha}])^4$ was tried next, but values of b were found to be a function of velocity contrary to claims of Friehe and Schwarz (26). A very small variation in the equivalent velocity yielded considerable scatter in the parameters they suggested for determination of b . Therefore, it appeared that a less sensitive method was required. It seemed logical that the complete heat transfer relationship rather than the velocity should be proportional or in some way directly related to the angles $\bar{\alpha}$, $\bar{\beta}$ and $\bar{\gamma}$. Since the heat transfer is directly proportional to the electrical power dissipated, then electrical power should be proportional to the angle. It was found that the modified power, $MP_{\bar{\alpha}}$, obtained with the sensor at

an angle α , could be related to the modified power when the wire was perpendicular to the flow, MP_{90} , for a fairly large range of velocities by the equation

$$\sqrt{\frac{MP_{\alpha}}{MP_{90}}} = C_1 + C_2 \sin^{\frac{1}{2}} \alpha .$$

This is shown in Figure 12. As described in Data Reduction, this equation was a primary factor in the method used to obtain mean velocity and angular values.

Turbulence intensities and Reynolds stresses

A direct analogy based on the steps required to derive Equation C-23 was used to obtain three of the required equations and the remaining three auxiliary equations were derived from basic principles.

Equations C-25, C-27 and C-29 were substituted into Equation C-19 successively and a form of Equation C-23 resulted (the square root was not taken). More nomenclature was introduced to reduce the length of the equations. First, Equation C-23 was used in the form

$$\begin{aligned} \bar{e}^2 &= \left\{ \frac{N K_3 \bar{U}^{N-1}}{2 K_1 \bar{E}} \right\}^2 \bar{U}^2 \\ \bar{e}^2 &= \kappa^2 \bar{u}^2 \end{aligned} \quad (C-31)$$

Also defined were

$$A_u = \left(1 - (1 - k_1^2) \cos^2 \bar{\alpha} \right)$$

$$A_v = \left(1 - (1 - k_2^2) \cos^2 \bar{\beta} \right)$$

$$A_w = \left(1 - (1 - k_3^2) \cos^2 \bar{\gamma} \right)$$

$$B_u = (1-k_1^2) \frac{\cos^2 \bar{\alpha} \cos \bar{\gamma}}{\sin \bar{\gamma}}$$

$$B_v = (1-k_2^2) \frac{\cos^2 \bar{\beta} \cos \bar{\gamma}}{\sin \bar{\gamma}}$$

$$B_w = (1-k_3^2) \sin \bar{\gamma} \cos \bar{\gamma}$$

$$C_u = (1+k_1^2) \frac{\cos \bar{\alpha} \cos \bar{\beta}}{\sin \bar{\gamma}}$$

$$C_v = (1+k_2^2) \frac{\cos \bar{\alpha} \cos \bar{\beta}}{\sin \bar{\gamma}}$$

$$C_w = 0$$

$$\kappa_u = \frac{N_u K_{3u}(\bar{U})^{(N_u-1)}}{2 K_{1u} \bar{E}_u}$$

$$\kappa_v = \frac{N_v K_{3v}(\bar{V})^{(N_v-1)}}{2 K_{1v} \bar{E}_v}$$

$$\kappa_w = \frac{N_w K_{3w}(\bar{W})^{(N_w-1)}}{2 K_{1w} \bar{E}_w}$$

$$\bar{\epsilon}_{uu} = \frac{\bar{e}_u^2}{\bar{e}_u}$$

$$\bar{\epsilon}_{vv} = \frac{\bar{e}_v^2}{\bar{e}_v}$$

$$\bar{\epsilon}_{ww} = \frac{\bar{e}_w^2}{\bar{e}_w}$$

With these definitions and using Equation C-31 for the final form, three of the equations became

$$\bar{\epsilon}_{uu} = \kappa_u^2 A_u^{-1} \left\{ A_u^2 \bar{q}_s^2 + B_u^2 \bar{q}_n^2 + C_u^2 \bar{q}_t^2 \right. \\ \left. \pm 2A_u B_u \bar{q}_s \bar{q}_n \pm 2A_u C_u \bar{q}_s \bar{q}_t \pm 2B_u C_u \bar{q}_n \bar{q}_t \right\} \quad (C-32)$$

$$\bar{\epsilon}_{vv} = \kappa_v^2 A_v^{-1} \left\{ A_v^2 \bar{q}_s^2 + B_v^2 \bar{q}_n^2 + C_v^2 \bar{q}_t^2 \right. \\ \left. \pm 2A_v B_v \bar{q}_s \bar{q}_n \pm 2A_v C_v \bar{q}_s \bar{q}_t \pm 2B_v C_v \bar{q}_n \bar{q}_t \right\} \quad (C-33)$$

$$\bar{\epsilon}_{ww} = \kappa_w^2 A_w^{-1} \left\{ A_w^2 \bar{q}_s^2 + B_w^2 \bar{q}_n^2 \pm 2A_w B_w \bar{q}_s \bar{q}_n \right\}. \quad (C-34)$$

All terms in Equations C-32, C-33 and C-34 were considered known except for \bar{q}_s^2 , \bar{q}_n^2 , \bar{q}_t^2 , $\bar{q}_s \bar{q}_n$, $\bar{q}_s \bar{q}_t$, and $\bar{q}_n \bar{q}_t$. It is therefore seen that three more equations are required in order to solve for the unknowns. If the instantaneous form of Equation C-31 was written in terms of q_s , q_n , and q_t the result is

$$e_u = \kappa_u A_u^{-1/2} \left\{ \pm A_u q_s \pm B_u q_n \pm C_u q_t \right\} \quad (C-35)$$

$$e_v = \kappa_v A_v^{-1/2} \left\{ \pm A_v q_s \pm B_v q_n \pm C_v q_t \right\} \quad (C-36)$$

$$e_w = \kappa_w A_w^{-1/2} \left\{ \pm A_w q_s \pm B_w q_n \right\} \quad (C-37)$$

From the previous sign convention, if q_s is positive for one wire it is positive for all wires, if q_n is negative for one wire it is negative for all and if q_t is positive for the u-wire it will be negative for the v-wire. This particular set of signs was used in conjunction with

Equations C-35, C-36 and C-37. By putting Equations C-35, C-36 and C-37 into the effective velocity notation the results were

$$e_u = \kappa_u u$$

$$e_v = \kappa_v v$$

$$e_w = \kappa_w w .$$

A correlation between the sensor signals can be found by determining

$$\overline{e_u e_v} = \kappa_u \kappa_v \overline{uv}$$

$$\overline{e_u e_w} = \kappa_u \kappa_w \overline{uw}$$

$$\overline{e_v e_w} = \kappa_v \kappa_w \overline{vw}$$

where

$$\overline{e_u e_v} = \frac{1}{4} \left(\overline{(e_u + e_v)^2} - \overline{(e_u - e_v)^2} \right)$$

$$\overline{e_u e_w} = \frac{1}{4} \left(\overline{(e_u + e_w)^2} - \overline{(e_u - e_w)^2} \right)$$

$$\overline{e_v e_w} = \frac{1}{4} \left(\overline{(e_v + e_w)^2} - \overline{(e_v - e_w)^2} \right)$$

which are easily obtainable signals using a correlator and an RMS meter.

Again, terms were redefined so that

$$\overline{\epsilon_{uv}} = \overline{e_u e_v}$$

$$\overline{\epsilon_{uw}} = \overline{e_u e_w}$$

$$\overline{\epsilon_{vw}} = \overline{e_v e_w} .$$

Then the auxiliary equations were comprised of the three correlation equations expressed as

$$\begin{aligned} \bar{\epsilon}_{uv} = & \kappa_u \kappa_v A_u^{-\frac{1}{2}} A_v^{-\frac{1}{2}} \left\{ A_u A_v \overline{q_s^2} + B_u B_v \overline{q_n^2} - C_u C_v \overline{q_t^2} \right. \\ & + (A_v B_u + A_u B_v) \overline{q_s q_n} + (A_u C_v - A_v C_u) \overline{q_s q_t} \\ & \left. + (B_u C_v - B_v C_u) \overline{q_n q_t} \right\} \end{aligned} \quad (C-38)$$

$$\begin{aligned} \bar{\epsilon}_{uw} = & \kappa_u \kappa_w A_u^{-\frac{1}{2}} A_w^{-\frac{1}{2}} \left\{ A_u A_w \overline{q_s^2} - B_u B_w \overline{q_n^2} \right. \\ & + (A_w B_u - A_u B_w) \overline{q_s q_n} - A_w C_u \overline{q_s q_t} + B_w C_u \overline{q_n q_t} \left. \right\} \end{aligned} \quad (C-39)$$

$$\begin{aligned} \bar{\epsilon}_{vw} = & \kappa_v \kappa_w A_v^{-\frac{1}{2}} A_w^{-\frac{1}{2}} \left\{ A_v A_w \overline{q_s^2} - B_v B_w \overline{q_n^2} \right. \\ & + (A_w B_v - A_v B_w) \overline{q_s q_n} + A_w C_v \overline{q_s q_t} - B_w C_v \overline{q_n q_t} \left. \right\}. \end{aligned} \quad (C-40)$$

Equations C-32, C-33, C-34, C-38, C-39 and C-40 make up a set of six simultaneous equations and six unknowns. Three hot-wire anemometer channels with correlators and RMS meters are recommended for instrumentation to obtain the data required to solve the six equations. For the particular experimental investigation involved it was assumed that since the measurements were taken near a flat surface and flow separation was absent on the end wall, then it was sufficient to assume $\bar{\gamma} = 90^\circ$ and wire three could be eliminated.

Assuming $\bar{\gamma}$ to be 90° reduced the six equations to

$$\bar{\epsilon}_{uu} = \kappa_u^2 A_u^{-1} \left\{ A_u^2 \overline{q_s^2} + C_u^2 \overline{q_t^2} - 2 A_u C_u \overline{q_s q_t} \right\} \quad (C-41)$$

$$\bar{\epsilon}_{vv} = \kappa_v^2 A_v^{-1} \left\{ A_v^2 \bar{q}_s^2 + C_v^2 \bar{q}_t^2 + 2 A_v C_v \bar{q}_s \bar{q}_t \right\} \quad (C-42)$$

$$\bar{\epsilon}_{ww} = \kappa_w^2 A_w^{-1} \left\{ \bar{q}_s^2 \right\} \quad (C-43)$$

$$\bar{\epsilon}_{uv} = \kappa_u \kappa_v A_u^{-1} A_v^{-1} \left\{ A_u A_v \bar{q}_s^2 - C_u C_v \bar{q}_t^2 + (A_u C_v - A_v C_u) \bar{q}_s \bar{q}_t \right\} \quad (C-44)$$

$$\bar{\epsilon}_{uw} = \kappa_u \kappa_w A_u^{-1} A_w^{-1} \left\{ A_u \bar{q}_s^2 - C_u \bar{q}_s \bar{q}_t \right\} \quad (C-45)$$

$$\bar{\epsilon}_{vw} = \kappa_v \kappa_w A_v^{-1} A_w^{-1} \left\{ A_v \bar{q}_s^2 + C_v \bar{q}_s \bar{q}_t \right\}. \quad (C-46)$$

It is interesting to note that if $\kappa = 0$, $\alpha = \beta = 45^\circ$ and the wires are matched then Equations C-41, C-42 and C-43 are effectively the three equations generally used for determining the turbulence intensities and Reynolds stress, as outlined in Sandborn (65) as well as other references. First a single wire is placed normal to the flow and using Equation C-43 the streamwise turbulence intensity is determined. Next Equations C-41 and C-42 are solved simultaneously using measurements from the 45° oriented wires.

Equations C-41, C-42 and C-44 were programmed for this experiment in an attempt to determine the turbulence intensities and one of the Reynolds stresses independent of the angle that the mean velocity vector made with the sensors, provided that it was inside the quadrant formed by the sensors and in the plane of the sensors. Measurements were made with a single wire normal to the stream at the exit of the mating section. The same profile was repeated with two different probes (called the x-wire boundary layer probe and a split "v" boundary layer

probe) oriented at different angles of $\bar{\alpha}$. Streamwise turbulence intensity was determined from Equation C-43 for the single wire and was solved for simultaneously from Equations C-41, C-42 and C-44 for the boundary layer probes. The results are shown in Figure 64 which indicates an error in the technique because the value of $\overline{q_s^2}$ predicted by the 90° wire and the wires at 45° were comparable but the predicted values for an angle of flow of 60° with respect to one wire are too high. Various techniques were attempted to make the 45° and 60° predictions coincide but were unsuccessful. A more basic investigation of the problem was then conducted which seemed to indicate that the original basic mathematical model might be incorrect. It assumed that turbulence and mean flow follow the same type of distribution with respect to changes in angle. Most flow models appear to be based on mean flow measurements, then hypothesized to be valid for instantaneous flow. From the instantaneous model, a theoretical mathematical model in terms of mean and fluctuating velocities is developed and then divided into mean and fluctuating equations which are the models for calculating the two types of flow phenomena. Mean voltage ratios and mean velocity ratios represent the same trend when plotted as a function of angle if the ratios are obtained by normalizing with the value determined at the 90° angle. If it could be hypothesized that a ratio of the same type using fluctuating voltages would indicate the type of model to use for the fluctuating velocities, then as illustrated in Figure 65, the total fluctuating velocity vector could possibly be represented by a model similar to the mean velocity vector but a considerably different slope would be involved. A suggested

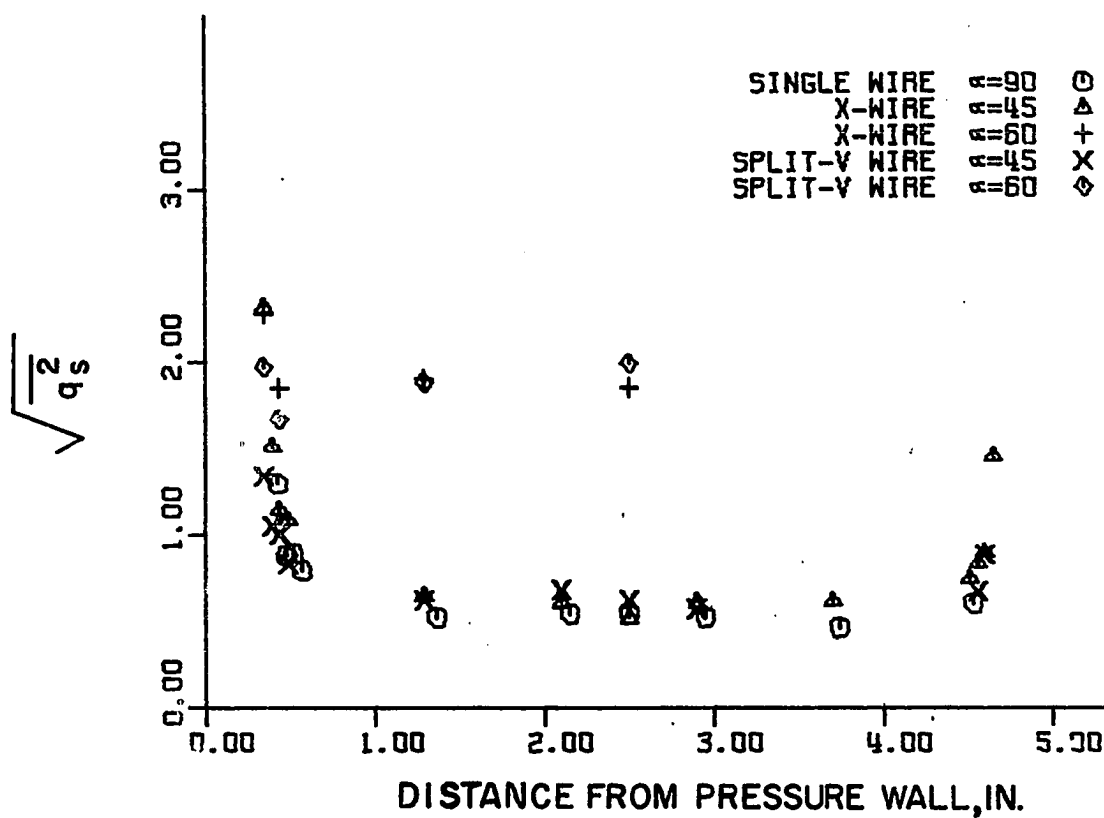


Figure 64. Turbulence distribution as measured by three probes near duct midheight at mating section exit

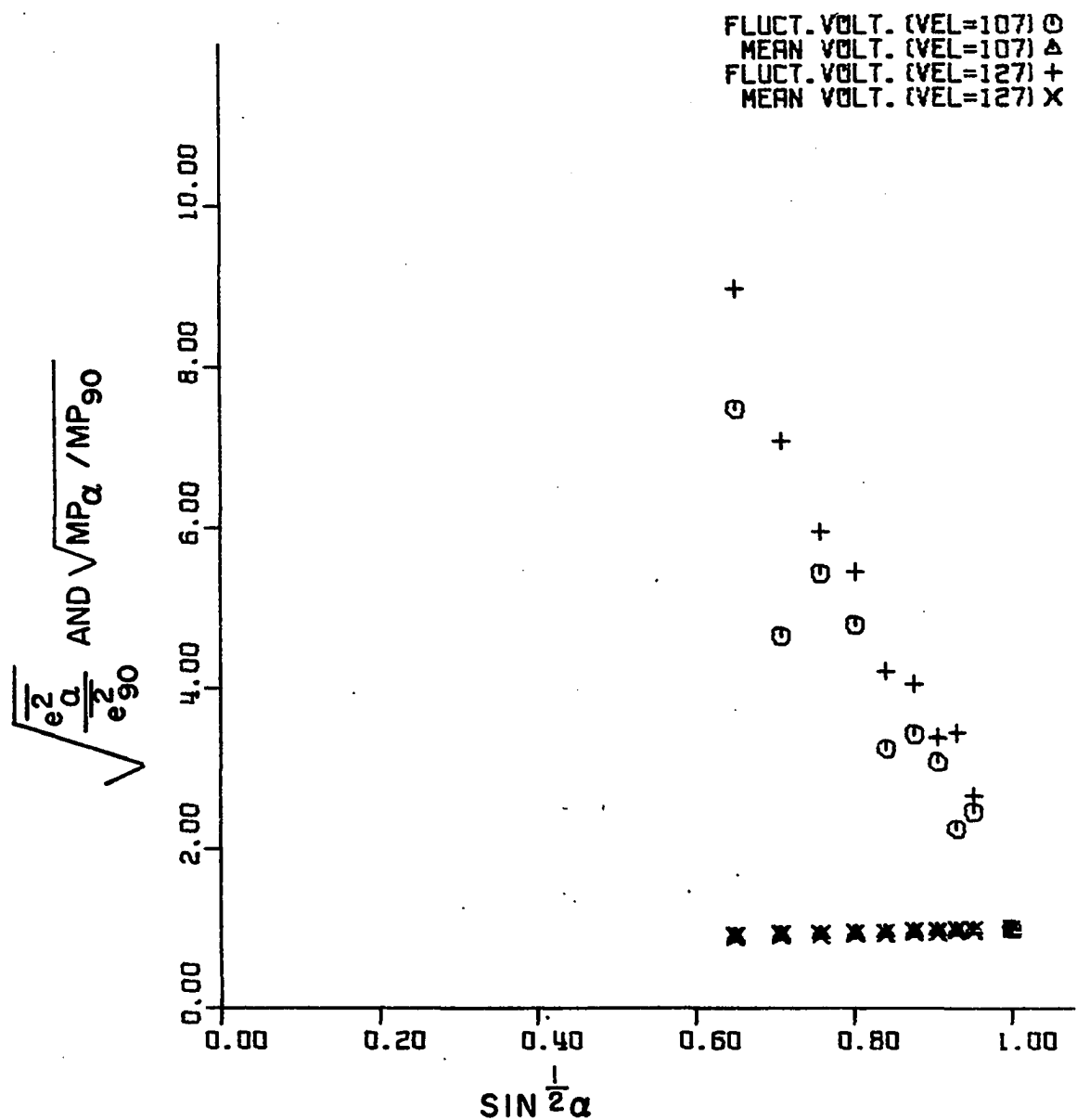


Figure 65. Fluctuating voltage change with respect to velocity and angle

form would be

$$\vec{U} = f(\alpha) \vec{q}_S + g(\alpha) \vec{q}_T .$$

More work in this area needs to be done to determine a better method for turbulence measurement.

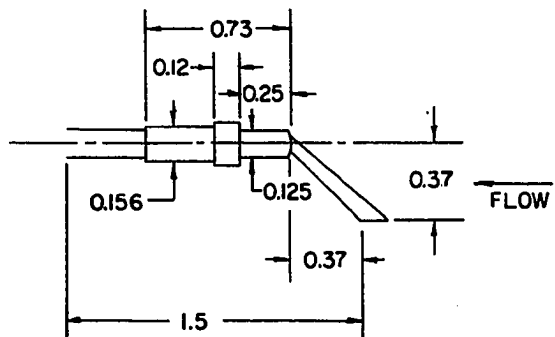
Hot-Wire Probe Designs

Design criteria for the probes were primarily dictated by the size of the test section, the measurements desired and the physical restrictions imposed on the movement of the probe. The size of the passage was relatively small and if a probe was inserted from the top of the section to survey the floor of the section, then the blockage factor became too large. A miniature probe was tried in order to eliminate the blockage factor problem but the probe bent and vibrated considerably in the flow. Another objection to insertion of the probe from the top is that only discrete positions could be surveyed without destroying the integrity of the test section. Since a trial survey was to be conducted to determine the positions where the profiles were to be measured, then a maximum amount of probe position resolution was desired. The foregoing difficulties and restrictions precluded the use of the relatively simple method and type of probe used by Francis (24) for measurement of mean velocities and angles.

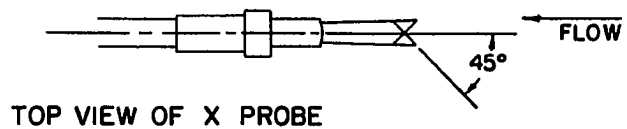
As a result of the imposed criteria, the probe was designed with two sensors to enable the technique to be used which was developed and explained in the Data Reduction Section. This probe was used to measure velocity and direction at a station without rotating the sensors. The

two sensors are aligned at 45° with respect to the axis of the probe and mounted on needle supports having an angle which places the probe body downstream of the sensors and away from the surface over which the boundary layer is formed. Two probes were designed and tested. One had sensors in an x-configuration and the other a split "v" configuration and are shown on Figure 66. The split "v" was chosen over the x-configuration because the space between the two wires at the intersection of the "x" was sufficient to cause the wires to be in two velocity fields near a surface and erroneous mean velocity and angular data resulted. Also the angular range of the probe was decreased because the needle supports on the x-configuration influenced the flow over the opposite wire.

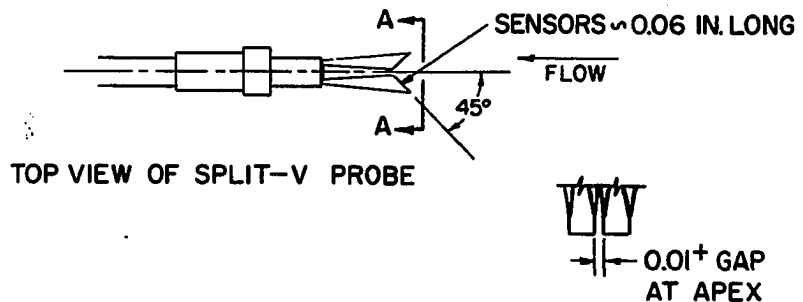
The split "v" probe, Figure 67, appeared to work well for mean velocity and directional measurements and seemed suitable to mount on rotating parts. An extension of the technique and an addition of another wire perpendicular to the other two would allow truly three-dimensional measurements.



SIDE VIEW - TYPICAL FOR BOTH PROBES



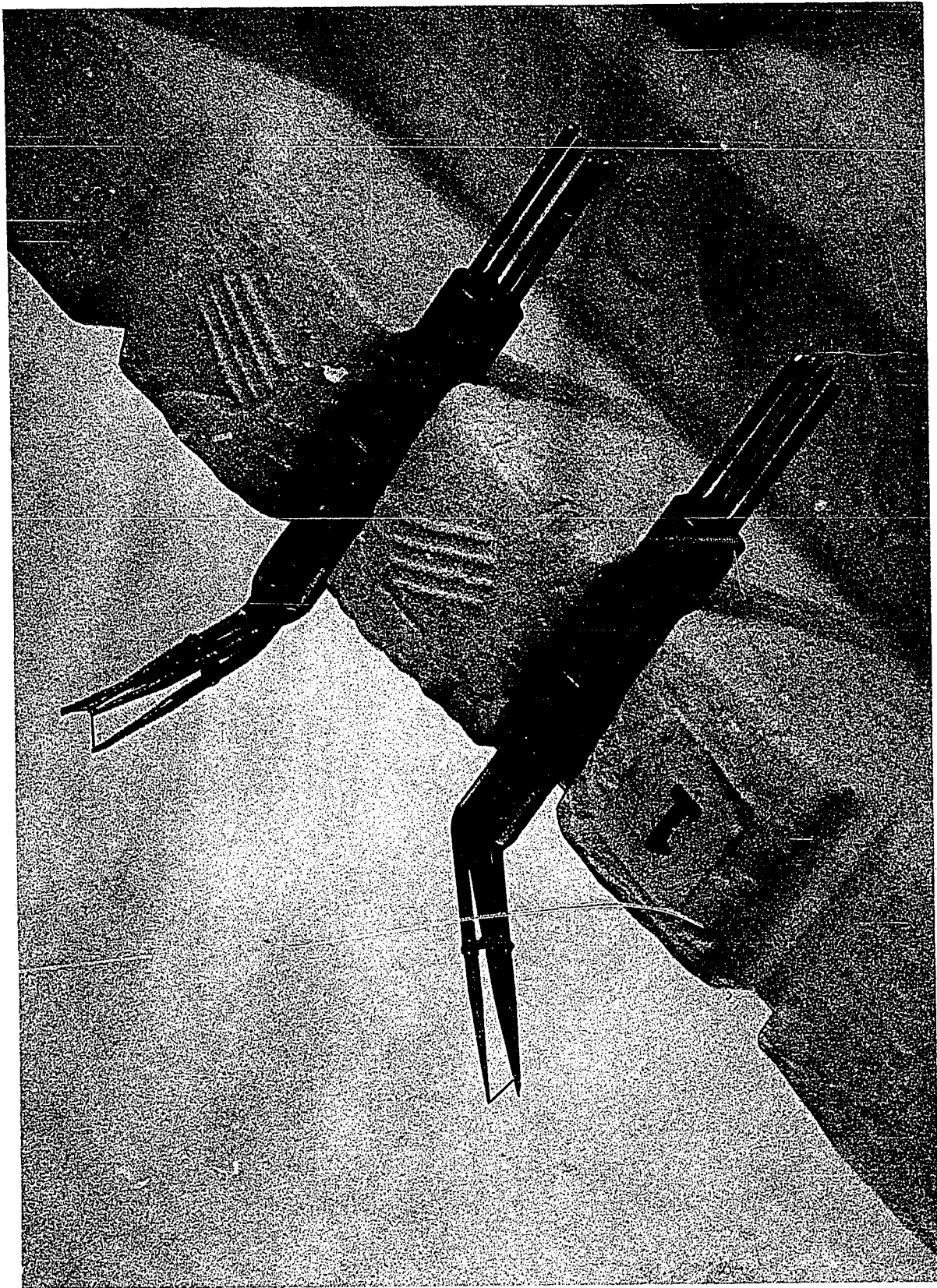
TOP VIEW OF X PROBE



VIEW A-A

Figure 66. Hot-wire probe drawings

Figure 67. The split-V boundary layer probe



APPENDIX D. DIFFUSER EXPERIMENTAL DATA

Table 9. Diffuser experimental profile data

PROFILE NUMBER = 1500S1

RADIUS = 14.108 ANGLE OF TURN = 0.0 VEL.(B.L.EDGE)= 134.76

VELOCITY	ETA/DELTA	U/Q	W/Q	ALPHA
73.64	0.058	0.546	-0.029	-3.06
80.56	0.068	0.598	0.005	0.48
85.18	0.080	0.632	0.017	1.53
88.14	0.097	0.654	0.016	1.43
91.11	0.114	0.676	0.019	1.60
93.71	0.135	0.695	0.021	1.74
96.86	0.156	0.718	0.020	1.63
99.33	0.178	0.737	0.021	1.65
101.28	0.216	0.751	0.020	1.53
107.37	0.300	0.797	0.012	0.86
116.25	0.427	0.863	0.007	0.49
120.91	0.512	0.897	0.001	0.05
124.13	0.596	0.921	0.002	0.13
128.21	0.681	0.951	0.004	0.26
131.48	0.765	0.976	-0.006	-0.37
133.22	0.850	0.989	-0.002	-0.12
134.65	0.934	0.999	-0.001	-0.07
134.79	1.019	1.000	0.000	0.03
135.20	1.103	1.003	-0.001	-0.08
135.44	1.188	1.005	-0.003	-0.16

PROFILE NUMBER = 1500C1

RADIUS = 15.000 ANGLE OF TURN = 0.0 VEL.(B.L.EDGE)= 128.74

VELOCITY	ETA/DELTA	U/Q	W/Q	ALPHA
76.69	0.081	0.595	0.022	2.08
80.23	0.095	0.622	0.029	2.68
81.65	0.109	0.633	0.033	2.97
84.90	0.128	0.659	0.030	2.63
86.99	0.147	0.675	0.026	2.24
89.07	0.166	0.691	0.028	2.33
90.80	0.185	0.705	0.025	2.02
92.79	0.209	0.720	0.023	1.85
95.57	0.233	0.742	0.028	2.14
97.16	0.256	0.754	0.030	2.31
98.50	0.280	0.765	0.029	2.14
99.33	0.304	0.771	0.026	1.92
101.95	0.351	0.791	0.029	2.08
105.68	0.399	0.821	0.020	1.39
109.31	0.446	0.849	0.013	0.88
116.65	0.589	0.906	0.008	0.50
123.89	0.779	0.962	0.005	0.31
129.04	1.016	1.002	-0.000	-0.03
129.27	1.277	1.004	0.001	0.08
129.39	1.752	1.005	0.001	0.04

Table 9 (Continued)

PROFILE NUMBER = 1500P1

RADIUS = 15.887 ANGLE OF TURN = 0.0 VEL.(B.L.EDGE)= 112.98

VELOCITY	ETA/DELTA	U/Q	W/Q	ALPHA
75.10	0.022	0.665	0.015	1.32
75.97	0.032	0.672	0.016	1.38
77.70	0.046	0.688	0.015	1.26
77.42	0.060	0.685	0.017	1.42
78.04	0.075	0.691	0.017	1.42
80.06	0.099	0.708	0.014	1.11
80.85	0.121	0.716	0.011	0.86
83.28	0.142	0.737	0.012	0.95
84.65	0.163	0.749	0.011	0.82
86.08	0.199	0.762	0.015	1.13
87.78	0.234	0.777	0.008	0.59
90.26	0.270	0.799	0.011	0.76
93.48	0.341	0.827	0.014	0.94
95.58	0.412	0.846	0.015	1.00
97.95	0.483	0.866	0.035	2.28
105.57	0.625	0.934	0.007	0.43
108.88	0.732	0.964	-0.003	-0.18
112.63	0.909	0.997	-0.001	-0.07
113.50	1.158	1.005	0.003	0.14
113.55	1.406	1.005	0.003	0.16

PROFILE NUMBER = 1508C1

RADIUS = 15.000 ANGLE OF TURN = 8.00 VEL.(B.L.EDGE)= 117.04

VELOCITY	ETA/DELTA	U/Q	W/Q	ALPHA
64.80	0.058	0.548	0.076	7.89
68.00	0.070	0.576	0.079	7.85
69.84	0.082	0.592	0.076	7.35
72.39	0.101	0.613	0.079	7.31
74.73	0.120	0.634	0.077	6.95
76.79	0.140	0.652	0.073	6.41
77.91	0.159	0.662	0.071	6.16
79.28	0.179	0.673	0.073	6.18
80.83	0.198	0.687	0.069	5.77
84.19	0.237	0.717	0.063	5.02
87.18	0.276	0.743	0.058	4.45
90.22	0.315	0.769	0.054	4.04
97.33	0.431	0.830	0.049	3.38
103.50	0.548	0.884	0.035	2.24
109.80	0.664	0.938	0.017	1.02
113.75	0.781	0.972	0.004	0.22
116.17	0.897	0.993	0.001	0.04
117.41	1.053	1.003	0.000	0.02
117.81	1.247	1.007	0.001	0.05
117.63	1.441	1.005	-0.000	-0.02

Table 9 (Continued)

PROFILE NUMBER = 1516S1

RADIUS = 13.847 ANGLE OF TURN = 16.00 VEL.(B.L.EDGE)= 113.83

VELOCITY	ETA/DELTA	U/Q	W/Q	ALPHA
61.31	0.063	0.521	0.138	14.84
62.45	0.071	0.531	0.138	14.61
64.35	0.080	0.547	0.143	14.70
65.05	0.095	0.554	0.140	14.21
66.12	0.110	0.563	0.141	14.08
66.41	0.125	0.565	0.144	14.26
70.51	0.155	0.603	0.143	13.30
74.98	0.200	0.646	0.131	11.48
76.82	0.229	0.664	0.121	10.35
81.66	0.289	0.706	0.130	10.41
86.46	0.348	0.754	0.095	7.20
91.07	0.408	0.795	0.092	6.59
95.04	0.468	0.831	0.080	5.49
97.89	0.527	0.857	0.069	4.60
103.01	0.617	0.903	0.054	3.40
107.96	0.706	0.948	0.028	1.72
110.67	0.825	0.972	0.018	1.07
113.31	0.944	0.995	0.004	0.25
114.32	1.063	1.004	-0.003	-0.19
114.40	1.212	1.005	-0.004	-0.21

PROFILE NUMBER = 1516C1

RADIUS = 15.000 ANGLE OF TURN = 16.00 VEL.(B.L.EDGE)= 111.18

VELOCITY	ETA/DELTA	U/Q	W/Q	ALPHA
51.81	0.053	0.453	0.110	13.71
53.95	0.060	0.470	0.121	14.48
57.18	0.069	0.495	0.140	15.80
59.00	0.079	0.513	0.135	14.75
60.92	0.091	0.531	0.133	14.09
63.01	0.107	0.550	0.138	14.11
64.59	0.122	0.565	0.134	13.29
66.54	0.138	0.583	0.136	13.16
68.09	0.170	0.597	0.136	12.84
74.10	0.232	0.655	0.124	10.75
78.40	0.295	0.697	0.104	8.47
82.26	0.356	0.734	0.096	7.48
86.47	0.421	0.774	0.079	5.85
92.26	0.515	0.828	0.058	4.00
96.70	0.609	0.868	0.046	3.04
102.91	0.703	0.925	0.031	1.92
106.85	0.798	0.961	0.009	0.56
111.03	0.955	0.999	0.001	0.08
111.53	1.112	1.003	-0.002	-0.09
111.74	1.269	1.005	-0.002	-0.13

Table 9 (Continued)

PROFILE NUMBER = 1516P1
RADIUS = 15.507 ANGLE OF TURN = 16.00 VEL.(B.L.EDGE)= 106.25

VELOCITY	ETA/DELTA	U/Q	W/Q	ALPHA
53.03	0.065	0.482	0.129	14.99
53.56	0.074	0.487	0.130	14.89
55.45	0.082	0.505	0.132	14.69
56.01	0.093	0.512	0.126	13.83
58.06	0.106	0.531	0.127	13.45
58.75	0.134	0.541	0.116	12.11
64.33	0.188	0.596	0.109	10.36
68.50	0.243	0.637	0.099	8.84
71.56	0.297	0.667	0.091	7.75
78.81	0.406	0.738	0.072	5.54
86.25	0.516	0.811	0.043	3.00
91.59	0.625	0.861	0.041	2.72
96.49	0.734	0.908	0.020	1.28
103.39	0.897	0.973	-0.002	-0.11
102.60	0.843	0.966	0.001	0.04
105.00	0.952	0.988	0.007	0.43
106.44	1.007	1.002	-0.002	-0.09
106.57	1.116	1.003	-0.002	-0.14
106.68	1.225	1.004	-0.001	-0.07
106.79	1.361	1.005	-0.004	-0.21

PROFILE NUMBER = 1524C1
RADIUS = 15.000 ANGLE OF TURN = 24.00 VEL.(B.L.EDGE)= 106.76

VELOCITY	ETA/DELTA	U/Q	W/Q	ALPHA
49.76	0.033	0.443	0.146	18.26
51.39	0.041	0.457	0.150	18.14
54.30	0.049	0.481	0.166	19.00
56.47	0.060	0.501	0.171	18.83
58.14	0.073	0.517	0.171	18.31
59.22	0.087	0.527	0.172	18.08
61.76	0.114	0.553	0.171	17.22
64.38	0.141	0.579	0.170	16.33
68.00	0.195	0.615	0.167	15.24
73.95	0.277	0.676	0.149	12.45
78.27	0.358	0.722	0.129	10.11
82.84	0.440	0.768	0.110	8.15
92.41	0.630	0.863	0.065	4.31
102.59	0.820	0.961	0.024	1.41
104.78	0.901	0.981	0.010	0.56
106.94	1.010	1.002	-0.000	-0.03
107.35	1.173	1.006	-0.002	-0.10
107.05	1.336	1.003	-0.002	-0.13
107.17	1.499	1.004	-0.002	-0.10
107.30	1.662	1.005	-0.000	-0.01

Table 9 (Continued)

PROFILE NUMBER = 1532S1

RADIUS = 14.333 ANGLE OF TURN = 32.00 VEL.(B.L.EDGE)= 105.30

VELOCITY	ETA/DELTA	U/Q	W/Q	ALPHA
50.57	0.033	0.460	0.139	16.85
54.74	0.040	0.495	0.159	17.86
57.13	0.047	0.517	0.165	17.71
59.61	0.057	0.539	0.173	17.83
61.28	0.066	0.557	0.169	16.88
63.33	0.080	0.575	0.175	16.90
65.06	0.099	0.593	0.173	16.26
66.48	0.122	0.604	0.183	16.81
69.30	0.146	0.634	0.178	15.65
72.87	0.193	0.672	0.166	13.92
75.57	0.240	0.700	0.158	12.72
80.78	0.358	0.755	0.135	10.13
87.60	0.476	0.826	0.100	6.90
93.32	0.594	0.883	0.070	4.54
99.01	0.711	0.939	0.042	2.54
103.00	0.829	0.978	0.019	1.12
105.28	0.994	1.000	0.000	0.02
105.64	1.159	1.003	-0.002	-0.11
105.76	1.324	1.004	-0.002	-0.14
105.83	1.489	1.005	-0.003	-0.16

PROFILE NUMBER = 1532C1

RADIUS = 15.000 ANGLE OF TURN = 32.00 VEL.(B.L.EDGE)= 97.45

VELOCITY	ETA/DELTA	U/Q	W/Q	ALPHA
50.42	0.030	0.488	0.171	19.28
53.70	0.037	0.521	0.180	19.02
55.89	0.043	0.543	0.185	18.81
57.29	0.053	0.557	0.189	18.71
58.29	0.062	0.564	0.200	19.56
62.02	0.080	0.608	0.189	17.30
63.49	0.103	0.623	0.191	17.06
64.44	0.117	0.635	0.186	16.33
65.49	0.140	0.647	0.183	15.81
68.90	0.185	0.687	0.168	13.76
69.92	0.231	0.699	0.164	13.18
72.47	0.277	0.730	0.139	10.81
75.10	0.323	0.760	0.126	9.38
79.34	0.414	0.808	0.103	7.28
82.05	0.506	0.838	0.085	5.78
87.32	0.597	0.894	0.057	3.68
91.35	0.689	0.937	0.035	2.14
95.48	0.826	0.980	0.011	0.65
97.26	0.963	0.998	0.002	0.11
97.94	1.112	1.005	-0.004	-0.22

Table 9 (Continued)

 PROFILE NUMBER = 1532P1

RADIUS = 16.009 ANGLE OF TURN = 32.00 VEL.(B.L.EDGE)= 103.91

VELOCITY	ETA/DELTA	U/Q	W/Q	ALPHA
60.60	0.024	0.551	0.192	19.22
62.88	0.029	0.572	0.198	19.10
64.93	0.035	0.590	0.204	19.10
66.88	0.043	0.615	0.189	17.03
69.04	0.054	0.636	0.194	16.94
70.00	0.064	0.646	0.190	16.36
70.98	0.075	0.658	0.185	15.73
72.84	0.095	0.678	0.177	14.65
73.88	0.132	0.688	0.179	14.60
74.68	0.174	0.699	0.168	13.50
77.47	0.215	0.730	0.152	11.74
80.22	0.277	0.761	0.131	9.74
82.64	0.360	0.788	0.107	7.72
85.16	0.443	0.815	0.089	6.22
89.00	0.526	0.854	0.069	4.62
95.06	0.650	0.914	0.039	2.42
99.56	0.774	0.958	0.020	1.20
102.45	0.898	0.986	0.007	0.41
104.20	1.023	1.003	-0.001	-0.06
104.43	1.126	1.005	-0.002	-0.13

PROFILE NUMBER = 1540C1

RADIUS = 15.000 ANGLE OF TURN = 40.00 VEL.(B.L.EDGE)= 100.38

VELOCITY	ETA/DELTA	U/Q	W/Q	ALPHA
51.86	0.026	0.495	0.147	16.57
56.49	0.032	0.540	0.158	16.27
58.67	0.038	0.561	0.165	16.36
60.46	0.044	0.579	0.167	16.12
62.40	0.052	0.598	0.171	15.99
63.75	0.061	0.611	0.174	15.94
64.79	0.071	0.620	0.180	16.21
65.96	0.091	0.632	0.181	16.01
69.51	0.111	0.669	0.179	15.00
70.73	0.131	0.683	0.174	14.34
72.52	0.161	0.702	0.172	13.73
74.14	0.190	0.720	0.166	13.03
75.16	0.220	0.731	0.162	12.47
77.58	0.280	0.758	0.149	11.08
79.37	0.359	0.779	0.135	9.80
84.74	0.458	0.838	0.106	7.20
87.98	0.557	0.873	0.077	5.01
92.58	0.656	0.921	0.053	3.32
98.75	0.855	0.984	0.012	0.68
100.89	1.053	1.005	0.000	0.01

Table 10. Diffuser correlation parameter data

1500S1			1500C1		
WC/WCL	ETA/DELTA	W/QE+1-U/Q	WC/WCL	ETA/DELTA	W/QE+1-U/Q
-10.897	0.058	-0.501	0.788	0.081	0.823
0.354	0.068	0.567	0.937	0.095	0.940
0.909	0.080	0.921	1.000	0.109	1.000
0.867	0.097	0.882	0.926	0.128	0.927
0.939	0.114	0.942	0.831	0.147	0.835
0.999	0.135	0.999	0.852	0.166	0.851
0.952	0.156	0.952	0.770	0.185	0.774
0.961	0.178	0.959	0.722	0.209	0.728
0.910	0.216	0.906	0.803	0.233	0.793
0.585	0.300	0.597	0.847	0.256	0.832
0.362	0.427	0.381	0.803	0.280	0.786
0.042	0.512	0.129	0.743	0.304	0.727
0.107	0.596	0.150	0.786	0.351	0.762
0.203	0.681	0.191	0.583	0.399	0.565
-0.337	0.765	-0.183	0.400	0.446	0.403
-0.103	0.850	-0.057	0.240	0.589	0.245
-0.060	0.934	-0.040	0.158	0.779	0.140
0.021	1.019	0.015	-0.014	1.016	-0.011
-0.066	1.103	-0.048	0.042	1.277	0.023
-0.138	1.188	-0.098	0.022	1.752	0.009
1500P1			1508C1		
WC/WCL	ETA/DELTA	W/QE+1-U/Q	WC/WCL	ETA/DELTA	W/QE+1-U/Q
0.945	0.022	0.949	1.003	0.058	1.003
0.978	0.032	0.979	1.000	0.070	1.000
0.919	0.046	0.922	0.962	0.082	0.962
0.998	0.060	0.998	0.958	0.101	0.957
0.998	0.075	0.998	0.930	0.120	0.927
0.838	0.099	0.845	0.884	0.140	0.879
0.684	0.121	0.713	0.862	0.159	0.856
0.743	0.142	0.754	0.864	0.179	0.856
0.661	0.163	0.681	0.826	0.198	0.816
0.846	0.199	0.841	0.753	0.237	0.740
0.508	0.234	0.546	0.692	0.276	0.676
0.621	0.270	0.625	0.646	0.315	0.625
0.739	0.341	0.720	0.566	0.431	0.525
0.771	0.412	0.745	0.407	0.548	0.367
1.350	0.483	1.520	0.205	0.664	0.183
0.387	0.625	0.349	0.048	0.781	0.055
-0.197	0.732	-0.087	0.009	0.897	0.013
-0.073	0.909	-0.046	0.005	1.053	-0.000
0.140	1.158	0.097	0.012	1.247	0.000
0.158	1.406	0.110	-0.003	1.441	-0.007

Table 10 (Continued)

1516S1			1516C1		
WC/WCL	ETA/DELTA W/QE+1-U/Q		WC/WCL	ETA/DELTA W/QE+1-U/Q	
1.006	0.063	1.005	0.961	0.053	0.967
0.997	0.071	0.997	0.990	0.060	0.991
1.000	0.080	1.000	1.037	0.069	1.037
0.981	0.095	0.981	1.000	0.079	1.000
0.976	0.110	0.975	0.976	0.091	0.975
0.983	0.125	0.983	0.976	0.107	0.975
0.944	0.155	0.941	0.945	0.122	0.942
0.863	0.200	0.854	0.939	0.138	0.935
0.808	0.229	0.799	0.926	0.170	0.920
0.811	0.289	0.789	0.834	0.232	0.817
0.630	0.348	0.610	0.717	0.295	0.697
0.590	0.408	0.555	0.660	0.358	0.632
0.514	0.468	0.473	0.554	0.421	0.528
0.447	0.527	0.406	0.413	0.515	0.392
0.349	0.617	0.301	0.330	0.609	0.306
0.191	0.706	0.161	0.221	0.703	0.193
0.123	0.825	0.097	0.069	0.798	0.074
0.030	0.944	0.021	0.010	0.955	0.007
-0.023	1.063	-0.017	-0.012	1.112	-0.009
-0.026	1.212	-0.019	-0.017	1.269	-0.014
1516P1			1524C1		
WC/WCL	ETA/DELTA W/QE+1-U/Q		WC/WCL	ETA/DELTA W/QE+1-U/Q	
1.011	0.066	1.010	0.984	0.033	0.986
1.007	0.074	1.007	0.980	0.041	0.982
1.000	0.082	1.000	1.005	0.049	1.005
0.968	0.093	0.969	1.000	0.060	1.000
0.954	0.106	0.953	0.985	0.073	0.985
0.899	0.134	0.901	0.978	0.087	0.977
0.820	0.188	0.819	0.952	0.114	0.950
0.742	0.243	0.740	0.924	0.141	0.919
0.680	0.298	0.678	0.888	0.195	0.876
0.536	0.407	0.533	0.786	0.277	0.762
0.328	0.516	0.350	0.686	0.358	0.656
0.301	0.625	0.293	0.591	0.440	0.554
0.151	0.734	0.167	0.362	0.630	0.327
0.000	0.844	0.034	0.135	0.820	0.169
-0.020	0.898	0.017	0.056	0.901	0.047
0.050	0.953	0.037	-0.003	1.010	-0.003
-0.017	1.007	-0.010	-0.010	1.173	-0.010
-0.024	1.117	-0.015	-0.013	1.336	-0.009
-0.016	1.226	-0.012	-0.011	1.499	-0.009
-0.034	1.362	-0.022	-0.001	1.662	-0.006

Table 10 (Continued)

1532S1			1532C1		
WC/WCL	ETA/DELTA	W/QE+1-U/Q	WC/WCL	ETA/DELTA	W/QE+1-U/Q
0.973	0.033	0.979	1.018	0.030	1.016
1.009	0.040	1.008	1.010	0.037	1.009
1.004	0.047	1.003	1.003	0.043	1.003
1.008	0.057	1.007	1.000	0.053	1.000
0.974	0.066	0.976	1.026	0.062	1.027
0.975	0.080	0.976	0.952	0.080	0.951
0.952	0.099	0.952	0.944	0.103	0.941
0.972	0.122	0.971	0.919	0.117	0.914
0.929	0.146	0.926	0.900	0.140	0.894
0.861	0.193	0.853	0.822	0.185	0.809
0.811	0.240	0.798	0.799	0.231	0.784
0.692	0.358	0.670	0.696	0.277	0.681
0.517	0.476	0.489	0.628	0.323	0.610
0.367	0.594	0.337	0.518	0.414	0.497
0.220	0.711	0.192	0.430	0.506	0.413
0.102	0.829	0.082	0.293	0.597	0.275
0.002	0.994	0.001	0.180	0.689	0.166
-0.010	1.159	-0.009	0.058	0.826	0.053
-0.014	1.324	-0.012	0.010	0.963	0.007
-0.015	1.489	-0.014	-0.020	1.112	-0.016
1532P1			1540C1		
WC/WCL	ETA/DELTA	W/QE+1-U/Q	WC/WCL	ETA/DELTA	W/QE+1-U/Q
1.004	0.024	1.004	1.014	0.026	1.012
1.000	0.029	1.000	1.002	0.032	1.002
1.000	0.035	1.000	1.006	0.038	1.005
0.928	0.043	0.929	0.996	0.044	0.997
0.925	0.054	0.923	0.991	0.052	0.991
0.904	0.064	0.901	0.989	0.061	0.989
0.881	0.075	0.877	1.000	0.071	1.000
0.839	0.095	0.834	0.992	0.091	0.992
0.837	0.132	0.829	0.950	0.111	0.948
0.793	0.174	0.786	0.921	0.131	0.917
0.717	0.215	0.708	0.895	0.161	0.888
0.625	0.277	0.616	0.863	0.190	0.853
0.521	0.360	0.520	0.837	0.220	0.825
0.437	0.443	0.442	0.769	0.280	0.753
0.340	0.526	0.346	0.703	0.359	0.684
0.191	0.650	0.198	0.554	0.458	0.526
0.099	0.774	0.100	0.410	0.557	0.390
0.035	0.898	0.035	0.287	0.656	0.263
-0.005	1.023	-0.006	0.064	0.855	0.057
-0.011	1.126	-0.012	0.001	1.053	-0.004

Table 11. Diffuser shape factor data

PROFILE	B.L.THK	DISP.THK1	DISP.THK2	UQCL	WQCL	ALPHA-CL
1500S1	0.237	0.0352	-0.0011	0.695	0.021	1.75
1500C1	0.211	0.0345	-0.0027	0.633	0.033	2.96
1500P1	0.282	0.0375	-0.0028	0.690	0.017	1.43
1508C1	0.257	0.0440	-0.0093	0.575	0.079	7.86
1516S1	0.336	0.0651	-0.0244	0.547	0.143	14.70
1516C1	0.318	0.0691	-0.0204	0.513	0.135	14.75
1516P1	0.366	0.0861	-0.0206	0.505	0.132	14.65
1524C1	0.368	0.0819	-0.0337	0.501	0.171	18.83
1532S1	0.425	0.0807	-0.0392	0.575	0.183	17.60
1532C1	0.437	0.0782	-0.0381	0.564	0.191	18.73
1532P1	0.483	0.0805	-0.0401	0.590	0.204	19.10
1540C1	0.504	0.0851	-0.0455	0.620	0.180	16.21
PROFILE	MOM.THK11	MOM.THK12	MOM.THK21	MOM.THK2	H-1	H-2
1500S1	0.0251	0.0002	-0.0008	-0.0000	1.404	36.073
1500C1	0.0249	0.0007	-0.0022	-0.0001	1.386	43.635
1500P1	0.0292	0.0005	-0.0022	-0.0001	1.284	46.234
1508C1	0.0306	0.0025	-0.0068	-0.0005	1.438	17.619
1516S1	0.0433	0.0072	-0.0173	-0.0026	1.503	9.489
1516C1	0.0433	0.0065	-0.0139	-0.0020	1.595	10.067
1516P1	0.0538	0.0074	-0.0132	-0.0018	1.601	11.232
1524C1	0.0533	0.0108	-0.0230	-0.0044	1.537	7.678
1532S1	0.0548	0.0111	-0.0282	-0.0052	1.472	7.569
1532C1	0.0545	0.0107	-0.0274	-0.0052	1.436	7.362
1532P1	0.0590	0.0105	-0.0299	-0.0053	1.364	7.544
1540C1	0.0606	0.0115	-0.0346	-0.0061	1.404	7.420

**APPENDIX E. DIFFUSER SIDE WALL
COORDINATE SYSTEM**

The coordinate system affixed to the side walls is a curvilinear orthogonal set which resulted in a good approximation of the linear area distribution curved diffuser by Fox and Kline (23) and it also had the characteristics of the diffuser design for high loading near the diffuser throat by Sagi and Johnston (64). The approximation is best for large radii of curvature and becomes less appropriate for small radii of curvature. Figure 68 shows the coordinate system. The following equation relates the ideal turning angle from a line perpendicular to the centerline at the throat to variables of the coordinate system.

$$\theta = \tan^{-1} \left\{ \frac{R \sin (\psi - \theta') + (R - R_{ctr})}{R \cos (\psi - \theta')} \right\}$$

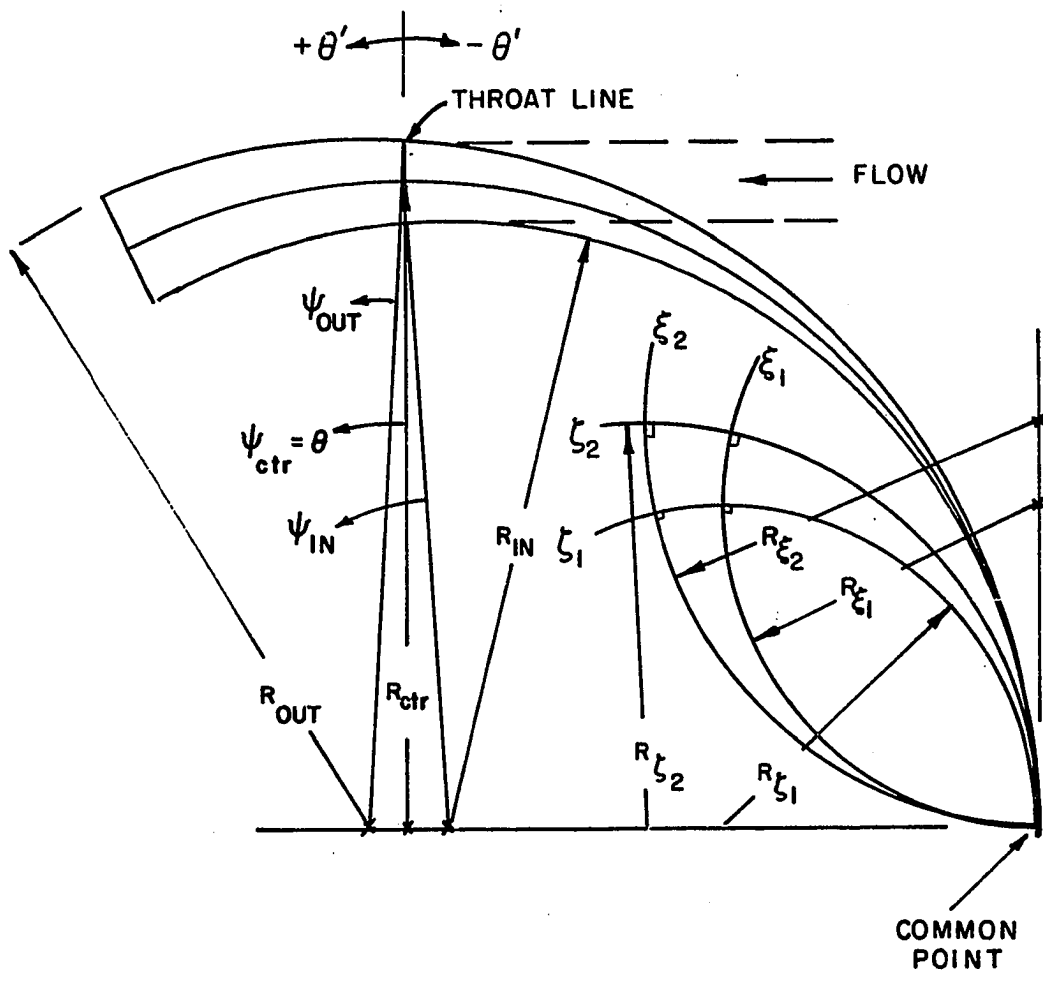
where

θ' = angle displacement from throat plane

R = radius of curvature of a given line

R_{ctr} = radius of curvature of the centerline at the throat

ψ = angle measured from a line with end points on the throat line and the center of curvature of R .



$$\theta' = \sin^{-1} \left\{ \frac{R - R_{ctr}}{R} \right\}$$

Figure 68. Orthogonal coordinate system for the diffuser side walls

APPENDIX F. SELECTED EXPERIMENTAL DATA

The data presented in this Appendix was obtained from the sources as indicated by the particular headings of the Tables and Figures. All data sets have twenty-two points per profile which were chosen from the original profiles. The integrated parameters were calculated from this set and they compared with sufficient accuracy with the values obtained by the originator. Boundary layer thickness for the data of Francis was obtained by using the twenty-two points to determine θ_{11}/δ and then using Francis calculated value of θ_{11} to determine δ . This was done since Francis data only contained values of η/δ and not η explicitly.

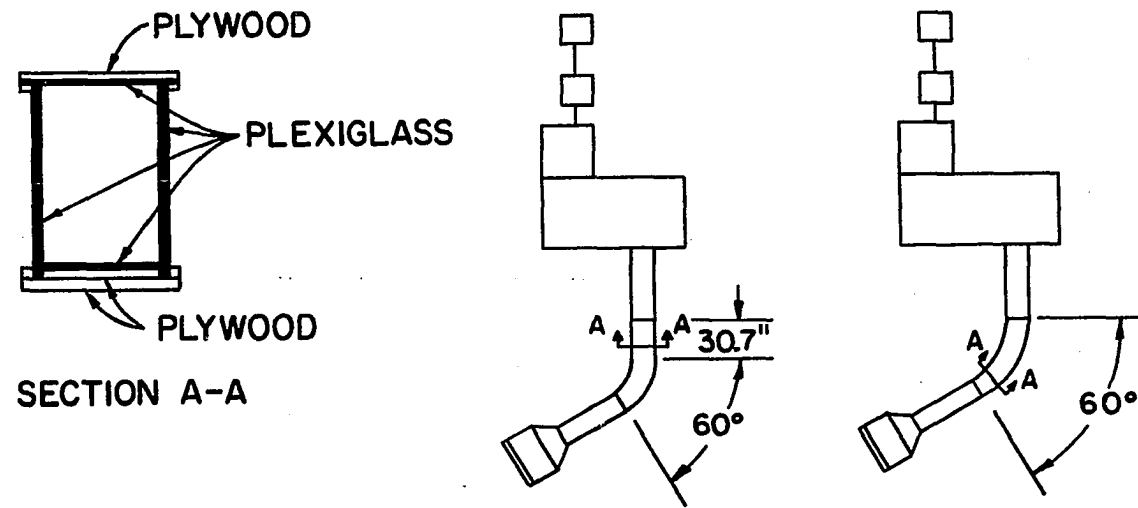


Figure 69. Schematic of test apparatus used by Francis (24)

Table 12. Experimental profile data - Francis (24)

550001			550601		
ETA/DELTA	DALPHA	U/Q	ETA/DELTA	DALPHA	U/Q
0.008	0.0	0.437	0.007	0.0	0.470
0.008	0.0	0.437	0.007	0.0	0.470
0.008	0.0	0.437	0.007	0.0	0.470
0.008	0.0	0.437	0.010	0.0	0.488
0.012	0.0	0.501	0.015	0.0	0.558
0.017	0.0	0.572	0.022	0.0	0.597
0.025	0.0	0.619	0.029	0.40	0.631
0.034	0.30	0.646	0.044	0.90	0.666
0.050	0.60	0.681	0.058	1.20	0.691
0.067	0.90	0.706	0.073	1.70	0.708
0.084	1.00	0.728	0.008	2.10	0.720
0.101	1.10	0.739	0.117	2.50	0.746
0.134	1.30	0.761	0.146	3.00	0.769
0.168	1.40	0.780	0.219	3.90	0.812
0.252	1.80	0.825	0.292	4.60	0.840
0.336	2.10	0.859	0.365	5.20	0.865
0.420	2.30	0.889	0.438	5.70	0.880
0.504	2.30	0.911	0.584	6.40	0.919
0.672	2.50	0.952	0.730	6.90	0.951
0.840	2.60	0.977	0.875	7.20	0.979
1.009	2.60	0.996	1.021	7.30	0.998
1.177	2.60	1.005	1.167	7.30	1.005
551201			551801		
ETA/DELTA	DALPHA	U/Q	ETA/DELTA	DALPHA	U/Q
0.007	0.0	0.383	0.005	0.0	0.359
0.007	0.0	0.383	0.008	0.0	0.429
0.009	0.0	0.449	0.011	0.0	0.483
0.013	0.0	0.513	0.016	0.0	0.535
0.020	0.0	0.567	0.022	0.70	0.566
0.027	0.70	0.596	0.033	1.40	0.599
0.040	1.10	0.634	0.044	1.90	0.627
0.053	1.60	0.659	0.055	2.40	0.649
0.067	2.10	0.676	0.066	2.80	0.665
0.080	2.50	0.692	0.088	3.60	0.691
0.107	3.10	0.716	0.109	4.30	0.705
0.133	3.70	0.741	0.164	6.00	0.745
0.200	5.20	0.787	0.219	6.50	0.776
0.266	6.30	0.817	0.274	7.70	0.807
0.333	7.40	0.849	0.328	9.90	0.834
0.399	8.40	0.870	0.438	11.80	0.878
0.533	9.90	0.909	0.547	13.40	0.911
0.666	10.90	0.942	0.657	15.00	0.942
0.799	11.80	0.969	0.766	15.90	0.972
0.932	12.30	0.988	0.876	16.60	0.983
1.065	12.70	1.001	0.985	16.90	0.994
1.198	12.70	1.005	1.095	17.30	1.001

Table 12 (Continued)

552401			553001		
ETA/DELTA	DALPHA	U/Q	ETA/DELTA	DALPHA	U/Q
0.005	0.0	0.366	0.005	0.0	0.392
0.007	0.0	0.441	0.007	0.0	0.483
0.010	0.0	0.511	0.010	0.0	0.529
0.015	0.0	0.565	0.015	0.0	0.587
0.021	0.90	0.597	0.020	0.60	0.617
0.031	1.40	0.634	0.030	1.20	0.657
0.041	2.10	0.659	0.039	1.70	0.686
0.051	2.40	0.674	0.049	2.10	0.708
0.062	2.70	0.687	0.059	2.50	0.722
0.082	3.40	0.712	0.079	3.20	0.750
0.103	4.10	0.731	0.099	3.90	0.769
0.154	5.70	0.766	0.148	5.40	0.804
0.205	7.10	0.789	0.197	6.70	0.823
0.257	8.60	0.809	0.247	7.90	0.840
0.308	9.70	0.824	0.395	11.20	0.873
0.410	11.90	0.858	0.493	13.00	0.894
0.513	13.90	0.888	0.592	14.80	0.919
0.616	15.60	0.918	0.691	16.50	0.943
0.718	17.00	0.947	0.888	18.80	0.979
0.821	18.30	0.975	0.987	19.70	0.994
0.924	19.20	0.987	1.086	20.20	1.001
1.129	19.70	1.005	1.184	20.20	1.005
553601			554201		
ETA/DELTA	DALPHA	U/Q	ETA/DELTA	DALPHA	U/Q
0.005	0.0	0.426	0.005	0.0	0.404
0.007	0.0	0.496	0.006	0.0	0.521
0.010	0.0	0.563	0.014	0.0	0.622
0.014	0.0	0.617	0.018	1.20	0.658
0.019	0.50	0.646	0.028	1.70	0.693
0.029	1.30	0.689	0.037	2.20	0.724
0.038	1.60	0.717	0.055	3.00	0.768
0.048	2.30	0.743	0.074	3.50	0.800
0.058	2.60	0.762	0.092	4.50	0.823
0.077	3.40	0.791	0.139	5.80	0.859
0.096	4.00	0.815	0.185	7.00	0.876
0.144	5.50	0.852	0.231	8.10	0.895
0.192	6.70	0.869	0.277	8.90	0.917
0.240	7.50	0.884	0.370	10.50	0.928
0.288	8.80	0.895	0.462	11.90	0.938
0.384	10.60	0.909	0.554	13.30	0.943
0.576	13.70	0.937	0.647	15.50	0.949
0.671	15.30	0.952	0.739	15.60	0.964
0.767	16.50	0.964	0.832	16.60	0.979
0.959	18.60	0.990	1.016	18.10	0.996
1.055	19.20	1.001	1.109	18.50	1.001
1.151	19.50	1.005	1.201	18.80	1.005

Table 12 (Continued)

554801			555401		
ETA/DELTA	DALPHA	U/Q	ETA/DELTA	DALPHA	U/Q
0.005	0.0	0.374	0.005	0.0	0.351
0.006	0.0	0.453	0.006	0.0	0.413
0.014	0.0	0.578	0.009	0.0	0.504
0.018	1.20	0.612	0.014	0.0	0.569
0.036	2.30	0.679	0.019	1.00	0.606
0.045	3.00	0.702	0.028	1.40	0.639
0.054	3.40	0.712	0.037	1.80	0.670
0.072	3.90	0.737	0.046	2.10	0.686
0.090	4.50	0.759	0.056	2.80	0.707
0.135	5.70	0.810	0.074	3.40	0.722
0.181	6.10	0.834	0.093	4.10	0.756
0.226	8.20	0.852	0.139	5.30	0.786
0.271	9.10	0.876	0.185	6.60	0.817
0.361	10.60	0.910	0.278	9.10	0.873
0.452	12.50	0.927	0.370	10.90	0.902
0.542	13.50	0.942	0.463	12.10	0.926
0.632	14.70	0.955	0.555	13.70	0.950
0.723	15.70	0.965	0.740	16.20	0.974
0.813	16.70	0.976	0.833	16.80	0.982
0.994	18.20	0.994	1.018	18.30	0.996
1.084	18.80	1.001	1.110	18.80	1.001
1.174	19.00	1.005	1.203	19.10	1.005
250001			251201		
ETA/DELTA	DALPHA	U/Q	ETA/DELTA	DALPHA	U/Q
0.009	0.0	0.457	0.008	0.0	0.381
0.009	0.0	0.457	0.008	0.0	0.381
0.009	0.0	0.457	0.008	0.0	0.381
0.009	0.0	0.457	0.011	0.0	0.482
0.012	0.0	0.524	0.015	0.0	0.532
0.017	0.0	0.557	0.023	0.0	0.570
0.026	0.0	0.599	0.031	1.00	0.595
0.034	0.60	0.626	0.046	1.90	0.630
0.051	1.20	0.661	0.061	2.80	0.654
0.068	1.60	0.689	0.076	3.50	0.677
0.085	1.90	0.710	0.092	4.10	0.692
0.102	2.10	0.724	0.122	5.00	0.720
0.136	2.60	0.748	0.153	6.00	0.747
0.170	3.00	0.769	0.229	7.90	0.793
0.256	3.70	0.812	0.305	8.90	0.822
0.341	4.20	0.844	0.382	10.80	0.851
0.426	4.60	0.873	0.458	12.00	0.875
0.511	4.90	0.904	0.610	13.60	0.917
0.682	5.50	0.942	0.763	14.70	0.959
0.852	5.70	0.976	0.916	15.40	0.987
1.022	5.70	0.998	1.068	15.80	1.001
1.193	5.70	1.005	1.221	15.90	1.005

Table 12 (Continued)

252401			253601		
ETA/DELTA	DALPHA	U/Q	ETA/DELTA	DALPHA	U/Q
0.007	0.0	0.388	0.006	0.0	0.376
0.007	0.0	0.388	0.008	0.0	0.451
0.009	0.0	0.457	0.011	0.0	0.502
0.013	0.0	0.495	0.017	0.0	0.546
0.020	0.0	0.529	0.023	1.90	0.580
0.027	1.20	0.555	0.034	3.50	0.617
0.040	2.50	0.587	0.045	4.60	0.643
0.053	3.70	0.615	0.057	5.40	0.663
0.066	4.40	0.631	0.068	6.10	0.681
0.080	5.00	0.649	0.091	7.40	0.711
0.106	6.60	0.672	0.114	8.60	0.732
0.133	7.60	0.690	0.170	11.00	0.761
0.199	10.40	0.736	0.227	13.10	0.781
0.265	12.70	0.768	0.284	15.10	0.795
0.332	14.70	0.805	0.341	17.00	0.812
0.398	16.70	0.829	0.454	20.60	0.846
0.531	20.00	0.882	0.568	23.70	0.890
0.663	22.70	0.924	0.681	26.60	0.927
0.796	24.70	0.960	0.795	29.00	0.958
0.929	25.90	0.989	0.909	30.60	0.983
1.061	26.60	1.000	1.022	31.60	0.998
1.194	27.10	1.005	1.249	32.00	1.005
254801			256001		
ETA/DELTA	DALPHA	U/Q	ETA/DELTA	DALPHA	U/Q
0.006	0.0	0.353	0.006	0.0	0.325
0.008	0.0	0.454	0.008	0.0	0.423
0.012	0.0	0.529	0.012	0.0	0.534
0.018	0.0	0.584	0.018	0.0	0.615
0.023	1.40	0.621	0.023	0.60	0.654
0.035	2.60	0.666	0.035	1.40	0.707
0.047	3.50	0.707	0.047	2.00	0.738
0.058	4.00	0.730	0.058	2.40	0.763
0.070	4.80	0.748	0.070	2.90	0.786
0.094	5.90	0.778	0.094	3.90	0.817
0.117	6.90	0.798	0.117	4.70	0.837
0.175	9.20	0.838	0.175	6.50	0.873
0.234	10.90	0.856	0.234	7.90	0.889
0.292	12.30	0.864	0.292	9.10	0.901
0.351	13.80	0.873	0.351	10.20	0.908
0.468	16.50	0.887	0.468	12.40	0.921
0.585	19.40	0.910	0.585	14.70	0.937
0.702	22.10	0.933	0.702	16.80	0.955
0.819	24.60	0.957	0.819	19.00	0.972
0.936	26.50	0.987	0.936	20.30	0.987
1.053	27.80	1.001	1.053	21.40	1.001
1.170	28.40	1.005	1.170	22.00	1.005

Table 13. Correlation parameter data - Francis (24)

550001			550601		
WC/WCL	ETA/DELTA W/Q ϵ +1-U/Q	WC/WCL	ETA/DELTA W/Q ϵ +1-U/Q	WC/WCL	ETA/DELTA W/Q ϵ +1-U/Q
1.000	0.008	1.000	1.000	0.007	1.000
1.000	0.008	1.000	1.000	0.007	1.000
1.000	0.008	1.000	1.000	0.007	1.000
1.000	0.008	1.000	1.000	0.010	1.000
1.000	0.012	1.000	1.000	0.015	1.000
1.000	0.017	1.000	1.000	0.022	1.000
1.000	0.025	1.000	0.966	0.029	0.965
0.925	0.034	0.925	0.922	0.044	0.917
0.843	0.050	0.843	0.894	0.058	0.885
0.753	0.067	0.756	0.845	0.073	0.834
0.721	0.084	0.720	0.804	0.008	0.792
0.688	0.101	0.688	0.761	0.117	0.743
0.618	0.134	0.620	0.704	0.146	0.682
0.581	0.168	0.580	0.591	0.219	0.564
0.418	0.252	0.429	0.494	0.292	0.469
0.279	0.336	0.307	0.402	0.365	0.382
0.175	0.420	0.214	0.318	0.438	0.311
0.175	0.504	0.195	0.189	0.584	0.194
0.062	0.672	0.086	0.088	0.730	0.101
0.002	0.840	0.024	0.022	0.875	0.034
0.002	1.009	0.005	-0.000	1.021	0.002
0.002	1.177	-0.004	-0.000	1.167	-0.005
551201			551801		
WC/WCL	ETA/DELTA W/Q ϵ +1-U/Q	WC/WCL	ETA/DELTA W/Q ϵ +1-U/Q	WC/WCL	ETA/DELTA W/Q ϵ +1-U/Q
1.000	0.007	1.000	1.000	0.005	1.000
1.000	0.007	1.000	1.000	0.008	1.000
1.000	0.009	1.000	1.000	0.011	1.000
1.000	0.013	1.000	1.000	0.016	1.000
1.000	0.020	1.000	0.976	0.022	0.975
0.967	0.027	0.966	0.952	0.033	0.948
0.947	0.040	0.943	0.933	0.044	0.926
0.921	0.053	0.913	0.915	0.055	0.904
0.895	0.067	0.884	0.900	0.066	0.885
0.873	0.080	0.858	0.868	0.088	0.847
0.839	0.107	0.819	0.839	0.109	0.814
0.804	0.133	0.777	0.765	0.164	0.728
0.708	0.200	0.668	0.741	0.219	0.694
0.630	0.266	0.584	0.682	0.274	0.624
0.544	0.333	0.493	0.561	0.328	0.504
0.458	0.399	0.412	0.440	0.438	0.381
0.314	0.533	0.279	0.323	0.547	0.275
0.204	0.666	0.178	0.190	0.657	0.163
0.095	0.799	0.086	0.107	0.766	0.087
0.030	0.932	0.029	0.037	0.876	0.037
-0.026	1.065	-0.015	0.005	0.985	0.009
-0.026	1.198	-0.019	-0.038	1.095	-0.021

Table 13 (Continued)

552401			553001		
WC/WCL	ETA/DELTA	W/QE+1-U/Q	WC/WCL	ETA/DELTA	W/QE+1-U/Q
1.000	0.005	1.000	1.000	0.005	1.000
1.000	0.007	1.000	1.000	0.007	1.000
1.000	0.010	1.000	1.000	0.010	1.000
1.000	0.015	1.000	1.000	0.015	1.000
0.971	0.021	0.970	0.981	0.020	0.980
0.955	0.031	0.951	0.961	0.030	0.957
0.932	0.041	0.924	0.944	0.039	0.937
0.922	0.051	0.912	0.930	0.049	0.920
0.911	0.062	0.899	0.916	0.059	0.903
0.887	0.082	0.869	0.891	0.079	0.871
0.862	0.103	0.838	0.866	0.099	0.839
0.801	0.154	0.766	0.809	0.148	0.769
0.745	0.205	0.702	0.757	0.197	0.709
0.680	0.257	0.632	0.706	0.247	0.651
0.630	0.308	0.580	0.552	0.395	0.493
0.520	0.410	0.467	0.457	0.493	0.401
0.408	0.513	0.360	0.353	0.592	0.304
0.301	0.616	0.262	0.245	0.691	0.208
0.205	0.718	0.173	0.079	0.888	0.068
0.107	0.821	0.087	0.007	0.987	0.010
0.033	0.924	0.032	-0.034	1.086	-0.021
-0.010	1.129	-0.011	-0.034	1.184	-0.025
553601			554201		
WC/WCL	ETA/DELTA	W/QE+1-U/Q	WC/WCL	ETA/DELTA	W/QE+1-U/Q
1.000	0.005	1.000	1.000	0.005	1.000
1.000	0.007	1.000	1.000	0.006	1.000
1.000	0.010	1.000	1.000	0.014	1.000
1.000	0.014	1.000	0.955	0.018	0.953
0.982	0.019	0.982	0.935	0.028	0.931
0.953	0.029	0.949	0.916	0.037	0.907
0.942	0.038	0.935	0.883	0.055	0.865
0.916	0.048	0.904	0.862	0.074	0.837
0.905	0.058	0.889	0.820	0.092	0.785
0.874	0.077	0.850	0.762	0.139	0.712
0.850	0.096	0.818	0.705	0.185	0.648
0.787	0.144	0.741	0.651	0.231	0.585
0.735	0.192	0.680	0.610	0.277	0.535
0.699	0.240	0.636	0.523	0.370	0.448
0.637	0.288	0.570	0.440	0.462	0.371
0.546	0.384	0.478	0.352	0.554	0.296
0.369	0.576	0.312	0.199	0.647	0.179
0.267	0.671	0.223	0.192	0.739	0.160
0.184	0.767	0.154	0.115	0.832	0.094
0.024	0.959	0.025	-0.009	1.016	-0.002
-0.026	1.055	-0.017	-0.044	1.109	-0.028
-0.051	1.151	-0.036	-0.071	1.201	-0.049

Table 13 (Continued)

554801			555401		
WC/WCL	ETA/DELTA	W/QE+1-U/Q	WC/WCL	ETA/DELTA	W/QE+1-U/Q
1.000	0.005	1.000	1.000	0.005	1.000
1.000	0.006	1.000	1.000	0.006	1.000
1.000	0.014	1.000	1.000	0.009	1.000
0.958	0.018	0.957	1.000	0.014	1.000
0.918	0.036	0.909	0.966	0.019	0.964
0.892	0.045	0.878	0.952	0.028	0.948
0.877	0.054	0.861	0.937	0.037	0.930
0.857	0.072	0.835	0.926	0.046	0.916
0.833	0.090	0.804	0.900	0.056	0.885
0.782	0.135	0.737	0.878	0.074	0.858
0.765	0.181	0.710	0.850	0.093	0.821
0.668	0.226	0.606	0.801	0.139	0.761
0.623	0.271	0.552	0.744	0.185	0.692
0.543	0.361	0.461	0.624	0.278	0.551
0.432	0.452	0.356	0.527	0.370	0.448
0.368	0.542	0.295	0.456	0.463	0.373
0.286	0.632	0.225	0.353	0.555	0.275
0.212	0.723	0.165	0.168	0.740	0.127
0.133	0.813	0.104	0.119	0.833	0.088
0.004	0.994	0.008	-0.015	1.018	-0.005
-0.052	1.084	-0.031	-0.064	1.110	-0.036
-0.071	1.174	-0.045	-0.094	1.203	-0.057
250001			251201		
WC/WCL	ETA/DELTA	W/QE+1-U/Q	WC/WCL	ETA/DELTA	W/QE+1-U/Q
1.000	0.009	1.000	1.000	0.008	1.000
1.000	0.009	1.000	1.000	0.008	1.000
1.000	0.009	1.000	1.000	0.008	1.000
1.000	0.009	1.000	1.000	0.011	1.000
1.000	0.012	1.000	1.000	0.015	1.000
1.000	0.017	1.000	1.000	0.023	1.000
1.000	0.026	1.000	0.961	0.031	0.960
0.934	0.034	0.934	0.924	0.046	0.920
0.862	0.051	0.860	0.885	0.061	0.879
0.810	0.068	0.806	0.854	0.076	0.843
0.769	0.085	0.763	0.826	0.092	0.813
0.741	0.102	0.733	0.782	0.122	0.764
0.665	0.136	0.659	0.731	0.153	0.707
0.600	0.170	0.595	0.624	0.229	0.592
0.475	0.256	0.473	0.562	0.305	0.525
0.374	0.341	0.378	0.433	0.382	0.407
0.287	0.426	0.296	0.341	0.458	0.324
0.216	0.511	0.224	0.205	0.610	0.201
0.060	0.682	0.093	0.100	0.763	0.098
0.003	0.852	0.026	0.028	0.916	0.029
0.003	1.022	0.004	-0.016	1.068	-0.010
0.003	1.193	-0.003	-0.027	1.221	-0.020

Table 13 (Continued)

252401			253601		
WC/WCL	ETA/DELTA W/QE+1-U/Q		WC/WCL	ETA/DELTA W/QE+1-U/Q	
1.000	0.007	1.000	1.000	0.006	1.000
1.000	0.007	1.000	1.000	0.008	1.000
1.000	0.009	1.000	1.000	0.011	1.000
1.000	0.013	1.000	1.000	0.017	1.000
1.000	0.020	1.000	0.959	0.023	0.958
0.972	0.027	0.971	0.923	0.034	0.918
0.940	0.040	0.937	0.898	0.045	0.889
0.910	0.053	0.903	0.879	0.057	0.867
0.892	0.066	0.882	0.863	0.068	0.846
0.876	0.080	0.863	0.832	0.091	0.808
0.833	0.106	0.815	0.802	0.114	0.772
0.805	0.133	0.783	0.741	0.170	0.703
0.721	0.199	0.689	0.685	0.227	0.643
0.645	0.265	0.608	0.628	0.284	0.586
0.574	0.332	0.530	0.572	0.341	0.530
0.497	0.398	0.455	0.455	0.454	0.419
0.354	0.531	0.316	0.344	0.568	0.308
0.218	0.663	0.195	0.228	0.681	0.202
0.104	0.796	0.096	0.121	0.795	0.109
0.029	0.929	0.026	0.044	0.909	0.041
-0.018	1.061	-0.009	-0.008	1.022	-0.002
-0.052	1.194	-0.032	-0.029	1.249	-0.021
254801			256001		
WC/WCL	ETA/DELTA W/QE+1-U/Q		WC/WCL	ETA/DELTA W/QE+1-U/Q	
1.000	0.006	1.000	1.000	0.006	1.000
1.000	0.008	1.000	1.000	0.008	1.000
1.000	0.012	1.000	1.000	0.012	1.000
1.000	0.018	1.000	1.000	0.018	1.000
0.965	0.023	0.963	0.981	0.023	0.980
0.933	0.035	0.927	0.954	0.035	0.949
0.910	0.047	0.897	0.934	0.047	0.924
0.896	0.058	0.879	0.920	0.058	0.906
0.874	0.070	0.852	0.903	0.070	0.883
0.844	0.094	0.813	0.867	0.094	0.837
0.815	0.117	0.777	0.838	0.117	0.800
0.747	0.175	0.692	0.770	0.175	0.714
0.694	0.234	0.632	0.713	0.234	0.649
0.649	0.292	0.584	0.663	0.292	0.593
0.598	0.351	0.533	0.615	0.351	0.542
0.501	0.468	0.440	0.512	0.468	0.440
0.386	0.585	0.335	0.394	0.585	0.331
0.268	0.702	0.231	0.274	0.702	0.225
0.146	0.819	0.130	0.136	0.819	0.114
0.045	0.936	0.039	0.046	0.936	0.041
-0.030	1.053	-0.018	-0.036	1.053	-0.023
-0.066	1.170	-0.043	-0.082	1.170	-0.054

Table 14. Shape factor data - Francis (24)

PROFILE	B.L.THK	DISP.THK1	DISP.THK2	UQCL	WQCL	ALPHA-CL
550001	0.627	0.0762	-0.0044	0.619	0.028	2.60
550601	0.722	0.0907	-0.0189	0.597	0.076	7.30
551201	0.787	0.1030	-0.0426	0.567	0.126	12.52
551801	0.954	0.1295	-0.0705	0.535	0.163	16.95
552401	1.013	0.1349	-0.0985	0.565	0.201	19.59
553001	1.060	0.1261	-0.1150	0.587	0.211	19.79
553601	1.105	0.1025	-0.1184	0.617	0.211	18.89
554201	1.161	0.0966	-0.1101	0.622	0.202	17.99
554801	1.172	0.1160	-0.1083	0.578	0.190	18.24
555401	1.135	0.1163	-0.1038	0.569	0.186	18.14
250001	0.615	0.0817	-0.0107	0.599	0.060	5.71
251201	0.685	0.0956	-0.0420	0.570	0.160	15.66
252401	0.784	0.1240	-0.0908	0.529	0.262	26.34
253601	0.912	0.1357	-0.1398	0.546	0.334	31.45
254801	0.897	0.1054	-0.1394	0.584	0.301	27.29
256001	0.910	0.0841	-0.1149	0.615	0.235	20.93
PROFILE	MOM.THK11	MOM.THK12	MOM.THK21	MOM.THK22	H-1	H-2
550001	0.0584	0.0010	-0.0034	-0.0001	1.304	66.696
550601	0.0704	0.0039	-0.0151	-0.0009	1.288	21.749
551201	0.0782	0.0088	-0.0340	-0.0037	1.318	11.647
551801	0.0970	0.0154	-0.0552	-0.0083	1.336	8.447
552401	0.1046	0.0198	-0.0794	-0.0144	1.289	6.829
553001	0.1002	0.0197	-0.0954	-0.0181	1.258	6.352
553601	0.0840	0.0159	-0.1029	-0.0184	1.220	6.450
554201	0.0792	0.0135	-0.0965	-0.0154	1.219	7.128
554801	0.0918	0.0162	-0.0921	-0.0145	1.264	7.473
555401	0.0905	0.0166	-0.0871	-0.0139	1.286	7.450
250001	0.0619	0.0025	-0.0082	-0.0004	1.320	29.508
251201	0.0719	0.0094	-0.0328	-0.0043	1.331	9.840
252401	0.0907	0.0221	-0.0691	-0.0162	1.367	5.609
253601	0.1028	0.0303	-0.1093	-0.0316	1.320	4.427
254801	0.0842	0.0226	-0.1175	-0.0306	1.252	4.551
256001	0.0680	0.0149	-0.1006	-0.0207	1.237	5.562

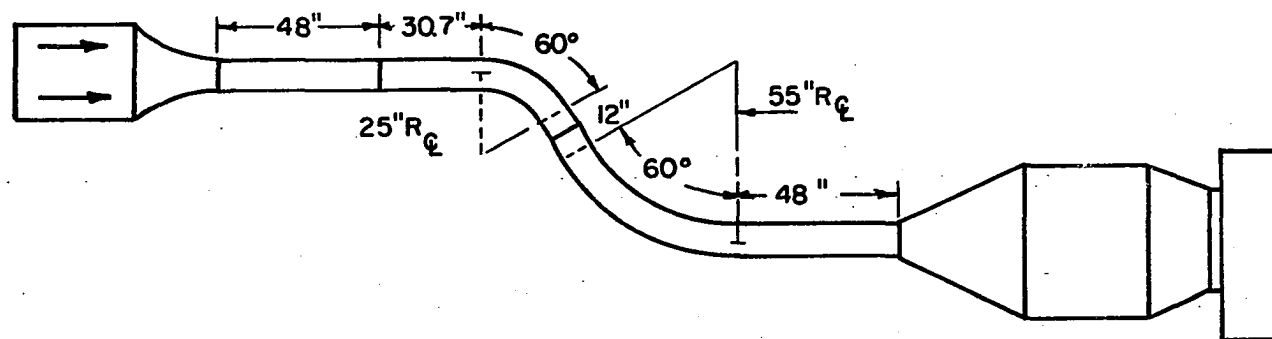


Figure 70. Schematic of test apparatus used by Pierce and Klinksiek (59)

Table 15. Experimental profile data - Pierce and Klinksiek (59)

250002			250602		
ETA	VELOCITY	ALPHA	ETA	VELOCITY	ALPHA
0.005	27.00	8.00	0.005	27.40	14.00
0.010	31.50	8.00	0.010	29.40	14.00
0.015	35.40	8.00	0.015	35.40	12.00
0.020	39.50	9.00	0.020	40.60	12.50
0.025	45.00	9.00	0.025	44.40	13.00
0.030	47.80	9.50	0.030	47.80	12.00
0.035	51.10	10.00	0.035	49.60	11.80
0.040	52.60	9.00	0.040	51.70	11.30
0.060	56.60	9.00	0.060	54.40	11.00
0.080	59.60	7.00	0.100	58.90	9.00
0.120	63.60	7.00	0.140	61.50	8.00
0.140	65.30	6.50	0.200	64.60	7.00
0.160	66.30	4.50	0.300	68.10	5.00
0.200	68.10	4.00	0.400	71.60	4.00
0.350	73.90	3.00	0.500	74.60	2.50
0.450	76.90	2.50	0.700	78.00	2.00
0.700	82.70	1.50	1.000	83.10	1.00
1.300	91.20	0.0	1.200	85.10	0.0
1.700	93.80	0.0	1.600	88.30	0.0
2.100	96.00	0.0	2.100	91.70	0.0
2.400	96.80	0.0	2.600	92.90	0.0
2.900	98.60	0.0	3.200	94.70	0.0
251202			252402		
ETA	VELOCITY	ALPHA	ETA	VELOCITY	ALPHA
0.005	27.00	20.00	0.005	33.40	42.50
0.010	29.70	20.00	0.010	36.90	42.50
0.015	34.40	20.00	0.015	46.70	38.50
0.020	41.10	19.00	0.020	50.80	34.50
0.025	46.70	18.50	0.025	55.40	32.50
0.030	50.80	19.50	0.030	57.00	31.00
0.035	52.90	17.50	0.035	58.90	29.50
0.040	55.10	17.50	0.040	60.90	28.00
0.060	58.30	15.00	0.060	64.90	27.50
0.080	61.50	15.50	0.080	66.70	25.50
0.100	62.50	15.00	0.100	68.40	24.00
0.120	64.90	14.00	0.120	69.80	22.50
0.180	68.10	12.00	0.200	73.10	19.50
0.250	69.80	10.50	0.400	75.00	13.00
0.350	72.70	9.00	0.600	78.40	9.00
0.500	76.50	5.50	0.900	84.30	4.50
0.900	82.70	2.00	1.300	89.60	2.50
1.500	89.60	1.00	1.800	92.50	0.50
1.700	91.20	0.0	2.100	93.80	0.0
2.000	93.40	0.0	2.600	95.10	0.50
2.500	95.50	0.0	2.700	95.50	0.0
3.100	97.70	0.0	2.900	96.00	0.0

Table 15 (Continued)

253602			254802		
ETA	VELOCITY	ALPHA	ETA	VELOCITY	ALPHA
0.005	30.10	42.00	0.005	33.40	35.00
0.010	40.60	42.00	0.010	36.40	35.00
0.015	50.20	38.00	0.015	47.20	33.00
0.020	54.40	40.00	0.020	53.20	32.00
0.025	58.60	37.50	0.025	58.90	32.00
0.030	61.20	35.00	0.030	62.20	30.50
0.035	63.60	34.00	0.035	64.90	30.00
0.040	66.30	32.00	0.040	66.70	30.00
0.060	69.80	31.00	0.060	71.30	28.00
0.080	72.70	29.00	0.080	74.20	26.50
0.100	74.60	27.00	0.100	76.50	25.00
0.120	76.50	26.00	0.120	78.80	24.50
0.180	80.30	22.50	0.180	81.90	21.00
0.250	82.30	20.00	0.250	84.70	20.00
0.450	84.30	15.00	0.300	85.90	17.00
0.600	83.10	15.00	0.450	87.10	13.50
0.900	85.10	9.00	0.550	87.50	12.00
1.300	88.70	3.00	1.000	88.30	5.50
1.700	92.50	1.00	1.700	92.10	2.00
2.200	94.70	0.0	2.100	93.80	0.50
2.600	95.50	0.0	2.400	94.70	0.0
2.900	96.40	0.0	2.900	96.00	0.0
256002			554202		
ETA	VELOCITY	ALPHA	ETA	VELOCITY	ALPHA
0.005	36.40	33.00	0.005	23.10	13.00
0.010	41.70	33.00	0.015	31.50	13.00
0.015	49.30	32.00	0.020	46.10	12.50
0.020	55.40	32.00	0.035	55.70	13.00
0.025	59.60	30.50	0.040	57.00	13.00
0.030	62.20	29.00	0.060	61.90	12.50
0.035	64.60	28.50	0.100	66.70	11.00
0.040	66.30	28.00	0.120	67.70	11.00
0.060	71.30	27.50	0.140	70.20	10.50
0.080	73.90	27.00	0.180	72.70	10.00
0.100	77.20	25.00	0.300	78.80	7.00
0.120	78.40	24.00	0.450	84.70	4.00
0.200	83.10	21.00	0.600	89.20	1.00
0.400	88.70	16.50	0.800	93.40	-1.00
0.700	90.80	10.50	1.100	96.00	-2.50
1.000	92.10	8.50	1.400	96.40	-2.00
1.300	92.90	5.50	1.700	96.80	-1.50
1.600	93.80	3.00	1.900	96.80	-1.00
2.000	94.70	1.50	2.200	96.80	-0.50
2.400	96.00	0.0	2.600	97.70	0.0
2.700	96.80	0.0	2.900	98.10	0.0
3.000	97.70	0.0	3.300	98.60	0.0

Table 16. Correlation parameter data - Pierce and Klinksiek (59)

250002			250602		
WC/WCL	ETA/DELTA W/QE+1-U/Q		WC/WCL	ETA/DELTA W/QE+1-U/Q	
0.885	0.002	0.945	1.035	0.002	1.023
0.885	0.004	0.935	1.035	0.003	1.024
0.885	0.005	0.927	0.962	0.005	0.971
0.945	0.007	0.960	0.981	0.007	0.983
0.945	0.009	0.954	1.000	0.008	1.000
0.973	0.011	0.976	0.962	0.010	0.961
1.000	0.013	1.000	0.954	0.011	0.951
0.945	0.014	0.946	0.933	0.013	0.928
0.945	0.022	0.942	0.921	0.020	0.910
0.817	0.029	0.817	0.826	0.033	0.806
0.817	0.043	0.805	0.772	0.046	0.747
0.781	0.050	0.766	0.712	0.065	0.681
0.611	0.057	0.627	0.571	0.098	0.553
0.562	0.072	0.582	0.486	0.131	0.472
0.452	0.126	0.471	0.337	0.163	0.359
0.391	0.161	0.411	0.280	0.229	0.298
0.254	0.251	0.282	0.151	0.327	0.185
0.0	0.466	0.070	0.0	0.392	0.097
0.0	0.610	0.044	0.0	0.523	0.063
0.0	0.753	0.021	0.0	0.686	0.027
0.0	0.861	0.013	0.0	0.850	0.014
0.0	1.040	-0.005	0.0	1.046	-0.005
251202			252402		
WC/WCL	ETA/DELTA W/QE+1-U/Q		WC/WCL	ETA/DELTA W/QE+1-U/Q	
1.013	0.002	1.007	1.000	0.002	1.000
1.013	0.003	1.008	1.000	0.004	1.000
1.013	0.005	1.009	0.952	0.006	0.950
0.987	0.007	0.989	0.900	0.007	0.890
0.973	0.008	0.975	0.873	0.009	0.851
1.000	0.010	1.000	0.852	0.011	0.824
0.945	0.012	0.943	0.830	0.013	0.795
0.945	0.014	0.941	0.807	0.015	0.764
0.868	0.020	0.859	0.799	0.022	0.740
0.884	0.027	0.868	0.766	0.030	0.698
0.868	0.034	0.849	0.740	0.037	0.664
0.834	0.041	0.808	0.713	0.044	0.630
0.761	0.061	0.726	0.655	0.074	0.557
0.699	0.084	0.664	0.504	0.148	0.428
0.631	0.118	0.592	0.387	0.222	0.329
0.442	0.169	0.430	0.221	0.333	0.196
0.188	0.304	0.234	0.131	0.480	0.108
0.099	0.507	0.124	0.028	0.665	0.041
0.0	0.574	0.062	0.0	0.776	0.018
0.0	0.676	0.039	0.028	0.961	0.014
0.0	0.845	0.018	0.0	0.998	0.000
0.0	1.047	-0.005	0.0	1.072	-0.005

Table 16 (Continued)

253602			254802		
WC/WCL	ETA/DELTA W/QE+1-U/Q		WC/WCL	ETA/DELTA W/QE+1-U/Q	
1.031	0.002	1.017	1.117	0.002	1.061
1.031	0.004	1.023	1.117	0.004	1.066
0.969	0.005	0.972	1.071	0.006	1.052
1.000	0.007	1.000	1.048	0.007	1.039
0.961	0.009	0.959	1.048	0.009	1.043
0.921	0.011	0.913	1.012	0.011	1.011
0.904	0.013	0.892	1.000	0.013	1.000
0.870	0.014	0.850	1.000	0.015	1.000
0.853	0.022	0.823	0.951	0.022	0.948
0.817	0.029	0.775	0.914	0.030	0.905
0.780	0.036	0.728	0.876	0.037	0.860
0.761	0.043	0.700	0.863	0.044	0.842
0.691	0.065	0.608	0.769	0.067	0.732
0.638	0.091	0.543	0.741	0.092	0.692
0.519	0.163	0.422	0.653	0.111	0.595
0.519	0.217	0.430	0.544	0.166	0.482
0.348	0.326	0.289	0.494	0.203	0.434
0.133	0.471	0.134	0.251	0.370	0.233
0.047	0.616	0.056	0.097	0.628	0.095
0.0	0.797	0.013	0.025	0.776	0.033
0.0	0.942	0.004	0.0	0.887	0.009
0.0	1.051	-0.005	0.0	1.072	-0.005
256002			554202		
WC/WCL	ETA/DELTA W/QE+1-U/Q		WC/WCL	ETA/DELTA W/QE+1-U/Q	
1.019	0.002	1.012	1.025	0.002	1.009
1.019	0.004	1.014	1.025	0.005	1.013
1.000	0.005	1.000	1.000	0.007	1.000
1.000	0.007	1.000	1.025	0.012	1.023
0.971	0.009	0.970	1.025	0.014	1.023
0.942	0.011	0.937	1.000	0.021	1.000
0.932	0.012	0.923	0.920	0.034	0.918
0.922	0.014	0.910	0.920	0.041	0.917
0.912	0.021	0.891	0.892	0.048	0.885
0.901	0.028	0.875	0.863	0.062	0.851
0.859	0.035	0.817	0.668	0.103	0.644
0.837	0.042	0.788	0.428	0.155	0.410
0.767	0.070	0.692	0.122	0.207	0.163
0.651	0.141	0.540	-0.134	0.275	-0.027
0.466	0.246	0.354	-0.364	0.379	-0.170
0.394	0.352	0.287	-0.284	0.482	-0.137
0.274	0.457	0.195	-0.207	0.585	-0.103
0.159	0.563	0.117	-0.134	0.654	-0.064
0.083	0.704	0.067	-0.066	0.757	-0.025
0.0	0.844	0.012	0.0	0.895	0.004
0.0	0.950	0.004	0.0	0.998	0.000
0.0	1.056	-0.005	0.0	1.136	-0.005

Table 17. Shape factor data - Pierce and Klinksiek (59)

PROFILE	B.L.THK	DISP.THK1	DISP.THK2	UQCL	WQCL	ALPHA-CL
250002	2.787	0.3037	-0.0376	0.513	0.090	10.00
250602	3.060	0.3302	-0.0508	0.459	0.106	13.00
251202	2.960	0.3457	-0.1004	0.472	0.167	19.50
252402	2.706	0.2918	-0.1978	0.332	0.304	42.50
253602	2.759	0.2600	-0.2781	0.435	0.365	40.00
254802	2.706	0.2075	-0.2646	0.597	0.345	30.00
256002	2.842	0.2038	-0.3066	0.483	0.302	32.00
554202	2.905	0.1884	-0.0137	0.616	0.137	12.50

PROFILE	MOM.THK11	MOM.THK12	MOM.THK21	MOM.THK22	H-1	H-2
250002	0.2323	0.0107	-0.0269	-0.0018	1.308	21.166
250602	0.2545	0.0150	-0.0358	-0.0033	1.297	15.477
251202	0.2675	0.0272	-0.0732	-0.0103	1.292	9.710
252402	0.2228	0.0473	-0.1505	-0.0354	1.310	5.581
253602	0.2069	0.0541	-0.2240	-0.0649	1.256	4.286
254802	0.1707	0.0407	-0.2239	-0.0556	1.215	4.757
256002	0.1658	0.0433	-0.2633	-0.0645	1.229	4.752
554202	0.1414	0.0135	-0.0002	-0.0069	1.332	1.984

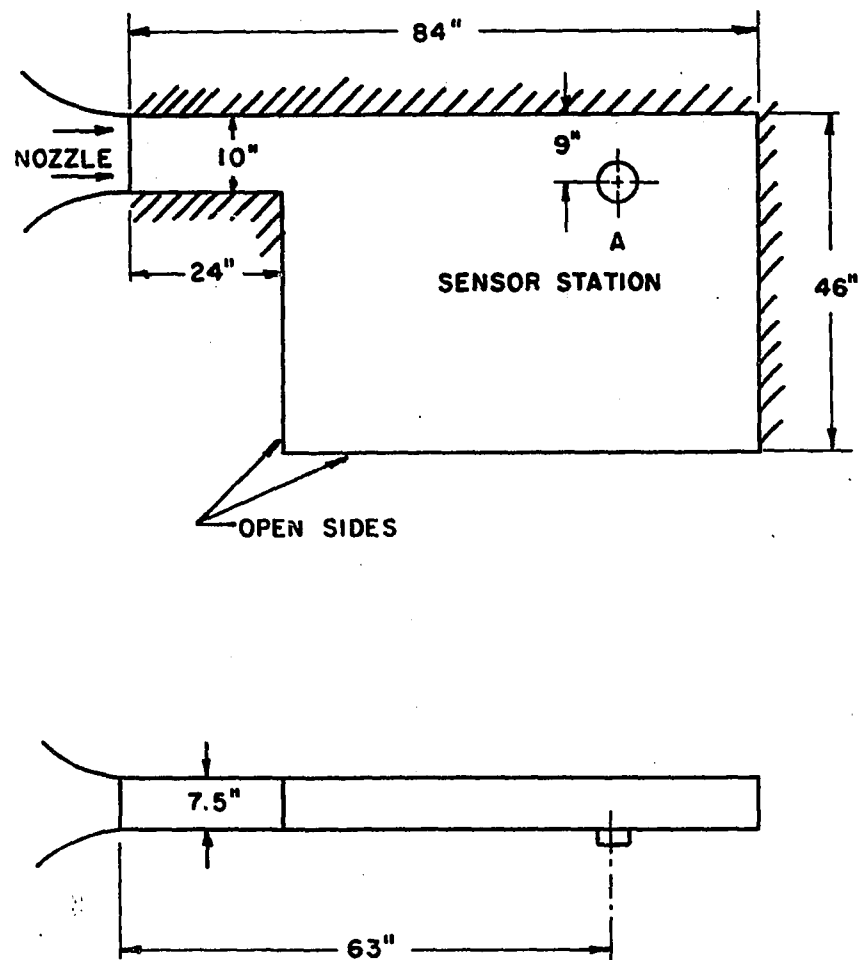


Figure 71. Schematic of test apparatus used by Pierce and Krommenhoek (60)

Table 18. Flow variable data - Pierce and Krommenhoek (60)

Profile number	U/v inlet ft $^{-1}$	dp/dx in H $_2$ O/in.	Pressure grad. direction ϕ deg.	α_{\max} deg.	$\tau_{wall} \times 10^2$ psf
010102	4.47×10^5	0.035	84	39	1.48
020102	5.29	0.060	84	35	2.15
030102	5.38	0.081	83	32	2.53
040102	6.56	0.107	83	29	3.07

Table 19. Experimental profile data - Pierce and Krommenhoek (60)

10102			20102		
ETA	VELOCITY	ALPHA	ETA	VELOCITY	ALPHA
0.014	34.40	39.00	0.014	43.50	35.00
0.019	35.70	39.00	0.019	45.60	34.00
0.034	37.60	39.00	0.034	46.60	33.00
0.059	39.50	38.00	0.059	47.60	32.00
0.084	40.60	37.00	0.084	49.10	30.00
0.109	41.80	36.00	0.109	51.50	28.00
0.159	42.90	35.00	0.159	53.70	27.00
0.209	43.50	33.00	0.209	54.60	25.00
0.259	44.00	30.00	0.259	55.90	23.00
0.309	45.10	28.00	0.309	56.80	20.00
0.409	47.20	23.00	0.409	59.20	17.00
0.509	48.70	18.00	0.509	61.10	14.00
0.609	50.50	14.00	0.609	63.00	11.00
0.709	52.80	10.00	0.709	65.30	9.00
0.809	54.20	8.00	0.809	68.50	7.00
0.909	55.90	6.00	0.909	69.50	6.00
1.009	57.60	5.00	1.009	70.70	6.00
1.109	59.20	4.00	1.109	72.10	5.00
1.209	60.00	2.00	1.259	72.90	4.00
1.359	60.70	1.00	1.409	73.60	3.00
1.609	61.50	0.0	1.559	74.20	2.00
1.709	61.90	0.0	1.709	74.80	0.0
30102			40102		
ETA	VELOCITY	ALPHA	ETA	VELOCITY	ALPHA
0.014	48.60	32.00	0.014	54.10	29.00
0.019	50.60	32.00	0.019	56.30	29.00
0.034	52.80	31.00	0.034	58.40	28.00
0.059	55.50	29.00	0.059	60.70	27.00
0.084	57.20	27.00	0.084	63.70	26.00
0.109	58.40	25.00	0.109	66.00	24.00
0.159	60.40	24.00	0.159	67.00	22.00
0.209	61.90	23.00	0.209	68.40	20.00
0.259	63.50	22.00	0.259	70.20	19.00
0.309	64.50	20.00	0.309	71.60	18.00
0.409	67.10	16.00	0.409	75.10	14.00
0.509	70.20	13.00	0.509	78.50	12.00
0.609	72.20	10.00	0.609	80.10	10.00
0.709	74.50	8.00	0.709	82.10	8.00
0.809	76.40	6.00	0.809	83.80	6.00
0.909	77.40	5.00	0.909	85.50	4.00
1.009	78.50	5.00	1.059	87.90	3.00
1.109	80.60	4.00	1.209	88.90	3.00
1.209	81.60	3.00	1.359	89.30	2.00
1.359	82.50	3.00	1.509	90.10	2.00
1.459	82.60	2.00	1.659	90.60	1.00
1.609	83.20	0.0	1.809	91.20	0.0

Table 20. Correlation parameter data - Pierce and Krommenhoek (60)

10102			20102		
WC/WCL	ETA/DELTA	W/QE+1-U/Q	WC/WCL	ETA/DELTA	W/QE+1-U/Q
1.000	0.009	1.000	1.000	0.009	1.000
1.000	0.012	1.000	0.982	0.012	0.981
1.000	0.021	1.000	0.964	0.021	0.962
0.983	0.036	0.982	0.945	0.037	0.942
0.966	0.051	0.963	0.908	0.052	0.900
0.948	0.067	0.944	0.868	0.067	0.853
0.931	0.097	0.923	0.848	0.098	0.825
0.895	0.128	0.883	0.806	0.129	0.778
0.840	0.159	0.822	0.763	0.160	0.728
0.801	0.189	0.778	0.693	0.191	0.656
0.699	0.250	0.664	0.618	0.253	0.571
0.585	0.312	0.550	0.536	0.315	0.487
0.484	0.373	0.449	0.445	0.377	0.400
0.370	0.434	0.340	0.379	0.439	0.329
0.307	0.495	0.280	0.308	0.501	0.247
0.239	0.557	0.215	0.269	0.563	0.211
0.203	0.618	0.169	0.269	0.625	0.197
0.166	0.679	0.124	0.230	0.686	0.156
0.087	0.740	0.068	0.188	0.779	0.120
0.044	0.832	0.036	0.145	0.872	0.086
0.0	0.985	0.001	0.099	0.965	0.053
0.0	1.046	-0.005	0.0	1.058	-0.005
30102			40102		
WC/WCL	ETA/DELTA	W/QE+1-U/Q	WC/WCL	ETA/DELTA	W/QE+1-U/Q
1.000	0.009	1.000	1.000	0.008	1.000
1.000	0.012	1.000	1.000	0.011	1.000
0.980	0.021	0.979	0.977	0.020	0.977
0.938	0.037	0.934	0.954	0.035	0.952
0.895	0.053	0.886	0.931	0.049	0.924
0.850	0.069	0.838	0.883	0.064	0.869
0.827	0.100	0.808	0.832	0.094	0.814
0.803	0.132	0.779	0.779	0.123	0.757
0.779	0.163	0.749	0.751	0.153	0.723
0.729	0.195	0.694	0.723	0.182	0.689
0.621	0.258	0.578	0.601	0.241	0.559
0.531	0.321	0.479	0.534	0.300	0.478
0.431	0.384	0.383	0.462	0.359	0.407
0.359	0.447	0.309	0.385	0.418	0.331
0.281	0.510	0.237	0.301	0.476	0.256
0.239	0.573	0.199	0.210	0.535	0.179
0.239	0.636	0.188	0.161	0.624	0.124
0.196	0.699	0.137	0.161	0.712	0.114
0.150	0.762	0.098	0.110	0.800	0.078
0.150	0.856	0.088	0.110	0.889	0.070
0.102	0.919	0.059	0.057	0.977	0.033
0.0	1.014	-0.005	0.0	1.065	-0.005

Table 21. Shape factor data - Pierce and Krommenhoek (60)

PROFILE	B.L.THK	DISP.THK1	DISP.THK2	UQCL	WQCL	ALPHA-CL
10102	1.633	0.2871	-0.2657	0.474	0.384	39.00
20102	1.615	0.2400	-0.2419	0.479	0.335	35.00
30102	1.587	0.2165	-0.2200	0.518	0.324	32.00
40102	1.698	0.2052	-0.2056	0.543	0.301	29.00
PROFILE	MOM.THK11	MOM.THK12	MOM.THK21	MOM.THK22	H-1	H-2
10102	0.1903	0.0813	-0.1843	-0.0747	1.509	3.557
20102	0.1692	0.0569	-0.1876	-0.0529	1.419	4.576
30102	0.1554	0.0493	-0.1733	-0.0467	1.393	4.707
40102	0.1507	0.0428	-0.1640	-0.0401	1.362	5.129